White lighting; an assessment of different organic, hybrid, non-conventional and theoretical methods

Submitted by

Enrico Angioni

A thesis submitted in fulfilment of the requirements for the degree of Doctor of Philosophy in Department of Pure and Applied Chemistry, University of Strathclyde

2016

This thesis is the result of the author's original research. It has been composed by the author and has not been previously submitted for examination, which has led to the award of a degree.

Signed:

Date:

Acknowledgements

I thank the EPSRC for funding my research and Prof. Peter Skabara for allowing me the opportunity to undertake the research under his continued supervision and support during my PhD studies.

I would like to thank the postdoctoral researchers Dr. Neil Findlay, Dr. Alex Kanibolotsky, Dr. Ruper Taylor, Dr. Joseph Cameron and Dr. Anto Inigo. They have always been willing to provide assistance and guidance on a daily basis, often sacrificing their own time to help during my studies.

I am particularly thankful to Dr. Wojciech Domagała from the Silesian University of Technology (Poland) for giving me the opportunity to take part in the Marie Curie International Research Staff Exchange Scheme as a visiting student for the Multicoloured ambipolar conducting polymers for single polymer optoelectronic devices (AmbiPOD) project.

I would like to thank Prof. Jean-Luc Brédas and all the members of his group for hosting and supporting me during my visit to Georgia Institute of Technology (USA). In particular I would like to thank Prof. Chad Risko e Dr. Veaceslav Coropceanu for their help and support on a daily basis.

I would like to thank Prof. Vladyslav Cherpak, Prof. Pavlo Stakhira and all the members of their group for hosting and supporting me during my visit to Lviv Polytechnic National University (Ukraine). Furthermore I would like to thank them for providing and characterising the devices for the studies carried out in chapter 3. In particular, I would like to thank Marian Chapran and Khrystyna Ivaniuk for their regular help and support, and for the great time spent together in Lviv.

I am grateful to all the researches that provided the some of the studies presented in chapter 3: Dr. Nataliya Kostiv (Lviv Polytechnic National University) for the photoluminescence measurements of the devices, Dr. Algirdas Lazauskas and Dr. Sigitas Tamulevičius (Kaunas University of Technology) for the X-ray diffraction and AFM measurements and analysis; Dr. Dmytro Volyniuk and Prof. Juozas Vidas

Grazulevicius (Kaunas University of Technology) for the ionisation potential measurements.

I would like to thank Prof. Robert Martin and the postdoctoral researchers Dr. Elaine Taylor-Shaw and Dr. Jochen Bruckbauer for the help in the fabrication and for the characterisation of the hybrid devices presented in chapter 2. Furthermore I would like to thank Dr. David Wallis from Plessey Semiconductors Ltd (University of Cambridge, UK) for providing blue LEDs for the studies carried out in chapter 2.

I would like to thank Dr. Ross Forgan and Ross James Marshall from the University of Glasgow for providing and characterising the MOFs and for the help in characterising the POPs presented in chapter 4.

I would like to thank Dr. Gary Conboy for the crystal structures that allowed me to perform the computational studies on the series of BBT molecules presented in chapter 5.

I would like to thank Dr. Tell Tuttle for the support and the help on the computational studies presented in chapter 2 and 3.

I would like to acknowledge all of the members of the Skabara group, past and present, for each contributing to an enjoyable working environment. Furthermore I am grateful to the technical staff in the department for all of their assistance: Patricia Keating, Alexandre Clunie, Denise Gilmour, Craig Irving and Lindsay McCulloch.

Finally I would like to thank my family that always supported and believed in me. A particular thanks goes to all my friends and to all the people that crossed my path during my PhD. Everyone in some way has contributed to my personal growth, with a smile, a chat and sometimes even with an argue.

Abbreviations

°C	degree Celsius
2D	two dimensional
3D	three dimensional
A	acceptor
A	Ampere
Å	Angstrom
AFM	atomic force microscopy
a.u.	arbitrary units
bBT	bis-benzothiadiazole
BBT	benzobisthiazole
bBT	bisbenzothiadiazole
BDT	benzodithiophene
BHJ	bulk heterojunction
BET	Brunauer–Emmett–Teller
BLA	bond length alternation
BODIPY	boron-dipyrromethene (4,4-difluoro-4-bora-3a,4a-diaza-s-indacene)
b.p.	boiling point
BT	benzothiadiazole
BTz	bisthiazole
bipy	4,4′-bipyridine
Bu	butyl
c	concentration
C	capacitance
ca.	*circa*
calc.	calculated
CB	chlorobenzene
CCT	Correlated Colour Temperature
CFL	compact fluorescent lamps
CHDV	1,4-cyclohexanedimethanol divinyl ether
CIE	Commission Internationale de l'Éclairage
conc.	concentrated
cm	centimetre

CRI	Colour Rendering Index
CT	charge transfer
CV	cyclic voltammetry
d	doublet
D	donor
dd	doublet of doublets
o-DCB	1,2-dichlorobenzene
DCM	dichloromethane
DFT	Density Functional Theory
DL	double layer
DMA	*N*,*N*-dimethylacetamide
DMF	N,N-dimethylformamide
DMSO	dimethyl sulfoxide
DPP	diketopyrrolopyrrole
DTP	dithienopyrrole
DSC	differential scanning calorimetry
e.g.	*exempli gratia*
e^-	electron
$E_{1/2}$	half-wave potential
E_a	band gap of the p-doped extrinsic semiconductor
E_{BLA}	bond length alternation energy
E_d	band gap of the n-doped extrinsic semiconductor
E_f	Fermi level
E_g	HOMO-LUMO energy gap
E_{int}	intramolecular energy
E_{ox}	oxidation potential
Et	ethyl
E_{red}	reduction potential
E_{res}	resonance energy
E_θ	planarization energy
eV	electron volts
EDOT	3,4-ethylenedioxythiophene
EL	electroluminescence
ELQY	electroluminescence quantum yield

EML	emissive layer
EQE	external quantum efficiency
ESIPT	excited state intramolecular proton transfer
ETL	electron transport layer
F	furan
Fc	ferrocene
Fc^+	ferrocenium
FWHM	full width at half maximum
g	gram
GPC	gel-permeation chromatography
h	hour
h	Planck's constant
h^+	hole
H_4tcbpe	4′,4‴,4⁗,4⁗′-(ethene-1,1,2,2-tetrayl)tetrakis ([1,10-biphenyl]-4-carboxylic acid)
HIL	hole injection layer
HIPE	high internal phase emulsion
HMDS	hexamethyldisilazane
HOMO	highest occupied molecular orbital
Hz	hertz
I	current
ICT	intramolecular charge transfer
iR	internal resistance
ISC	intersystem crossing
IUPAC	International Union of Pure and Applied Chemistry
ITO	indium tin oxide
J	Joule
J	coupling constant
K	Kelvin
L	Litre
LDA	lithium diisopropylamide
LED	light emitting diode
LiTMP	lithium tetramethylpiperidide
LUMO	lowest unoccupied molecular orbital

M	molarity
m	metre
m-MTDATA	4,4′,4″-tris[3-methylphenyl(phenyl)amino]triphenylamine
MALDI-TOF	matrix-assisted laser desorption/ionization – time of flight
Me	methyl
mg	milligram
MHz	megahertz
min	minute
mL	millilitre
mM	millimolar
mmol	millimole
MOF	metalorganic framework
mol	mole
MP2	Moller−Plesset perturbation wave function theory 2
mV	millivolt
m_s	spin momentum
NBS	N-bromosuccinimide
n-Bu	n-butyl
NIR	near infra-red
NP	nanoparticle
NPB	N,N′-di(1-naphthyl)-N,N′-diphenylbenzidine
NOx	mono-nitrogen oxides NO and NO_2 (nitric oxide and nitrogen dioxide)
n	non-bonding orbital
n	number
N	Avogadro's number
nm	nanometre
NMR	nuclear magnetic resonance
OFET	organic field-effect transistor
OLED	organic light-emitting diode
OTFT	organic thin film transistor
OPV	organic photovoltaic
OVS	octavinylsilsequioxane
p-	para-

P	pressure
P_0	saturated pressure of adsorbate gas
P3HT	poly(3-hexylthiophene)
PAc	polyacetylene
PAG	photo-acid generator
PBD	2-(4-biphenyl)-5-(4-tert-butylphenyl)1,3,4-oxadiazole
PC	phosphor conversion
PCE	power conversion efficiency
pdt	2,3-pirazinedithiol
PEG4000	polyethylene glycol 4000
PEDOT	poly(3,4-ethylenedioxythiophene)
PFO	poly(9,9-di-n-octylfluorenyl-2,7-diyl)
Ph	phenyl
PLED	polymer light-emitting diode
PLQY	photoluminescence quantum yield
PES	potential energy surface
PMMA	poly(methyl methacrylate)
POP	porous organic polymer
ppm	parts per million
PT	poly(thiophene)
PTV	poly(thienylenevinylene)
q	quartet
RI	resolution of identity
QSDFT	Quenched Solid Density Functional Theory
QY	quantum yield
QW	quantum well
R	alkyl substituent
RGB	red green blue colour model
RKu	kurtosis
RSk	skewness
r.t.	room temperature
s	second / singlet
SCLC	space-charge-limited current
SEC	spectroelectrochemistry

SI	standard international
SIE	self-interaction error
SL	single layer
SP	surface plasmon
SSL	solid-state lighting
STP	standard temperature and pressure
t	triplet
T_g	glass transition temperature
T_m	melting temperature
T	temperature
TADF	thermally activated delayed fluorescent
TBA	tetra-n-butylammonium
TD	time dependent
TGA	thermogravimetric analysis
Th	thiophene
THF	tetrahydrofuran
TEMED	Tetramethylethylenediamine
TIPS	triisopropylsilyl
TLC	thin-layer chromatography
TNT	Trinitrotoluene
TMS	trimethylsilyl
TOF	time of flight
TPA	triphenylamine
TPD	N,N′-diphenyl-N,N′-bis(methylphenyl)-1,1′-biphenyl-4,4′ diamine
UV	ultra-violet
V	Volt
V	operating voltage
Vis	visible
Vs.	*versus*
VSD	source-drain voltage
w/v	weight/volume
w	weight
W	Watt
WLED	white light-emitting diode

WOLED	white organic light-emitting diode
X	halide substituent

Greek

α	1st position on heterocycle
β	2nd position on heterocycle
Γ	emissive rate of fluorescence
δ	chemical shift
ε	dielectric constant
θ	torsion angle
σ	sigma bonding orbital
σ*	sigma anti-bonding orbital
λ	wavelength
λ_{max}	wavelength of maximum absorption or emission
λ_e	reorganisation energies for electrons
λ_h	reorganisation energies for holes
μ	micro
μ	charge-carrier mobility
ν	frequency
π	pi bonding orbital
π*	pi anti-bonding orbital
τ	fluorescence lifetime
Φ_e	radiant flux
Φ_V	luminous flux
η_c	current efficiency
η_{ex}	external quantum efficiency of the blue-LED
η_{ext}	extraction efficiency of light from a blue LED dye to a resin
η_{int}	quantum efficiency of the blue LED
η_Q	quantum efficiency
η_P	luminous efficiency of the radiation (also call luminous efficacy)
η_{phos}	wavelength conversion efficiency of the yellow phosphor
η_{pkg}	extraction efficiency of light from an LED package to air
η_Q	quantum efficiency

θ	number of sites of the surface which are covered with gaseous molecule
σ	average area occupied by each molecule in a complete monolayer
τ	transmission of the photodiode of the photodiode
$\phi(\lambda)$	emission spectrum of the OLED
Φ	flux
Φ_V	light output power (also call luminous flux)

Symbols

↑	spin ½
↓	spin −½

Abstract

During the last two decades, worldwide economic growth has highlighted the issue of new and more efficient lighting technologies. The swift development of new and high performing inorganic and organic emissive materials has brought to the market competitive and efficient solid state lighting (SSL) devices with promising performance features and efficiencies well beyond those of traditional artificial lighting. They are predicted to become the next generation of general illumination systems and researchers are working worldwide in order to improve device properties, cost and environmental impact of these technologies. The principal aim of this work is to develop new emissive materials that can be employed for lighting applications using different expedients. Furthermore, in order to do this, a deep understanding of the electronic processes and of the molecular interactions that are behind their properties is desired.

In the first chapter, the fundamentals of organic electronic materials, with a particular focus on OLEDs, are described. The principles that are behind the production of white light using organic materials are discussed, with practical examples able to summarise the state of the art technologies explored currently.

In the second chapter, novel emissive materials based on the under explored bis-benzothiadiazole (bBT) unit are presented. These have been successfully incorporated as down converters in simple hybrid inorganic-organic white LEDs and their performance studied.

In chapter 3, four OLED devices that employ a novel benzothiadiazole (BT) derivative molecule as the single emissive layer are presented. The performances of the devices depended on the architecture chosen, and they achieved colour qualities similar to those of commercial fluorescent tubes.

In chapter 4, a new way to make highly emissive materials has been explored, with two metal-organic frameworks (MOFs) and four porous organic polymers (POPs) synthesised and characterised.

Finally, the role of non-covalent interactions in dictating constricted geometries have been explored in a novel class of 4,8-benzobisthiazole (BBT) materials in chapter 5.

Table of contents

Chapter 1. Introduction

1.1. Band theory

The electronic structure of solid-state materials can be explained by Band Theory. The electrons of an atom are arranged in atomic orbitals. In basic molecular orbital theory, one assumes that when atoms are combined together, they form bonding, non-bonding and antibonding orbitals of different energies. For *n* atomic orbitals in a molecule, *n* molecular orbitals are produced. Thus, a molecule with three atoms (assuming one atomic orbital for each) forms three molecular orbitals. As the number of molecular orbitals increases, the energy difference between the highest bonding and the lowest antibonding orbitals decreases, while the space between each individual orbital decreases (Figure 1.1). When considering a metal solid material, there will be a number of atoms that tend to infinity, the spacing between the highest bonding and lowest antibonding orbital reaches a minimum and there are so many molecular orbitals close together that they blur into one another forming a continuous level of energies (band).[1]

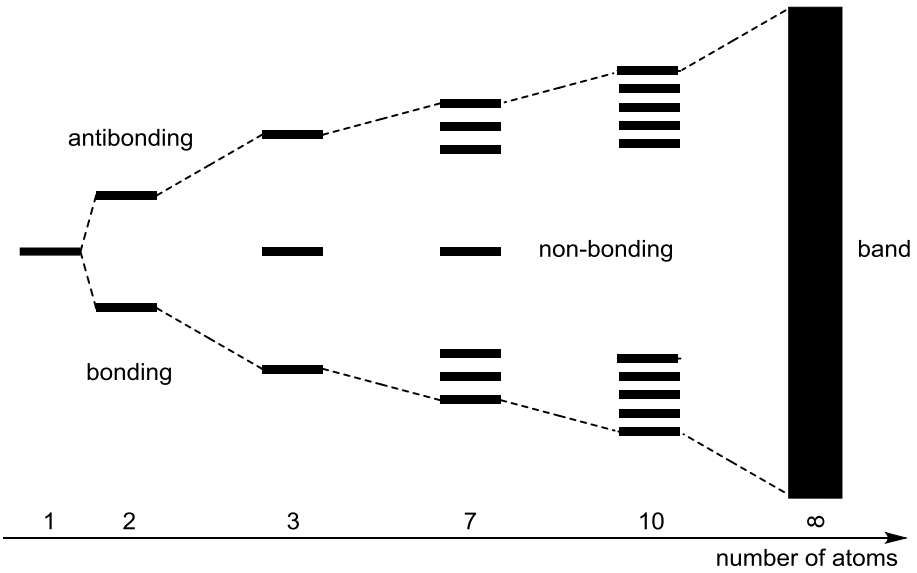

Figure 1.1. Schematic representation of the formation of a band by even increasing numbers of molecular orbitals.

According to the Fermi-Dirac distribution (a version of the Boltzmann distribution that takes into account the effect of the Pauli principle)[1] the valence electrons of these atoms will occupy the orbitals. They will fill the orbitals in order of ascending energy. Due to this behaviour, considering a system at 0 K, electrons will occupy the band until the so-called Fermi Level (E_f, valence band) and (due to continuous energy levels) there will be an unoccupied orbital at higher energy, very close to the

Fermi level. This allows the uppermost electrons to be excited into the next empty energy level of the band (conduction band) by the thermal motion of the atoms, and give rise to electrical conductivity.

An increase of temperature can provoke more vigorous thermal motion of the atoms in a conductive solid, so collisions between the moving electrons and the atoms are more likely. This can cause less efficient charge transport that decreases the electrical conductivity of a metallic solid.[1]

In many materials the valence band and the conduction band are separated by a large energy gap (E_g). In this case the electrons are unable to move between the valence and conduction bands. These materials are unable to conduct electricity and for this reason are called insulators.[1]

Otherwise, if there is just a small E_g between the valence band and the conduction band the thermal excitation or photoexcitation of the material allows partial transport of the electrons from the valence to the conduction band, leaving holes in the valence band. In this case the material will be a semi-conductor (Figure 1.2). Unlike conductors, the increase of temperature enhances the promotion of electrons in the conduction band, boosting the conductivity.[2, 3]

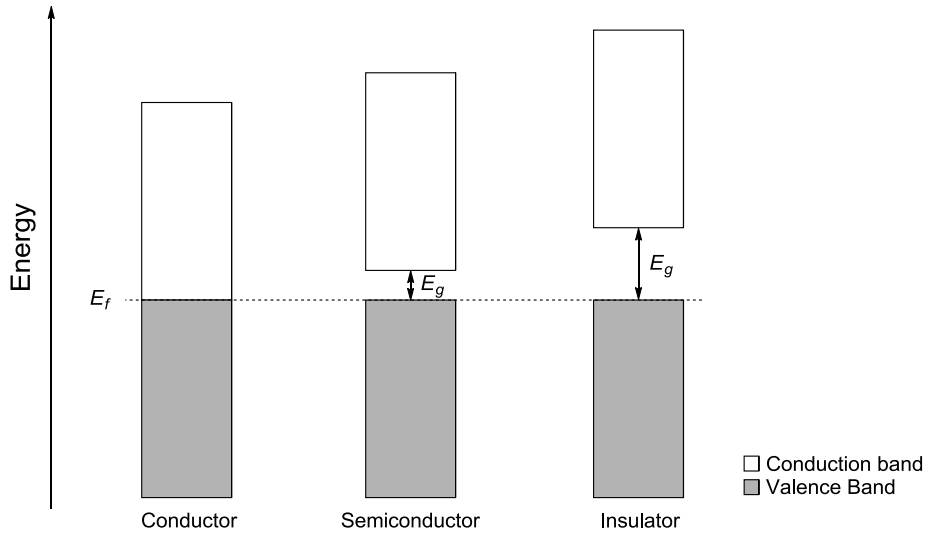

Figure 1.2. Representation of the valence and conduction band in a conductor, a semiconductor and an insulator, according to Band Theory. E_f is the Fermi level and E_g is the energy band gap between the valence and the conduction bands.

When thermal or photo excitation is not enough to induce conductivity in semiconductors, they can be doped in order to generate an additional energy level between the valence and conduction band that allows conductivity. In this case they

are called extrinsic semiconductors and can be positively (p-doped) or negatively (n-doped) doped (Figure 1.3).[2, 3]

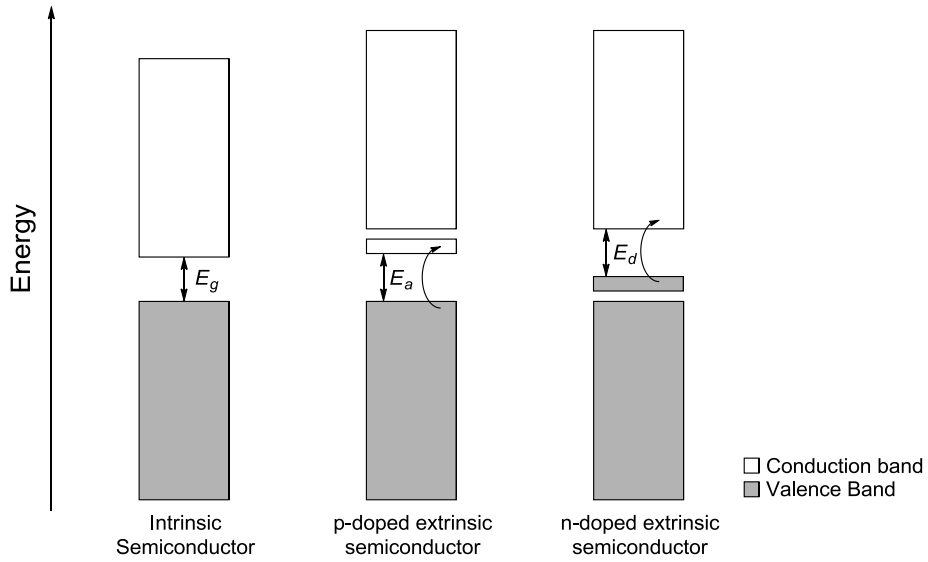

Figure 1.3. Schematic representation of intrinsic and extrinsic semiconductors. E_g is the band gap of the intrinsic semiconductor, E_a and E_d are the band gap of the p-doped and n-doped extrinsic semiconductor respectively.

In p-doped systems the addition of an element with less electrons (or of an electron-withdrawing group) extends the conduction band, reducing the energy bandgap; for n-doped systems the addition of an element with more electrons (or of an electron-donating group) extends the valence band reducing the energy bandgap.[2, 3]

1.2. Organic semiconductors and applications

The discovery of doped polyacetylene (PAc, Figure 1.4), the first organic conductive material,[4] was the driving force for research into new intrinsically conductive organic materials.

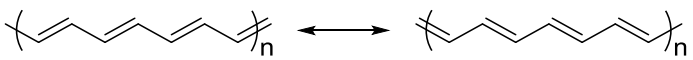

Figure 1.4. Representation of polyacetylene resonance forms.

The conductivity of this material is due to the alternation of single and double bonds. Considering the polyacetylene monomer, the two carbon atoms are linked together with a single σ bond between sp^2 orbitals and with a π bond between the p_z orbitals (Figure 1.5). This results in a large energy gap between the highest occupied molecular orbital (HOMO, π bonding orbital) and the lowest unoccupied molecular orbital (LUMO, π* antibonding orbital). Now, considering the polymer, even though

the atoms of carbon are still linked with single bonds between sp^2 orbitals, the π bonds, while formally alternating every two carbon atoms, are actually delocalised along the entire chain. In this way, considering a polymer with an infinite number of atoms, the p_z orbitals overlap, make the energy gap between the band formed with highest occupied molecular orbitals (valence band, or π bonding band) and the band formed with the lowest unoccupied molecular orbitals (conduction band, or π* antibonding band) relatively small, and this confers semiconductivity.[2, 3] Similarly this is also applicable to discrete organic molecules with extensive conjugation.[5, 6]

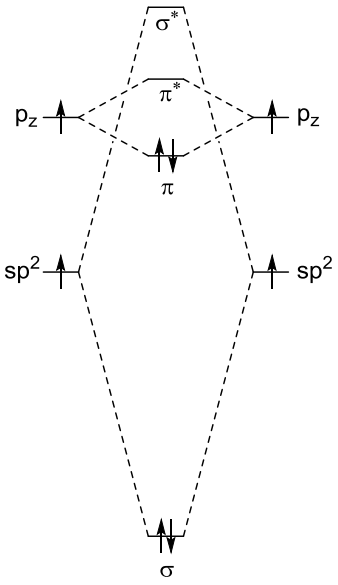

Figure 1.5. Diagram of molecular orbital formed in a carbon-carbon double bond.

The conductivity of this kind of material is strictly dependent on their energy levels and in particular on their HOMO-LUMO band gap energies.[3]

Organic semiconductors present several advantages over their inorganic analogues including flexibility, low cost, and easy processability.[7] Furthermore, oligomers are able to offer certain advantages over their polymeric analogues, such as knowledge of the precise molecular structure and complete synthetic reproducibility.[6] The applications of organic semiconductors range across electronic and photonic devices such as field-effect transistors (FETs),[8-10] light-emitting diodes (LEDs),[11, 12] solar cells,[13, 14] semiconductor lasers (SLs),[15] sensors[16] and electrochromic devices.[17]

1.3. Energy gap engineering of organic semiconductors

In order to design new organic semiconducting materials in the field of organic electronics, fine tuning of the relative positions of the HOMO and LUMO energies (and therefore of the band gap) is necessary. The energy gap can be described by the contribution of five different energetic terms that Roncali rationalised in a linear equation (Equation 1.1).[7]

$$E_g = E_{BLA} + E_{Res} + E_{Sub} + E_{\theta} + E_{Int} \qquad \text{Equation 1.1}$$

These terms play different roles and are of extreme importance for the design and the prediction of the proprieties of new materials (Figure 1.6).

Bond length alternation (BLA) provides the greatest contribution to the bandgap of the material.[18] BLA is defined as the difference between the average length of a single and double bond and was firstly studied in linear systems of trans-polyacetylene (PAc). In ideal PAc, single and double bonds should be perfectly delocalised and this should lead to a zero band gap. Unfortunately PAc does not exist as a perfectly delocalised system and its band gap is larger than zero. Consequently, synthetic approaches that lead to structural modifications resulting in a reduced BLA can be expected to produce a decrease in the HOMO-LUMO gap. For example the BLA can be reduced by inducting a quinoidal resonance structure in a material.[19, 20]

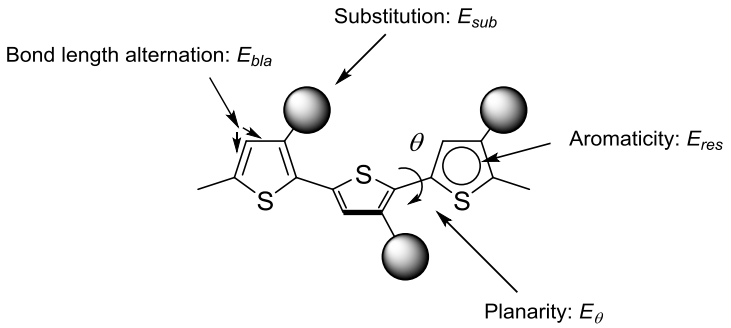

Figure 1.6 Representation of the structural factors determining the band gap of materials derived from linear π-conjugated systems.

The term E_{res} quantifies the difference in energy between the quinoidal and aromatic resonance structures. The aromatic stabilisation resonance energy of an aromatic unit tends to confine the π electrons within the aromatic ring increasing the band gap. The quinoidal form is required in order to achieve a delocalisation of the π-electrons.

However, an equilibrium between these two forms is required since the aromatic form is energetically more stable than the quinoidal form.[21]

A destabilisation contribution also derives from the loss of planarity of a conjugated system. In fact, it limits the delocalization of π-electrons along a conjugated backbone and hence it increases the band gap by a quantity termed E_θ. Considering polythiophene (PT), a straightforward strategy that can be used to decrease its energy gap consists of the introduction of double bonds between the thiophene units, leading to poly(thienylenevinylene) (**PTV**).[22] In fact E_g decreases from 2.00 eV of **PT** to 1.70 eV of **PTV**. This is due to the ethylene linkage units that allow a planarization of the backbone with a simultaneous reduction of the aromatic character in **PTV**.

These effects were further explored, comparing the electronic properties of three similar conjugated oligomers (**1.1-1.3**) containing an equal number of π electrons (Figure 1.7).

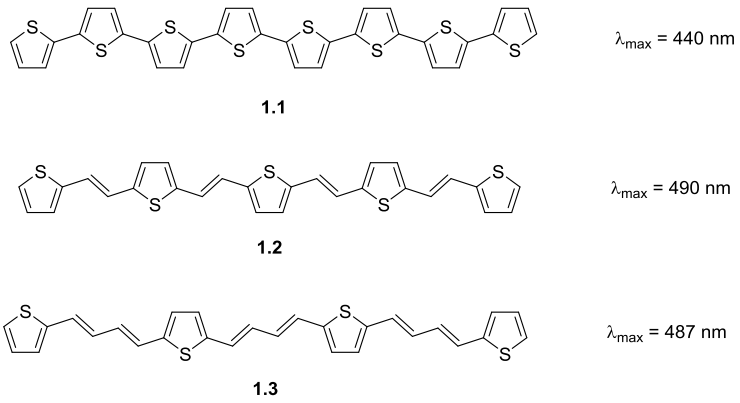

Figure 1.7 The chemical structures of oligomers **1.1-1.3**, showing the effect of adding double bonds between the thiophene units in the molecule.

There is red shift of 50 nm in the absorption maxima from **1.1** to **1.2** as consequence of adding ethylene units between thiophene rings. This is plausible due to the combined effect of planarization and adoption of a more quinoidal structure (as discussed above). However when a second ethylene linkage unit is added between the thiophene rings, a small blue shift of the absorbance maxima between **1.2** and **1.3** is observed. In fact, the planarization and quinoidal structure effect became less important here because they are counterbalanced by an increase of the vibrational freedom of the system.[23]

Furthermore the introduction of electron-withdrawing or electron-donating substituents is an immediate and efficient technique in order to tune the energy and relative position of the HOMO and LUMO levels of a conjugated material.

When an acceptor group (*e.g.* cyano) is added to the 3- position of the thiophene units of **PT** (**1.4**), or at the vinylene linkage of dithienylethylene (**1.5**, Figure 1.8), it is possible to observe an increase of the oxidation potential (increase of the HOMO level energy) and a considerable reduction of the band gap.[24, 25] This can be explained in terms of an extension of the quinoidal character of the ground state of these materials.[26]

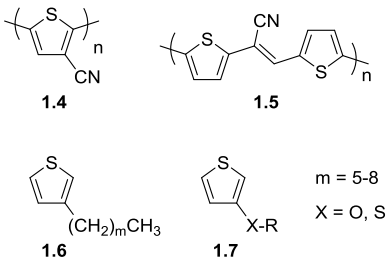

Figure 1.8 Structure of the polymers **1.4**, **1.5** and of the building blocks **1.6** and **1.7**.

On the other hand, the introduction of an electron-donor group (*e.g.* alkyl chains, alkoxy or thioalkoxy groups) generally decreases the reduction potential (reduction of the LUMO level energy), with a reduction of the band gap (**1.6**, **1.7**).[27] An excessive stabilisation by the introduction of bulky substituents can induce steric problems in the polymerisation process of these materials.[28]

Alternatively, compounds such as 3,4-ethylenedioxythiophene (EDOT) can be easily polymerised by chemical or electrochemical methods that lead to highly conductive polymers with a small band gap. In particular the EDOT unit can create noncovalent, intramolecular, sulfur-oxygen interactions (Figure 1.9) that can induce rigidification.[29]

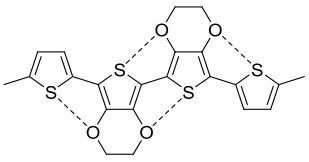

Figure 1.9 Intramolecular interactions between sulfur and oxygen atoms of an EDOT containing small molecule.

Another way to increase the quinoidal character is to slightly dearomatise an aromatic ring. The fusion of the thiophene heterocycle with the benzene ring is an excellent example. In fact the aromatic electrons of the thiophene will tend to localise in the benzene, that has a higher resonance energy (E_{res}), decreasing the band

gap through a higher quinoidal character. For example the band gap goes from 2.0 eV of **PT** to 1.1 eV of poly(benzo[c]thiophene) (Figure 1.10).[30]

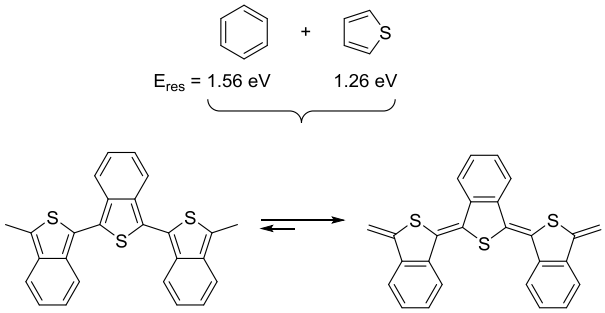

Figure 1.10 Aromatic (bottom left) and quinoidal (bottom right) resonance structure of the poly(benzo[c]thiophene).

A further approach widely used to reduce the band gap is the alternation of electron donor and electron acceptor units, in small molecules to polymers. This should broaden both the valence and conduction bands leading to a reduction of the band gap.[31-35] It is obvious that a synergetic combination of the effects discussed herein is ideal in order to maximise the reduction of the band gap; polymer **1.8**, containing an EDOT (donor, D) and thienopyrazine (acceptor, A) unit is a perfect example. This is termed a D-A polymer where a quinoidal structure is induced introducing median groups to the **PT** backbone. Furthermore, oxygen-sulphur intramolecular interactions confer a rigid structure leading to an E_g of just 0.36 eV.[36]

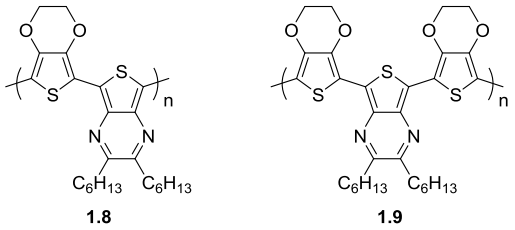

Figure 1.11 Chemical structure of polymers **1.8** and **1.9**.

Additionally, it has been discovered that a regular 1:1 D-A alternation is effective for a maximum reduction of the band gap. This is clear when the polymers **1.8** and **1.9**, containing the same donor and acceptor units, are compared. In **1.8** the D-A ratio is 1:1 with a band gap of 0.36 eV, whereas this increases to 1.10 eV in **1.9** where the D-A ratio is 2:1.[37] This synergetic combination of chemical modifications that leads to materials with very low band gaps is often associated with certain drawbacks. In particular, very low solubility of these rigid conjugated structures is common; introducing long alkyl chains along the polymer backbone only partially solves this

problem. In fact the enhanced solubility is counterbalanced with the general loss of stability of the material.[38]

Therefore the design of new organic semiconductor materials with low band gaps is a delicate equilibrium of the major factors discussed herein. It is the responsibility of the synthetic chemist to find this equilibrium, sometimes preferring an individual property instead of another, while always considering the final purpose of the material.

1.4. Light absorption and emission in organic semiconductors

Since the aim of this work is the synthesis and characterisation of new emissive materials for lighting applications, the principles of light absorption and emission will be discussed. Considering a molecule in space, it has various kinds of energy: electronic, vibrational and rotational. A molecule can move from one energetic state to another only through transitions that involve a discrete amount of energy. In particular, these electronic transitions are based on the Franck-Condon principle; electronic transitions are faster (10^{-15} s) than the movement of the nuclei.[39]

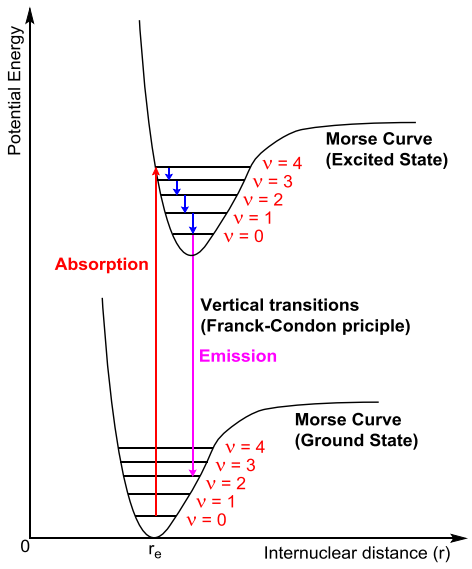

Figure 1.12 Representation of vertical absorption and emission.

By representing these electronic states in Morse curves (Figure 1.12), the electronic transitions can be symbolised by a vertical line connecting the two curves. Considering organic semiconductor molecules these transitions correspond to promotion of an electron from the valence to the conduction band. This energy, usually in the range of 3.5 to 0.3 eV corresponds to absorption in the Ultraviolet

(UV)-Visible (Vis)-Near Infrared (NIR) region of the electromagnetic spectrum (Figure 1.13).

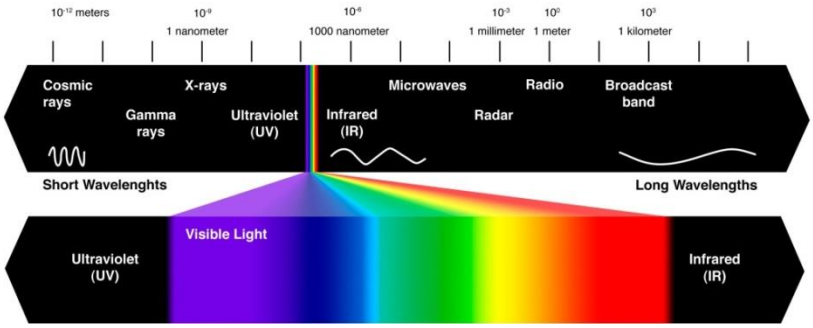

Figure 1.13 The electromagnetic spectrum (top), with an expanded view of the ultraviolet-visible-infrared portion of the spectrum (bottom).

In a conjugated organic molecule that contains heteroatoms it is possible to classify five different kinds of orbitals: bonding orbitals (σ and π), antibonding orbitals (σ* and π*), and the non-bonding orbitals (n).

Absorption electronic transitions generally involve the movement of an electron between a bonding or non-bonding orbital and an anti-bonding orbital (Figure 1.14).[40]

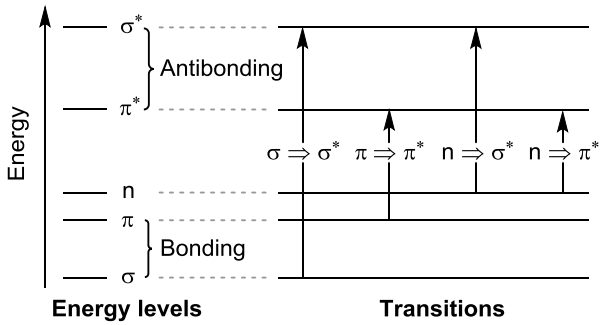

Figure 1.14 Representation of the energy levels and energy transitions in an organic molecule.

Organic molecules in their ground state generally have singlet spin. Considering the selection rules, the absorption transitions must be only between electronic states with the same spin multiplicity.[41]

When a species undergoes an electronic transition due to absorption of radiation of an appropriate wavelength (or energy) it generates an electronically excited species. This, being unstable, tends to relax and loses the absorbed excess energy in order to restore its initial energetic state. There are several relaxation processes, with the most efficient being a vibrational non-radiative process (average lifetime 10^{-12} s), consisting of a transfer of heat to the surrounding environment.[39]

The radiative relaxation processes, namely the phenomenon of luminescence, can be of two types: fluorescence and phosphorescence. They generally follow the rule of Kasha, which asserts that the more probable emission starts from the lowest vibrational level of the electronic excited state.[39]

Fluorescence results when the photon emission occurs from an electronic relaxation from the first excited energy level with the same spin multiplicity as the ground state (Figure 1.15).

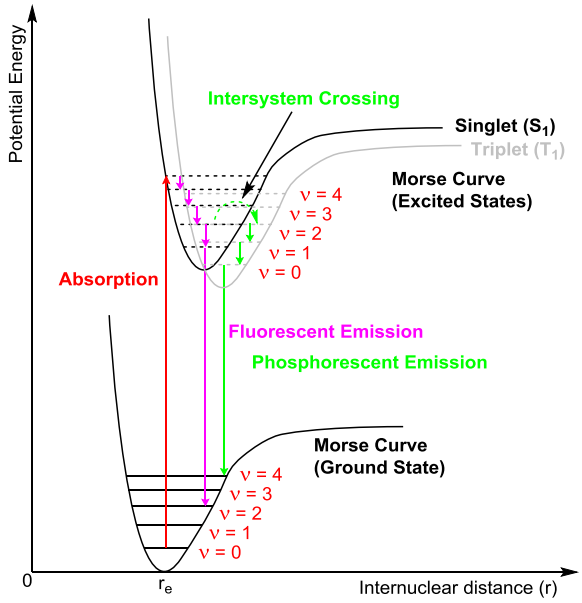

Figure 1.15 Representation of the fluorescent and phosphorescent emissions.

The frequency of the emitted radiation depends on the energy difference between the lowest vibrational level of the electronic excited state and the final vibrational level of the electronic ground state. The rate of this kind of transition is between 10^{-9} and 10^{-5} s.[39]

On the other hand, phosphorescence is the emission of a photon involving the phenomenon of intersystem crossing (ISC). The excited state undergoes a variation of the spin multiplicity, generally from singlet to the lower energy triplet. This phenomenon is possible by the overlap of the vibrational energy states of two or more electronic excited states (Figure 1.15). The singlet–triplet transition is very unlikely and the rate of this phenomenon is in the range 10^{-2} s to a few hours.

The typical electronic band shape is due to the overlapping of consecutive transitions from different vibrational levels of the excited electronic level.[39]

All the relaxation processes are competing with each other and their yield is dependent on the nature of the species involved and the reaction environment, such as the solvent ability to accept energy after relaxation of the excited species.[39]

A way to rationalise the importance of these phenomena is to express the so-called quantum yield (QY) and fluorescence lifetimes. The QY is defined as the number of emitted photons relative to the number of absorbed photons. Substances with the largest quantum yields, approaching unity, such as rhodamines, display the brightest emissions. Depending on the phenomena used to excite the material, photoluminescent and electroluminescent quantum yields are defined (PLQY and ELQY, respectively). The first is obtained when excitation is achieved with electromagnetic radiation, the second using an applied voltage. Independently from the absolute values that can change depending on the excitation method, the QY is defined as:[39]

$$QY = \frac{\Gamma}{\Gamma + k_{nr}} \qquad \text{Equation 1.2}$$

where Γ is the emissive rate of the fluorophore and k_{nr} is the rate of non-radiative decay of the fluorophore from the excited to the ground state (Figure 1.16).

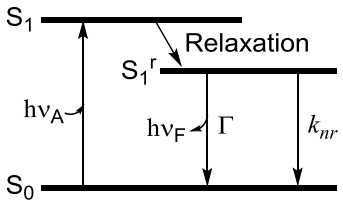

Figure 1.16 Simplified Jablonski diagram to illustrate the meaning of quantum yields and lifetimes.

The lifetime of the excited state is defined by the average time the molecule spends in the excited state prior to return to the ground state (Equation 1.3). Generally, fluorescence lifetimes are in the region of 10 ns.

$$\tau = \frac{1}{\Gamma + k_{nr}} \qquad \text{Equation 1.3}$$

Therefore QY and lifetimes are dependent on the ratio between Γ and k_{nr}; in particular they decrease when the rate of the non-radiative decay increases. There are

different non-radiative decay processes which are generally called quenching processes:

- Collisional quenching occurs when the excited fluorophore experiences contact with an atom or molecule that can facilitate non-radiative transitions to the ground state. These include electron transfer, spin-orbit coupling, and intersystem crossing to the excited triplet state without chemical alteration, resulting in deactivation of the fluorophore and return to the ground state. Common quenchers include O_2, I^-, Br^-, Cs^+ or even other fluorophores. When the quencher is the same fluorophore this is called self-quenching.[39]
- In some cases a fluorophore can form a stable complex with another molecule. If this ground-state is non-fluorescent then the fluorophore is statically quenched. In this case the lifetime of the sample will not be reduced since those fluorophores which are not complexed will have normal excited state properties.
- The presence of heavy atoms close to the fluorophore influences the spin-orbit coupling and increases the rate of intersystem crossing between the excited fluorophore and a radiationless transition of the fluorophore.[42] This effect can be internal if the heavy atom is present in the fluorescent molecule or external if the heavy atom is in an external molecule.
- Other quenching effects include ground state complex formation, excited state reactions and molecular rearrangements.

1.5. Organic light emitting diodes

The aim of this project is the synthesis of organic semiconductor materials with light emitting properties in the visible region of the electromagnetic spectrum for lighting applications. For this reason, the general operation principles of organic light emitting diodes (OLEDs) will be discussed.

Electroluminescence (EL) is an optical and electrical phenomenon in which a material emits light in response to the passage of an electric current through it or to a strong electric field. From the first organic material (1963) presenting this phenomenon[43] several research groups have successfully discovered new emissive organic semiconductors. These kinds of molecules present several advantages

compared to their inorganic counterparts, such as low cost, ease of processing and facile tuning of their properties by chemical or morphological modifications.[7]

The fundamental OLED architecture is composed of at least three semiconductor layers sandwiched by two electrodes. The anode, that acts also as hole injector, typically consists of a glass support covered with Indium-Tin oxide (ITO), a transparent material with a high work function, while the cathode that acts as an electron-injector is typically metallic (*e.g.* calcium, silver). The emissive organic semiconductor material (EML) is sandwiched by a hole injection layer (HIL) (usually an aromatic amine with a low ionization potential) and an electron transport layer (ETL) (Figure 1.17).[12]

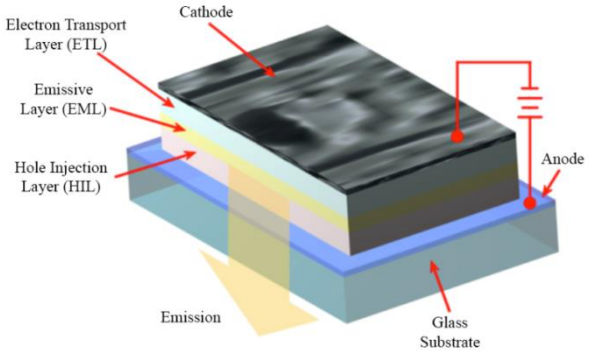

Figure 1.17 Schematic representation of a typical OLED device.

When a forward bias is applied to the electrodes, it induces hole (h^+) and electron (e^-) injection (mainly from the HOMO of the HIL and from the LUMO of the ETL) in the device. These tend to migrate through the semiconductor layers in the direction of the opposite electrode. The full device can be considered as a unique semiconductor, with the valance and conduction bands constituted as combination of the HOMO and LUMO levels of the different layers, respectively (Figure 1.18).[12]

Depending on the speed of this process and of the mobility of the charges, there will be a recombination of the holes and the electrons in their excited states, called an exciton, that corresponds to the singlet or triplet excited state of the emissive material. This then undergoes the relaxation process that is the origin of fluorescent and phosphorescent phenomena.[12]

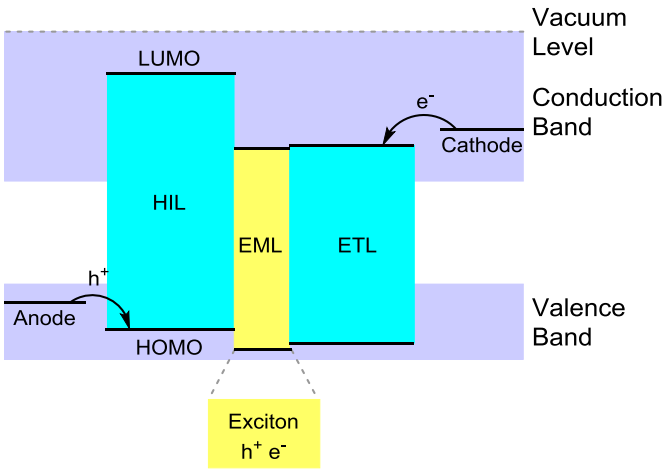

Figure 1.18 Energy levels of a multilayer OLED device. HIL: hole injection layer; EML: emissive layer; ETL: electron transport layer.

1.6. Excited states

The recombination of a hole and an electron by electrostatic Coulomb attraction generates an excited state called an exciton. A Frenkel exciton is obtained when the electron-hole pair is small, within the same order as the size of the unit cell, whereas a Wannier-Mott exciton, is obtained when the pair has a radius larger than the lattice spacing (Figure 1.19).[44] Intermediate excitons, also known as charge-transfer excitons, are obtained when the pair has a radius of only one or two-molecular distances in size.

The excitons in organic semiconductor materials are mainly Frenkel and intermediate excitons and they can even be localised in a single polymeric chain or small molecule. They can have singlet or triplet states depending on the different spin orientations of the electron-hole pair (Figure 1.20). In a singlet state the electron and hole have opposite spins (spin momentum, $m_s = 0$), and the total angular momentum equals zero because they are out of phase ($S_{total} = 0$, combination of $(\uparrow -\downarrow)$).

There are three combinations of the spins of the hole and the electron that can give a triplet state:

- the spins are both "up" ($S_{total} = 1$, $m_s = 1$, combination of $(\uparrow +\uparrow)$);
- the spins are both "down" ($S_{total} = 1$, $m_s = -1$, combination of $(\downarrow + \downarrow)$);
- the spins are opposite but in phase ($S_{total} = 1$, $m_s = 0$, combination of $(\uparrow\downarrow + \downarrow\uparrow)$).

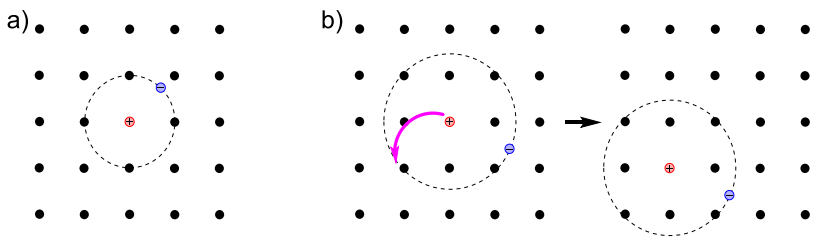

Figure 1.19 a) Frenkel exciton, bound electron-hole pair where the hole is localized at a position in the crystal represented by black dots. b) Wannier-Mott exciton, bound electron-hole pair that is not localized at a crystal position. This figure schematically shows diffusion of the exciton across the lattice.

These three triplet states are degenerate, but it is possible to separate them in energy under the effect of a magnetic field.

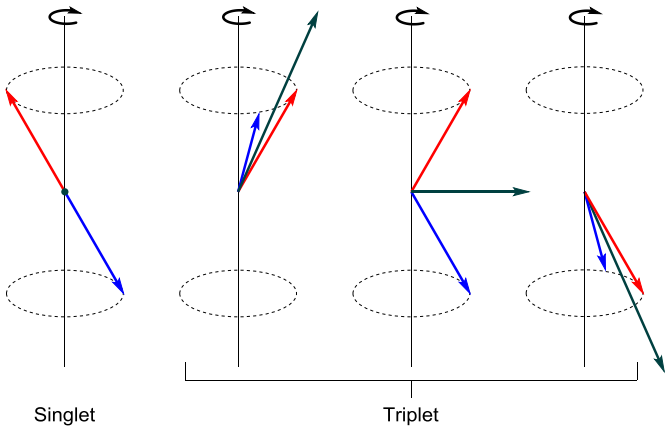

Figure 1.20 A vector base representation of the singlet and triplet spin configurations. The blue and red arrows represent the hole and electron spins and the green one represents the total angular momentum.

During an electrical excitation, if singlets and triplets are formed with equal probability, 25% of the excitons would be singlets and 75% would be triplets. Therefore, the quantum efficiency of fluorescence (transition from singlet excited states to ground states) has an upper limit of 25%. According to quantum mechanics, the radiative relaxation from triplet states to ground states is generally forbidden (*i.e.* happens in a very slow time scale). However, it has been shown that with the introduction of a phosphorescent emitter in a host-guest system,[45] the transition from the excited triplet states to ground states becomes much faster than the non-radiative relaxation. Moreover, through inter-system crossing, the 25% excitons formed as singlet states can also be utilised and therefore it is theoretically possible to achieve 100% internal quantum efficiency in phosphorescent OLEDs.

1.7. Device characteristics and performance

Since OLEDs are mainly related to visible light emission (*e.g.* illumination, signs and displays) their optical characteristics are usually given and compared in photometric units. For this reason, the sensitivity of the human eye has to be involved in the calculation of light emission and output efficiencies. The spectral response of the human eye under daylight conditions (referred to as photopic or cone vision) was standardized by the International Lighting Commission (CIE) in 1924.[46] They deduced from experiments with a representative human sample the photopic spectral luminous efficiency function $V(\lambda)$. This yields the connection between the four radiometric fundamental quantities (radiant flux Φ_e in Watts, radiant intensity I_e in W/steradian, irradiance E_e in W/m^2, and radiance L_e in $W/(m^2 sr)$) and their photometric equivalents (luminous flux Φ_V in lumen, luminous intensity I_V in $lm/sr = cd$, illuminance E_V in $lm/m^2 = lux$, and luminance L_V in $lm/(m^2 sr) = cd/m^2$).[47] As an example, the connection between radiant flux and luminous flux is defined by the following equation:

$$\Phi_V = K_m \int_{380\ nm}^{770\ nm} \Phi_e(\lambda) V(\lambda) d\lambda \qquad \text{Equation 1.4}$$

Where $K_m = 683\ \ lm/W$ is the conversion constant.

To easily convert radiometric and photometric quantities, the radiation luminous efficacy K_r is defined. The total radiant flux can be written as ˆ

$$\Phi_e = \int_0^{\infty} \Phi_e(\lambda) d\lambda \qquad \text{Equation 1.5}$$

Therefore the radiation luminous efficacy can be defined as follows:

$$K_r = \frac{\Phi_V}{\Phi_e} = K_m \frac{\int_{380\ nm}^{770\ nm} \Phi_e(\lambda) V(\lambda) d\lambda}{\int_0^{\infty} \Phi_e(\lambda) d\lambda} \qquad \text{Equation 1.6}$$

The radiation luminous efficacy is not an efficiency, but gives the effectiveness of a beam of radiation in stimulating the perception of light in the human eye. Typical

values of K_r are about 500 lm/W for small band green light emission (typical for LEDs), about 125 lm/W for red, about 75 lm/W for a typical saturated blue, and around 220 lm/W for a constant white light emission. OLEDs are mainly characterized by three efficiency values:

(1) The system luminous efficacy K_s (in lm/W) gives the ratio of total light output in lumens to the electrical power in Watts. In this work it is also referred to as luminous or power efficiency η_P.

(2) The current efficiency η_c (in cd/A), defined by the ratio of the luminous intensity in forward direction $I_{V,0}$ and the current flowing through the OLED (same as luminance in forward direction $L_{V,0}$ divided by current density).

(3) The quantum efficiency η_Q (in %), defined as the ratio between the number of emitted photons and the number of injected electrons.

The third value is expressed in radiometric units, whereas K_s and η_c are in photometric units.

These definitions have the consequence that the same quantum efficiency for a red, green and blue emitting OLED gives strongly different current and luminous efficiencies, due to different radiation luminous efficacy of the three LEDs.

If η_c is the current efficiency in cd/A at an operating voltage V then the power efficiency η_P can be calculated as:

$$\eta_P = \frac{f_D}{V}\eta_c \qquad \text{Equation 1.7}$$

f_D is a factor which depends on the angular distribution of the light emitted from the substrate into one half-sphere. The quantum efficiency η_Q is related to the current efficiency η_c in the equation:

$$\eta_Q = f_D\,\pi\,\eta_c\,\frac{e}{K_r E_{mean}} \qquad \text{Equation 1.8}$$

where E_{mean} is the average photon energy, in a first order approximation related to the wavelength of maximum emission λ_{max} by $E_{mean} = h\,c/\lambda_{max}$, where h is the Planck-constant and c the speed of light.

In order to obtain the current efficiency of an OLED, one needs to know its luminance in the forward direction $L_{V,0}$ (in cd/m^2, $L_{V,0} = I_{V,0}/A_L$). The experimental setup usually used is schematically drawn in Figure 1.21.

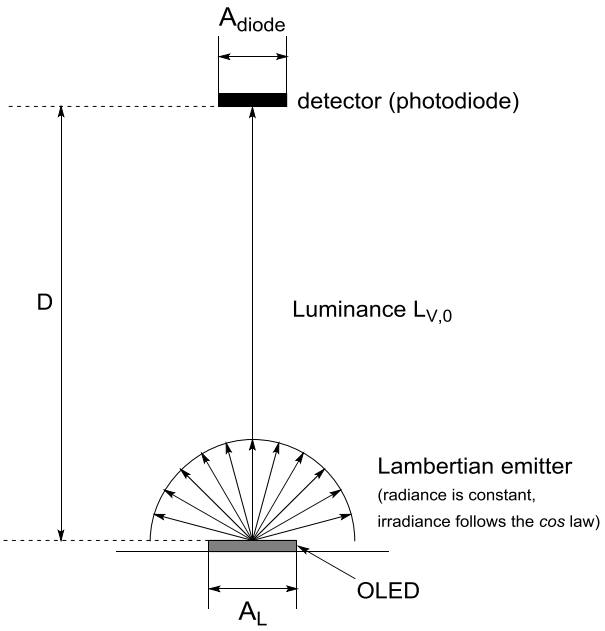

Figure 1.21 Experimental setup to measure the luminous intensity in forward direction of an OLED.

A photodiode (area A_{diode}, transmission of their windows τ, relative spectral sensitivity $s_{r,diode}(\lambda)$) is placed above an OLED (area A_L, emission spectrum $\phi(\lambda)$) at a distance D. The photodiode is connected to an amplifier circuit, which generates a voltage V_{diode} proportional to the irradiance of the photodiode. The photodiode/amplifier-unit has to be calibrated (experimentally or from data sheets). This calibration can be expressed by a sensitivity of the photodiode/amplifier unit at the wavelength of maximum sensitivity S_{max} in irradiance-Watt per voltage V_{diode}. Then the luminance in forward direction can be calculated to:

$$L_{V,0} = K_r V_{diode} \frac{S_{max}}{FF} \frac{D^2}{\tau A_L A_{diode}} \qquad \text{Equation 1.9}$$

where K_r accounts for the conversion of the radiometric irradiance measured by the photodiode to the photometric luminous intensity that wants to be calculated (equation 1.2). FF is a fill-factor which weights the emission spectra of the OLED with the spectral sensitivity dependence of the photodiode. The values of K_r and FF

depend on the emission spectra of the measured OLED. The Equation 1.9 give a good approximation only for $D >> A_{diode}$ and D >> A_L.[47]

1.8. White solid state lighting

The modern "illumination age" began in the latter stages of the 18th century with the first incandescent light bulb made by Joseph Wilson Swan and refined by Thomas Alva Edison. [48] From this invention, home lighting technology has not evolved significantly. In fact, in our homes we can still find incandescent bulbs virtually identical to those perfected by Edison more than 100 years ago. They are very inefficient, converting only 5% of electrical energy to light.[48]

The arrival of gas-discharge lamps and the compact fluorescent lamps (CFLs, also called energy-saving) were two major updates that illuminated our lives, having efficiencies of up to 30%.[48] More recently, we are witnessing the emergence and the gradual improvement of so-called solid-state lighting (SSL).

SSL technology refers to a type of lighting that uses semiconductor light-emitting diodes (LEDs), organic light-emitting diodes (OLED), or polymer light-emitting diodes (PLED) as a source of illumination rather than electrical filaments, plasma (used in fluorescent lamps), or gas. They are predicted to become the next generation of general illumination system (Figure 1.22).[49]

Inorganic white light emitting diodes (WLEDs) are commercially used nowadays for general illumination purposes (*e.g.* automotive lighting, indoor and outdoor lighting).[50] They have achieved laboratory efficiencies exceeding 300 lm/W and are already commercially available.[51]

Nevertheless, the high fabrication cost of this technology could inhibit its worldwide adoption. White organic light emitting diodes (WOLEDs) instead are widely used mainly as low-cost alternatives for back-lights in flat panel displays.[52] They present several advantages compared to their inorganic counterparts, such as lower cost, ease of processing and facile tuning of their properties by chemical modifications (Table 1.1).[7, 52] Furthermore, they can be fabricated as flexible panels with wide viewing angles and a superior white colour balance.[53]

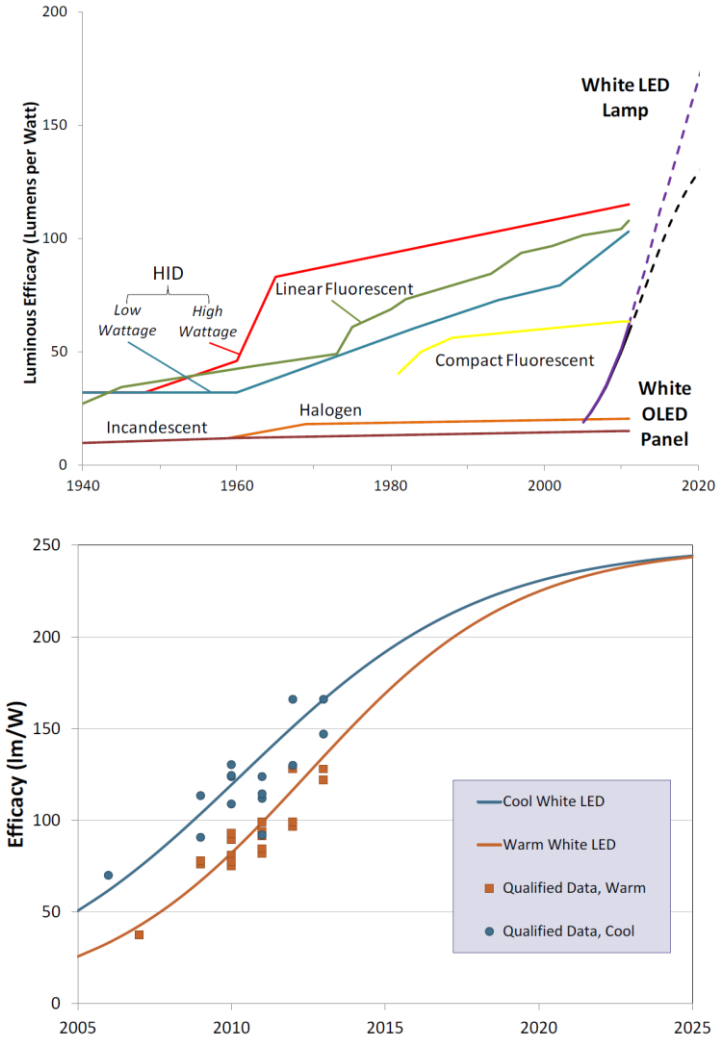

Figure 1.22 Historical (updated at 2012) and predicted efficacy of light sources (top). White-light pc-led package efficacy projections (updated to 2014) for commercial product, all products produced (to 2014) use phosphor-converted or hybrid architectures (bottom) [54]

Table 1.1 Main advantages and disadvantages of principal white light sources.

Source	Advantages	Disadvantages
Incandescent	Low cost; blackbody source with CRI: 100	Low operational lifetime: 1000 h; low efficiency: 10 to 20 lm⁄W
Fluorescent	Low cost; efficiencies of 40 to 80 lm⁄W; operational lifetimes of 10000 h	Contains hazardous materials like Hg; CRI < 80
Inorganic LED	Operational lifetime of >50000 h; efficiencies >100 lm⁄W; CRI: 80 to 90	High manufacturing cost; point source
Organic LED	Efficiencies >100 lm⁄W; operational lifetime >10000 h; CRI > 90	Low brightness; low cost manufacturing of large area panels remains challenging

White SSL can be achieved using different approaches, with the most common summarised in Figure 1.23. However, the commercially successful methods include: (I) combining a blue (*ca.* 460 nm) LED and a yellow phosphor pumped from the blue light of the LED;[55-57] (II) combining a single chip emitting UV light which is absorbed in the LED package by three phosphors (red, green and blue) and re-emitted as a broad spectrum of white light[58, 59] or (III) three different LED chips, each emitting a different wavelength [red, green and blue (RGB)] in order to simulate the RGB colour model.[11, 58-63] The design of these configurations is not straightforward and to achieve competitive efficiencies and luminosity the use of hybrid (inorganic-organic) solutions has been explored.[11, 60, 61, 64]

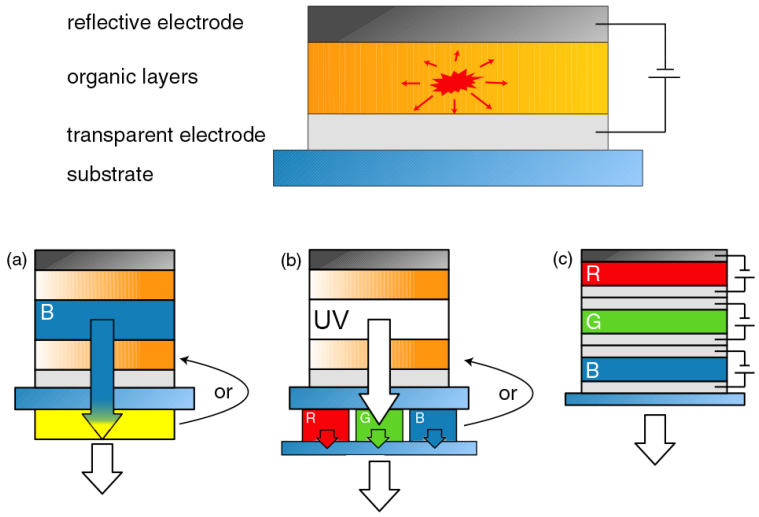

Figure 1.23 Top: Schematic cross section of a bottom-emitting OLED. Bottom: Various device layouts to realize white light emission. (a) blue LED with downconversion layer, (b) UV LED with red, green, blue downconversion layers, (c) Vertically stacked red, green, blue OLED. Shaded layers represent optional functional layers, e.g., transport layers [not shown for (a) and (b) for better visibility]. UV, R, G, Y and B stand for ultra violet, red, green, yellow and blue, respectively.[65]

Commercial white light is most often achieved with LEDs using phosphor conversion. For LEDs, phosphor down-conversion is most commonly based on a blue or near-ultraviolet inorganic light emitting diode that is combined with a yellow-emitting phosphor, or a combination of different phosphors that produce a broad energy distribution.

The phosphor may be incorporated into the LED package, or may be located remotely. As demonstrated by several commercial entities (such as PHILIP, OSRAM, CREE), the blue-LED with a yellow phosphor strategy is one of the best options used to fabricate cheap and straightforward devices.[66, 67] However, further

developments are essential to make this technology commercially competitive with existing CFLs.

A common advantage of this technology is that it has matured so that high-volume manufacturing processes are available. The devices achieve high luminous flux and high efficacy, with a comparatively low cost. On the other hand they usually present high correlated colour temperatures (cool blue) and can suffer from colour variability in beam.

It is clear that fine tuning of the characteristics of the device is necessary in order to obtain the best performance possible. Different strategies are used involving different methodologies. For example, the internal quantum efficiency can be increased by epitaxial growth (called epitaxy) of the LED wafer in order to have the highest crystal quality or by coupling effects between the light-emitting quantum well (QW) and surface plasmons (SP) using suitably nanostructured metals.[68, 69]

The white light produced in this fashion is difficult to fine-tune, in particular when a mixture of several emitters is used.[70] In order to simplify the device architecture, several strategies have been used to fabricate single molecular layer WOLEDs.[53]

1.8.1. Panchromatic emission

Panchromatic emission originates when a molecule can exist in different constitutional isomers (*e.g.* tautomers) that produce different light emission processes. The generation of white-light with this process is rarely observed in literature. Heagy *et al.* employed *N*-aryl-2,3-naphthalimides with low symmetry (Figure 1.24) that exhibited dual fluorescent emission.[71, 72]

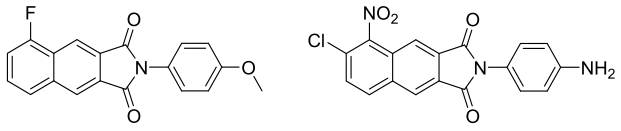

Figure 1.24 Structure of the N-aryl-2,3-naphthalimides synthesised from Heagy *et al.*[71, 72]

These molecules can achieve different exited states depending on the energy of excitation. When **1.2** is excited at 380 nm it produces a green colour emission, whereas when excited at 360 nm it results in a relatively balanced emission from different excited states leading to pure white-light emission.

1.8.2. Halochromic emission

When protonated (or deprotonated) forms of a molecule have a large difference in the electron delocalisation they can show different emission profiles. Liu *et al.* observed white solid-state luminescence as well as electroluminescence from the controlled protonation of two molecular blue fluorophores (Figure 1.25).[73] NMR studies support that there is an intramolecular charge transfer (ICT) between the protonated quinazoline moiety and the diphenylamine (or carbazole) terminal unit. This provokes a strength enhancement of the fluorophore after the protonation that induces an orange emission (*ca.* 600 nm). In solid state devices, the addition of 0.1 wt % of (solid) camphorsulfonic acid efficiently balances the two emissive forms producing white light (Figure 1.25, b).

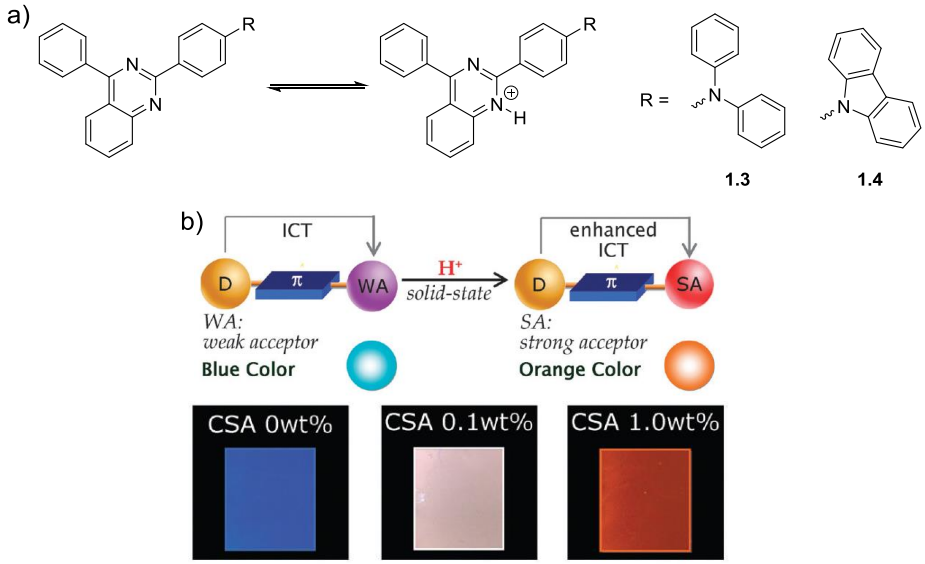

Figure 1.25 a) Structure of **1.3** and **1.4** and their neutral and protonated forms. b) Blue dye with induced orange emission through intramolecular charge transfer strength enhancement and images of the **1.4** with different camphorsulfonic acid concentrations.

1.8.3. Excited-state-intramolecular-proton-transfer emission

Excited state intramolecular proton transfer (ESIPT) is a photochemical process that produces a tautomer with a different electronic structure from the original excited form.1 [74] It is a four-level photo-cycle ($E \rightarrow E^* \rightarrow K^* \rightarrow K$) scheme implemented by the enol (E) - keto (K) phototautomerisation process (Figure 1.26).[75] The pre-requisite for ESIPT is the presence of an intramolecular hydrogen bond (H-bond) between the proton donor (–OH and $–NH_2$) and the proton acceptor (=N– and –C=O) groups in close proximity to each other in a molecule.[75] These systems were found

to be the first examples of compounds which violates Kasha's rule and show dual emission.[53]

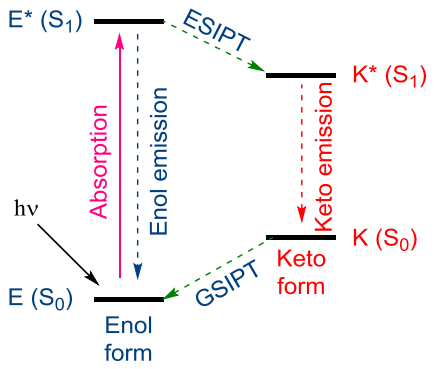

Figure 1.26 Basic principle of the dual emission from ESIPT based systems. GSIPT (ground state - intramolecular-proton-transfer).

Chou *et al.* showed white-light emission in a single ESIPT system by fine-tuning the energetics of the excited state.[76] In the series of compounds **1.5-1.7** the introduction of a larger aromatic ring increases the conjugation and therefore the stabilisation of the excited state of the keto-enolic tautomerisation (Figure 1.27).

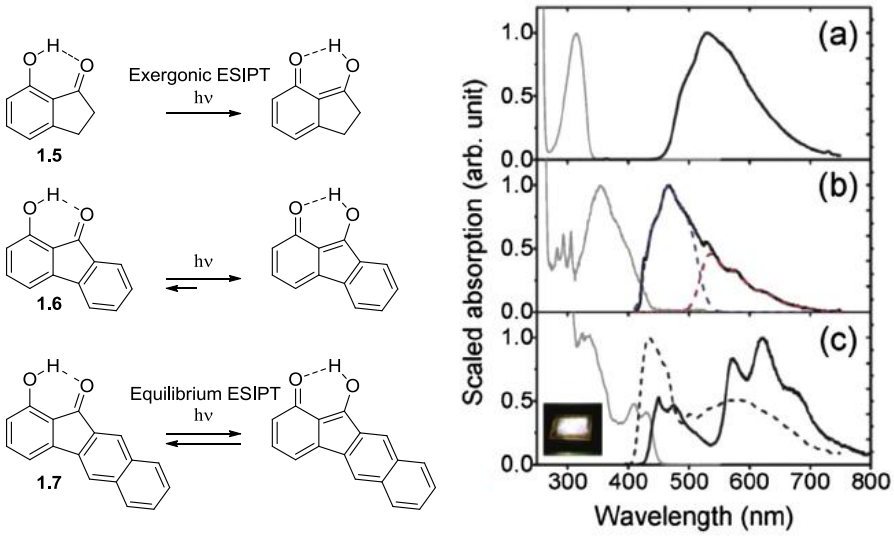

Figure 1.27 Structures and ESIPT mechanism for 1.5-1.7 (left). Solid lines: steady-state UV-Vis absorption spectra (grey) and photoluminescence spectra (black) of (a) **1.5**, (b) **1.6** and (c) **1.7** in cyclohexane. Dotted lines in (b) depict the decomposed PL spectra assigned for normal (blue) and tautomer (red) species, respectively. Dashed line in (c) depicts the PL spectrum of amorphous solid powder sample **1.7**. The photograph shows a piece of solid vinyl-matrix doped with **1.7** and irradiated with laboratory UV lamp (366 nm).

In **1.5** an ultrafast ESIPT allows emission only from the tautomer emission, whereas in **1.6** and **1.7** there is an excited-state equilibrium between the tautomeric species, that leads to a white emission in **1.7**.

1.8.4. Dimeric excited-state emission

White-light emission can be also achieved from intermolecular interactions or complex formations, *e.g.* excimers or exciplexes.[70, 77-81] Excimers are possible in single component organic materials due to the resonance interaction of a molecular exciton with a neighbouring non-excited molecule,[82-84] whereas exciplexes can be formed in a bi- or multi-component molecular solid when the formation of bimolecular excited states is facilitated by electron transfer between the donor and acceptor components (Figure 1.28).[85, 86]

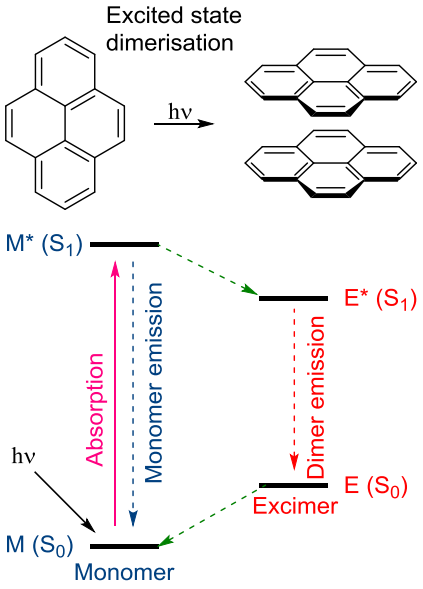

Figure 1.28 Illustration of the basic principle of excimer emission in organic fluorophores, pyrene is used as example.

In 2002 Wang and co-workers reported a highly efficient white device based on the exciplex at the interface between a boron (**1.8**) and *N*,*N*′-di(1-naphthyl)-*N*,*N*′-diphenylbenzidine (**NPB**) (Figure 1.29).[87]

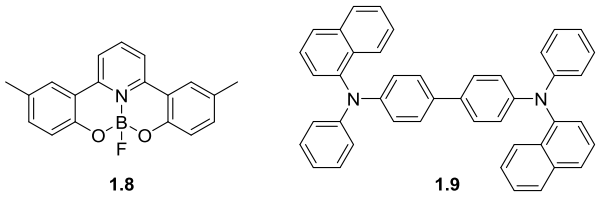

Figure 1.29 Scheme of the boron complexes **1.8** and structure of **NPB** (**1.9**).

Qiu and co-workers observed exciplex type white-light emission from the interface of a bilayer electroluminescent device consisting of a new electron transport material, anthracene-9,10-diylbis(diphenyl-phosphine oxide) (DPPA) and *N*,*N*'-bis(naphthalen-1-yl)-*N*,*N*'-bis(phenyl)benzidine (NPB)[77] as the hole-transporting

layer. Recently, Cherpak *et al.* reported a new approach for the fabrication of a WOLED that consists of the combination of the blue phosphorescence emission from the iridium (III) bis[4,6-difluorophenyl]-pyridinato-N,C2′]-picolinate (**1.10**) complex and the highly efficient thermally activated delayed fluorescent (TADF) emission from the exciplex formed at the interface between the star-shaped hole transporting material tri(9-hexylcarbazol-3-yl)amine (**1.11**) and **1.10** (Figure 1.30).[81]

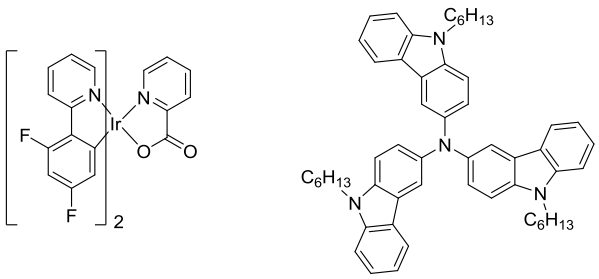

1.10 **1.11**

Figure 1.30 Chemical structure of **1.10** and **1.11**.

1.9. White light parameters

For the design of a new light source different fundamental parameters that define the quality of the light produced must be considered.[66]

Since 1931, the Commission Internationale d'Eclairage (CIE) released different colour space chromaticity diagrams. They link [with two coordinates (x, y)] physical pure colours (*i.e.* wavelengths) in the electromagnetic visible spectrum with physiological perceived colours in human colour vision (Figure 1.31). The diagram from the 1931 is the most generally used and the coordinates of calibrated white light are (0.33, 0.33).[88] The Correlated Colour Temperature (CCT) describes the relative colour appearance of a white light source, indicating whether it appears warm (tendency to yellow/gold colour tonalities) or cold (tendency to blue tonalities), in terms of the range of available shades of white. CCT is given in Kelvin (SI unit of absolute temperature) and refers to the appearance of a theoretical black body heated to high temperatures. As the black body gets hotter, it turns red, orange, yellow, white, and finally blue. The CCT of a light source is the temperature (in K) at which the heated black body matches the colour of the light source in question.[88]

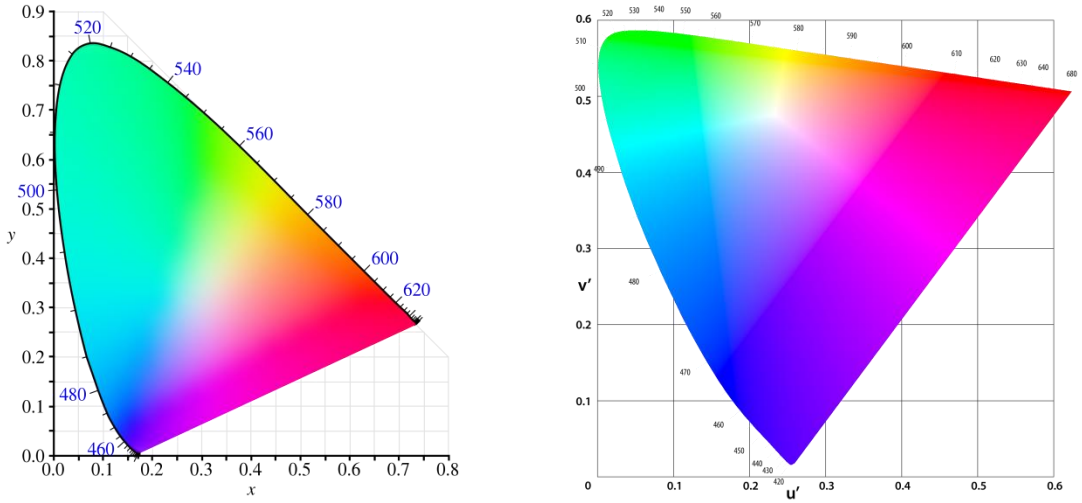

Figure 1.31. The CIE 1931 (left) and 1976 (right) chromaticity diagrams.

The Planckian locus or black body locus is the path or locus that the colour of an incandescent black body would take in a particular chromaticity space as the blackbody temperature changes (Figure 1.32).[88]

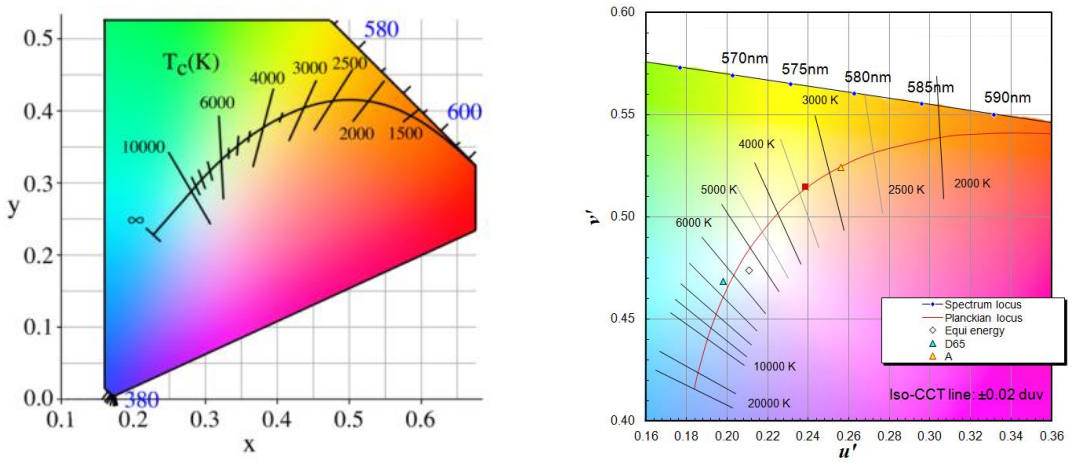

Figure 1.32 Planckian locus on the CIE 1931 (left) and 1976 (right) chromaticity diagrams.

The Colour Rendering Index (CRI) indicates how well a light source renders colours, on a scale of 0 to 100, compared to a reference light source of similar colour temperature. The test procedure established by the CIE involves measuring the extent to which a series of eight standardized colour samples differ in appearance when illuminated under a given light source, relative to the reference source. The average "shift" in those eight colour samples is reported as Ra or CRI. In addition to the eight colour samples used by convention, some lighting manufacturers report an "R9" score, which indicates how well the light source renders a saturated deep red colour.

CRI values less than 70 are unacceptable for indoor lighting applications and, in general, CCT values in the range 2500-6500 K are required for indoor lighting applications.[11, 12, 68]

A standard illuminant is a theoretical source of visible light with a profile (its spectral power distribution) that provides a reference to determine unknown light sources. In particular, standard illuminants provide a basis for comparing images or colours recorded under different lighting. The CIE introduced three standard illuminants in 1931: A, Incandescent bulb simulator; B, daylight simulator (direct) and C, daylight simulator (shade). Recently, a D series of illuminants that attempts to portray standard illumination conditions in the open-air in different parts of the world were introduced. D65 is commonly used and corresponds roughly to the average midday light in Western Europe/Northern Europe (comprising both direct sunlight and the light diffused by a clear sky), hence it is also called a daylight illuminant.[89] It has CIE 1931 coordinates (0.31, 0.33) and a CCT of 6504 K.

Chapter 2. Down converting materials for hybrid white OLEDs

2.1. Introduction

2.1.1. Project overview

The broad aim of this project is to create new devices that are commercially competitive for white lighting. To do this, an interdisciplinary effort is needed to be able to exploit new materials and implementations, while an alternative white LED architecture is required. This new class of hybrid white LED uses efficient down–converting organic small molecules in tandem with inorganic blue LEDs. The working device comprises of the commercial inorganic blue LED emitting at *ca.* 444 nm and of a yellow down-converting material able to absorb the blue light and re-emit in the yellow region at *ca.* 570 nm (Figure 2.1).

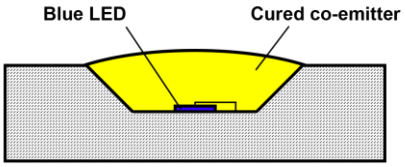

Figure 2.1 Scheme of the hybrid device.

The use of this proposed device requires the design, synthesis and characterisation of new discrete molecules that must satisfy the following general requirements:

- have a strong absorption in the region 410-470 nm;
- have an efficient emission in the region 550-584 nm, in order to be mixed with the blue LED emission to obtain a white light;
- show minimal self-absorption, in order to be enhance LED efficiency;
- be solution-processable so as to reduce the fabrication costs of any device.

Furthermore, these characteristics must be associated with a chemical and morphological stability under the device operating conditions, avoiding phase segregation between the metal and organic components and thermal/optically-induced degradation.

The main approach to achieve this is to synthesise new compounds based on extensively conjugated donor-acceptor systems of polycyclic aromatic or heteroaromatic compounds in order to obtain materials with a low energy level gap. For this purpose, three different types of molecules were selected as the building-blocks for a new class of down-converter molecules.

The 2,1,3-benzothiadiazole (BT) molecule is widely used for the synthesis of low energy gap semiconducting materials for different applications.[90-93] It has been used as good electron acceptor as it possesses a relatively high reversible reduction potential and high electron-affinity.[94] Furthermore it is amenable to facile ring modification, in particular at positions 4 and 7.[95] In order to extend the acceptor capability of BT recently the bis-2,1,3-benzothiadiazole (bBT) unit has been adopted for different applications, including OPV[96-98] and electrochemical supercapacitors.[99]

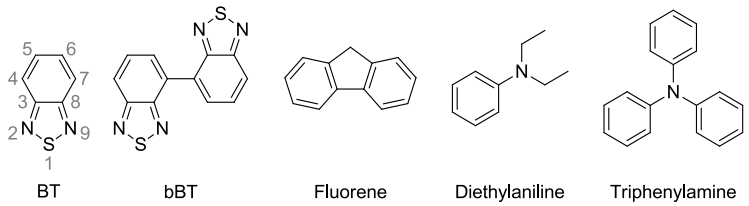

Figure 2.2. The molecules used as building-blocks for the synthesis of the down converting materials.

Due to their strong electron-withdrawing capacity, the BT-containing compounds generally afford well-organized crystal structures due to their significant polarisability, leading to intermolecular interactions such as heteroatom···heteroatom contacts and π-π* interactions.[100] In particular the bBT unit adopts a twisted structure in 4,4′-bis(7-(1-pyrrolidinyl)-2,1,3-benzothiadiazole) (**2.A**),[101] 4,4′-bis(7-iodo-2,1,3-benzothiadiazole)[102] (**2.B**), 2,7-di(bisbenzothiadiazolyl)-9,9-dioctylfluorene[103] (**2.C**) and 7,7′-di(9,9-dioctylfluoren-2-yl)-4,4′-bis(2,1,3-benzothiadiazole) (**2.D**)[103] (Figure 2.3) with twist angles between the two BT units of 43°, 48°, 43.8-54.0° and 37.7°, respectively. However, the monocation of **2.A** (as PF_6 salt)[101] is almost too planar (3.6-4.6°).

Fluorene and poly(fluorene)s have aroused interest as components of organic light-emitting diodes (OLEDs) because of their thermal and chemical stability and exceptionally high solution and solid-state fluorescence quantum yields (0.6-0.8).[104, 105] The facile introduction of alkyl substituents at the 9-position of monomeric fluorenes allows the synthesis of more soluble and processable molecules.[5, 106-108]

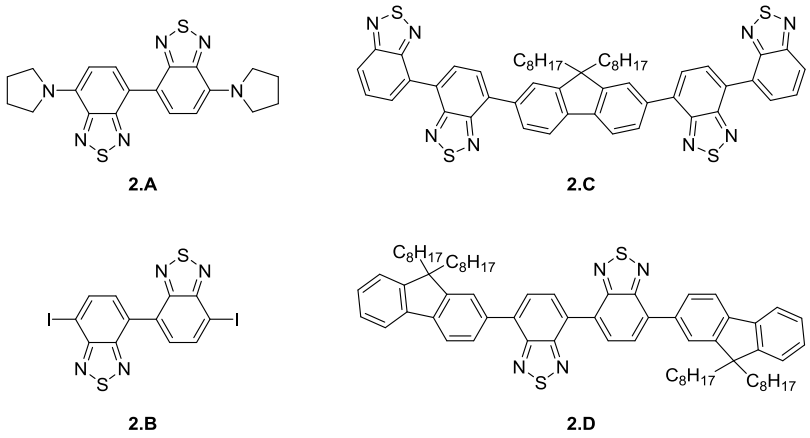

Figure 2.3 Four molecules containing the bBT unit.

Tertiary amines, such triphenylamine and diethylaniline are widely used units for hole-transporting layer (HTL) materials in OLEDs[109-111] even though problems such as surface diffusion and relatively low thermal stability have retarded practical applications. Incorporation of these bulky units in small molecules may overcome these problems and tend to suppress intermolecular aggregation, reduce the crystallisation propensity and improve the hole-transporting ability of the materials.[112]

Based on the properties described above, these three classes of molecules have been combined to form novel down-converter molecules, with each structural unit playing an important role. The bBT unit has been used as an absorbing core and its conjugation has been extended by functionalisation at the 2- and 7-positions with 3-alkyl-thiophene or alkyl-fluorene in order to extend the conjugation and increase the solubility. This core has been extended further with the incorporation of tertiary amines that should act as electron donating arms (Figure 2.4).

Figure 2.4. Schematic representation of the new phosphor molecules.

2.1.2. White LED and phosphor performances

In order to increase performance, the properties and characteristics of the components of these devices must be considered from another point of view. The luminous efficiency of the radiation (η_P) (also call luminous efficacy) can be expressed as the light output light power (also call luminous flux, Φ_V) from a device

(measured in lumens, that is the unit of light intensity perceived by the human eye) per electrical power input (measured in watts).[66]

$$\eta_P = \frac{\Phi_V}{V_f \cdot I_f} \qquad \text{Equation 2.1}$$

V_f and I_f are the LED operating voltage and current, respectively.

In particular, for a blue-LED with a yellow phosphor, the luminous flux is, for simplicity, mainly dependant on the external quantum efficiency of the blue-LED (η_{ex}) and the wavelength conversion efficiency of the yellow phosphor (η_{phos}).

$$\Phi_V \propto \eta_{phos} \cdot \eta_{ex} \qquad \text{Equation 2.2}$$

The external quantum efficiency is proportional to the internal quantum efficiency (η_{int}) of the blue LED, to the extraction efficiency (η_{ext}) of light from a blue LED die to a resin and to the extraction efficiency of light from an LED package to air (η_{pkg}).[113] In addition, there is a factor related to the absorption efficiency of the phosphor, which is often ignored. This is the rate of energy transfer from the lighting source (blue-LED) to the yellow phosphor material (Equation 2.3).[114]

$$\eta_{ex} \propto \eta_{int} \cdot \eta_{ext} \cdot \eta_{pkg} \qquad \text{Equation 2.3}$$

2.1.3. White emitting devices based on down-converting compounds

Duggal *et al.* were the first to implement the idea in the field of OLEDs generating white light by combining a blue OLED based on a commercial polyfluorene-based blue polymer (Cambridge Display Technologies) with a down-conversion system based on a mixture of organic molecules (perylene orange and perylene red) and inorganic phosphor particles (Y(Gd)AG:Ce).[115] They achieved an efficacy of 15 lm/W at 1000 cd/m^2, limited by the low efficiency of the blue OLED.[116]

In 2006 Krummacher *et al.* fabricated a white-emitting device that combined a highly efficient solution processed phosphorescent blue OLED based on an iridium phosphorescent dye (FIrpic)[117] and a commercial (OSRAM) down-conversion phosphor system (a nitridosilicate phosphor, $[Sr,Ba,Ca]_2Si_5N_8:Eu^{2+}$).[118] The

luminance efficacy of 14 lm/W of the blue OLED was enhanced to 25 lm/W in the white light-emitting diode. This strong enhancement was attributed to the isotropic radiation pattern of the excited phosphor particles.

In 2011 top emitting white OLEDs were demonstrated with a single or a duplex of organic down-converting layers.[119] The blue OLED was based on the fluorescent blue emitter system 2-methyl-9,10-bis(napthalen-2-yl)anthracene doped with 1 wt.% of 2,5,8,11-tetra-*tert*-butylperylene (TBPe). Two white OLEDs were obtained using the 4-dicyanomethylene-2-methyl-6-p-dimethylaminostyryl-4H-pyran doped at 1 wt.% in an Alq3 matrix alone and in combination with an extra layer of the yellow fluorescent dye N4,N4′-bis-(4-tert-butyl-phenyl)-N4,N4′-di-fluoranthen-3-yl-diphenylether-4,4′-diamine. The multi down converting layers OLED showed a broad emission spectrum with spectral contributions from each of the two down conversion materials. At 1000 cd/m^2 showed current efficacy, luminous efficacy and external quantum efficiency values of 1.4 cd/A, 0.88 lm/W and 0.83%, respectively.

In 2014 Findlay *et al.* presented a white hybrid LED, based on a inorganic commercial blue LED (Plessey Semiconductors Ltd) and the organic down converting material **[BODFluTh]$_2$FB** (Figure 2.5).The device combined the best of both the technology. The blue LED achieved excellent performance and the organic semiconductor avoided the use of rare-earth compounds, offering a broad and tunable emission.[120, 121]

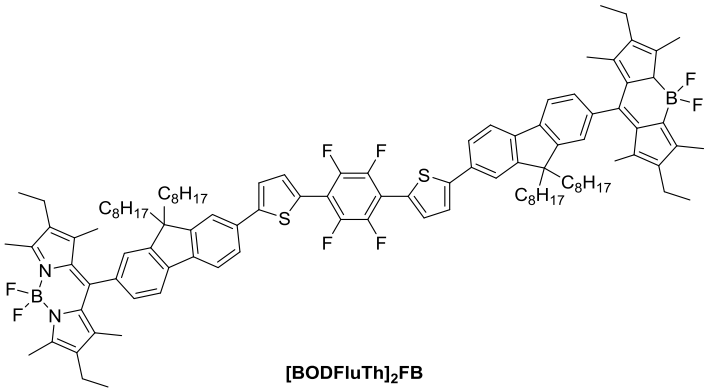

Figure 2.5 Structure of compound **[BODFluTh]$_2$FB**.

Following the approach described by Findlay *et al.* the synthesis, characterisation and application of four new emissive materials will be discussed in the following section.

2.2. Results and discussion

2.2.1. Synthesis of new emissive materials

Five new emissive materials **2.1-2.5** based on the bisbenzothiadiazole (bBT) core were synthesised using the convergent approach. The 7,7′-substituents of the bBT core will often be called "arms" in the following results and discussions (Figure 2.6).

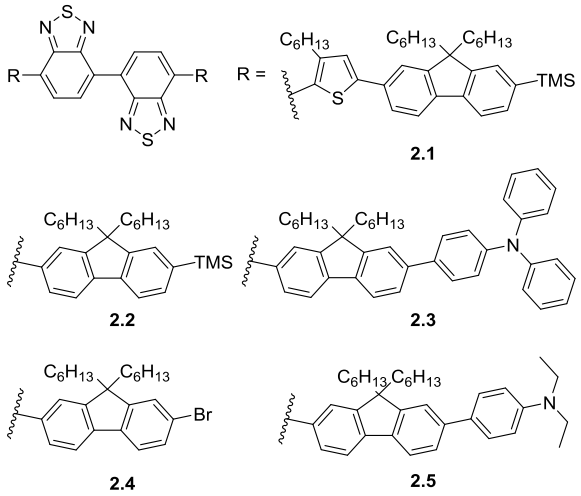

Figure 2.6 The structure of the five new emissive materials **2.1-2.5**.

The bBT core (**2.7**) was synthesised in good yields (80%) *via* the homo-coupling of 4-bromobenzothiadiazole with palladium acetate as catalyst, potassium carbonate as base and polyethylene glycol 4000 (PEG4000) as surfactant in *N*,*N*-dimethylformamide.[122] 7,7′-Diiodo-bBT (**2.8**) was then obtained in decent yield (45%) adding a solution of iodine and silver sulfate in sulfuric acid at 120ºC to **2.7**.[97]

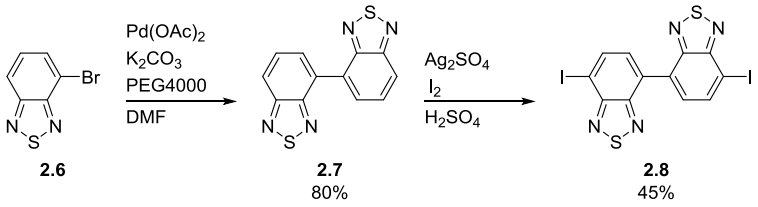

Scheme 2.1 Synthesis of 7,7'-diiodo-4,4'-bibenzo[c][1,2,5]thiadiazole (**2.8**).

Compound **2.8** was used as the core in **2.1-2.5** and it was initially coupled with 3-hexylthiophene-2-(boronic acid pinacol ester) **2.10**. Compound **2.10** was synthesised according to a literature procedure that consisted of the lithiation of the 2-position of 3-hexylthiophene (**2.9**), followed by consecutive quenching with triisopropyl borate and pinacol (Scheme 2.2).

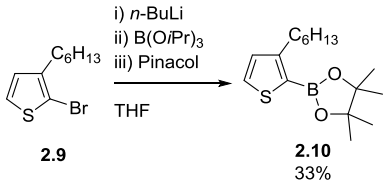

Scheme 2.2 Synthesis of **2.10**.

Compound **2.10** was coupled in low yield (18%) with **2.8** *via* Suzuki-Miyaura cross-coupling using the catalytic system of barium hydroxide/tetratra butyl ammonium bromide/tetrakis(triphenylphosphine)palladium(0). The obtained compound **2.11** was then stannylated at the thiophenyl α-position by direct lithiation followed by quenching with trymethyltin chloride to obtain compound (**2.12**) in good yield (88%).

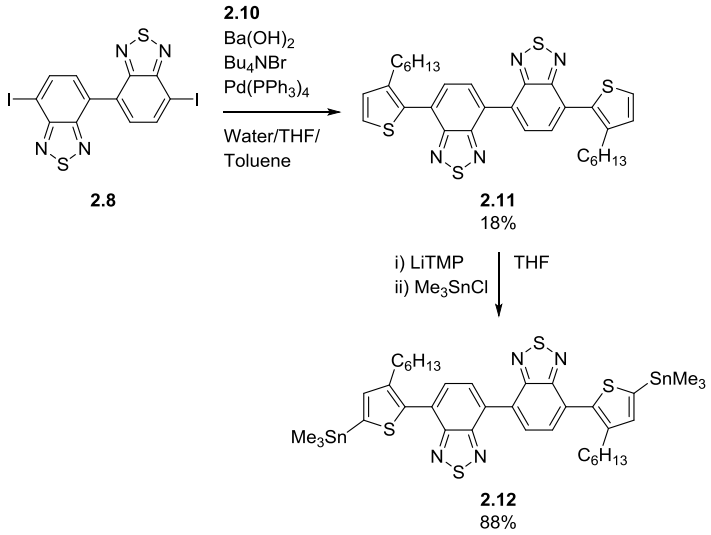

Scheme 2.3 Synthesis of **2.12**.

Commercially available fluorene (**2.13**) was alkylated with hexyl bromide in order to increase its solubility in organic solvents. 9,9-Dihexyl-9H-fluorene (**2.14**) was brominated with bromine in the presence of iodine to obtain 2,7-dibromo-9,9-dihexyl-9H-fluorene (**2.15**). This was protected in the 2-position with a trimethylsilyl group in order to obtain (7-bromo-9,9-dihexyl-9H-fluoren-2-yl)trimethylsilane (**2.16**) (Scheme 2.4).

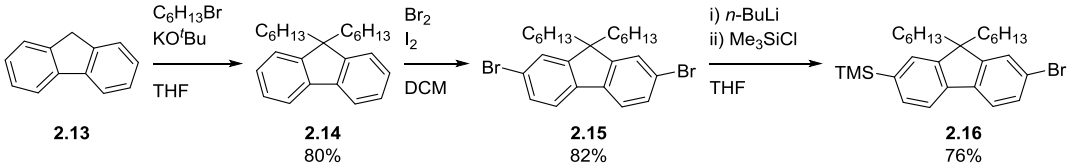

Scheme 2.4 Synthesis of compound **2.16**.

Compound **2.1** was then obtained *via* Migita-Kosugi-Stille coupling between **2.16** and **2.12**, using tetrakis(triphenylphosphine)palladium(0) as the catalyst (Scheme 2.5).

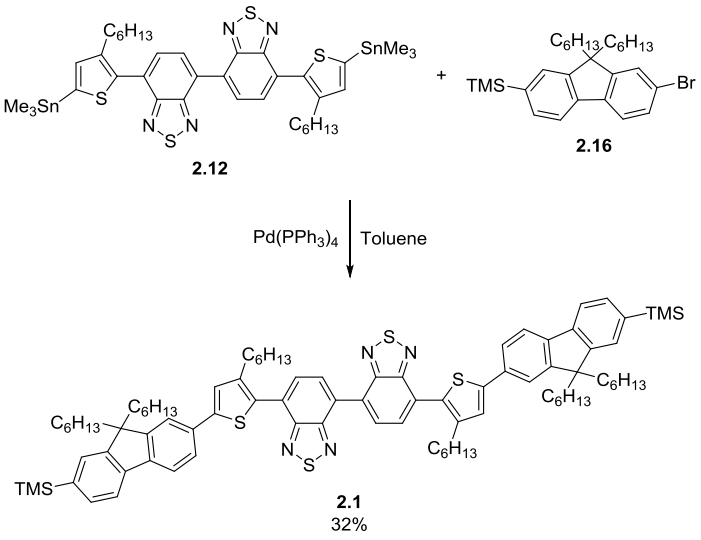

Scheme 2.5 Synthesis of compound **2.1**.

Following this, compound **2.15** was protected in the 2-position with a trimethylsilyl group and boronic acid **2.17** was obtained in good yields by lithiation followed by capping with triisopropyl borate.

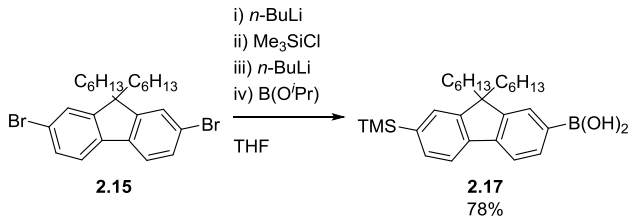

Scheme 2.6 Synthesis of compound **2.17**.

Compound **2.17** was coupled with **2.8** in good yield (62%) *via* Suzuki cross-coupling using potassium carbonate/tetrakis(triphenylphosphine)palladium(0) as catalytic system to obtain **2.2**. This was successively brominated in good yield (90%) by adding a bromine solution in dichloromethane to the mixture **2.2**/sodium acetate/triethylamine in THF (Scheme 2.7).

Compound **2.4** was then coupled with the commercially available (4-(diphenylamino)phenyl)boronic acid (**2.18**) and (4-(diethylamino)phenyl)boronic acid (**2.19**) *via* Suzuki-Miyaura cross-coupling using the catalytic system of barium hydroxide/tetra butyl ammonium bromide/tetrakis(triphenylphosphine)palladium(0) to obtain **2.3** and **2.5** respectively in good yields (Scheme 2.8).

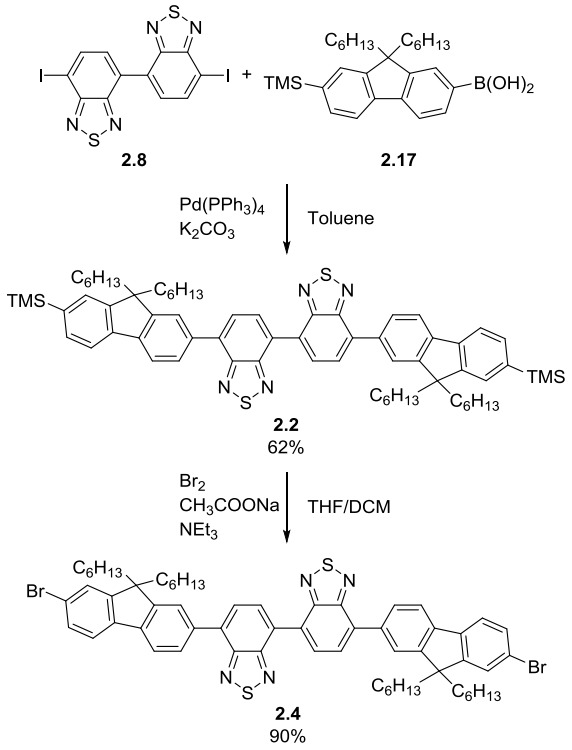

Scheme 2.7 Synthetic route to obtain **2.4**.

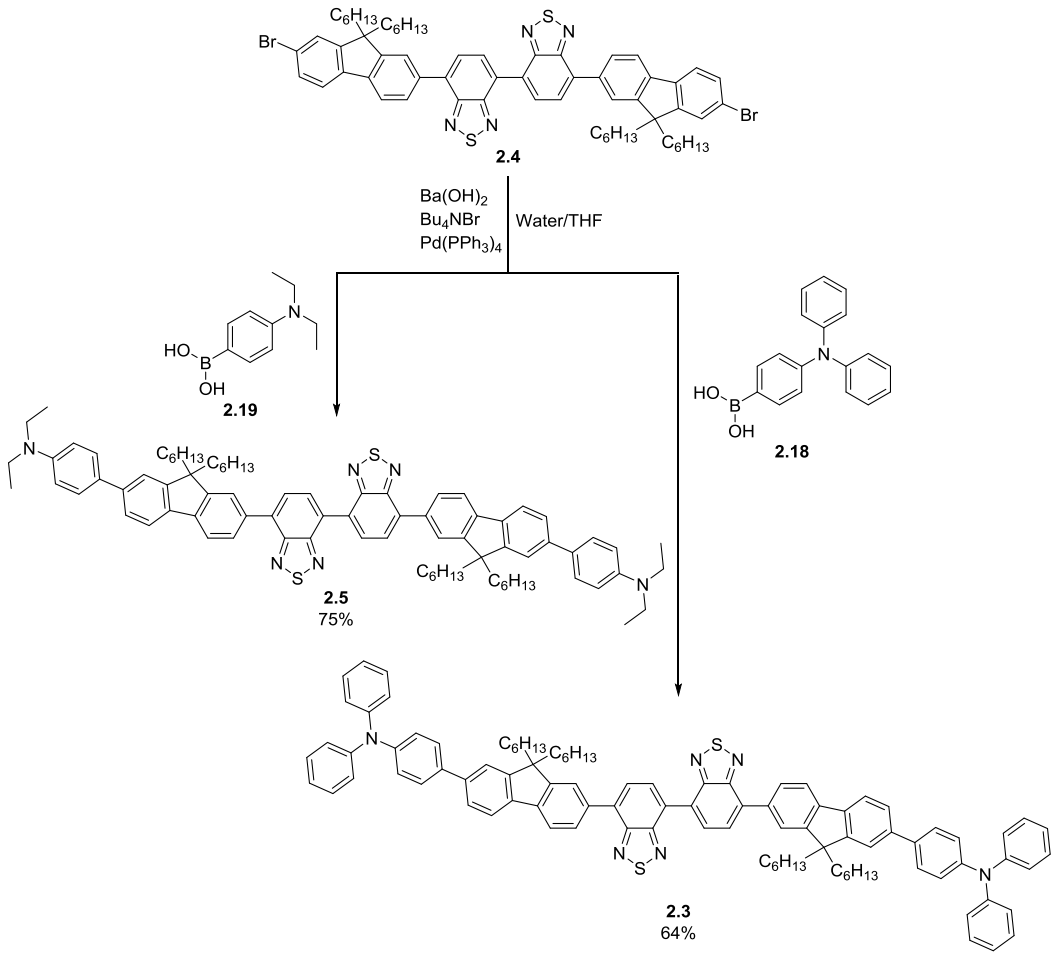

Scheme 2.8 Synthesis of **2.3** and **2.5**.

2.2.2. Characterisation of the new emissive materials

Absorption and emission spectra of **2.1-2.5** were recorded in dichloromethane media at concentrations of 1×10^{-5} and 1×10^{-6} M, respectively (Figure 2.7).

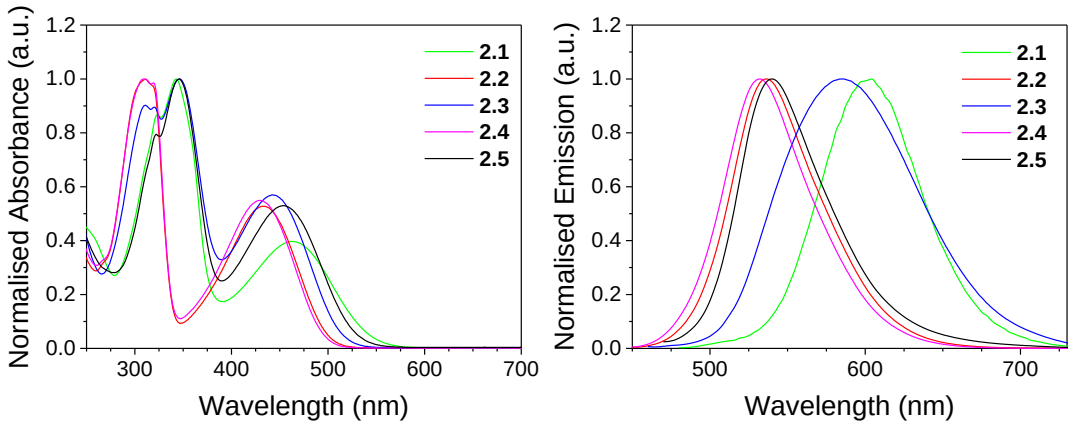

Figure 2.7 Normalised absorption (left) and emission (right) spectra of **2.1-2.5**.

Compounds **2.2** and **2.4** show very similar absorption spectra with two maxima at 430-433 and 309-311 nm, respectively. The more intense, higher energy band is usually associated with the BT core.[96, 103] Here it is slightly red shifted at longer wavelengths than those of BT, likely due to the longer conjugation of the bBT core. The weakest bands correspond to an interaction between the fluorene arms and the bBT core. Compounds **2.1**, **2.3** and **2.5** show a similar behaviour with two main absorptions at *ca.* 443-463 and 343-347 nm. The first, lower energy band can be attributed to the interaction between the donor-acceptor segments and it has a charge transfer character. The second band, as in compounds **2.2** and **2.4**, is associated with the BT core, and it is further red shifted due to the strong electron-acceptor character of the bBT core, emphasised from the particular structure of compounds **2.1**, **2.3** and **2.5**. Photoluminescence Quantum Yields (PLQYs) were recorded at 300K using as the excitation wavelength the appropriate less energetic λ_{max} of absorption. This was chosen in order to have a better estimation of the QY at the operative wavelength of the down converting materials (blue LED emission = 443-445 nm). PLQYs were obtained for the encapsulated powders (pressed against two glass substrates) and they show values from 4.1 to 18.8%.

Table 2.1 UV-Vis absorption maxima with molar attenuation coefficient, emission maxima and optical HOMO-LUMO gaps for **2.1-2.5**.

Compound	λ_{max} (nm) Absorption[a]	λ_{max} (nm) Emission[b]	HOMO-LUMO gap[h] (eV)	PLQY (solid state)[i]
2.1	463 (39700), 343 (100000), 323 sh (86700)	604[c]	2.3	5.1[c]
2.2	433 (33400), 311 (63400)	537[d]	2.5	18.8[d]
2.3	443 (47500), 347 (83300), 321 (74600), 311 (75200)	585[e]	2.4	14.5[e]
2.4	430 (42300), 319 sh (76000), 309 (77100)	532[f]	2.5	11.9[f]
2.5	454 (42500), 346 (80300), 322 (63900)	540[g]	2.4	4.1[g]

[a] measured in 1×10^{-5} M solution (dichloromethane); [b] measured in 1×10^{-6} M solution (dichloromethane); [c] *via* excitation at 463 nm; [d] *via* excitation at 433 nm; [e] *via* excitation at 443 nm;[f] *via* excitation at 430 nm; [g] *via* excitation at 454 nm; [h] calculated from the longest wavelength absorption edge; [i] measured in the powder pressed against two glass substrates.

The higher PLQY of **2.2** when compared with the analogue **2.4** is likely due to the quenching effect of the heavy atoms (TMS *vs* Bromine). Also, the higher value for compound **2.3** when compared with the analogue **2.5** is due to the bulky triphenyl amine terminal substituent that likely avoids aggregation in the solid state when compared with the smaller diethylphenylamine substituents.[39]

The optical HOMO-LUMO gap calculated from the onset of the lower energy absorption bands are very similar in the series (2.3-2.5 eV) but the emission of these materials ranges from 532 to 604 nm. This is likely due to the large differences in the donor-acceptor character of the molecules and will be discussed in the theoretical calculations section.

The redox properties of **2.1-2.5** are summarised in Table 2.2 and the cyclic voltammograms are shown in Figure 2.7-2.11. The five compounds show two similar reduction waves with a reversible/quasi reversible character likely attributable to the bBT core that is a recognised electron acceptor molecule.[123, 124]

Table 2.2 Redox and electronic properties of **2.1-2.5**.

Compound	E (V) Reduction	E (V) Oxidation	HOMO (eV)[a]	LUMO (eV)[a]	HOMO-LUMO Gap (eV)[b]
2.1	−1.88/−1.71; −2.07/−1.95	0.76/0.70; 1.30/1.17; 1.39/-	−5.5	−3.1	2.4
2.2	−1.85/−1.75; −2.03/−1.96	0.98/0.88	−5.6	−3.1	2.5
2.3	−1.87/−1.72; −2.03/−1.93	0.47/0.41; 0.98/0.88	−5.2	−3.1	2.1
2.4	−1.81/−1.73; −1.99/−1.93	1.09/0.98	−5.7	−3.1	2.6
2.5	−1.84/−1.76; −2.04/−1.95	0.27/0.21; 0.89/0.80	−5.0	−3.1	1.9

[a] calculated from the onset of the first peak of the corresponding redox wave and referenced to ferrocene which has a HOMO of -4.8 eV; [b] energy gap between HOMO and LUMO levels.

Compound **2.2** and **2.4** show a similar oxidation behaviour with only one quasi reversible oxidation at $E_{½}$ = 0.93 and 1.04 V, respectively. In fact, the fluorene moiety tends to lose one electron at the 9-position and the radical cationic character (charge) is stabilised by delocalisation across the aromatic region of the moiety.[5, 125] Compounds **2.3** and **2.5** show two oxidation waves; the first at $E_{½}$ = 0.44 and 0.24 V for **2.3** and **2.5**, respectively, has a reversible character and can be attributed to the simultaneous loss of one electron from the amine segments resulting in radical cations.[126-129] The second oxidation process at higher voltages ($E_{½}$ = 0.93 and 0.85 V for **2.3** and **2.5**, respectively) has a quasi-reversible character like **2.2** and **2.4** and is likely attributable to the removal of electrons from fluorene moieties generating radical cations.[126] Compound **2.1** exhibits a reversible oxidation process at $E_{½}$ = 0.73 V attributable to the fluorene segments. In this case the radical cations are generated at lower voltages when compared with the other compounds in the series; this is likely due to the presence of the thiophene unit between the bBT and fluorene moieties that increases the donor character of the fluorene. In addition, a quasi-reversible oxidation process ($E_{½}$ = 1.24 V) and a non-reversible anodic wave (E = 1.39 V), that can be attributable to the successive removal of two electrons from the thienyl groups, were observed.[130]

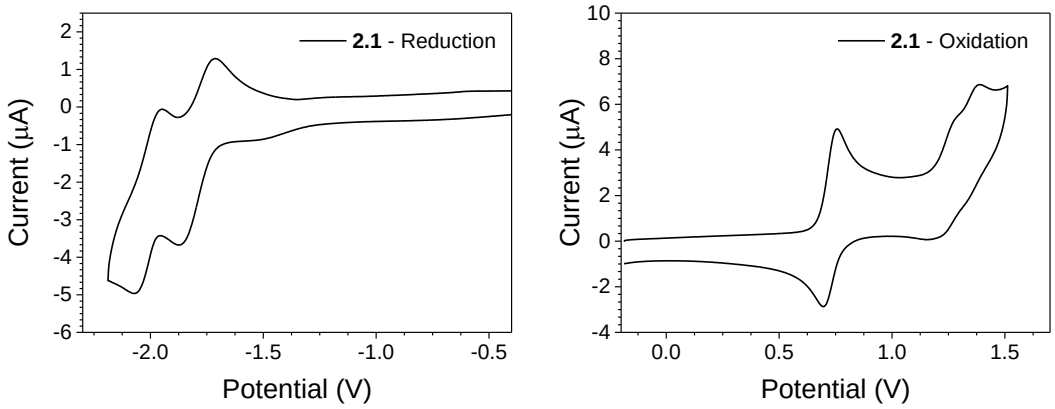

Figure 2.8 Cathodic (left) and anodic (right) waves from cyclic voltammetry of **2.1** referenced against the $E_{1/2}$ of the F_c/F_c^+ redox couple; 1×10^{-4} M solution in 0.1 M *n*-Bu_4NPF_6 (dichloromethane); scan rate 0.1 V s^{-1}.

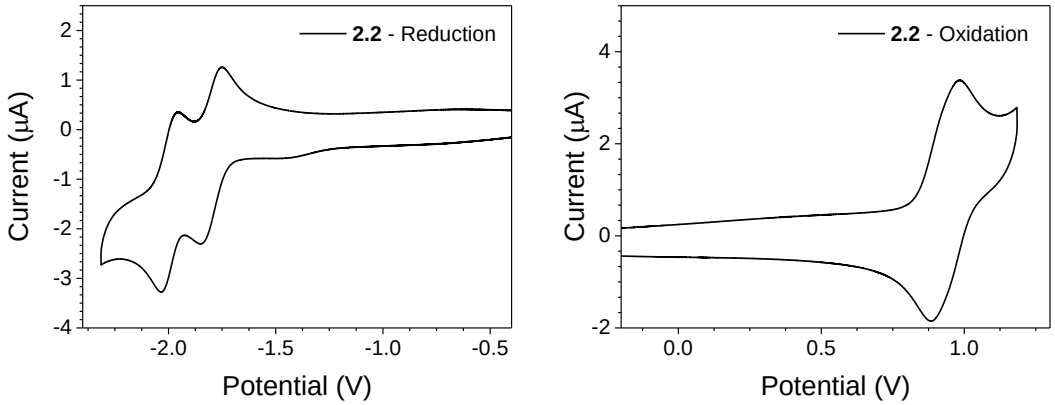

Figure 2.9 Cathodic (left) and anodic (right) waves from cyclic voltammetry of **2.2** referenced against the $E_{1/2}$ of the F_c/F_c^+ redox couple; 1×10^{-4} M solution in 0.1 M *n*-Bu_4NPF_6 (dichloromethane); scan rate 0.1 V s^{-1}.

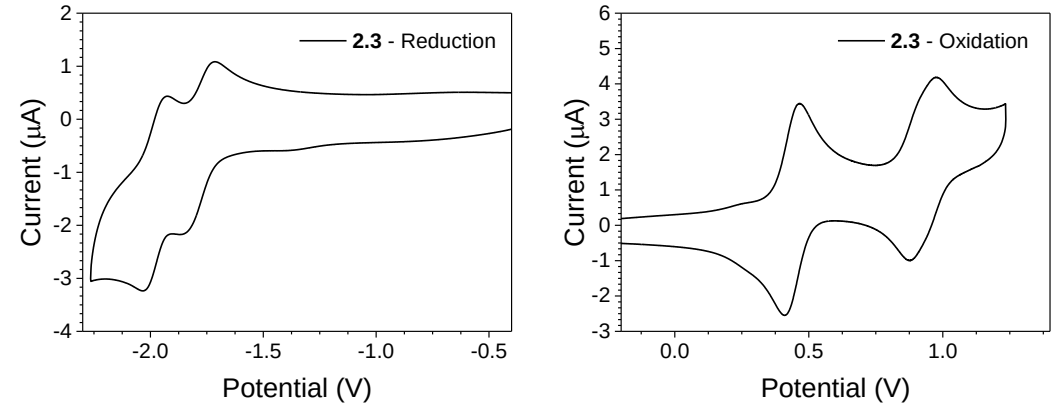

Figure 2.10 Cathodic (left) and anodic (right) waves from cyclic voltammetry of 2.3 referenced against the $E_{1/2}$ of the F_c/F_c^+ redox couple; 1×10^{-4} M solution in 0.1 M *n*-Bu_4NPF_6 (dichloromethane); scan rate 0.1 V s^{-1}.

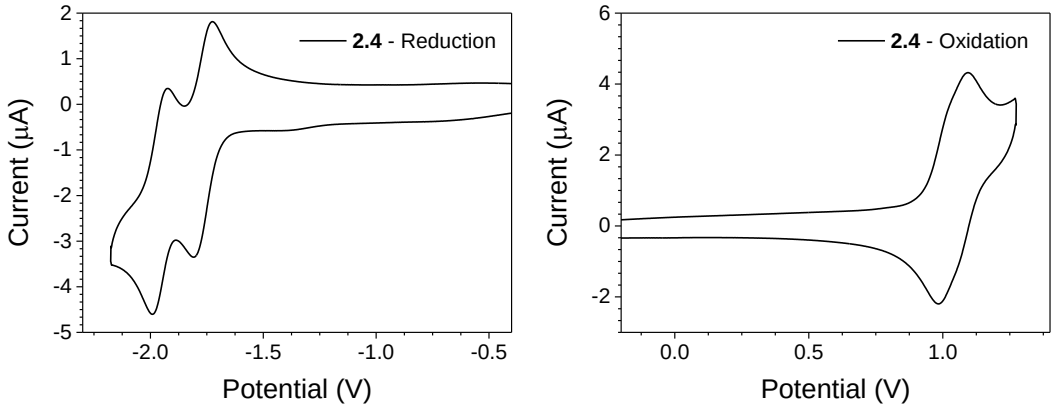

Figure 2.11 Cathodic (left) and anodic (right) waves from cyclic voltammetry of 2.4 referenced against the $E_{1/2}$ of the F_c/F_c^+ redox couple; 1×10^{-4} M solution in 0.1 M *n*-Bu_4NPF_6 (dichloromethane); scan rate 0.1 V s^{-1}.

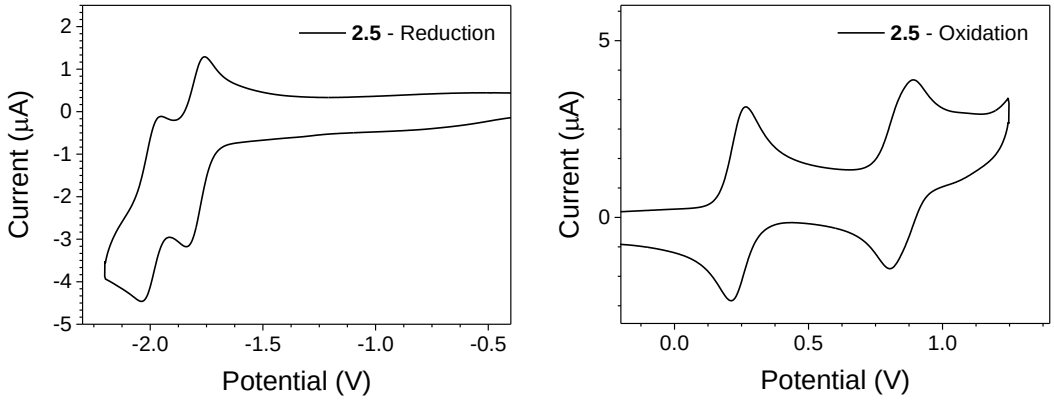

Figure 2.12 Cathodic (left) and anodic (right) waves from cyclic voltammetry of 2.5 referenced against the $E_{1/2}$ of the F_c/F_c^+ redox couple; 1×10^{-4} M solution in 0.1 M *n*-Bu_4NPF_6 (dichloromethane); scan rate 0.1 V s^{-1}.

The electrochemical HOMO and LUMO values were estimated from the onset of the oxidation and reduction peaks respectively and referenced to the ferrocene/ferrocenium redox couple, which has a known value of −4.8 eV.[131] The LUMO energy is the same in the series **2.1-2.5** due to the shared bBT core, however the HOMO energy changes from a minimum of −5.7 eV for **2.4** to a maximum of −5.0 for **2.5**. For this reason the electrochemical HOMO-LUMO gaps change according with the electron donor character of the peripheral arms: Br-Fluorene > TMS-Fluorene > TMS-Fluorene-Thiophene > TPA-Fluorene > Bepa-Fluorene.

The materials are thermally stable with 5% mass loss observed only upon heating to 367°C (and above) with thermal transitions measured by differential scanning calorimetry (DSC, Figure 7.1) evident only at temperatures above 170°C for **2.2-2.5** and at 67°C for **2.1** (Table 2.3). Since these materials would be integrated in hybrid devices they should have thermal properties compatibles with those of the inorganic

blue LED. Inorganic LEDs have operating temperatures in the range from −40ºC to *ca.* 130ºC, with the highest temperature usually reached at the junction. For these reasons compounds **2.1** and **2.4** with T_m of only 67 and 70ºC, respectively, should not be suitable for a working device. On the other hand, compounds **2.2**, **2.3** and **2.5** presented thermal transitions well above the operating temperatures of the blue LEDs, and they should thermally perform well. Compound **2.5** showed the best thermal proprieties with a single melting transition at 302ºC and 5% mass loss at 423ºC. Interestingly compounds **2.3** and **2.4** showed two melting transitions and additional glass transitions that can affect the performance of the materials when included in working devices. In fact glass transitions are associated with changes in the mechanical properties of the material usually linked to changes in the mobility of the molecules in the lattice.

Table 2.3 Principal thermal proprieties of **2.1-2.5** determined with thermal gravimetric analyses and differential scanning calorimetry.

	2.1	**2.2**	**2.3**	**2.4**	**2.5**
5% mass loss (°C)	367	401	412	418	423
10% mass loss (°C)	403	412	428	436	441
DSC transtions (°C)	67 (T_m)	197 (T_m), 223 (T_m)	216 (T_m), 221 (T_m), 166 (T_g), 337 (T_g)	70 (T_m), 170 (T_m), 116 (T_g)	302 (T_m)

2.2.3. Theoretical calculations

In order to explain the experimentally observed absorption and emission spectra and the electrochemical behaviour quantum chemical calculations were performed for **2.1-2.5** using density functional theory (DFT) and its time resolved counterpart (TD-DFT).[132, 133] All the calculations were performed with the software package Gaussian09 (Revision A.02).[134] The hexyl alkyl side chains that are largely uninvolved in the electronic processes studied were replaced by methyl groups to reduce the computational cost. The calculations were performed using the CAM-B3LYP/6-31G(p,d) level of theory. The functional used combines the hybrid qualities of B3LYP and includes a long-range correction[135] in order to perform better when systems with extensive conjugation are treated. In fact, the B3LYP functional includes a constant amount of 20 % Hartree-Fock (HF) exchange, whereas the

amount of HF exchange varies from 19 to 85 % in the CAM-B3LYP functional depending on distance.[136] The 6-31G(d,p) basis set has been used as good compromise between accuracy and computation cost.

In order to assess the starting configuration for the geometry optimisations, the main torsional potential energy surfaces (PESs) were calculated for **2.1-2.5** considering the rotation between the different units of the molecules. In particular, fragments of the compounds obtained were considered as the half molecule with addition of a hydrogen atom (**2.1s-2.5s**, *e.g.* for **2.2s** in Figure 2.13) and used to determine the PESs for the rotations: BT-Thiophene(fluorene(TMS)), BT(thiophene)-fluorene, BT-Fluorene(TMS), BT-Fluorene(triphenylamine), BT(fluorene)-triphenylamine, BT-Fluorene(Br), BT-Fluorene(diethylphenylamine) and BT(fluorene)-diethylphenylamine (see appendix, Figure 7.2 and Table 7.1).

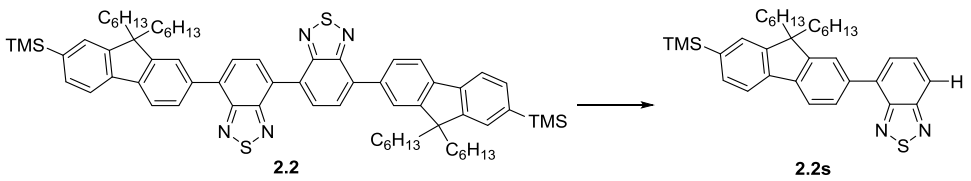

Figure 2.13 Fragment **2.2s** obtained from **2.2** considering half molecule and adding a hydrogen atom.

The ground geometries were then optimised for **2.1-2.5** and the analyses of the vibrational frequencies indicate the location of the sought-for energy minimum for all the molecules. The optimised geometries are reported in Figure 2.14. In all the compounds the bBT core is twisted along the C-C bond between the two benzothiadiazole units. The dihedral angles are of *ca.* 147-149 (33-31) degrees along the **2.1-2.5** series. This values are slightly smaller when compared with the non-substituted bBT unit and 7,7′-disubstituted bBT compounds.[101, 102, 103]

The calculated HOMO and LUMO energies respectively underestimate and overestimate the electrochemical values. This results in an overestimation of the calculated HOMO-LUMO gaps energies in respect to both the electrochemical and optical experimental measurements. However the general trend obtained experimentally in the series is respected qualitatively (by the levels of relative disposition) apart from the gap calculated for **2.5** that is slightly overestimated in the series (Table 2.4 and Figure 2.15).

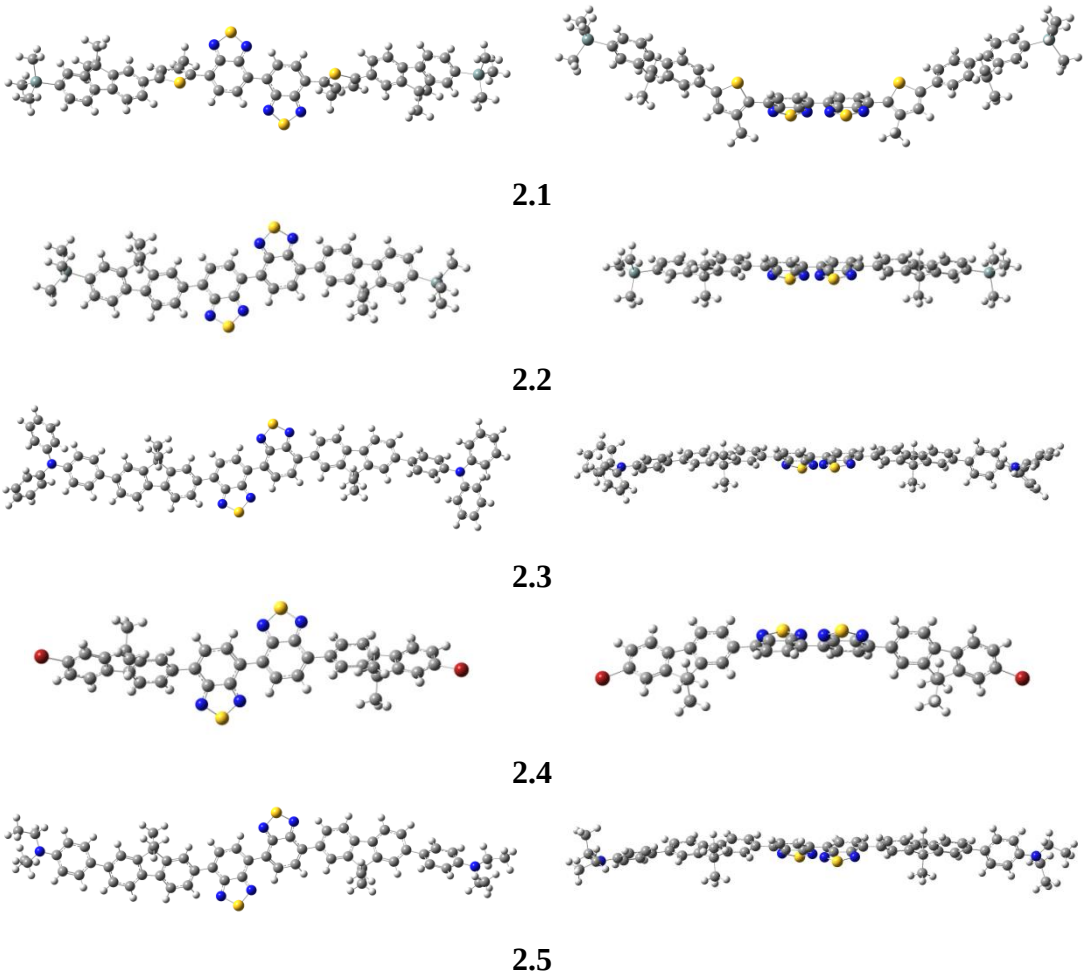

Figure 2.14 Optimised geometries for **2.1-2.5** calculated at the CAM-B3LYP/6-31G(d,p) level of theory.

Table 2.4 Electrochemical and calculated (at the CAM-B3LYP/6-31G(d,p) level of theory) HOMO and LUMO energies; electrochemical, optical and calculated (at the CAM-B3LYP/6-31G(d,p) level of theory) HOMO-LUMO gap energies for **2.1-2.5**.

	Compound	2.1	2.2	2.3	2.4	2.5
Energy (eV)	**LUMO (CAM-B3LYP/6-31G(d,p))**	−1.6	−1.5	−1.5	−1.6	−1.4
	HOMO (CAM-B3LYP/6-31G(d,p))	−6.4	−6.6	−6.1	−6.7	−6.1
	LUMO (Electrochemical)	−3.1	−3.1	−3.1	−3.1	−3.1
	HOMO (Electrochemical)	−5.5	−5.6	−5.2	−5.7	−5.0
	HOMO-LUMO gap (CAM-B3LYP/6-31G(d,p))	4.8	5.1	4.6	5.1	4.7
	HOMO-LUMO gap (Electrochemical)	2.4	2.5	2.1	2.6	1.9
	HOMO LUMO gap (Optical)	2.3	2.5	2.4	2.5	2.4

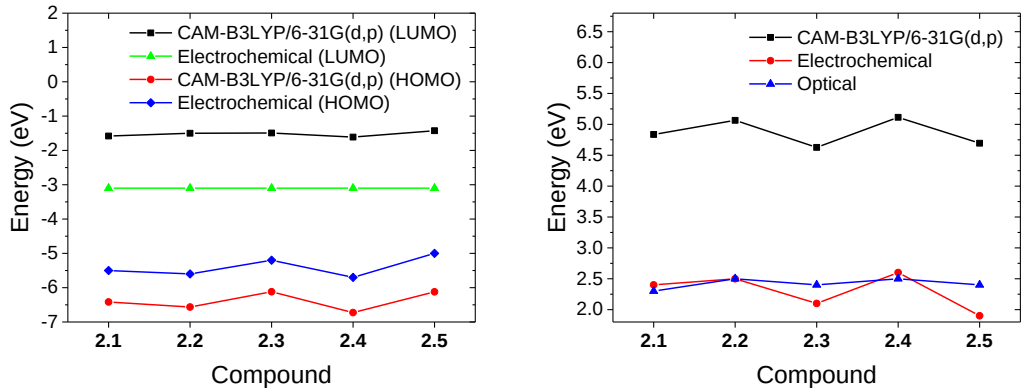

Figure 2.15 Electrochemical and calculated (at the CAM-B3LYP/6-31G(d,p) level of theory) HOMO and LUMO energies for **2.1-2.5** (left). Electrochemical, optical and calculated (at the CAM-B3LYP/6-31G(d,p) level of theory) HOMO-LUMO gap energies for **2.1-2.5** (right).

The first 20 singlet vertical transitions were calculated for compunds **2.1-2.5** (in vacuum) using the TD-DFT/CAM-B3LYP/6-31G(d,p) level of theory and fitted with Gaussian curves (full width at half maximum (FWHM) = 0.3 eV) using the software GaussSum 3.0 (Figure 2.16).[137] The calculated vertical absorptions overestimate the experimental absorption maxima energies of 0.2-0.4 eV, but the trends are reproduced (Figure 2.17). The major contributions to each transition were calculated and they are summarised in the appendix (Figure 7.3, Figure 7.4, Table 7.2-Table 7.6). Considering the longest wavelength vertical absorption in each spectrum, it is possible to distinguish two different behaviours in the series. For **2.2** and **2.4** these are between the HOMO and LUMO orbitals, mainly localised in the linear aromatic conjugated backbone and in the bBT core respectively, leading to the largest energies in the series. Alternatively, there are two different contributions to the vertical transition for compounds **2.1**, **2.3** and **2.5**: HOMO → LUMO and HOMO−2 → LUMO. The energy of the transition depends on the ratio between these two contributions at the transition: a higher HOMO → LUMO contribution corresponds to a smaller energy for the transition. In other words, increasing the contribution of the transition from the electron-donating arms towards the electron-acceptor core results in smaller energies. This is evident in the graphical representation of the orbitals, in fact the HOMO → LUMO transition are between orbitals mainly distributed in the arms toward orbitals distributed in the bBT core, while the HOMO−2 → LUMO transitions are between orbitals localised mainly in the core portions (only in **2.1** the HOMO −2 orbital is partially distributed along the fluorene arms).

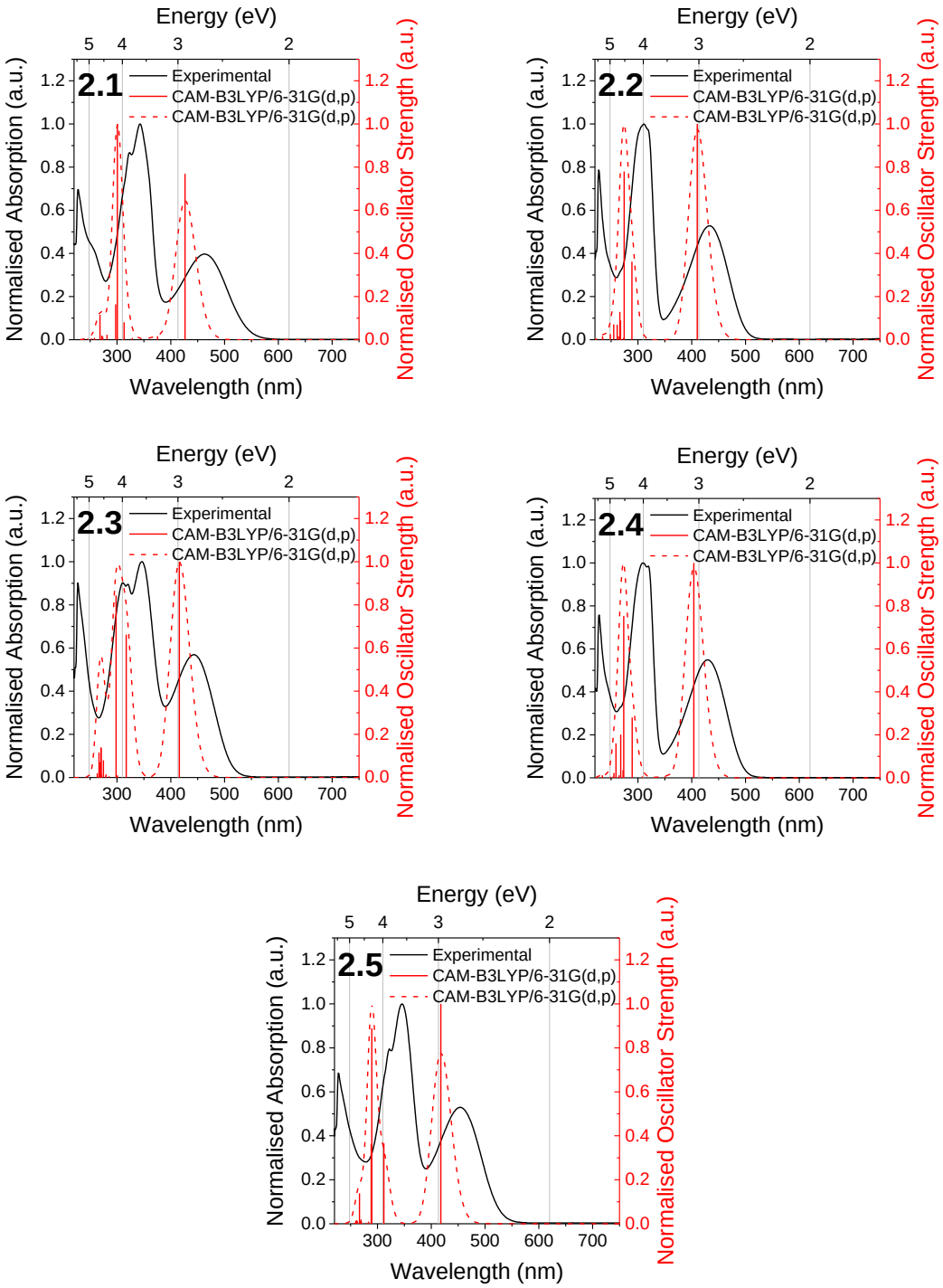

Figure 2.16 Experimental UV-Vis absorption spectra (black), calculated vertical absorptions (red) and Gaussian fitted (FWHM = 0.3 eV) absorption spectra at the TD-DFT/ CAM-B3LYP/6-31G(d,p) level of theory (dashed red) on the vacuum for **2.1**-**2.5**.

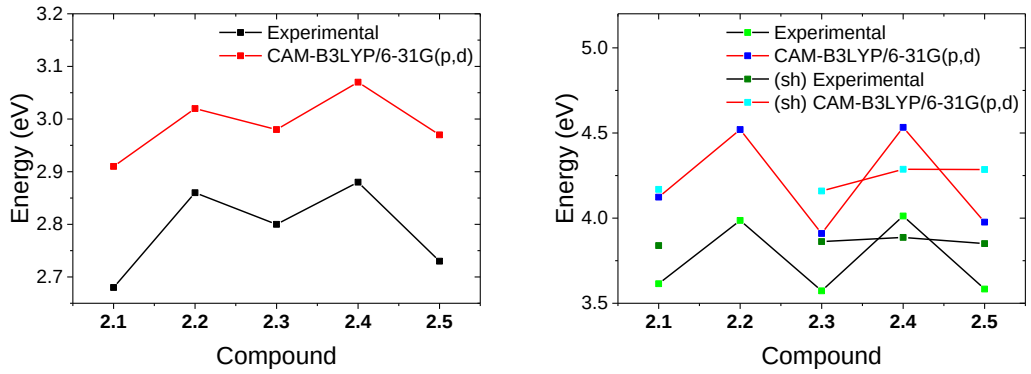

Figure 2.17 First transition (left) and second transition with shoulder (right) for **2.1-2.5**, experimental (absorption maxima) and calculated (significant vertical transition) at the TD-DFT/CAM-B3LYP/6-31G(d,p) level of theory.

In compounds **2.3** and **2.5** the fluorene segment can act as both the electron-accepting and electron-donating unit; their electronic clouds are always more delocalised. In compound **2.1** the thiophene unit acts as the main electron-donating moiety, decreasing the donor contribution of the fluorene segment and decreasing both the HOMO-LUMO gap and the first excited state energy.

The second main absorption band is more difficult to interpret, although the calculated energies qualitatively (by the levels of relative disposition) agree with the experimental one (Figure 2.17). For completeness, representative orbitals involved in the second transition are reported in the appendix (Figure 7.4).

2.2.4. Device fabrication and characterisation

With the aim of fabricating white light emitting hybrid devices, **2.1-2.3** and **2.5** were incorporated as co-emitters in hybrid devices alongside a commercial blue LED. This LED was designed in order to host the organic material on top of the chip. Different methods can be employed to incorporate the organic compound in such a structured device; these can be distinguished depending on the solubility of the compound in organic solvents. If the material is soluble, drop casting, spin coating, doctor blade coating, dip coating or spray coating techniques can be generally adopted. On the other hand, if the organic material is insoluble, more expensive techniques such as vacuum thermal evaporation, organic vapour phase deposition or organic molecular beam deposition can be used. Compounds **2.1-2.3** and **2.5** are very soluble in common organic solvents such as dichloromethane, chloroform, THF and toluene. For this reason they were initially tested for deposition by drop casting on top of glass slides. Unfortunately, this straightforward and generally convenient

technique showed discouraging preliminary results; the film was poor quality, cracked easily and would not completely coat the LED, resulting in a significant amount of blue light passing through. In fact, deposition by drop casting has few drawbacks such as a poor uniformity of the deposited layers, with micro-ordered sites that require extended annealing times in order to obtain morphologically uniform films. For this reason the co-emissive materials were incorporated in a non-emissive matrix, as recently reported by A. Kuehne *et al.*,[138] obtained *via* the polymerisation of 1,4-cyclohexanedimethanol divinyl ether (CHDV) in the presence of a catalytic amount of the photoacid generator (PAG) 4-octyloxy diphenyliodonium hexafluoroantimonate. The dispersion in a non-emissive matrix allows the use of low concentrations of the bulk solutions for deposition (*e.g.* 0.5-3% w/v), a rapid curing of the matrix and retention of the existing solution-state optical properties. As a non-conventional technique in the field of organic emissive compounds, recently it was successfully adopted by Skabara *et al.* in the fabrication of an efficient hybrid white LED device[64] analogous to those disclosed in this chapter.

The solution of the organic material in CHDV containing 1% w/v of the PAG was deposited on top of the blue LED chip, specifically designed to host *ca.* 1.5 μL of solution, as shown in Figure 2.1. The solutions were rapidly cured by exposure to UV light (254 nm) for 5 minutes, producing a hardened layer that fully covered the blue LED chip.

The CIE coordinates, maximum emission and maximum luminous flux of the commercial blue LEDs used were initially measured (Table 2.5 and Figure 2.18). The standard method consists of measuring the electroluminescence (EL) properties of an LED placed inside an integrating sphere with an applied forward current of 25 mA. The calibrated integrating sphere collects the emitted light recording an absolute intensity measurement. The EL spectra were corrected for the system response and then used to determine the chromaticity coordinates (x, y) in the CIE 1931 colour space chromaticity diagram and the correlated colour temperature (CCT).

The CIE coordinates and the emission maxima of all the LEDs tested did not change significantly; all had CIE 1931 coordinates of *ca.* (0.16, 0.02) and emission maxima of *ca.* 444 nm corresponding to the electron-hole recombination in the quantum well structure of the LED.[139] However, the values of the maximum luminous flux changed significantly from 0.225 to 0.409 mW nm^{-1}. For this reason, when possible,

LEDs with similar maximum luminous flux were used for the same co-emitter to allow close comparison of results.

Table 2.5 Characteristic of the blue LEDs used.

Blue LED	Max emission (nm) and Max luminous flux (mW/nm)		CIE Coordinates		Blue LED	Max emission (nm) and Max luminous flux (mW/nm)		CIE Coordinates	
			x	y				x	y
B22	444	0.389	0.157	0.021	**B18**	443	0.263	0.159	0.019
B41	443	0.409	0.159	0.019	**B43**	445	0.351	0.157	0.021
B14	444	0.393	0.158	0.020	**B46**	445	0.365	0.157	0.021
B21	445	0.361	0.159	0.019	**B59**	445	0.364	0.157	0.021
B19	444	0.242	0.158	0.021	**B75**	443	0.377	0.158	0.020
B15	445	0.371	0.157	0.021	**B31**	445	0.261	0.157	0.021
B17	444	0.372	0.158	0.020	**B33**	443	0.225	0.158	0.020
B25	444	0.351	0.158	0.021	**B35**	443	0.288	0.158	0.020
B26	443	0.371	0.158	0.020	**B57**	443	0.279	0.158	0.020

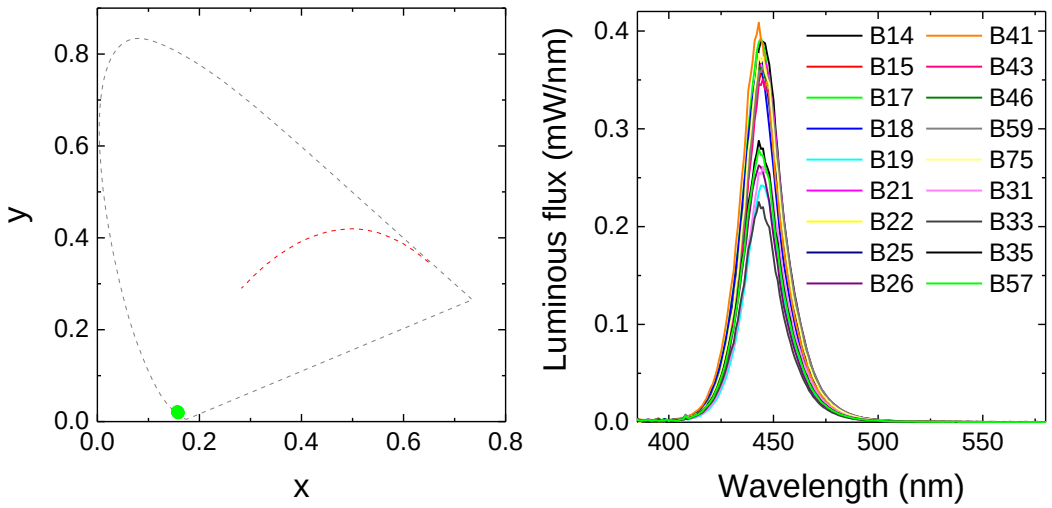

Figure 2.18 CIE coordinates (left) and emission spectra (right) of the blue LED used driven at 25 mA.

In order to achieve the best results, different concentrations of bulk solutions of **2.1**, **2.2**, **2.3** and **2.5** were tested in the range of 0.5 to 3% w/v. Specifically, for the first batch of devices, solutions ranging from 0.5 to 2% for **2.1**, from 0.5 to 1% for **2.2**, from 0.5 to 2% for **2.3** and from 0.5 to 3% for **2.5**, were prepared. The properties of the first batch of devices obtained (**A**-**J**) are summarised in Table 2.6.

The emission spectra of the devices exhibit two maxima. The more energetic peak at *ca.* 444 nm is characteristic of the inorganic commercial LED. The second is

generated from the emission of the organic down-converter and the energy depends on the nature of this material.

Please note that the properties of the devices obtained with compound **2.5** are not reported due to the inconsistency of the results. Compound **2.5** was relatively insoluble in CHDV and the morphology of the encapsulated films obtained indicated that dispersing the material was not controllable. Compound **2.1** was not suitable for further investigations; the hybrid devices **A**-**B** had colour qualities not suitable for the production of white light.

Table 2.6 Characteristics of the first batch of hybrid devices (**A-J**).

Device	Blue LED	Compound	Concentration (w/v %)	Correlated colour temperature (K)	CIE 1931 Coordinates	
					x	y
A	B22	**2.1**	0.5	22000	0.18	0.04
B	B41	**2.1**	2.0	1710	0.43	0.25
C	B14	**2.2**	0.5	22000	0.22	0.19
D	B21	**2.2**	0.7	22000	0.21	0.16
E	B19	**2.2**	0.8	22000	0.24	0.23
F	B15	**2.2**	1.0	4685	0.38	0.53
G	B17	**2.3**	0.5	22000	0.19	0.09
H	B25	**2.3**	1.5	22000	0.25	0.17
I	B26	**2.3**	1.8	5632	0.33	0.31
J	B18	**2.3**	2.0	3632	0.41	0.44

The combination of the emission of **2.1** (a maximum at *ca.* 600 nm in the devices) with the blue emission from the commercial LED results in colour coordinates well below the white Planckian locus (corresponds to light emitted from a black body radiator at various colour temperatures, a measure of the "whiteness" of a white light source) of the CIE 1931 diagram (Figure 2.21). The resulting emissions had a strong red component. Compound **2.2** was not suitable for further investigation for the opposite reason, its emission (a maximum at *ca.* 538 nm in the devices), combined with that of the blue LED, leads to colour coordinates above the white Planckian locus of the CIE 1931 diagram (Figure 2.21), with emission showing a strong yellow component. Contrarily, compound **2.3** indicated it was an ideal candidate. Using bulk solutions in the range 1.8-2.0% w/v, it was possible to obtain different tonalities (shades) of white light, with the best result obtained with device **I** (1.8%) that

achieved the CIE 1931 coordinates (0.33, 0.31) with a colour correlated temperature of 5632 K. These are values close to those of the D65 standard illuminant (0.31, 0.33) and to the colour temperature of the mid-morning/mid-afternoon daylight (5503 K), respectively.[88]

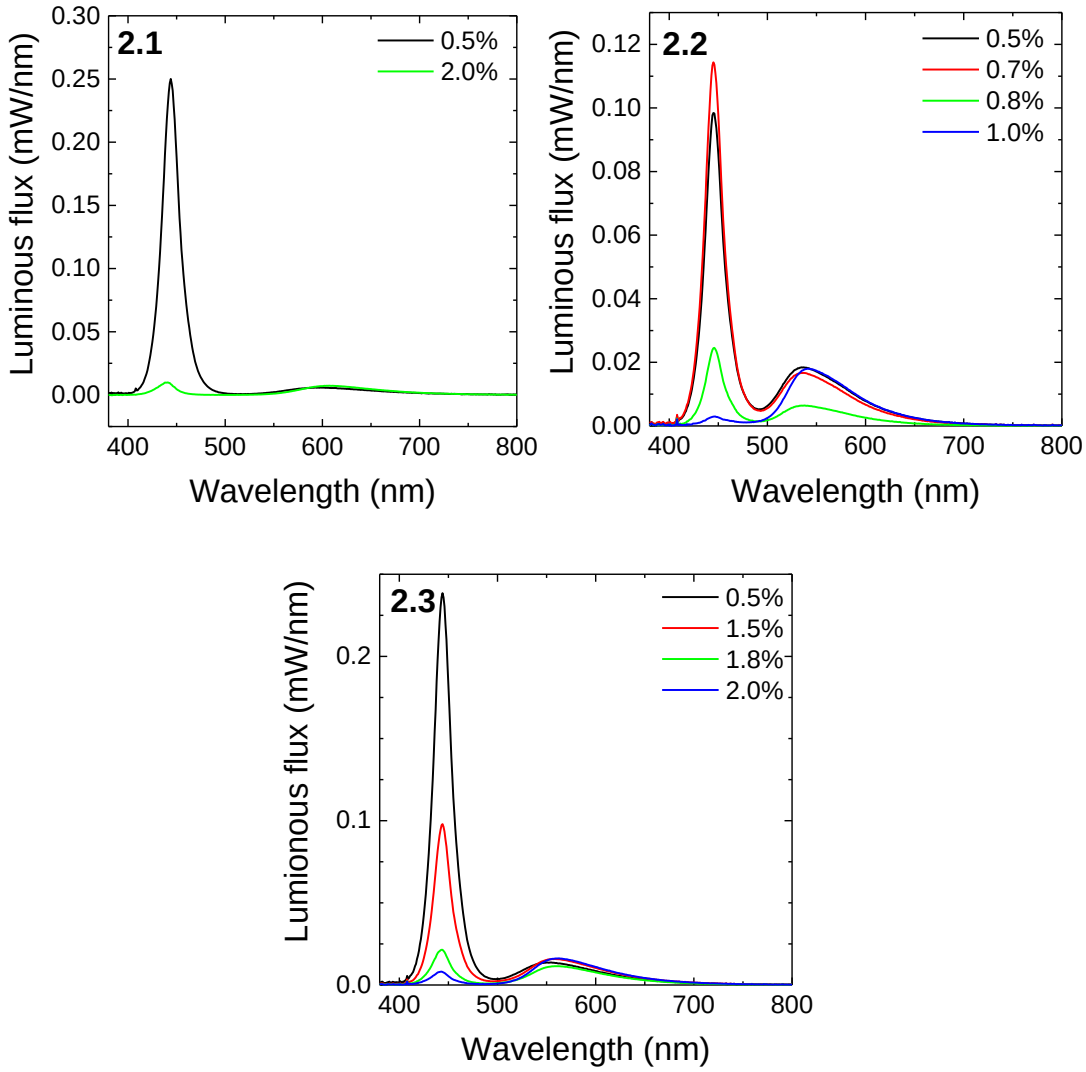

Figure 2.19 Emission spectra of devices **A-J** driven at 25 mA.

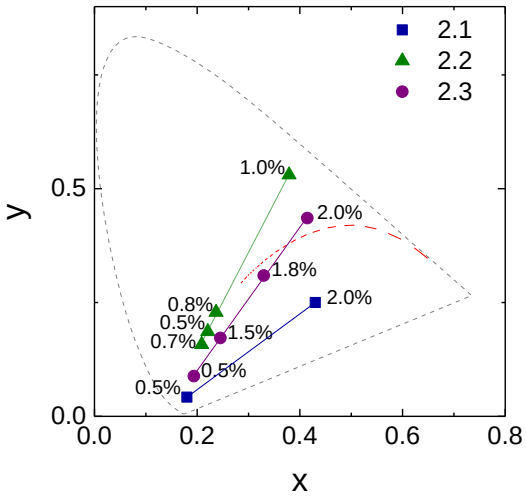

Figure 2.20 CIE 1931 coordinates for the device **A**-**J**.

Figure 2.21 shows the ratio between the emission maxima of the blue LED and the co-emitter change with concentration. For devices **A-J** the max luminous flux of the co-emitter remained almost constant with increasing concentration, with values of approximately 10^{-2} mW nm^{-1}. However the max luminous flux of the blue LED decreased by more than one order of magnitude with increasing concentration of the co-emitter (Figure 2.21). The ratio between the two maxima of luminous flux present in the spectra of the different devices is represented in blue in Figure 2.21. It has a decreasing quasi-linear behaviour for the three compounds and the value goes below 1 (the value of the max luminous flux relative to the co-emitter emission is bigger than that relative to blue LED emission) only for high values of concentration of the co-emitter, for example in device **F** (co-emitter **2.2** at 1% w/v) and in device **J** (co-emitter **2.3** at 2 % w/v).

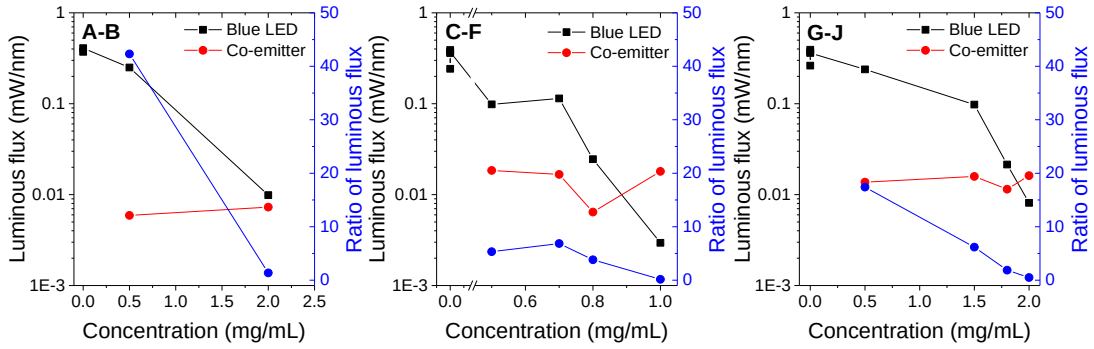

Figure 2.21 Luminous flux maxima and ratio of luminous flux (blue LEDs/co-emitter) at different concentrations for the devices **A-J**.

The luminous efficacy was calculated for the pure blue LEDs and for the hybrid devices. This is a measure of the efficiency with which the devices provide visible light from the electricity provided. The luminous efficacy is very similar for all the blue LEDs used (*ca.* 3 lm/W), whereas it slightly decreases with increasing the concentration of the co-emitter when the hybrid devices are considered. The ratio between the luminous efficacy of the blue LED and of the hybrid devices stays almost constant when the concentration of the co-emitter is increased for devices **A-J** (Figure 2.22). All these results are evidence of an inefficient conversion of the blue LED light by the organic materials.

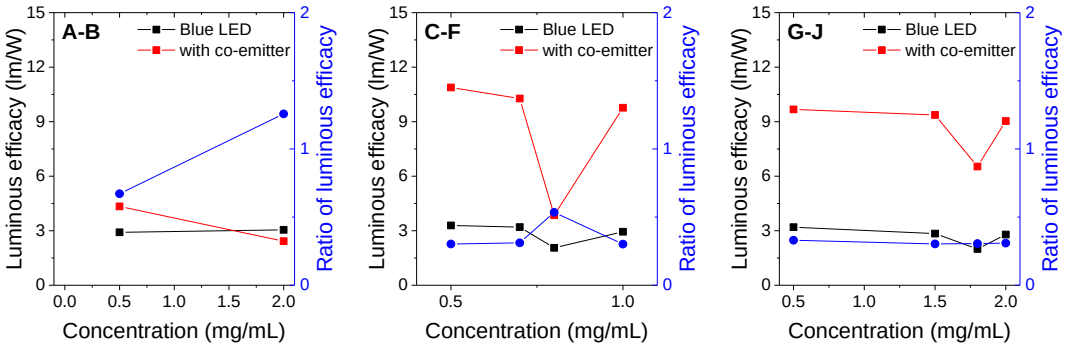

Figure 2.22 Luminous efficacy maxima and ratio of luminous efficacy (blue LED/hybrid LED) at different concentrations for the devices **A-J**.

This behaviour is not desirable in such devices, in fact one expects that both the luminous flux and the luminous efficacy of the hybrid LEDs increase with the concentration of the co-emitter. To better understand this, compound **2.3** was explored further. In order to understand if the solvent media and the concentration influence its absorption and emission properties, the intensities of the absorption and emission maxima were measured for different solutions of **2.3** in dichloromethane and for different cured films of **2.3** deposited on quartz slides. These were obtained depositing 0.1 mL of different solutions of **2.3** in CHDV with 1% of PAG (same conditions used in the hybrid devices) on quartz slides (1 × 1 cm^2) and curing them for 5 minutes under UV light (254 nm). The absorption and emission spectra recorded are presented in Figure 2.23 and Figure 2.24 for the dichloromethane and CHDV cured film, respectively. The intensity of the absorption at 443 nm, the key peak for the absorption of the blue LED light in hybrid devices (emission maxima at *ca.* 444 nm), and of the emission of compound **2.3** (excitation at 443 nm), was plotted against the concentration of the solutions. In both media the absorbance

shows a linear behaviour with increasing concentration of solution. While the emissions for low concentrations increase with the concentration, they reach a plateau at 5×10^{-5} M in dichloromethane and 1.27×10^{-3} M for the cured films, followed by an emission intensity decrease at higher concentrations. Furthermore the emission maximum stays at 585 nm for the solution, however, for the cured films it is blue shifted and changes with the concentration. For example, the emission maximum red shifts from 543 to 555 nm when the concentration of **2.3** in the cured film is increased from 3.5×10^{-4} to 1.41×10^{-3} M. The emission behaviour is in accordance with the luminous efficacies, and both the dichloromethane solutions and CHDV cured films indicate that likely an aggregation effect that quenches the emission at high concentrations is operating,[39, 140] as indicated by the formation of a plateau in the graph concentration vs max absorption.

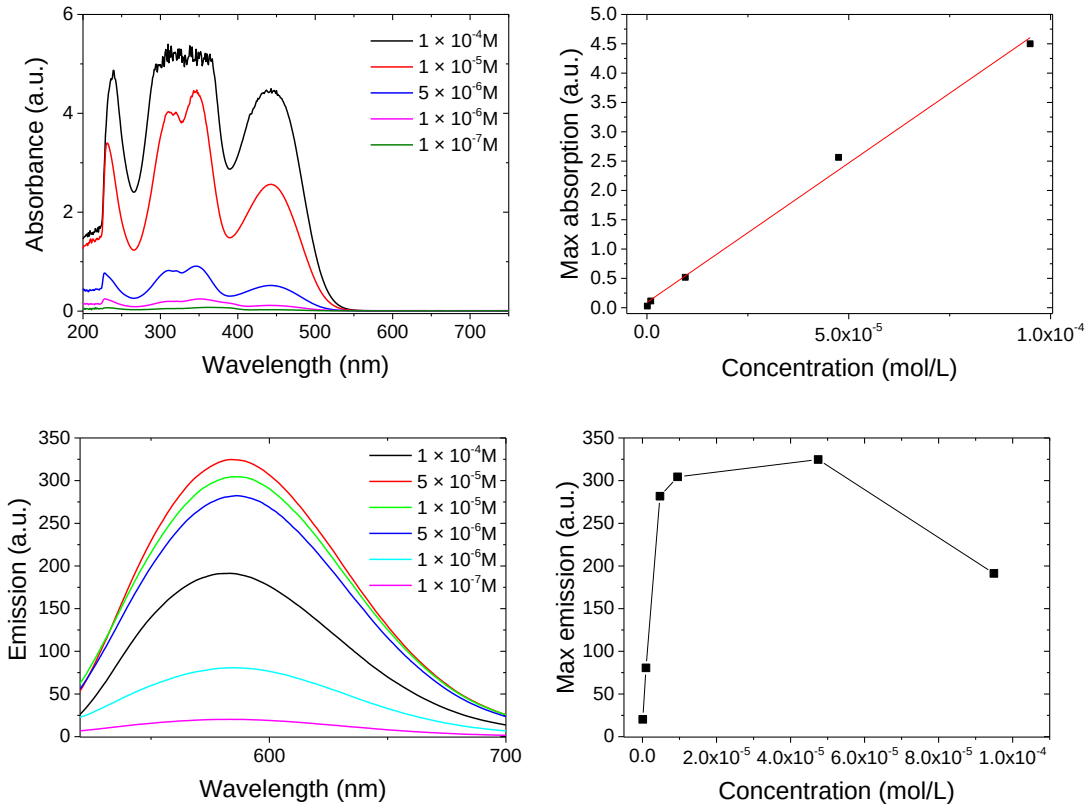

Figure 2.23 Absorbance and emission spectra, maximum absorbance (at 443 nm) and maximum emission (at 585 nm) for solutions of **2.3** in dichloromethane (1×10^{-4} to 1×10^{-7} M).

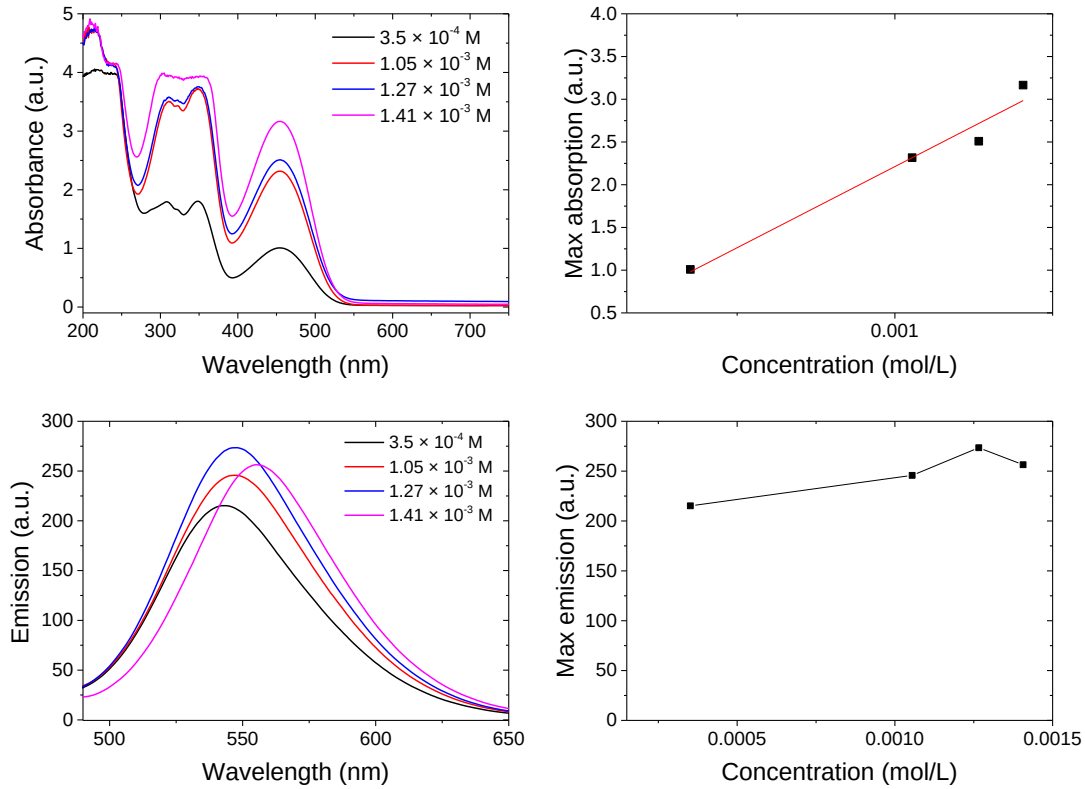

Figure 2.24 Absorbance and emission spectra, maximum absorbance (at 443 nm) and maximum emission (at 585 nm) for solutions of **2.3** in CHDV with 1% of PAG (from 3.5×10^{-4} to 1.41×10^{-3} M).

More hybrid LEDs containing the co-emitter **2.3** were investigated. In particular solutions with concentrations from 1.3 to 1.9% (w/v) were prepared (Table 2.7).

Table 2.7 Characteristics of the second batch of hybrid devices. **2.2.A-2.2.D** were fabricated with the solutions promptly after the preparation and **2.3.A-2.3.D** one day after the preparation.

Device	Blue LED	Compound	Concentration (w/v %)	Correlated colour temperature (K)	CIE 1931 Coordinates	
					x	y
K	B43	**2.3**	1.3	22000	0.19	0.08
L	B59	**2.3**	1.5	3772	0.41	0.45
M	B46	**2.3**	1.8	3286	0.46	0.51
N	B75	**2.3**	1.9	3239	0.47	0.52
O	B33	**2.3**	1.3	22000	0.20	0.10
P	B31	**2.3**	1.5	22000	0.26	0.20
Q	B57	**2.3**	1.7	6565	0.32	0.29
R	B35	**2.3**	1.8	3669	0.42	0.46

Using the solutions immediately after their preparation and after 24 hours, eight hybrid LEDs were fabricated and tested in two batches **K-N** (second batch) and **O-R**

(third batch), respectively. The spectra of these hybrid LEDs are presented in Figure 2.25. The luminous flux and luminous efficacy of the hybrid LEDs show a similar behaviour for the second and third batch of hybrid LEDs; they increase with concentration reaching maxima at 1.5 and 1.7% concentration of organic material, respectively. The absolute values of the luminous flux and luminous efficacy decrease when comparing those devices fabricated immediately and those fabricated after 24 hours, indicating that storing compound **2.3** in CHDV solution (with 1 % of PAG) for one day decreases its converting properties.

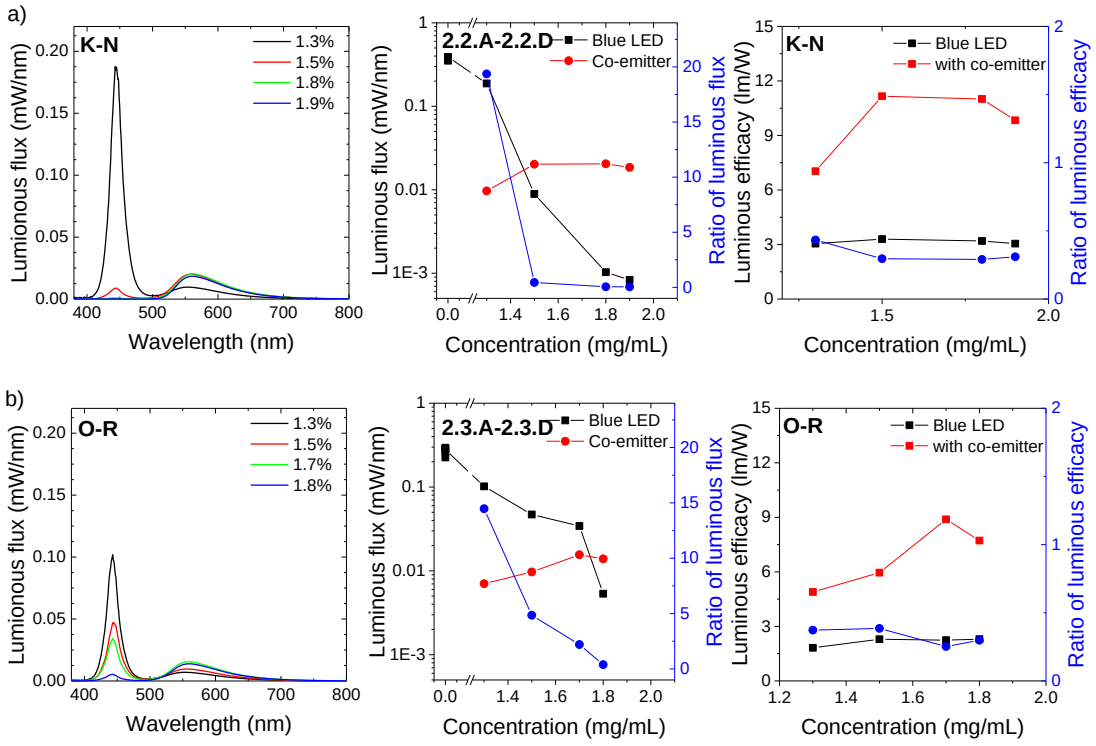

Figure 2.25 Emission spectra, luminous flux maxima and ratio of luminous flux (blue LEDs/co-emitter) and luminous efficacy maxima and ratio of luminous efficacy (blue LED/hybrid LED) at at different concentrations for the devices **K-N** (a) and **O-R** (b) driven at 25 mA.

The CIE 1931 colour coordinates of the three batches of hybrid LED fabricated with the co-emitter **2.3** are reported in Figure 2.26. Considering any associated errors, the linear fit of the three sets of coordinates has the same fitting equation (Table 2.8). This means that all of the CIE coordinates of the devices that can be fabricated with co-emitter **2.3** follow this equation but that the relative disposition of those coordinates in line with the concentration of the organic material is unpredictable. This is principally due to the challenging reproducibility of the fabrication method; the deposition method, the curing process, the morphology of the cured matrix at

different concentration, the temperature (external and generated from the blue LED) and the aging time all have an effect on the final hybrid device.

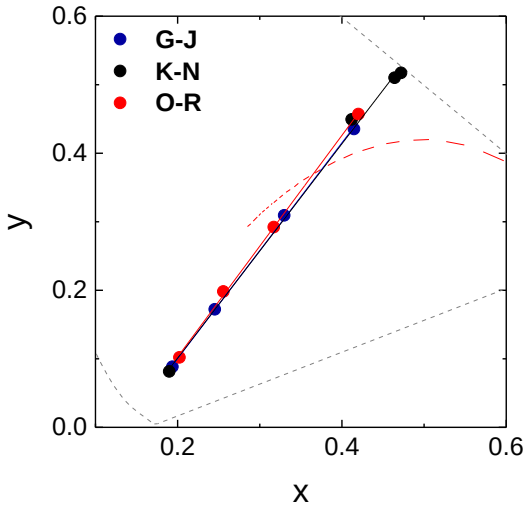

Figure 2.26 CIE 1931 coordinates and linear fitting of the **G-J** (first batch), **K-N** (second batch) and **O-R** (third batch) hybrid devices.

Table 2.8 Pearson product-moment correlation coefficient, coefficient of determination, intercept and slope with relative standard errors for the linear fittings of the CIE 1931 coordinates of the the **G-J** (first batch), **K-N** (second batch) and **O-R** (third batch) hybrid devices.

Devices	Pearson's r	Adj. R^2	Intercept	Error	Slope	Error
G-J	1.000	0.999	-0.214	0.008	1.574	0.025
K-N	0.998	0.995	-0.212	0.025	1.564	0.061
O-R	1.000	0.999	-0.221	0.010	1.617	0.031

2.3. Conclusions

Five new bBT derivatives have been synthesised and characterised. All show a characteristic large energy gap between the more energetic absorption band (430-463 nm) and the less energetic emission band (530-604 nm). For this reason they have been used as co-emitters in hybrid devices in combination with commercial inorganic blue LEDs. Compound **2.3** was revealed to be a good candidate to down-convert the blue light emitted from the commercial blue LED into the yellow-orange part of the visible electromagnetic spectrum. The combination of the partially absorbed blue light and of the re-emitted yellow-orange light produced white light with varying colour correlated temperatures and CIE coordinates in relation to the concentration of the deposited organic material. The concentration of the organic material and its effect on the emitted light was inconsistent. This is likely a result of

the high number of variables that are challenging to control in this prototype version of the hybrid devices. These variables include the deposition method, the curing process and the morphology of the film of the organic material.
Part of this chapter has been included in a peer reviewed paper.[141]

2.4. Future work

The results obtained with compound **2.3** are good, although it is discouraging that non-reproducibility of the colour is characteristic of the devices obtained. For this reason, future work should be initially directed to the development and testing of different deposition methods that provide reproducible results. Stability tests of the organic materials used should be performed in the matrix media. The adoption of different deposition techniques can be explored (*e.g.* spin coating) and the measurement of the principal characteristics of the obtained films (*e.g.* thickness, presence of defects, mechanical properties such as stress and strain) can be performed in order to obtain and select films with ideal and consistent proprieties.
The development and improvement on the fabrication method of the devices should be then associated with a perfection of the organic materials. Higher quantum yields and luminous efficacy are necessary in order to enhance the properties of the devices. The easiest approach involve the use of different electron donating arms, in particular the study of the properties of series of different materials that differ only for a segment of the molecule can reveal the fundamental key answers for the direction to follow in the development of new down converting organic material using the bBT core. Methods to improve the performance of these classes (kinds) of materials can involve the use of different organic units or the combination of those in different orders (*e.g.* carbazoles, substituted cyclic triamines). A few examples of new down converting materials are shown in Figure 2.27.

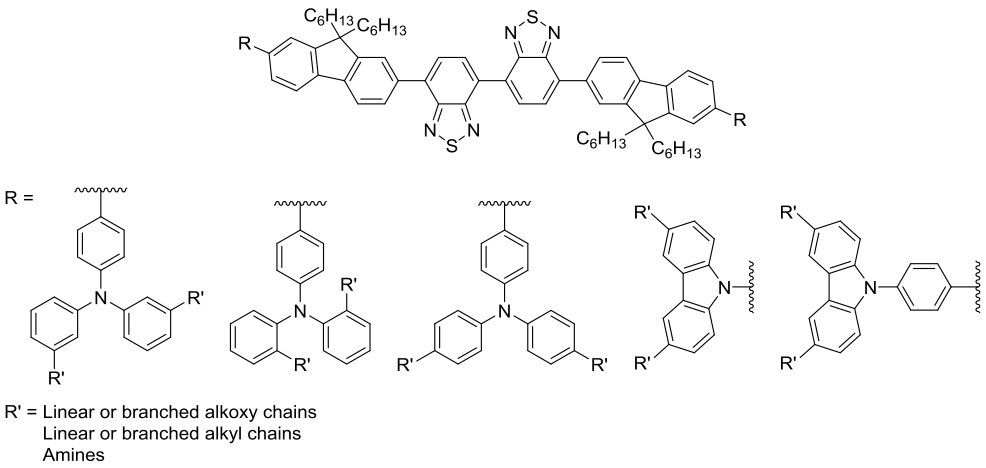

Figure 2.27 New proposed down converting materials.

Furthermore the technique of inclusion of the organic down converting material can be translated from commercial successful devices. In particular, commercial strategies include the fabrication of hybrid devices where the organic down converting material is included in a packaging shell moulded in the shape of conventional incandescence bulbs, or cured to the shape of a hemisphere on top of the blue LED chip. A method that includes the inclusion of multiple blue LEDs disposed in order to form 360 degree coverage, with the organic material cured around the chips forming a uniform sphere could be interesting (Figure 2.28).

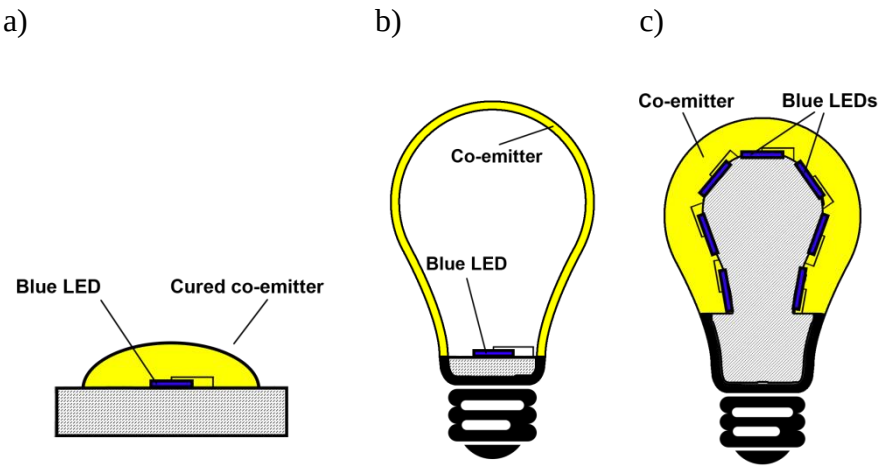

Figure 2.28 Commercial (a, b) and proposed (c) techniques of inclusion of the organic down converting material in hybrid white LEDs.

Chapter 3. Small donor-acceptor esters for lighting applications

3.1. Introduction

With the aim of obtaining new emissive small molecules for lighting applications, the design and characterisation of new benzothiadiazole (BT) donor-acceptor (D-A) derivatives incorporating ester functionalities will be discussed in this chapter. BT is well known to be an electron poor unit and an excellent and flexible building block for D-A molecules.[93, 142, 143] Herein it has been used as the electron acceptor and it has been linked to five different electron donor moieties: thiophene, dithiophene, EDOT, anisole and thiazole. The donor capacity of these molecules was slightly modified through addition of terminal ester functionality in order to equilibrate the aromatic and quinoidal character of the molecules.[7]

The molecules discussed have been involved in the fabrication of single emissive layer white OLED devices. The emission of white light from a single emissive layer can be achieved using different approaches, as widely discussed in the first chapter. One of these, recently a very hot topic in the field of organic electronic devices, is the creation of homo or hetero molecular emissive excited states.[80, 81, 144]

3.1.1. Bimolecular excited states

There are different kinds of excited states classified according to their molecular nature. They can be molecular excited states (localised excitons), or bimolecular (BM) excited species: excimers, electromers, exciplexes and electroplexes. The molecular excited states are Frenkel excitons, also called locally excited excimers, while the BM ones are usually Wannier-Mott or intermediate excitons also called charge-transfer excimers.[145] BM excited states are classified as electrically balanced excited states formed under energy and charge exchange between neighbouring molecules, and they can have either a singlet or a triplet character.[146]

In single component organic solids composed of chemically identical molecules which do not aggregate in the ground state, bimolecular (BM) excited states are possible due to resonance interactions of a molecular exciton with neighbouring non-excited molecules, they are called excimers. Exciplexes can be formed in a bi- or multi-component molecular solid when the formation of bimolecular excited states is facilitated by electron transfer between the donor and acceptor components.[85, 86] It is considered as an excited state complex that is formed by an electronically excited state donor molecule (or acceptor) with a complementary acceptor molecule (or donor) in its their ground state.[147]

Usually when an excimer state is formed during EL excitation, a secondary excited state called an electromer is observed. This is originated by the recombination of a pair of trapped carriers under an electronic interaction and its emission is red shifted in respect to the fluorescence. In the same manner, a second excited state called an electroplex is associated with the exciplex emission obtained with EL excitation. This excited state is usually described as the excited state formed by the combination of a donor molecule-located hole and an acceptor molecule-located electron in a donor–acceptor molecular system.[46, 145]

3.1.2. Excited species in OLED

The fabrication of an OLED device includes the stacking, by successive deposition, of different compounds in layers that can interact at the interfaces between each other. In this situation the formation of bimolecular excited states by electron transfer from different molecules is highly facilitated. The excited states can be generated electrically in an OLED device (EL) by recombination of electrons and holes. Different excited states can exist simultaneously, providing characteristic emission profiles. In 2000 Giro *et al.* demonstrated the emission obtained from single layer (SL) and double layer (DL) OLEDs based on N,N′-diphenyl-N,N′-bis(methylphenyl)-1,1′-biphenyl-4,4′-diamine (TPD) and 2-(4-biphenyl)-5-(4-tert-butylphenyl)1,3,4-oxadiazole (PBD) molecules incorporated in a bisphenol-A–polycarbonate (PC) matrix was a combination of different excited states formed in the devices.[70] They were able to deconvolute the emission spectra obtained from the two devices (a, SL: ITO/(40%TPD:40%PBD:20%PC)(60 nm)/Ca and b, DL: ITO/(75%TPD:25%PC)(60 nm)/PBD (60 nm)/Ca) and to define the excited states involved in the emission. The excited states were ascribed to be an excimer and electroplexes (1, 3 and 4) from TPD, and an exciplex (2) between TPD and PBD (Figure 3.1).

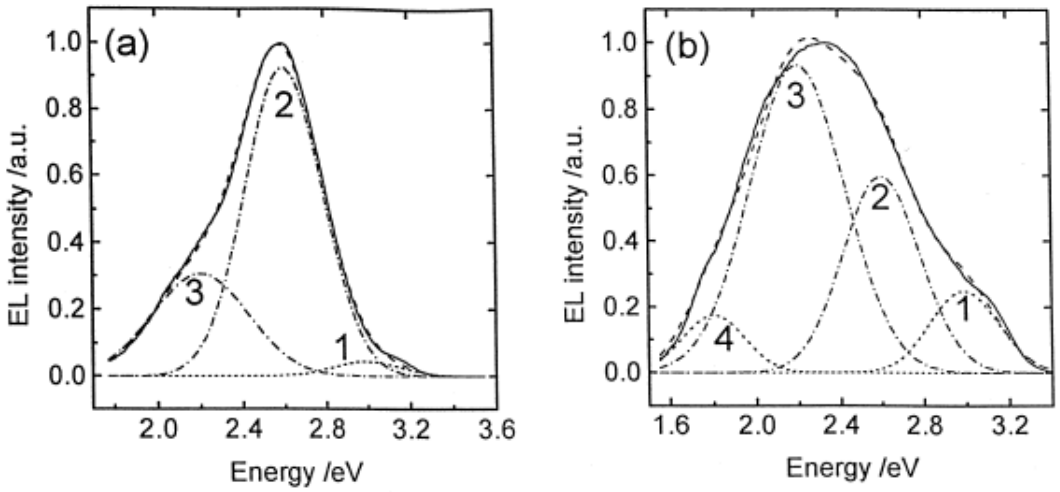

Figure 3.1 Normalized EL spectra and their Gaussian profile analysis for the SL LED device at 18 V (a), and the DL LED device at 20 V (b) Solid line: experimental results (a, b), dashed line: three Gaussian band fit (a) and four Gaussian fit (b). Note differences between contributions of the bands ascribed to TPD excited excimer (1), exciplexes (2) and electroplexes (3, 4). As related by the area under the fitted gaussian profiles they are distributed as follows: 1:2:3 = 8%:75%:17% for the SL device (a), and 1:2:3:4 = 18%:35%:44%:3% for the DL device (b).[70]

Kalinowski *et al.* in 2007 demonstrated that it is possible to obtain white light, with CRI close to unity, by combining excimer and exciplex emissions in a device based on the donor-acceptor bimolecular system co-evaporated under vacuum in a molecular proportion of 1:1. The electron acceptor was platinum [methyl-3,5-di-(2-pyridyl) benzoate] chloride (PtL_2Cl), and the electron donor was 4,4′,4″-tris(N-(3-methylphenyl)-N-phenylamino)triphenylamine (m-MTDATA).[41] The excimer emission is provided from a dimeric PtL_2Cl complex and the exciplex from a PtL_2Cl:m-MTDATA complex.

Following these principles, in this chapter the fabrication of four different OLED devices used to achieve white light based on a single emitting layer will be discussed.

3.2. Results and discussion

3.2.1. Synthesis of the new emissive materials

Five different 4,7-disubstituted BT small donor-acceptor esters (**3.1**–**3.5**) (Figure 3.2) were synthesised using different approaches. These approaches differed through either the coupling of the preformed aromatic ester substituent directly onto the BT moiety (**3.2**–**3.4**) or in the direct esterification of the 4,7-disubstituted BT molecules (**3.1** and **3.5**).

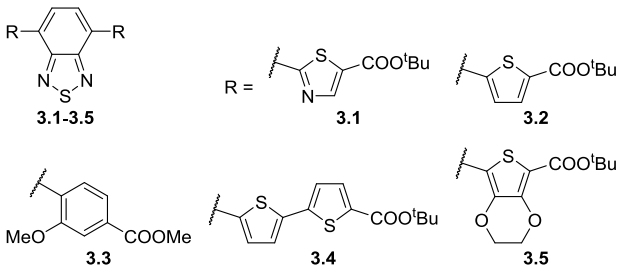

Figure 3.2 The small donor-acceptor esters synthesised.

The synthesis of two preformed aromatic ester substituents, the *t*-butyl 5-bromothiophene-2-carboxylate (**3.7**) and methyl 4-iodo-3-methoxybenzoate arms (**3.11**), is shown in Scheme 3.1 and Scheme 3.2, respectively.

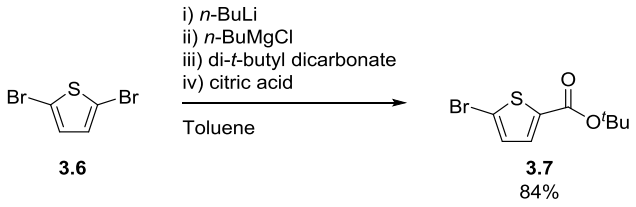

Scheme 3.1 Synthesis of *t*-butyl 5-bromothiophene-2-carboxylate.

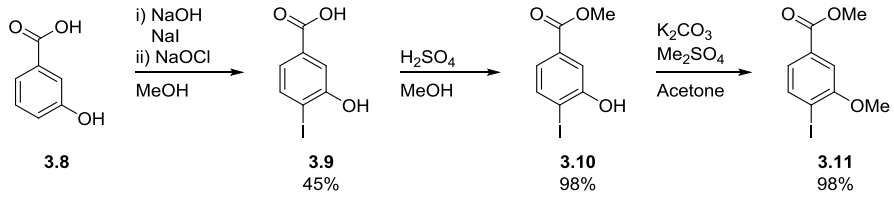

Scheme 3.2 Synthesis of the methyl 4-iodo-3-methoxybenzoate.

Compound **3.7** was synthesised in good yield (84%) starting from 2,5-dibromothiophene with a method recently developed by Balsells *et al.*[148] Selective metal–halogen exchange with lithium tri-*n*-butylmagnesium-ate complex followed by quenching with di-*t*-butyl dicarbonate furnished compound **3.7** directly. Compound **3.11** was synthesised *via* a three step procedure recently reported in

literature.[149] Iodination at the 4-position of compound **3.8**, followed by acid-catalysed esterification (Fisher-Speier) and etherification with dimethyl sulfate, provides compound **3.11** in high yield. Compounds **3.2** and **3.3** were then synthesised in good yields (77 and 58%, respectively) from commercially available compound **3.12** *via* Suzuki-Miyaura cross-coupling with **3.7** and **3.11** respectively (Scheme 3.3).

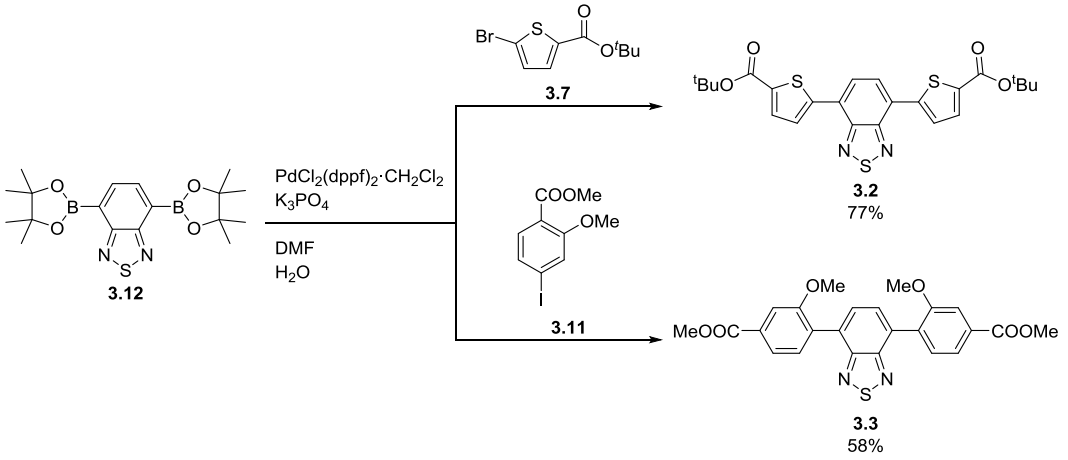

Scheme 3.3 Synthesis of compounds **3.2** and **3.3**.

A similar approach was used for compound **3.4**, which was synthesised in good yield (61%) *via* Migita-Kosugi-Stille coupling between compound **3.7** and the 4,7-bis(5-(trimethylstannyl)thiophen-2-yl)benzo[c][1,2,5]thiadiazole (**3.13**) (Scheme 3.4).

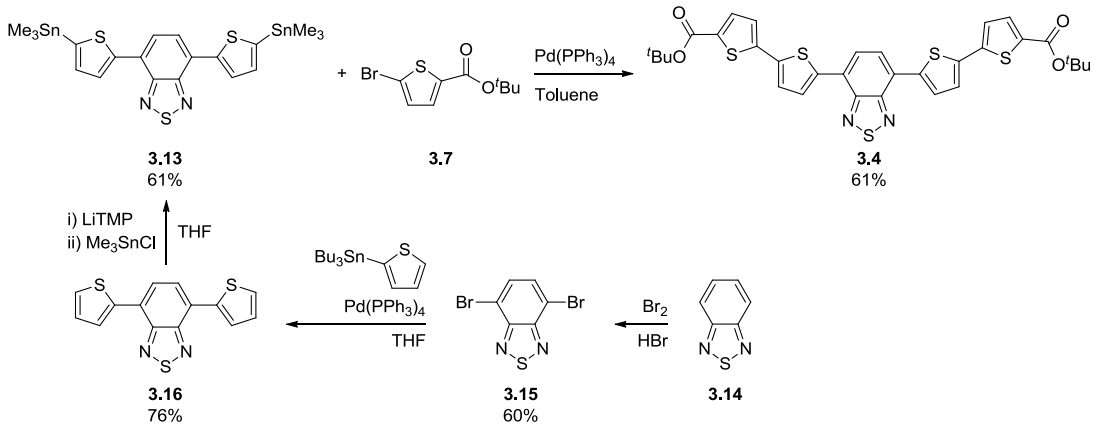

Scheme 3.4 Synthesis of compound **3.4.**

Distannylated compound **3.13** was synthesised from a literature method that starts with the 4,7-dibromination of the commercially available BT, followed by Stille coupling with commercially available 2-tributylstannylthiophene to obtain the intermediate 4,7-di(thiophen-2-yl)benzo[c][1,2,5]thiadiazole (**3.16**). This was then

stannylated at the α-position of the thiophene by direct lithiation followed by quenching with trymethyltin chloride producing **3.13** in good yield (61%).

Compounds **3.1** and **3.5** were synthesised by direct esterification of the corresponding 4,7-disubstituted benzo[c][1,2,5]thiadiazole starting from thiazole (**3.17**) and 3,4-ethylenedioxythiophene (**3.18**). Each was stannylated at the α-position by direct lithiation followed by quenching with tributyltin chloride or trymethyltin chloride to obtain 2-(tributylstannyl)thiazole (**3.19**) and (2,3-dihydrothieno[3,4-b][1,4]dioxin-5-yl)trimethylstannane (**3.20**), respectively.

Compounds **3.19** and **3.20** were used to synthesise 4,7-di(thiazol-2-yl)benzo[c][1,2,5]thiadiazole (**3.21**) and 4,7-bis(2,3-dihydrothieno[3,4-b][1,4]dioxin-5-yl)benzo[c][1,2,5]thiadiazole (**3.22**) respectively *via* Migita-Kosugi-Stille coupling with **3.15**. Compounds **3.1** and **3.5** were then obtained in low yields (4 and 17% respectively) by direct esterification of **3.21** and **3.22**. The reaction consists of a direct *α*-lithiation with in *situ* synthesised lithium 2,2,6,6-tetramethylpiperidide (LiTMP) followed by trapping with di-*t*-butyl dicarbonate (Scheme 3.5).

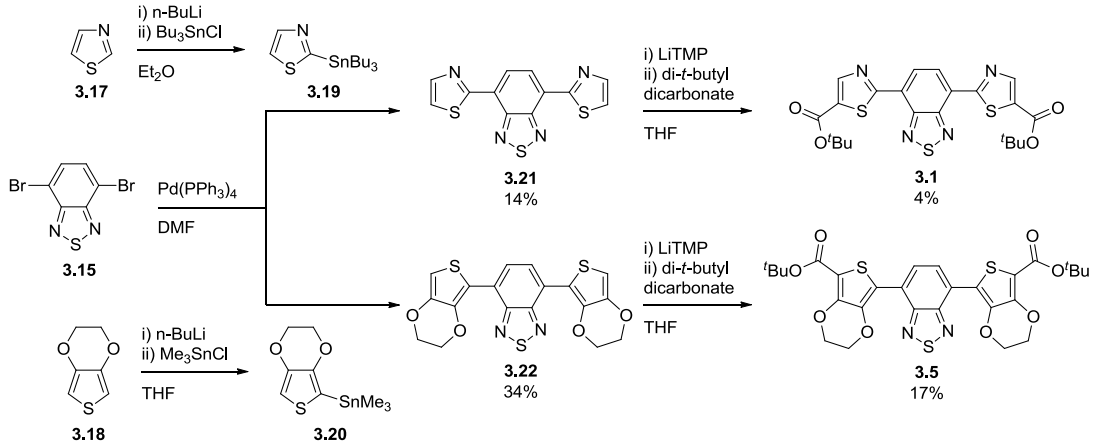

Scheme 3.5 Synthesis of **3.1** and **3.5**.

3.2.2. Characterisation of the new emissive materials

Absorption and emission spectra of the compounds **3.1**-**3.5** were recorded in dichloromethane (10^{-5} M and 1×10^{-6} M for the absorption and emission, respectively) and are reported in Figure 3.3.

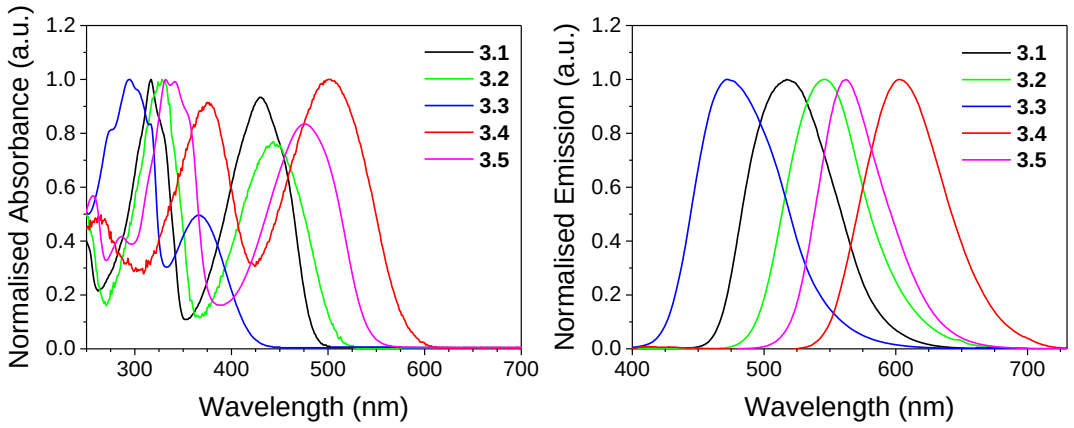

Figure 3.3 Normalised absorbance and emission spectra of **3.1 – 3.5** in solution (1×10^{-5} and 1×10^{-6} M in dichloromethane respectively).

PLQYs were recorded for compounds **3.2-3.5** at 300K using the appropriate longest λ_{max} of absorption as the excitation wavelength. Values were obtained for dilute dichloromethane solutions (10^{-6} M) and for encapsulated powders (pressed against two glass substrates). The values are similar for compounds **3.2**, **3.3** and **3.5** with the PLQY ranging from 45 to 50% in solution and from 2 to 7% in the solid state. Compound **3.4** has much smaller values in both solution and solid state, which is likely due to the longer conjugation backbone and the presence of heavy atoms enhancing quenching mechanisms. Radiationless deactivation is more efficient for the rotation or vibration of side groups containing heavy atoms, in particular when the conjugation length is increased. Furthermore, the fact that the molecular units are not linked through rigid bonds and the rotation between them is free enhances the quenching due to intra and inter molecular interactions.[150-152]

The optical HOMO-LUMO gaps were obtained from the longest wavelength absorption edge of the UV-Vis absorption spectra as described in Chapter 2. These results are summarised in Table 3.1.

It is possible to distinguish two main absorption bands for each compound. The typical absorption band of the BT unit (*ca*. 300 nm)[95, 100, 153, 154] is either blue or red shifted along the ester series from a minimum of 295 to a maximum of 376 nm. This depends on the electron-withdrawing and electron-attractive character of the aromatic substituents. In a similar fashion, the less energetic band, attributable to the interaction between the peripheral aromatic rings and the core (HOMO-LUMO transition, see Section 3.2.3) is shifted depending on the degree of conjugation in each compound. These aspects will be considered in detail in Section 3.2.3 with the support of DFT calculations.

Table 3.1 UV-Vis absorption maxima, emission maxima, photoluminescence quantum yields and optical HOMO-LUMO gaps for **3.1** – **3.5**.

Compound	λ_{max} (nm) Absorption[a]	λ_{max} (nm) Emission[b]	PLQY (solution)[h]	PLQY (solid state)[i]	HOMO-LUMO gap[j]
3.1	430 (14900), 317 (16000)	517[c]	n/a	n/a	2.6
3.2	444 (23600), 328 (30900)	546[d]	49.8 %	6.9 %	2.5
3.3	366 (9500), 295 (19300)	473[e]	49.9 %	5.6 %	3.0
3.4	502 (47500), 376 (42800)	602[f]	5.8 %	0.2 %	2.1
3.5	476 (20900), 332 (25000)	562[g]	45.4 %	2.2 %	2.3

[a] measured in 1×10^{-5} M solution (dichloromethane); [b] measured in 1×10^{-6} M solution (dichloromethane); [c] *via* excitation at 430 nm; [d] *via* excitation at 444 nm; [e] *via* excitation at 366 nm;[f] *via* excitation at 502 nm; [g] *via* excitation at 476 nm; [h] measured in 10^{-6}M solution (dichloromethane); [i] measured in the powder pressed against two glass substrates; [j] calculated from the longest wavelength absorption edge.

Cyclic voltammograms were recorded in dichloromethane and exhibit a common semi reversible redox pair in the cathodic range, $E_{1/2} = -1.40$ to -1.93 V (Figure 3.4-Figure 3.8). This is attributable to the semi-reversible reduction of the BT unit, known as a strong electron acceptor.[94] Additionally, the cathodic waves of compound **3.1** and **3.5** indicate a second semi-reversible reduction, $E_{1/2} = -1.74$ and -2.04 V respectively. This can be attributable to the thiazole and the EDOT moieties that play an important role delocalising the additional charge.[94, 155]

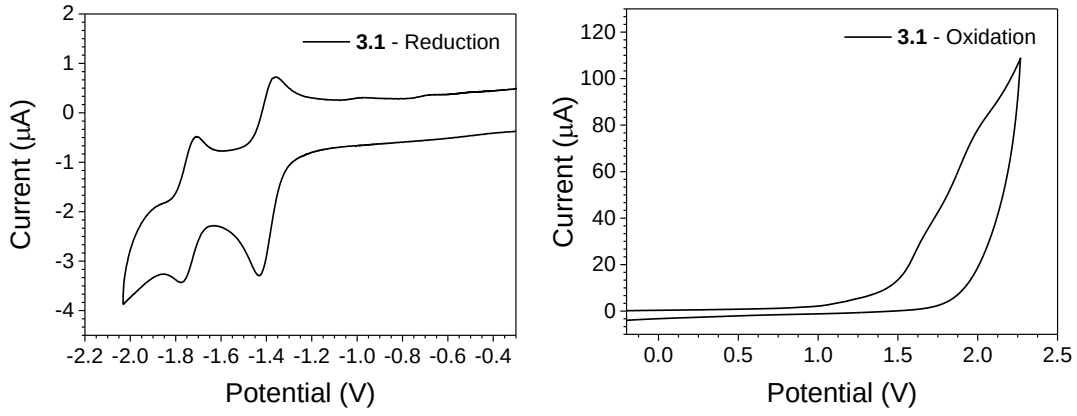

Figure 3.4 Cathodic (left) and anodic (right) waves from cyclic voltammetry of **3.1** referenced against the $E_{1/2}$ of the F_c/F_c^+ redox couple; 1×10^{-4} M solution in 0.1 M *n*-Bu_4NPF_6 (dichloromethane); scan rate 0.1 V s^{-1}.

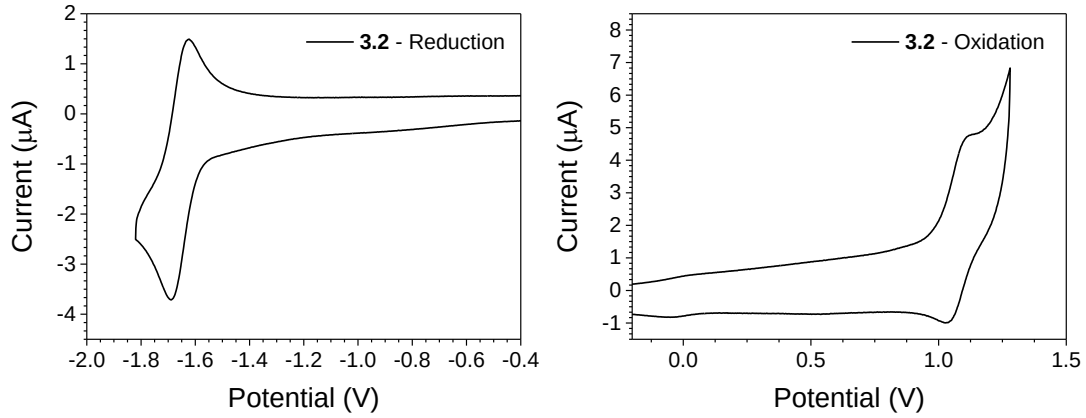

Figure 3.5 Cathodic (left) and anodic (right) waves from cyclic voltammetry of **3.2** referenced against the $E_{1/2}$ of the F_c/F_c^+ redox couple; 1×10^{-4} M solution in 0.1 M *n*-Bu_4NPF_6 (dichloromethane); scan rate 0.1 V s^{-1}.

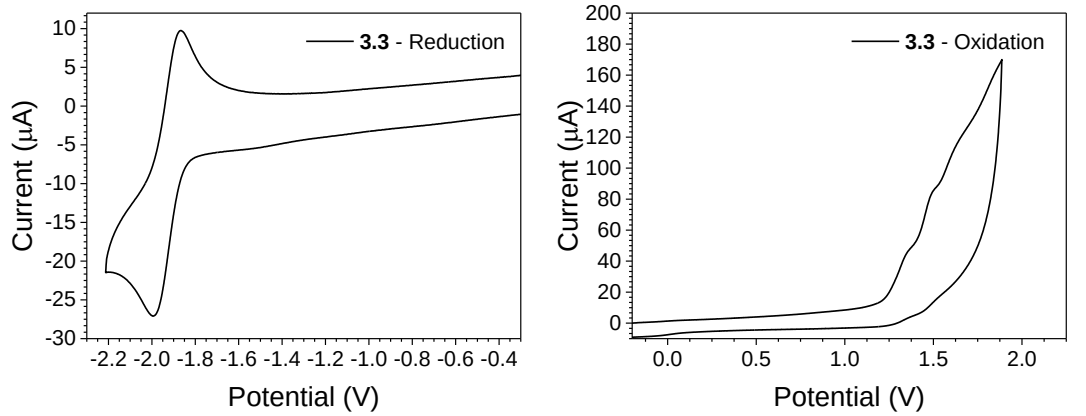

Figure 3.6 Cathodic (left) and anodic (right) waves from cyclic voltammetry of **3.3** referenced against the $E_{1/2}$ of the F_c/F_c^+ redox couple; 1×10^{-4} M solution in 0.1 M *n*-Bu_4NPF_6 (dichloromethane); scan rate 0.1 V s^{-1}.

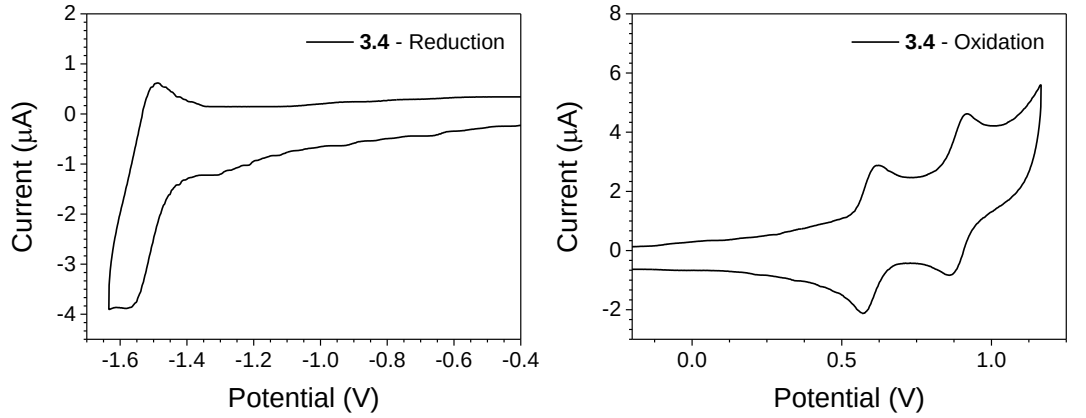

Figure 3.7 Cathodic (left) and anodic (right) waves from cyclic voltammetry of **3.4** referenced against the $E_{1/2}$ of the F_c/F_c^+ redox couple; 1×10^{-4} M solution in 0.1 M *n*-Bu_4NPF_6 (dichloromethane); scan rate 0.1 V s^{-1}.

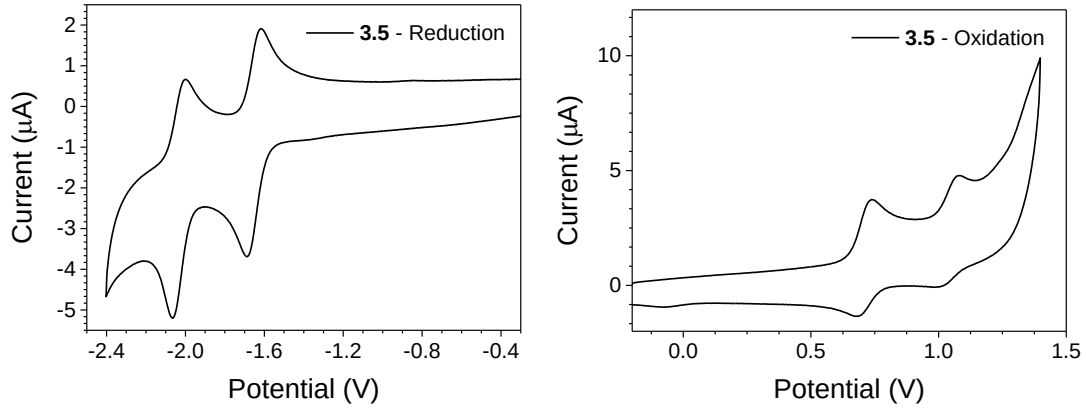

Figure 3.8 Cathodic (left) and anodic (right) waves from cyclic voltammetry of **3.5** referenced against the $E_{1/2}$ of the F_c/F_c^+ redox couple; 1×10^{-4} M solution in 0.1 M *n*-Bu_4NPF_6 (dichloromethane); scan rate 0.1 V s^{-1}.

Compound **3.2** shows a quasi-reversible redox pair in the anodic range, $E_{1/2}$ = 1.08 V attributable to the presence of a single electron donating thiophene moiety on each arm. In a similar fashion, due to the presence of two thiophene moieties in each arm, compound **3.4** shows two reversible redox pairs in the anodic range, $E_{1/2}$ = 0.60 and 0.89 V.[94] The anodic curve of compound **3.5** shows two quasi-reversible redox pairs, $E_{1/2}$ = 0.71 and 1.04 V, attributable to the 3,4-ethylenedioxythiophene moieties. Compound **3.1** and **3.3** show two and three irreversible anodic peaks, respectively (Table 3.2).

Table 3.2 Redox and electronic properties of **3.1 – 3.5**.

Compound	E (V) Reduction	E (V) Oxidation	HOMO (eV)[a]	LUMO (eV)[a]	HOMO-LUMO Gap (eV)[b]
3.1	−1.43/−1.36; −1.77/−1.71	1.61/-; 1.94/-	−6.3	−3.5	2.8
3.2	−1.69/−1.62	1.12/1.03	−5.8	−3.2	2.5
3.3	−1.99/−1.87	1.36/-; 1.50/-; 1.63/-	−6.0	−2.9	3.1
3.4	−1.58/−1.49	0.62/0.57; 0.92/0.86	−5.3	−3.4	1.9
3.5	−1.69/−1.61; −2.07/−2.00	0.74/0.67; 1.08/1.00	−5.5	−3.2	2.3

[a] calculated from the onset of the first peak of the corresponding redox wave and referenced to ferrocene which has a HOMO of -4.8 eV; [b] energy gap between HOMO and LUMO levels.

In compound **3.1** they are attributable to the oxidation process likely localised in the thiazole,[156, 157] whereas in compound **3.3** they are likely localised on the methoxy

groups as revealed in similar 4,7-bis substituted BT compounds.[158, 159] The electrochemical HOMO and LUMO values were estimated from the onset of the oxidation and reduction peaks respectively and are referenced to the ferrocene/ferrocenium redox couple, which has a known value of −4.8 eV.[131] The optical and electrochemical gaps agree qualitatively by the levels of relative disposition, but in each case the optical values are lower in agreement with Bredas.[160] These values and their disposition are dependent on the degree of conjugation of the ester and generally are dependent on the degree of planarity and rigidity of the molecule.[161] The smallest absolute value in the series is for compound **3.4**, which shows the largest electronic delocalisation of both LUMO and HOMO (see Section 3.2.3). Conversely compound **3.3**, with the smaller delocalisation due to the non-planarity of the molecule (dihedral core-arm *ca.* 40º), shows the biggest energy gap in the series.

3.2.3. Theoretical calculations

To explain the experimentally observed PL spectra and the electrochemical behaviour, quantum chemical calculations were performed for compounds **3.1-3.5** and for their ester free counterparts **3.1f**-**3.5f** (replacing the ester group with a hydrogen atom) using density functional theory (DFT) and its time dependant counterpart (TD-DFT).[132, 133] All the calculations were performed with the software package Gaussian09 (Revision A.02).[134] In order to select the best level of theory to simulate the vertical transitions associated with the absorption spectra, a benchmark was performed. Using the TD-DFT method incorporating the polarizable continuum model (PCM)[162] (dichloromethane), the vertical transitions were calculated for the well-known literature compound 4,7-dithiophenyl-benzothiadiazole (**3**),[100] using a combination of five different functionals (B3LYP[163], wB97xD,[164] CAM-B3LYP,[136] M06-2X,[165] PBE0)[166] and three different basis sets (6-31G, 6-311G(d,p), 6-311+G(2d,p), DGDZVP). Six excited states were calculated at each level of theory and each fitted with Gaussian curves (full width at half maximum (FWHM) = 0.37 eV) using the software GaussSum 3.0.[137] The two maxima obtained with this procedure were compared to the experimental maxima absorption bands of **3**. The mean signed and mean square errors (MSiE and MSqE, eV) and maximal deviations (Max-Min, eV) are reported in the appendix (Table 7.7). The PBE0/6-311G(d,p) level of theory showed the smallest mean signed and mean square errors (smallest

shift of the vertical absorptions calculated in comparison with the experimental data) and it was used for all the further calculations.

To investigate the torsional potentials between the BT core and adjacent aryl units of the series, shortened versions of compounds **3.1-3.5** (**3.1sh-3.5sh**), obtained by switching one peripheral aryl unit for a hydrogen atom and removing the ester functionality, were used. The dihedral angle between the BT core and the aromatic substituent was fixed from 0° to 180°, at 10° intervals, and geometry optimizations on all remaining degrees was performed (Figure 3.9).

The results of these calculations were straightforward for **3.1sh**, **3.2sh**, **3.4sh** and **3.5sh** showing global minima at the 180, 0, 10 and 180 dihedral angles respectively (Table 7.8). These dihedral angles were used as starting geometries for the optimisation of **3.1**, **3.2**, **3.4**, **3.5** and **3.1f**, **3.2f**, **3.4f**, **3.5f**. Compound **3.3sh** showed only a 0.04 kcal/mol difference between the energy minima for the 40 and 120 degrees geometries. For this reason, the ground state geometry and frequencies were calculated for four different hypothesised geometric isomers of **3.3** (**a-d**) produced using minimum energy combinations of the core-substituent dihedral angles (Table 3.3).

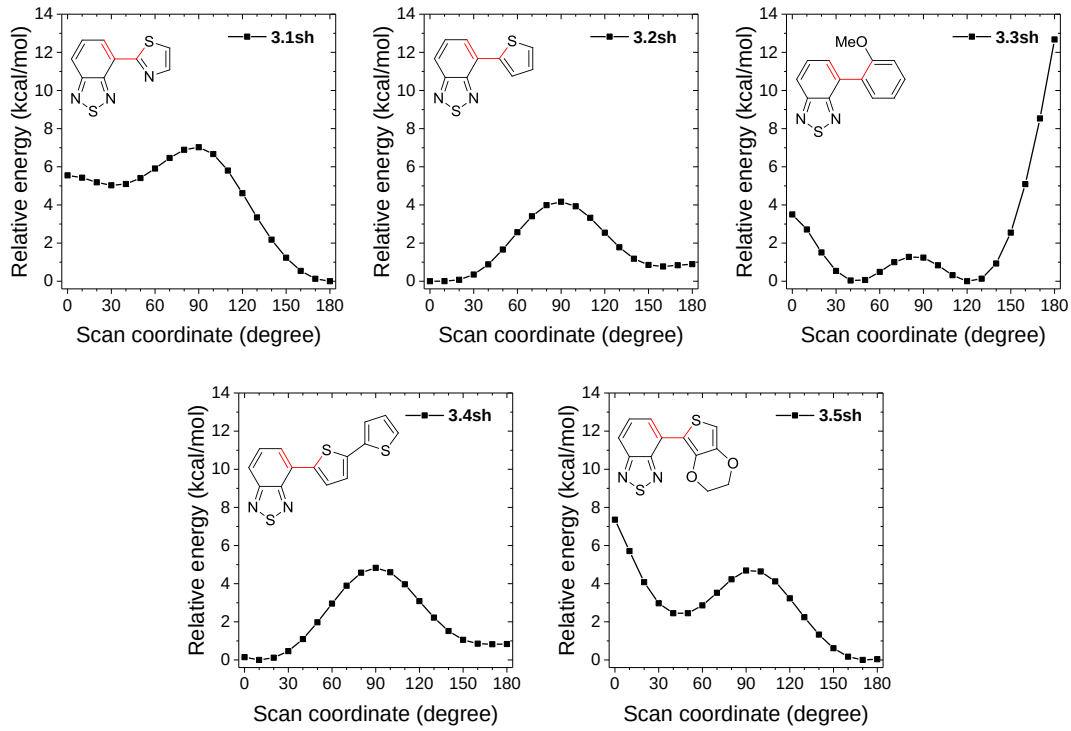

Figure 3.9 Torsional potential surface for **3.1sh-3.5sh** calculated at the PBE0/6-311G(d,p) level of theory. Rotation occurs around the inter-ring C−C bond marked in red, starting from the shown conformation (0°).

Table 3.3 Dihedral angles of the starting isomers and final dihedral angles and total energies of the optimised isomer of **3.3** (**a-d**) at the PBE0/6-311G(d,p) level of theory.

Isomer	Dihedral angles (degrees)		Relative total energy
	Starting geometry	Optimised geometry	(kcal/mol)
a	120.0 / 120.0	122.1 / 122.1	0.588
b	120.0 / −120.0	123.7 / −123.7	0.577
c	−40.0 / 40.0	−42.7 / 42.7	0.102
d	40.0 / 40.0	43.5 / 43.5	0.000

Negative frequencies were not calculated, meaning that all the isomers are settled in different potential energy minima with an absolute minimum for the isomer **d**, that was used as model for compound **3.3**. The ground state geometries for compounds **3.1-3.5** (Figure 3.10) and for **3.1f-3.5f** were optimised; the analyses of the vibrational frequencies indicated the location of the sought-for energy minimum.

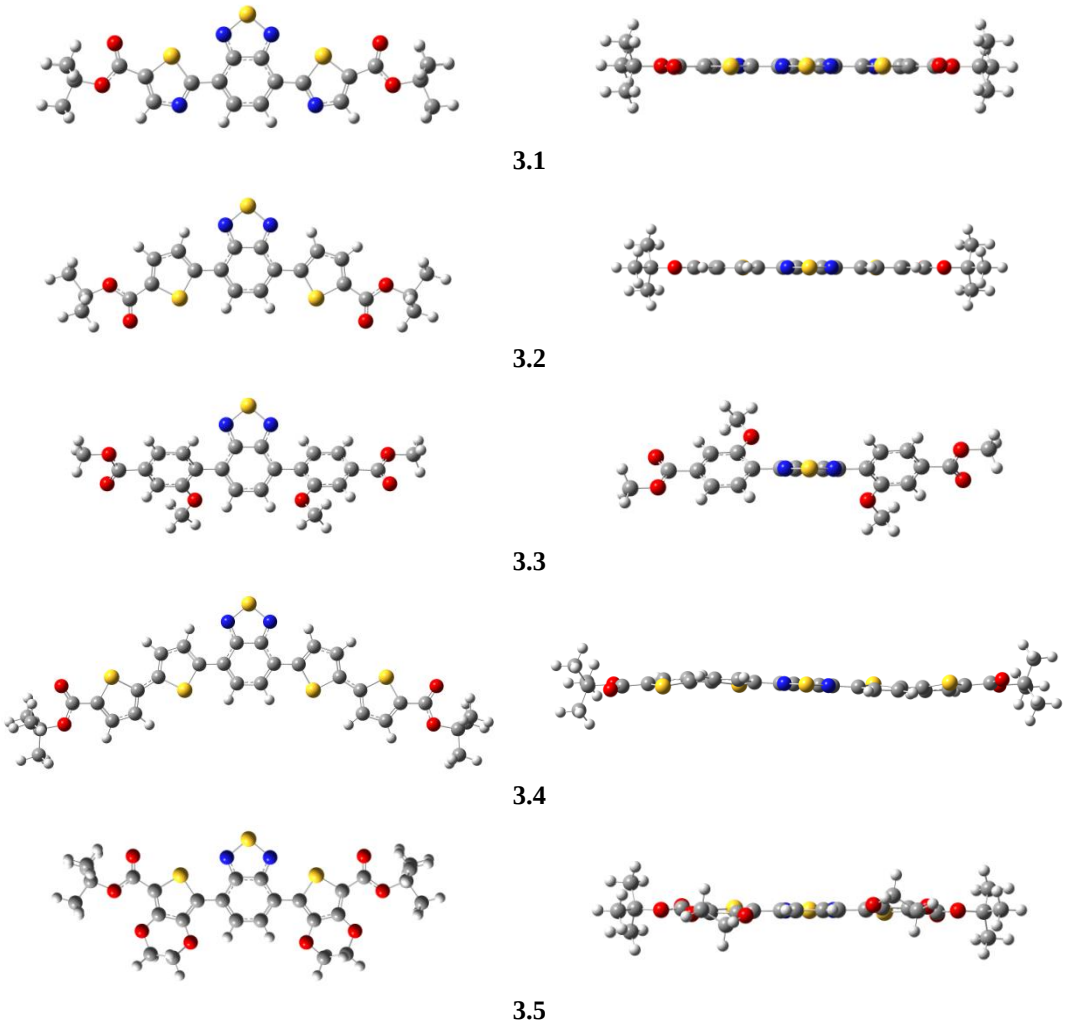

Figure 3.10 Optimised geometries for **3.1-3.5** at the x = 0º (left) and x = 90º (right) viewing orientation at the PBE0/6-311G(d,p) level of theory.

The disubstituted BT backbone is planar for compounds **3.1** and **3.2**, with slight distortion for compounds **3.4** and **3.5** (*ca.* 6-7 degrees, Table 3.4) in agreement with the torsional potential surfaces calculated for **3.1sh-3.5sh**. In contrast, the 3-methoxybenzoate substituents of **3.3** are oriented at *ca.* 43.5º in respect to the BT central core, resulting in the least conjugated molecule in the series with the larger experimental HOMO-LUMO gap.

Table 3.4 Dihedral angles of the optimised geometries of **3.1-3.5** at the PBE0/6-311G(d,p) level of theory.

Dihedral angles (degrees)				
3.1	**3.2**	**3.3**	**3.4**	**3.5**
179.37	0.01	-43.52	6.62	174.48
179.39	-0.03	-43.54	6.62	174.48

The calculated orbital wave functions and the Kohn-Sham molecular orbital diagram for **3.1-3.5** are reported in Figure 3.11 (extended versions are reported in Figure 7.6 and Figure 7.5).

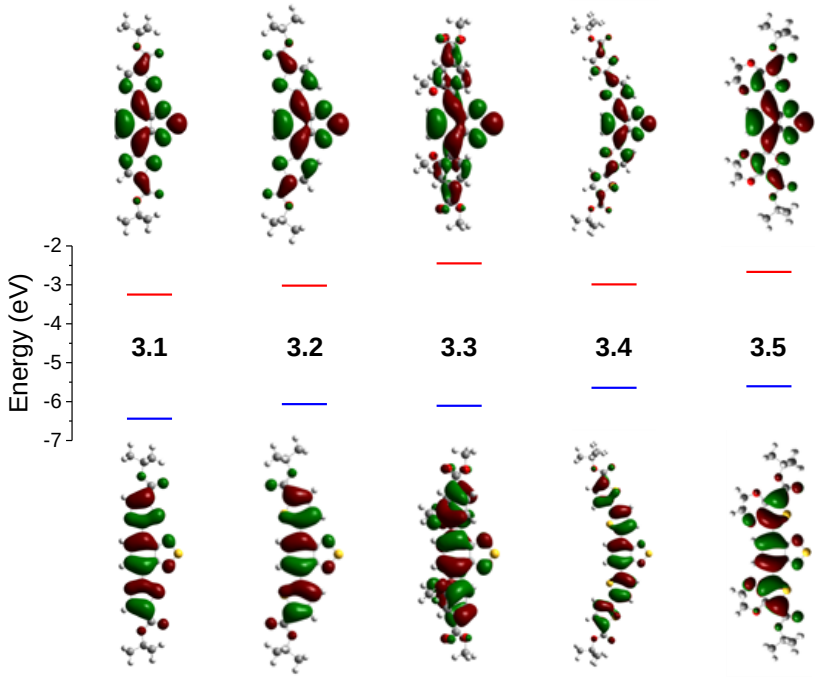

Figure 3.11 Kohn-Sham molecular orbital diagram and graphical representation (isosurface 0.02) of the HOMO and LUMO for **3.1-3.5** calculated at the PBE0/6-311G(d,p) level of theory.

Both the HOMO and LUMO are delocalised across the aromatic portion of the molecules. The calculated HOMO and LUMO energies agree qualitatively (by the

levels of relative disposition) and even quantitatively with the ones obtained through the electrochemical experiments (Figure 3.12 and Table 3.5).

Table 3.5 Electrochemical and calculated (at the PBE0/6-311G(d,p) level of theory) HOMO and LUMO energies; electrochemical, optical and calculated (at the PBE0/6-311G(d,p) level of theory) HOMO-LUMO gap energies for **3.1-3.5**.

	Compound	3.1	3.2	3.3	3.4	3.5
Energy (eV)	**LUMO (PBE0/6-311G(d,p))**	-3.25	-3.02	-2.45	-2.99	-2.67
	HOMO (PBE0/6-311G(d,p))	-6.44	-6.07	-6.11	-5.64	-5.61
	LUMO (Electrochemical)	-3.5	-3.2	-2.9	-3.4	-3.2
	HOMO (Electrochemical)	-6.3	-5.8	-6	-5.3	-5.5
	HOMO-LUMO gap (PBE0/6-311G(d,p))	3.19	3.05	3.66	2.66	2.94
	HOMO-LUMO gap (Electrochemical)	2.8	2.5	3.1	1.9	2.3
	HOMO LUMO gap (Optical)	2.6	2.5	3	2.1	2.3

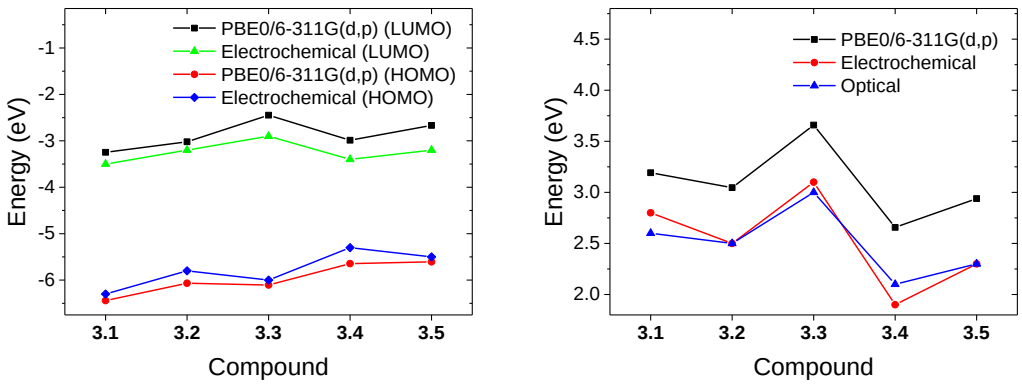

Figure 3.12 Electrochemical and calculated (at the PBE0/6-311G(d,p) level of theory) HOMO and LUMO energies for **3.1-3.5** (left). Electrochemical, optical and calculated (at the PBE0/6-311G(d,p) level of theory) HOMO-LUMO gap energies for **3.1-3.5** (right).

As a general trend, the calculated HOMO energies underestimate and the calculated LUMO energies overestimate the electrochemical values. This results in an overestimation of the calculated HOMO-LUMO gaps energies in respect to both the electrochemical and optical experimental measurements. However the general trend obtained experimentally in the series is respected qualitatively (by the levels of relative disposition). In particular due to its non-planarity, compound **3.3** has the largest gap while compound **3.4**, due to its extended delocalisation length (two thiophene units as substituents), has the smallest gap. The energy gaps instead decrease in the series **3.1** > **3.2** > **3.4**. The calculated HOMO and LUMO energies of the model compounds **3.1f-3.5f** are slightly destabilised compared to the **3.1-3.5** ones (Figure 3.13). The ester functionality stabilises the LUMOs (*ca.* 0.3 eV in average) more than the HOMOs (*ca.* 0.2 eV in average), in agreement with its electron-

withdrawing effect. This effect is more evident in compound **3.3** where a strongly electron-donating methoxy group is positioned in *meta* to the ester functionality. In this case the ester partially delocalises the excess of charge present in the benzyl ring stabilising the LUMO to a greater extent than the HOMO. This results in the largest stabilisation in the series; the HOMO-LUMO gap decreases by 0.31 eV from **3.3f** to **3.3**. The differences in the HOMO-LUMO gaps for the other compounds in the series are very small 0.01-0.05 eV (deviations included in the error).

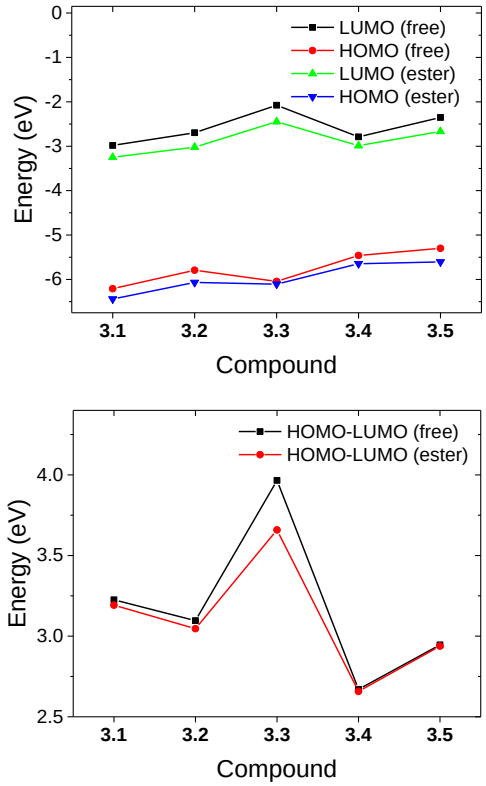

Figure 3.13 Calculated HOMO and LUMO energies for **3.1-3.5** and **3.1f-3.5f** at the PBE0/6-311G(d,p) level of theory (left). Calculated HOMO-LUMO gap energies for **3.1-3.5** and **3.1f-3.5f** at the PBE0/6-311G(d,p) level of theory (right).

The first 20 singlet excited states were calculated for compounds **3.1-3.5** in the vacuum using the TD-DFT/PBE0/6-311G(d,p) level of theory and they were fitted with Gaussian curves (full width at half maximum (FWHM) = 0.3 eV) using the software GaussSum 3.0.[137] These data are plotted against the experimental absorption spectra in Figure 3.14. The theoretical values show a good agreement with the experimental values, with an absolute deviation of 0.16-0.40 and vertical singlet excitation energies ranging from 0.2 to 0.9 eV when compared to the corresponding experimental absorption maxima and fluorescence onset values, respectively. This is in agreement with the errors expected for the level of theory

used.[167] The energetic trend in the series is respected (Figure 3.15); the first singlet state in each molecule corresponds to the HOMO to LUMO transition and the second excited state (with relevant oscillator strength) to the HOMO to LUMO+1 transition.

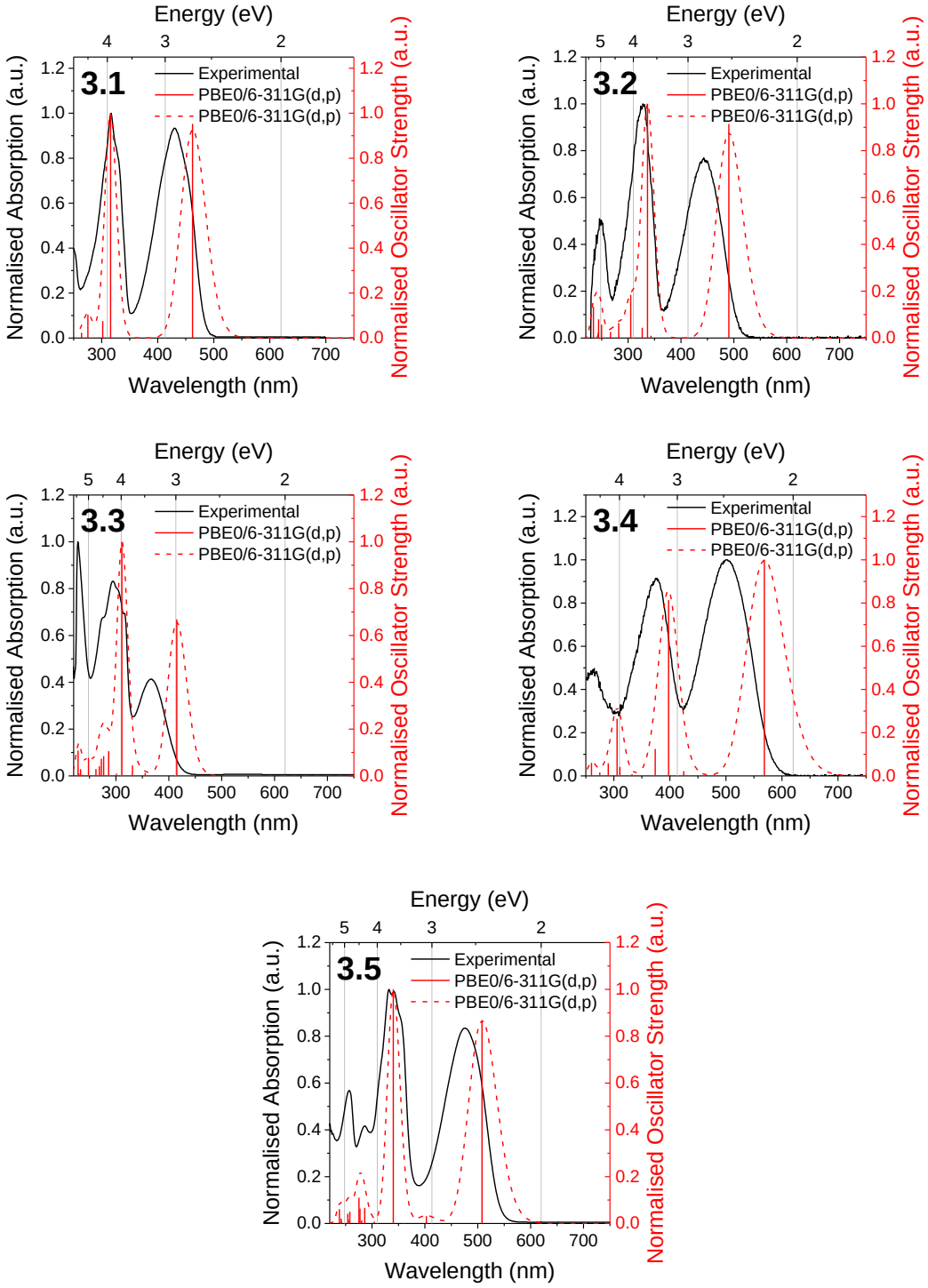

Figure 3.14 Experimental UV-Vis absorption spectra (black), calculated vertical absorptions (red) and Gaussian fitted (FWHM = 0.3 eV) absorption spectra at the TD-DFT/ PBE0/6-311G(d,p) level of theory (dashed red) on the vacuum for **3.1-3.5**.

Both the transitions are from orbitals localised mainly in the linear aromatic backbone to orbitals slightly localised in the thiadiazole portion of the BT core. This confirms what is expected for these small donor-acceptor molecules where the BT core plays an acceptor role[168] and the 4,7- substituents a donor role.

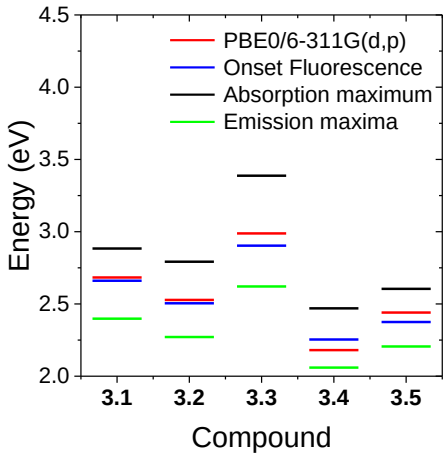

Figure 3.15 Experimental (black) and calculated at the TD-DFT/PBE0/6-311G(d,p) level of theory (red) first excited states for **3.1-3.5**.

3.2.4. Devices fabrication and characterisation

Preliminary tests were performed in the Lviv Polytechnic National University (Lviv, Ukraine) by the research group of Prof V. Cherpak and Prof P. Stakhira on compounds **3.1-3.5**. They attempted to incorporate these materials in working OLED devices, however only compound **3.3** showed promising results and for this reason was explored further.

The morphology and crystallinity of thin films of **3.3** were studied. The films were formed by vacuum depositing **3.3** at different deposition rates on glass substrates: (a) < 0.1Å s^{-1}, (b) 1.5 Å s^{-1} and (c) 10 Å s^{-1}. Three-dimensional atomic force microscopy (AFM 3D) images of the thin films were recorded (Figure 3.16). The images, which were acquired in air using contact mode, show a random distribution of the surface mounds that were orientated at different angles to each other. The mean height of the peaks (18.41 nm, 20.07 nm and 25.53 nm) and the root mean square roughness (9.38 nm, 10.62 nm and 15.99 nm) increase with the deposition rate. The surfaces are dominated by peaks with a Skewness (*RSk*) of 2.25, 1.63 and 1.29, respectively, and they have a Leptokurtic distribution of the morphological features with a Kurtosis (*RKu*) of 11.10, 7.58 and 5.20, respectively.

The X-ray diffraction patterns, which were recorded for the same samples at a grazing incidence angle of 1.50º, do not show any crystalline diffraction peaks (or long range inter-molecular order) or any significant change with the deposition rate (Figure 3.17). In fact, only two broad bands are present in the diffraction patterns (the first one from *ca.* 15 to 40 degrees and the second from *ca.* 40 to 80 degrees) confirming the amorphousness of compound **3.3** when deposited with this technique.

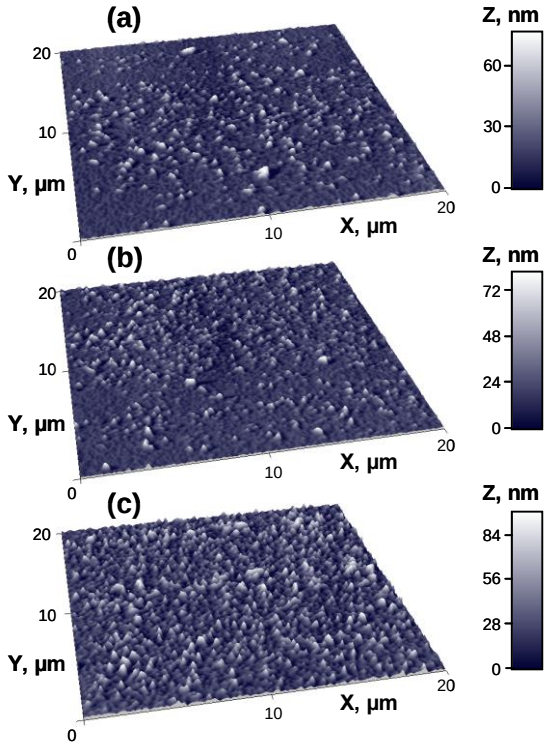

Figure 3.16 AFM 3D topographical images with normalized Z axis in nm of thin films (30 nm) of **3.3** prepared by vacuum evaporation at different deposition rates on glass substrates: (a) <0.1Å/s, (b) 1.5 Å/s and (c) 10 Å/s. The images were acquired in air using contact mode.

The space-charge-limited current (SCLC) technique was used to evaluate the charge-transporting properties of compound **3.3**, as SCLC can be used to measure the charge carrier mobility in thin films of low molar mass compounds.[169] Hole-only and electron-only devices were prepared using 4,4′,4″-tris[3-methylphenyl(phenyl)amino]triphenylamine (*m*-MTDATA) as the hole-injecting/electron-blocking layer and 1,3,5-tris(*N*-phenylbenzimidazol-2-yl)benzene (TPBi) as the electron-injecting/hole-blocking layer. The two devices were fabricated by successive deposition onto a pre-cleaned indium tin oxide (ITO) coated glass substrate under a vacuum of 10^{-6} Torr, with architectures of: ITO/m-MTDATA(20 nm)/**3.3**(60 nm)/m-MTDATA(20 nm)/Al(60 nm) (hole-only) and ITO/TPBi(20 nm)/**3.3**(60 nm)/TPBi (20 nm)/Ca(10 nm)/Al(60 nm) (electron only).

The hole mobility of **3.3** (7.6×10^{-7} cm^2 V^{-1} s^{-1} at 9.6×10^5 V cm^{-1}) has a higher value than the electron mobility (1.7×10^{-7} cm^2 V^{-1} s^{-1} at 9.6×10^5 V cm^{-1}). The fitted parameters μ_0 and γ are 2.6×10^{-8} cm^2 V^{-1} s^{-1} and 3.4×10^{-3} cm V^{-1}, and 2.8×10^{-9} cm^2 V^{-1} s^{-1} and 4.2×10^{-3} cm V^{-1} for holes and electrons, respectively (Figure 3.18). The disagreement between the experimental and fitted curves can be explained by taking into account the existence of electron and hole traps in compound **3.3** due to its morphology.

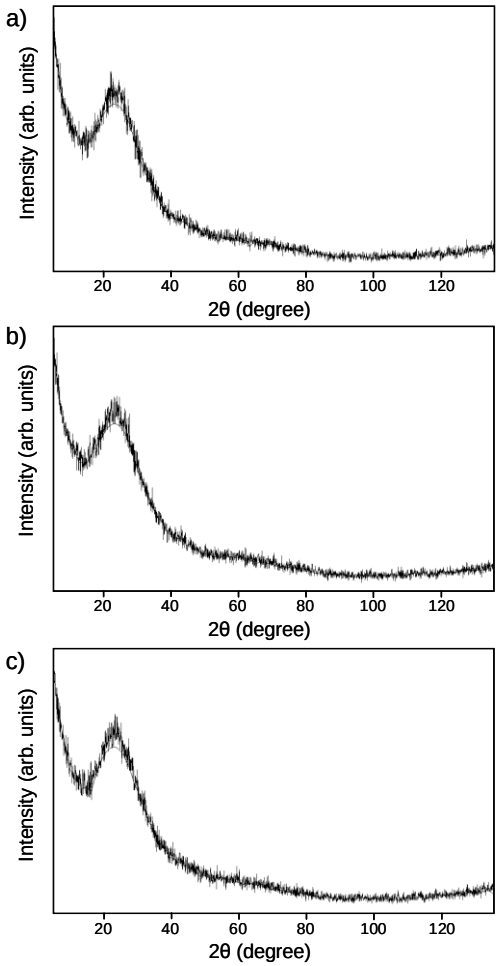

Figure 3.17 X-ray diffraction patterns a grazing incidence angle of 1.50º of thin films of **3.3** prepared by vacuum evaporation at different deposition rates on glass substrates: (a) <0.1Å/s, (b) 1.5 Å/s and (c) 10 Å/s.

Despite the low charge mobility, compound **3.3** was included successfully as a single emitting layer in the fabrication of multilayer OLEDs, due to the nano-scale thicknesses required for the fabrication of these devices.[170]

Different electroluminescent devices (OLEDs) were fabricated by successive deposition onto a pre-cleaned indium tin oxide (ITO) coated glass substrate under a vacuum of 10^{-5} Torr.

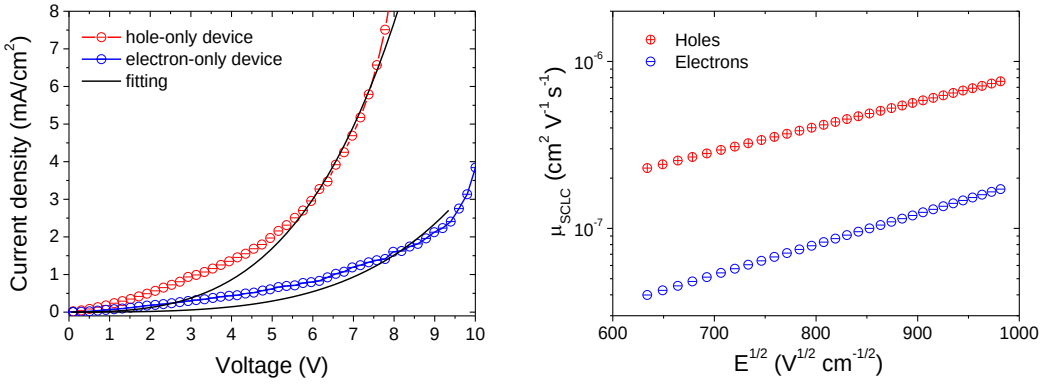

Figure 3.18 (a) Current density-voltage characteristic curves and fittings of the hole only and electron only devices with **3.3**. (b) Hole and electron mobility of **3.3** at different square root of the applied electric field.

The active area of the obtained devices was 3 × 2 mm^2 and additional passivation was not used. N,N′-Bis(3-methylphenyl)-N,N′-diphenylbenzidine (**TPD**) was used as hole-transporting material to promote a cross-interaction between the excess of electrons from the LUMO of **3.3** and the excess of holes from the HOMO of **TPD** with the aim of inducing the formation of a dimeric excited state (*e.g.* exciplex). 2-(4-Biphenylyl)-5-phenyl-1,3,4-oxadiazole (**PBD**) was used as an electron-transporting and hole-blocking material. Additionally, CuI was used as a hole-injecting material. The first two OLEDs fabricated had the structure: **ITO**/CuI (8 nm)/**TPD** (10 nm)/compound **3.3** (80 nm)/**PBD** (10 nm)/Ca (7 nm)/Al (100 nm) (OLED **A**) and **ITO**/CuI (8 nm)/**TPD** (10 nm)/compound **3.3** (30 nm)/**PBD** (10 nm)/Ca (7 nm)/Al (100 nm) (OLED **B**) (Figure 3.19).

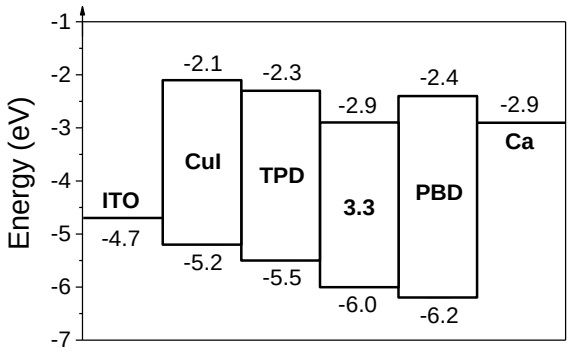

Figure 3.19 Energy-band diagram of OLEDs **A** and **B**. Aluminium was used on the cathode for the passivation of the calcium electrode, in order to investigate the properties of the OLEDs in ambient atmosphere.

The electroluminescence (EL) spectra of the two OLEDs were recorded in air at room temperature immediately after device fabrication (Figure 3.20). Additionally,

thin films of compound **3.3** and of a mixture of compound **3.3** and **TPD** were prepared by spin coating appropriate solutions of each (1:1 w/w, *ca.* 0.01 M in THF) onto clean quartz substrates. They were used to measure the photoluminescence (PL) spectra (Figure 3.20), and luminescence decay times (Figure 3.21) at 488 and 580 nm respectively for compound **3.3** and the mixture of compound **3.3/TPD**.

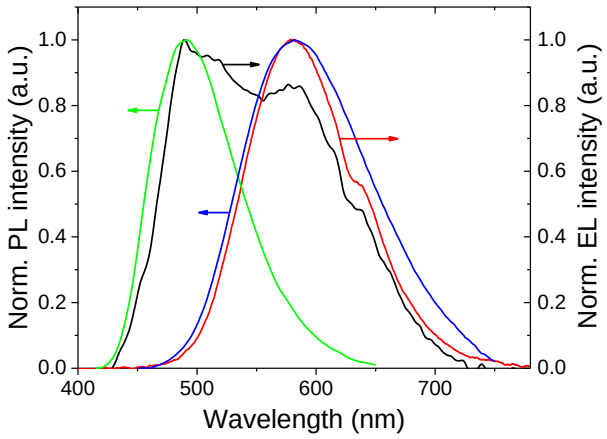

Figure 3.20 Electroluminescence spectra of the OLEDs **A** (black) and **B** (red) and photoluminescence spectra of the thin films of **3.3** (green) and of the mixture of **3.3** with **TPD** (1:1 w/w; blue).

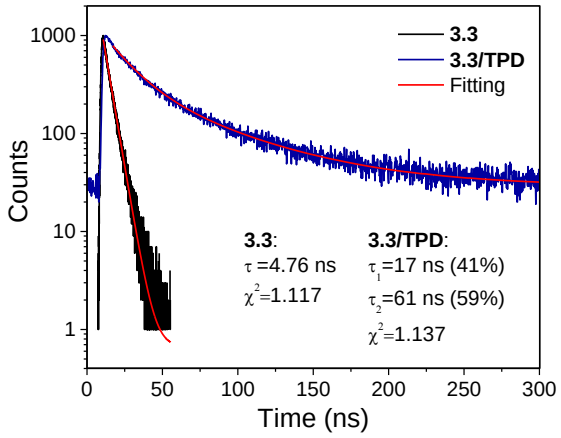

Figure 3.21 The decay fluorescence spectra of **3.3** (at 488 nm) and of the **3.3**/**TPD** (at 580 nm) films.

The EL and PL data, as well as the decay time measurements are summarised in the Table 3.6. OLED **A** shows a broad emission with two maxima at 488 and 577 nm and a shoulder at 634 nm, while OLED **B** instead shows only an emission centred at 579 nm with a shoulder at 634 nm. The emission band at 488 nm for OLED **A** is characteristic of the pure fluorescence emission of compound **3.3** in the solid state, as demonstrated with the PL maxima of 490 nm and the PL decay time of 4.8 ns measured for the thin film of compound **3.3**.[41]

Table 3.6 Emission maxima for the electroluminescence of OLEDs **A** and **B**. Emission maxima and luminescence decay times for the photoluminescence of the spin coated films of compound **3.3** and of the mixture **3.3**/**TPD** (1/1 w/w).

Electroluminescence (nm)		**Photoluminescence (nm)**	
OLED A	**OLED B**	**3.3**	**3.3/TPD**
488, 577, 634 (sh)	579, 634 (sh)	490	582
		4.8 ns	17 ns (41%), 61 ns (59%)

The second band, present in the spectra of both OLEDs **A** and **B**, is difficult to interpretate. It is not characteristic of the pure exciton emission from any material present in the OLED. For this reason the PL spectra and decay times for the thin film of the **3.3**/**TPD** mixture were recorded. The measured PL maximum of 582 nm is in agreement with the EL band present in both OLEDs **A** and **B**. Furthermore the PL decay times of 17 ns (41%) and 61 ns (59%) are typically associated with the emission from a dimeric excited state commonly known as an exciplex.[41, 81, 145, 171] In the OLEDs **A** and **B** the exciplex is then generated at the heterojunction between compound **3.3** and **TPD** and it is characterised by the low energy of both **3.3** and **TPD** excited exciton states. The exciplex state is usually generated from a combination of factors that coexist at the same time. In this case, when a direct bias is applied, likely due to the high energy barriers between **TPD** and **3.3** ($HOMO_{TPD}$ − $HOMO_{3.3}$ = 0.5 eV; $LUMO_{TPD}$ – $LUMO_{3.3}$ = 0.6 eV), electrons and holes accumulate at the interface between the two layers and, due to non-planar conformations, the electronic overlap of the donor (**TPD**) and acceptor (**3.3**) molecules is efficient for exciplex formation at the interface. The twisted nature of compound **3.3** makes self-stacking less likely, increasing the probability of a hetero-interaction with an adjoining molecule. The long-wavelength shoulder at 634 nm in the EL spectra of both OLEDs is attributable to a typical electroplex interaction that is associated with the exciplex emission.[41, 145]

From the combination of the different emissions (488, 577, 634(sh) nm), OLED **A** emits in the white region of the CIE 1931 colour space and for this reason was characterised further. The white emission depends on the relative thickness of the layers of compound **3.3** and **TPD** in the device architecture. In fact, by keeping constant the thickness of **TPD** (10 nm), the thickness of compound **3.3** in OLED **B**

of only 30 nm allows only exciplex/electroplex emission. Instead, by increasing the thickness of compound **3.3** to 80 nm (OLED **A**) it is possible that the combined emission from all excited states (exciton, exciplex, electroplex) is of the correct ratio to obtain a balanced white light. The current density−voltage characteristics and luminance−voltage characteristics were calculated (Figure 3.22) indicating an OLED turn on voltage of 6.4 V, which corresponds to an electroluminescence of 6.8 cd/m^2. The OLED exhibits a maximum current efficiency of 3.6 cd/A and a maximum brightness of 3153 cd/m^2 (at 15 V).

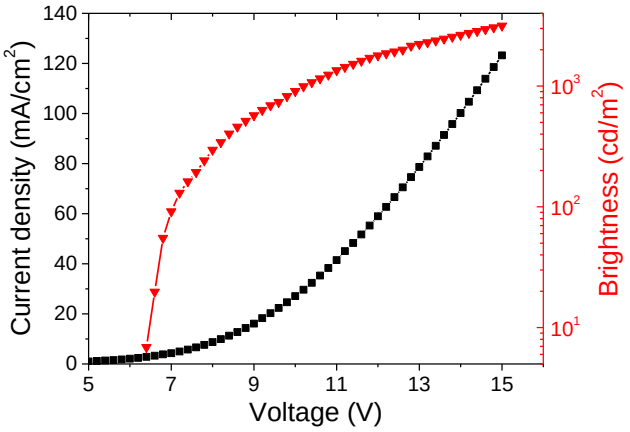

Figure 3.22 Current density−voltage and luminance−voltage characteristics of OLED **A**.

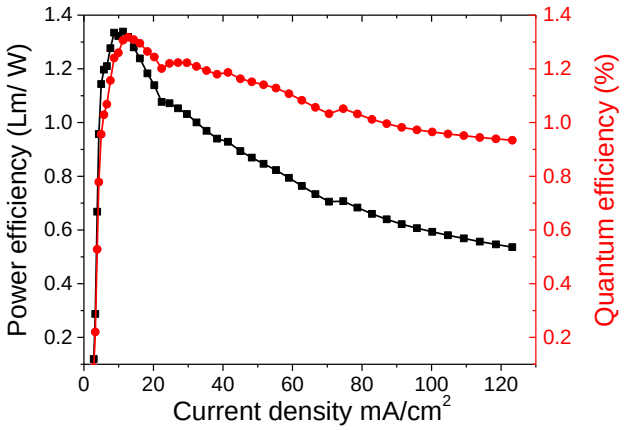

Figure 3.23 Power efficiency and external quantum efficiency of OLED **A**.

At maximum brightness an external quantum efficiency of 1.32%, a power efficiency of 1.34 Lm/W and a current efficiency of 3.35 cd/A were recorded (Figure 3.23 and Figure 3.24).The white light emitted from OLED **A** has Commission Internationale d'Eclairage (CIE 1931) coordinates of (0.34, 0.40) with a colour temperature of 4800K (Figure 3.25). The values of CIE coordinates are close to

those of balanced white light (0.33, 0.33) and the colour temperature is similar to that of direct sunlight (and commercial fluorescent tubes).[11, 12, 68]

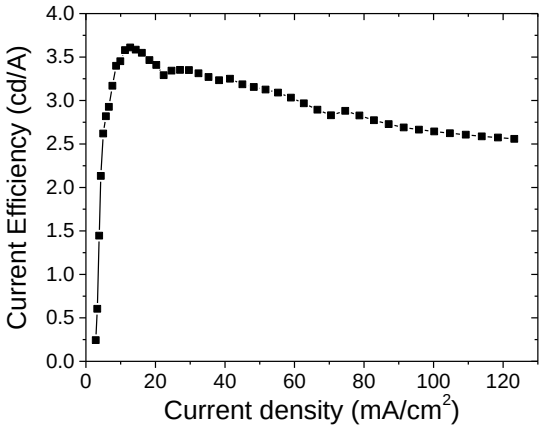

Figure 3.24 Current efficiency−current density characteristic of OLED **A**.

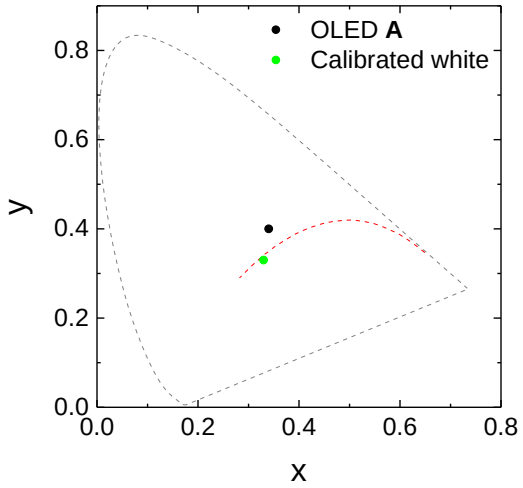

Figure 3.25 CIE 1931 coordinates of OLED **A** and of the calibrated white light.

A third OLED was fabricated using the same architecture shown in Figure 3.19 but using a different thickness and specific deposition rates for the different layers: ITO/CuI (8 nm, 0.1 nm s^{-1})/**TPD** (20 nm, 0.2 nm s^{-1})/compound **3.3** (30 nm, 1 nm s^{-1})/**PBD** (30 nm, 0.2 nm s^{-1})/Ca (7 nm, 0.1 nm s^{-1})/Al (100 nm, 0.1 nm s^{-1}) (OLED **C**). The spectra of the OLED were recorded at different applied voltages (from 8 to 15 V) in air at room temperature immediately after device fabrication. They are compared in Figure 3.26 with the spectra of thin films of compound **3.3** and of a mixture of compound **3.3** and **TPD** prepared by spin coating in the same manner used for OLEDs **A** and **B**. The higher energy emission shoulder (492 nm) is attributable to the pure fluorescence emission of compound **3.3** as for OLEDs **A** and

B. Its maxima do not change with increasing applied voltage although the relative intensities increase. The main emission maximum, also in this case attributable to the exciplex emission of the complex **TPD:3.3**, is blue shifted from 579 to 574 nm when the applied voltage is increased from 8 to 15 V. Conversely, both the position and the intensity of the shoulder at 636 remains effectively unchanged at all applied voltages.

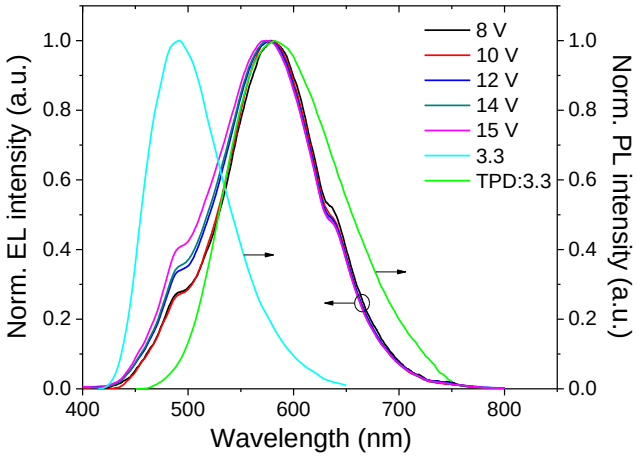

Figure 3.26 Electroluminescence spectra of the OLED **C** at selected applied voltages (from 8 to 15 V) and photoluminescence spectra of the thin films of **3.3** and of the mixture of **TPD:3.3** (1:1 w/w).

The current density-voltage characteristics and luminance-voltage characteristics were calculated (Figure 3.27) indicating an OLED turn on voltage of 4.0 V, which corresponds to an electroluminescence of 3.1 cd/m^2. The OLED exhibits a maximum current efficiency of 16 cd/A and a maximum brightness of 7400 cd/m^2 (at 15 V).

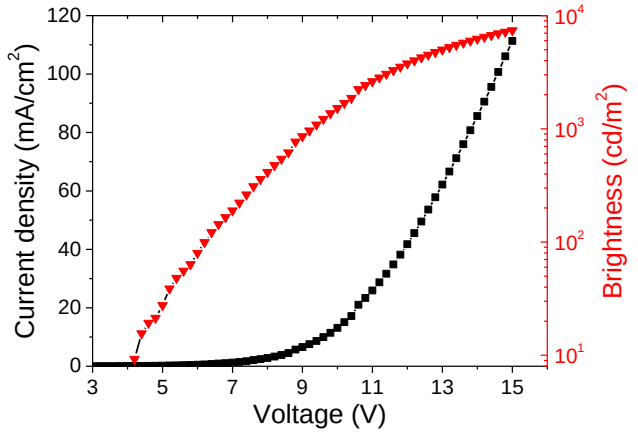

Figure 3.27 Current density−voltage and luminance−voltage characteristics of OLED **C**.

At maximum brightness an external quantum efficiency of 5.57 %, a power efficiency of 10.14 Lm/W and a current efficiency of 16.15 cd/A were recorded (Figure 3.28 and Figure 3.29).

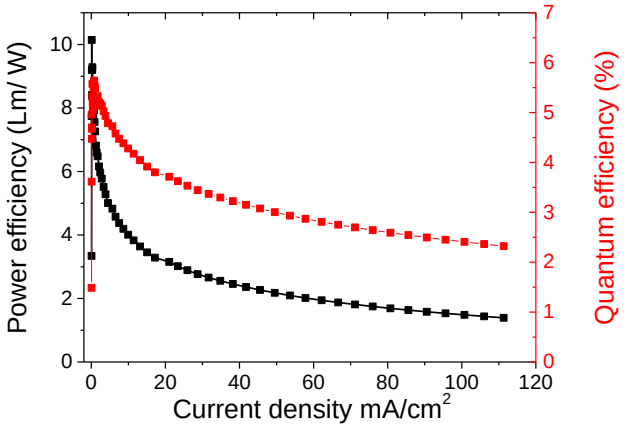

Figure 3.28 Power efficiency and external quantum efficiency of OLED **C**.

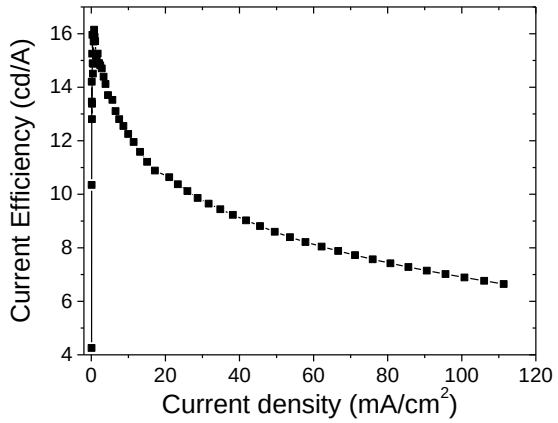

Figure 3.29 Current efficiency−current density characteristic of OLED **C**.

These enhanced values depend on the more efficient exciplex emission likely a result of the increased thickness of the **TPD** and **PBD** layers. Despite the increased values of the main characteristics of OLED **C**, the colour quality diverges from that of balanced white light. In fact the CIE 1931 coordinates are (0.42, 0.45) and the correlated colour temperature is 3800 K, making this light excessively yellow in tone for indoor lighting purposes.

In order to keep the enhanced characteristics of OLED **C** and to obtain a more balanced white light, 2,9-dimethyl-4,7-diphenyl-1,10-phenanthroline (**BCP**) was used as an electron-transporting and hole-blocking material in order to increase the injection of electrons from the calcium anode and to balance the amount of electrons

and holes that combine in the emissive layer. A fourth OLED (**D**) was fabricated with the following architecture: ITO/CuI (8 nm, 0.1 nm s^{-1})/**TPD** (10 nm, 0.2 nm s^{-1})/compound **3.3** (100 nm, 1 nm s^{-1})/**BCP** (30 nm, 0.2 nm s^{-1})/Ca (7 nm, 0.1 nm s^{-1})/Al (100 nm, 0.1 nm s^{-1}). The thicknesses of the layers of **TPD** and compound **3.3** were changed from 20 and 30 nm in OLED **C** to 10 and 100 nm in OLED **D**, respectively. This was performed with the aim to achieve a better colour quality of the white light, increasing the blue component associated to the fluorescence emission of compound **3.3**. The electroluminescence (EL) spectra of the OLED were recorded at different applied voltages (from 8 to 17 V) and are compared in Figure 3.30 with the spectra of thin films of compound **3.3** and of a mixture of compound **3.3** and **TPD** prepared by spin coating in the same manner used for OLEDs **A-C**.

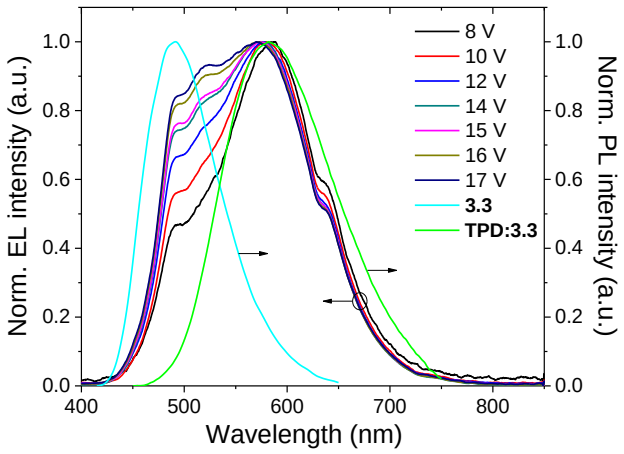

Figure 3.30 Electroluminescence spectra of the OLED **D** at selected applied voltages (from 8 to 17 V) and photoluminescence spectra of the thin films of **3.3** and of the mixture of **TPD:3.3** (1:1 w/w).

The electroluminescence (EL) spectrum of the OLED reveals four different emission bands. The higher energy emission band (494 nm) is characteristic of the pure fluorescence emission of compound **3.3** (as for the first three OLEDs). The maxima stay constant with increasing applied voltage, whilst the relative intensities increase. The main band at *ca.* 580 nm originates from the exciplex at the interface between compound **3.3** and the hole-transporting material **TPD.** It is blue shifted from 588 to 570 nm when the applied voltage is increased from 8 to 17 V. This is likely due to the high electric field reached at the small planar hetero-junction between the layers of compound **3.3** and **TPD**. By increasing the voltage the charges tend to accumulate at the interface between the two layers causing emission from a less relaxed excited state of the donor-acceptor complex.[172] The long-wavelength shoulder at 635 nm in

the EL spectra can be assigned to the typical (classic) electroplex interaction that is associated with the exciplex emission. Its maximum and relative intensity stay constant with increasing applied voltage. The band at *ca.* 520 nm can be attributed to an electromer interaction, which appears upon the injection of electrons and holes under the electric field effect in compound **3.3**.[146, 173] Its maximum stays constant but the relative intensity increases with increasing applied voltage. Therefore, the white emission of the OLED originates from the combination of the exciplex/electroplex emission at the interface between **TPD** and **3.3** and from the exciton/electromer emission of compound **3.3**. This is possible due to the thickness of the emissive layer (100 nm) that permits emission from all the excited states simultaneously. Despite these behaviours, the colour quality of the OLED is maintained at all applied voltages. The CIE coordinates change only slightly from (0.42, 0.44) when the EL is recorded at 8 V to (0.37, 0.44) at 17 V (Figure 3.31 and Table 3.7), due mainly to the increased relative intensity of the EL and of the electromer transition of compound **3.3**. However, at applied voltages higher than 15 V, the device tends to quickly degrade and the characteristics recorded are not maintained. For this reason the characterisation of OLED **D** was recorded up to a maximum applied voltage of 15 V.

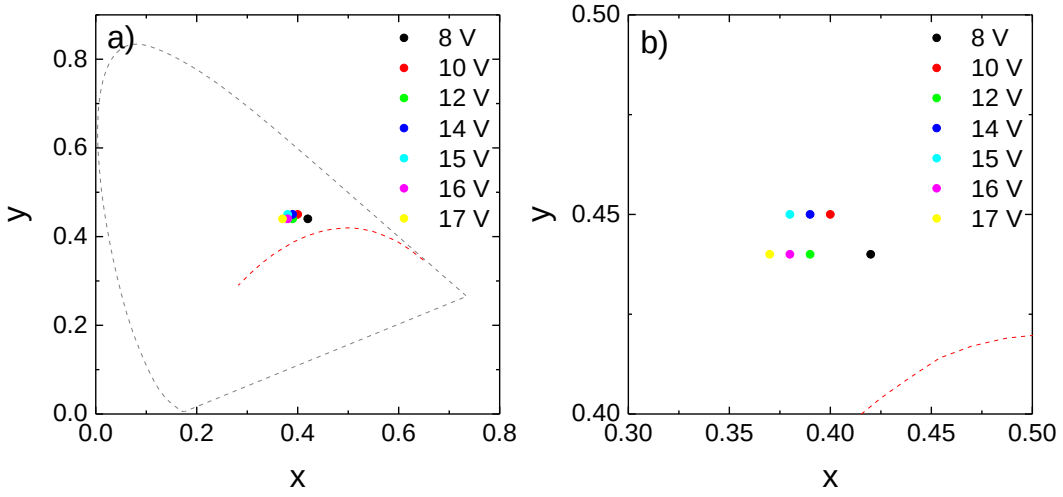

Figure 3.31 The different CIE 1931 colour coordinates of OLED **D** under different applied voltages.

The current density−voltage characteristics and luminance−voltage characteristics (Figure 3.32) indicate an OLED turn on voltage of 5.8 V, which corresponds to an electroluminescence of 1.4 cd m^{-2}. The OLED exhibits a maximum current efficiency of 6.5 cd A^{-1} and a maximum brightness of 5219 cd m^{-2} (at 15 V) (Figure 3.32). At maximum brightness an external quantum efficiency of 2.39% and power

efficiency of 2.60 Lm W^{-1} were recorded (Figure 3.33 and Figure 3.34). The white light emitted from the OLED at 15 V has Commission Internationale d'Eclairage (CIE 1931) coordinates of (0.38, 0.45), with a colour temperature of 4500K; values similar to those of commercial fluorescent tubes.[11, 12, 68]

Table 3.7 The different CIE 1931 colour coordinates of OLED **D** under different applied voltages.

Applied voltage (V)	CIE 1931 coordinates
8	(0.42, 0.44)
10	(0.40, 0.45)
12	(0.39, 0.44)
14	(0.39, 0.45)
15	(0.38, 0.45)
16	(0.38, 0.44)
17	(0.37, 0.44)

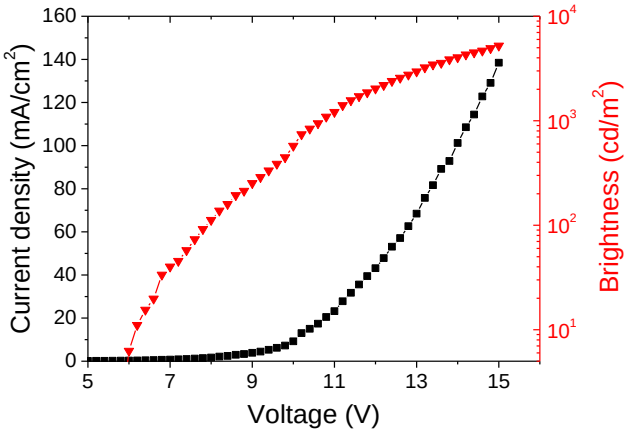

Figure 3.32 Current density−voltage and luminance−voltage characteristics of OLED **D**.

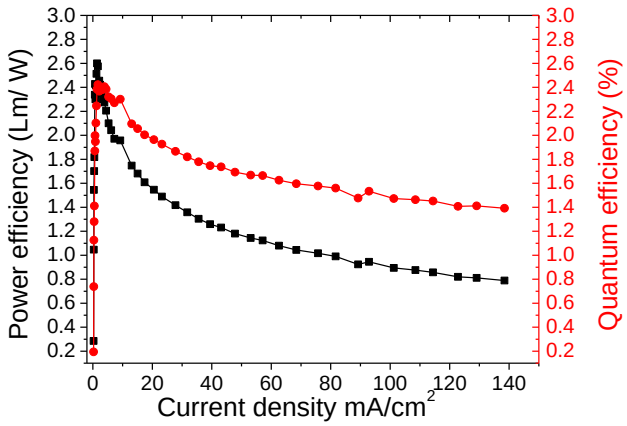

Figure 3.33 Power efficiency and external quantum efficiency of OLED **D**.

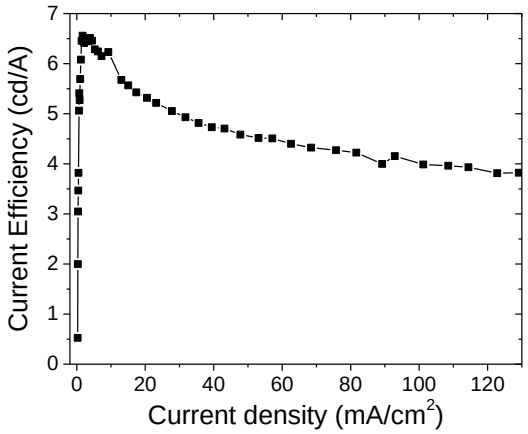

Figure 3.34 Current efficiency−current density characteristic of OLED **D**.

3.2.5. Theoretical interpretations

To explain the PL and EL spectra observed experimentally in addition to the theoretical calculations discussed in Section 3.2.3, quantum chemical calculations were performed for **TPD** and **TPD:3.3** complexes using density functional theory (DFT) and its time dependant counterpart (TD-DFT). The ground state geometries for **TPD** and for eight different **TPD:3.3** complexes (**a-h**, Figure 3.35) were optimised and the analyses of the vibrational frequencies indicate the location of the sought-for energy minimum. The **TPD:3.3**(**a**) complex shows the smallest total energy (Table 3.8) and it was used for the following calculations.

Table 3.8 Total energies and relative energies for the eight **TPD:3.3** complexes (**a-h**) calculated at the PBE0/6-311G(d,p) level of theory.

Complex	Total Energy (kcal/mol)	Relative energy (kcal/mol)
a	−2170873.3	0.00
b	−2170870.9	2.42
c	−2170870.3	2.97
e	−2170869.3	3.95
f	−2170872.0	1.30
g	−2170869.9	3.40
h	−2170870.0	3.29
i	−2170871.4	1.92

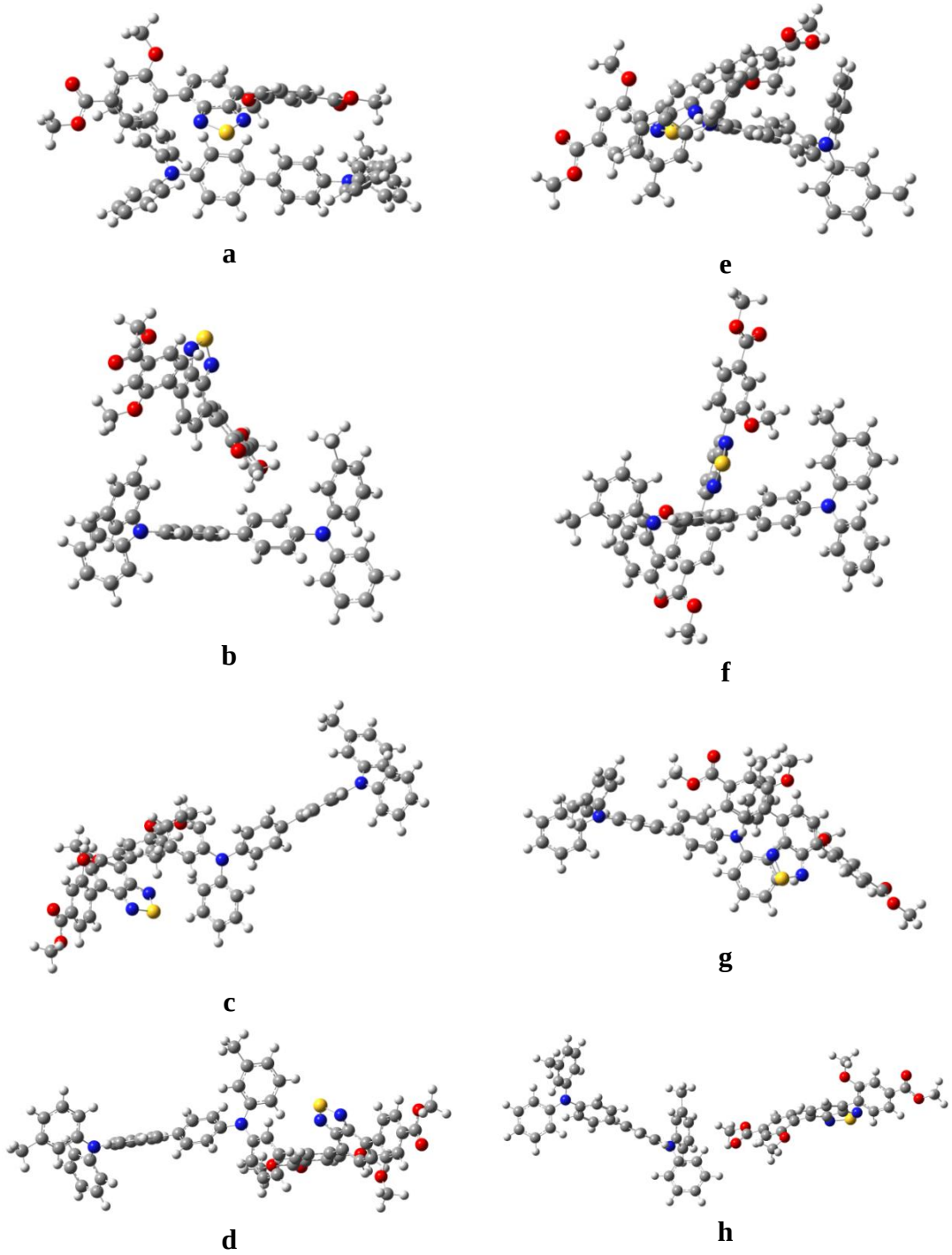

Figure 3.35 Optimised geometries for eight different **TPD:3.3** complexes (**a-h**), calculated at the PBE0/6-311G(d,p) level of theory.

The HOMO and LUMO orbitals are widely delocalised on the π backbone for **3.3** and **TPD** and their energy gaps agree qualitatively with the experimental data. The **TPD:3.3** complex shows a LUMO localised on **3.3** and a HOMO localised on the **TPD** molecule (Figure 3.36).

The reorganisation energies for electrons (λ_e) and holes (λ_h) were calculated theoretically[174] for compound **3.3** in order to predict its behaviour in devices. The

values obtained for λ_e = 0.425 eV and λ_h = 0.384 eV agree qualitatively with the experimental observations, as the reorganisation energy for the electrons is slightly higher than the corresponding value for holes. Note that the lower the λ value, the higher the charge-transport rate.[174]

The first 20 singlet and triplet excited states were calculated for **TPD** and **3.3**:**TPD** in the vacuum using the TD-DFT/PBE0/6-311G(d,p) level of theory (Table 7.14 and Table 7.15) and they were compared with the vertical transitions calculated for compound **3.3** and described in the previous section.

The energies of the first singlet excited state (S_1) of compound **3.3**, **TPD** and of the **TPD**:**3.3** complex are reported in Figure 3.37. They agree qualitatively, by the levels of relative disposition, with the experimental PL emission maxima of thin films of the mixture of **TPD:3.3** and compound **3.3**, and from the literature data for the film of **TPD**.[175]

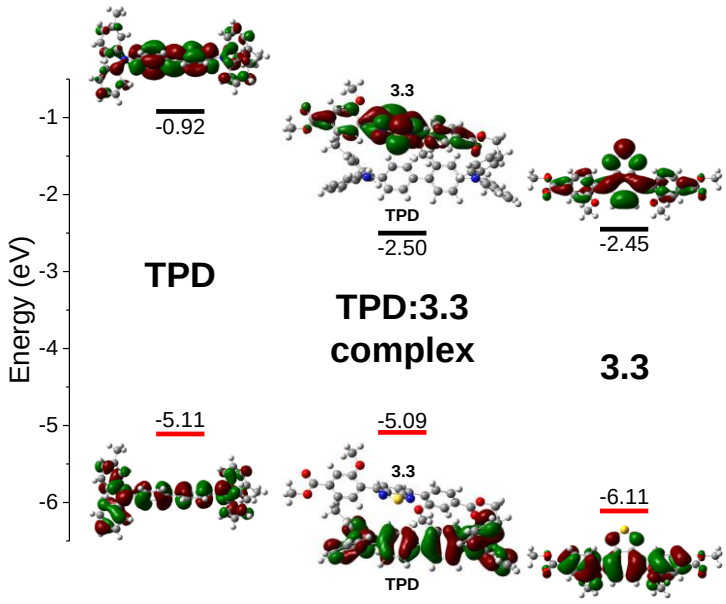

Figure 3.36 Kohn-Sham molecular orbital diagram and orbital graphical representations (HOMO and LUMO) of **3.3**, **TPD** and **TPD:3.3** complex calculated at the PBE0/6-311G(d,p) level of theory (isosurface 0.02).

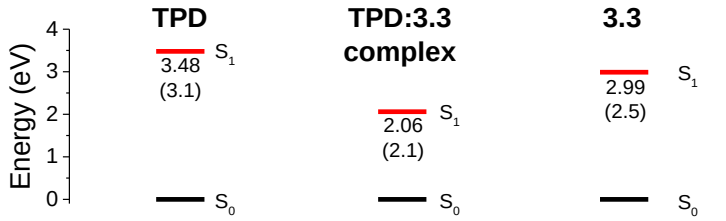

Figure 3.37 First singlet excited state energies calculated at the PBE0/6-311G(d,p) level of theory for TPD, **3.3** and for the complex **TPD:3.3**; the figures in parentheses are the energy levels determined experimentally.

The recombination process of an electron–hole pair with the electron located on the LUMO of compound **3.3** and the hole located on the HOMO of **TPD** should then be responsible for the EL maximum at *ca.* 580 nm for the device and explains the exciplex nature of this transition. Here the exciplex is considered as an excited state complex that is formed by an electronically excited state donor molecule (or acceptor) with a complementary acceptor molecule (or donor) in their ground state.[147]

The correlation of the experimental fluorescence emission maxima with the calculated vertical transitions seems to be a reasonable approximation in order to compare both phenomena. In fact the calculated vertical absorptions, that usually underestimate in energy (*ca.* 0.3 – 0.4 eV) the experimental absorption maxima are compared with the maxima of the emission bands.[167] Using these considerations, it is possible to attribute the EL maximum at *ca.* 577 nm for OLEDs **A-D** to the recombination process of an electron–hole pair with the electron located on **3.3** and the hole located on **TPD**. This corresponds visually to the HOMO → LUMO transition (Figure 7.7).

3.3. Conclusions

Five new esters (compounds **3.1-3.5**) based on a BT core were synthesised. These showed strong absorption and emission in the visible region of the electromagnetic spectrum, with molar absorption coefficients of 47000 – 16000 M^{-1} cm^{-1} and photo luminescence quantum yields of up to 50% in solution. The BT building block has shown a *facile* functionalisation with different electron-donating substituents. This has furnished different emission proprieties with the different substituents, with fluorescence maxima ranging from 473 to 602 nm. The introduction of the ester functionality decreases the HOMO-LUMO gap when compared with the non-functionalised analogues. In particular, compound **3.3** has shown the largest stabilisation and it was successfully used as a single emitting layer for the fabrication of white OLED devices.

The architecture of the devices allows for a characteristic electroluminescence spectrum to be recorded. This was proven to be a combination of the exciton fluorescence emission of compound **3.3** and of the exciplex/electroplex emission at the heterojunction between compound **3.3** and the hole transporting material **TPD**

for OLEDs **3.3.A** and **3.3.C**. In OLED **D** the enhanced performance is supported by the emission from an additional electromer excited state. The devices showed excellent colour quality with C.I.E. 1931 coordinates in the range (0.34, 0.40) to (0.42, 0.45) and a colour temperature in the range of 4800 - 3800K.
Part of this chapter has been included in a peer reviewed paper.[176]

3.4. Future work

In the future, from the promising results obtained with OLEDs **A-D**, the enhancement of the device performance can be made in two directions. Firstly, greater optimisation of the device architecture should be attempted. Incorporation of different layers can be tested, in particular changing the properties of the hole/electron transporting/blocking layers. New materials with these properties are constantly developed and they can be easily adopted in a systematic research for increasing the performance and colour quality of the devices. Secondly, different emissive layers can be developed and adopted. Higher electron/hole mobilities and photoluminescence quantum yield (PLQY) are desirable to achieve improved efficiencies, whereas the synthesis of more soluble materials is essential for the development of cheaper deposition methods. New emissive compounds can be developed starting from the promising compound **3.3**. The ester functionality of the methyl-(3-methoxy)benzoate moieties can be replaced with different substituents (*e.g.* alkyl chains, amines) in order to increase the donor capacity of the arms (Figure 3.38). Using alkyl chains as substituents have the addition effect of increasing the solubility of the material make it suitable for other deposition techniques as spin coating.

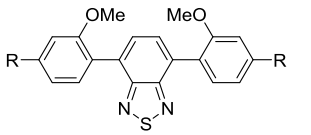

R = linear or branched alkyl chains
linear or branched alkoxy chains
amines

Figure 3.38 New proposed emissive compounds.

Chapter 4. MOFs and Porous Organic Polymers

4.1. Introduction

The most important non-radiative relaxation process that limits the quantum yield of a fluorophore (Chapter 1) is related to the aggregation of the molecules in the solid state causing collisional quenching. One expedient that can be used to limit this quenching mechanism is the introduction of the fluorophores in well ordered 3-dimensional systems where aggregation is restricted by rigid bonds. Herein will be discussed the synthesis and characterisation of new luminescent 3-dimensional materials that incorporate building blocks based on BT derivatives in metal-organic frameworks (MOFs) and porous organic polymers (POPs).

4.1.1. Metallic organic frameworks (MOFs)

MOFs are a class of hybrid organic-inorganic supramolecular materials able to form crystalline ordered networks. The organic ligands (*e.g.* carboxylates, amines) act as electron donor linkers and the metal cations (*e.g.* Zn^{2+}, Co^{2+}) as coordinating centre scaffolds.[177] The crystalline structures can have mono-, bi- or tri-dimensional order that gives them unique characteristics.[178]

They have initially become popular for their extremely high surface areas and for their tuneable pore size and functionality that has allowed them to act as hosts for a variety of guest molecules. The first applications of MOFs were mainly focused as frameworks for storage of gases such as hydrogen, oxygen, nitrogen or carbon dioxide.[178] In 1999 Li *et al.* reported the structure of MOF-5, a nanoporous material with an incredibility high surface area (> 3000 $m^2\ g^{-1}$)[179] that acted as trailblazer in the new field of supramolecular chemistry. During the last 20 years MOFs have gone through extensive exploration, with applications ranging from adsorption of gases, separation of mixtures, catalysis of chemical reactions, magnetism, sensing different analytes and drug delivery [178, 180-183] In contrast to other microporous materials such as zeolites, the presence of both organic and inorganic moieties allows high synthetic flexibility. The topology of the materials is highly dependent on the coordination chemistry of the metal involved and on the geometry and functionalisation of the organic linker.[177]

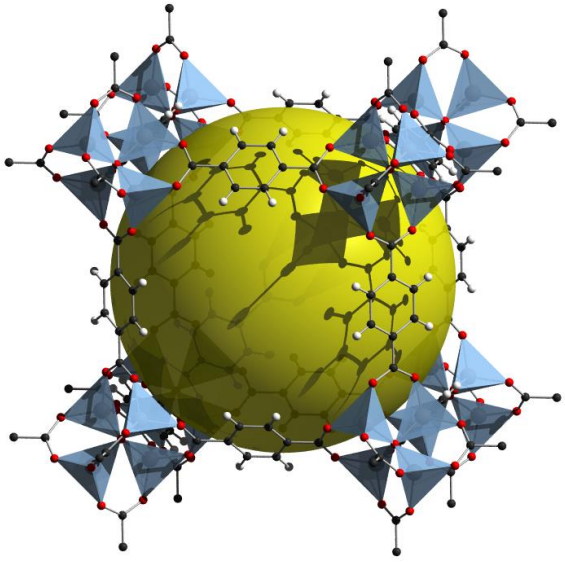

Figure 4.1 One of the cavities of the MOF-5 framework. The unit cell is constituted of eight $Zn_4(O)O_{12}C_6$ clusters (Zn, blue; O, green; C, grey; only seven visible) and it encloses a large cavity, indicated by a yellow sphere of diameter 18.5Å in contact with 72 C atoms.

4.1.1.1. General applications

MOFs can be used for a wide range of applications. One of the first uses described is the thermodynamic or kinetic separation of mixtures of gases or liquids. In particular, the purification of gases such as oxygen and nitrogen, or the removal of toxic or environmentally hazardous gases (*e.g.* carbon dioxide from natural gas, or hydrogen sulfide) has been widely explored. In 2008 Britt *et al.* presented an extensive work where the adsorption of different gases (*e.g.* sulfur dioxide, ammonia, chlorine, tetrahydrothiophene) was compared between different MOFs (*e.g.* MOF-5, IRMOF-3, MOF-74) and BLP carbon, a commonly used commercial activated carbon product.[184] At least one of the MOFs studied for each gas had a better performance than the commercial BLT carbon, in particular in the adsorption of ammonia.

MOFs can be also used as separation membranes, either integrated into a polymer matrix or grown directly as thin films.[185] The first case of impregnating a polymer with a MOF was presented by Won *et al.* in 2005 using Cu-4,4′-bipyridine in amorphous glassy polysulfone. They achieved a very high selectivity for hydrogen over methane (*ca.* 200 times greater at 5% weight loading).[186]

Thanks to the hybrid inorganic-organic composition and nanoporosity, MOFs have been successfully used to catalyse different reactions. The metallic framework is usually the active centre but the organic linker, in addition to its structural function, can also participate as coordination centre.[177]

MOFs have been reported to catalyse a large and diverse number of reactions, that have been extensively reviewed from Lee,[187] Ma[188] and co-workers; however, it is outside the scope of this thesis to go into great detail.

The metallic centres most commonly used are copper and zinc and, depending on the organic linkers and on the metallic coordination geometry, both are able to catalyse different reactions. The copper metal centre of the MOF composed with the 4,4′-bipyrine linker is able to catalyse epoxide alcoholysis,[189] whereas when the linker is 1,2,4,5-benzenetetracarboxylic acid 2,2′-bipyridine it catalyses the oxidation of olefins.[190] The zinc metal centre of the IRMOF-1 is able to catalyse both cycloaddition of carbon dioxide and epoxides,[191] as well as Friedel-Crafts alkylation.[192]

A palladium chloride catalyst can be built into the linker 2,2′-bipyridine-4,4′dicarboxylate and included in a copper-centered MOF; the resultant system is able to catalyse Suzuki-Miyaura coupling reactions.[193] Other functionalisation of the linker of the MOFs includes the deposition of nanoparticles, which can lead to catalysis in oxidation of alcohols[194] or oxidation of carbon monoxide.[195]

Use of the pores inherently present in MOFs for drug delivery has been very attractive for the scientific community from the early stages of MOF development. A large portion of the recent work in this field is focused on MIL compounds (Materials Institute Lavoisier, associated with Férey *et al.*).[196, 197] Lin and co-workers for example were able to post-synthetically modify nanoparticles (NPs) of amine functionalized MIL-101(Fe) with BODIPY type dyes and cisplatin prodrugs. These MOFs decompose in water to release their covalently bound payloads and the rate of release can be modulated by coating the NPs with a thin layer of silica. These coated nanoparticles are able to cross the cell membranes of HT-29 tumour cells and either inhibit growth or stain the cells depending on their functionality.[198]

MOFs have been used extensively as sensors for the detection of different analytes, ranging from water, alcohols, and metal cations, to radiation and nitro-explosives. The majority of these sensors employ the increases or decreases in luminescence signal on exposure to the analyte. For example Jiang and co-workers reported a MOF based on the ligand bipyridineaminoterephthalate that has very weak luminescence when desolvated. The addition of various solvents increases the fluorescence signal, with water, THF, and methanol providing the strongest responses.[199]

Another fascinating application is to use MOFs in electronic and optical devices. In particular with applications as electron and proton conducting materials, light emitting diode (LED) materials and nonlinear optical devices. Only a limited number of MOFs have shown proton or electron conductivity. Kitagawa *et al.* in 2009 demonstrated proton conductivity and electron conductivity in two different MOFs. The Zn-oxalate-adipic acid MOF contains ammonium ions, water and carboxylate groups that act as conductive vehicles in its honeycomb-shaped pores, and showed proton conductivity of 8×10^{-3} S/cm at 25 ° C and 98% relative humidity.[200] Whereas the $Cu[Cu(pdt)_2]$ (pdt = 2,3-pyrazinedithiol) MOF showed 6×10^{-4} S/cm electron conductivity at 300 K, attributed to a donor-acceptor relationship between the Cu I connector unit and the Cu III -2,3-pyrazinedithiolate complex.[201]

4.1.1.2. Light emitting applications

The use of MOFs for lighting applications has been explored widely and numerous papers and reviews have demonstrated the potential of this application.[202]

The origins of MOFs' luminosity include (Figure 4.2):

1. Linkers: the organic ligand has luminescent proprieties that allow emission in the visible region, which can be generated directly from the linker or by charge transfer.[203]
2. Coordinated metal ions: Lanthanoid ions (Ln(III)) can exhibit sharp but weak emission (transitions between atomic orbitals with the same symmetry such as s-s, p-p, d-d, or f-f are forbidden by electric dipole selection rules) that can be amplified by the proximity of an organic fluorophore present in the framework (or adsorbed).[204]
3. Adsorbed lumophores: emissive compounds can be adsorbed into the nanopores of the MOFs.
4. Excimer and exciplex formation: π-π interaction can occur between adjacent linkers providing emissive excited states.
5. Lumophores bound to the MOF surface: emissive materials can be hosted on the surface of the MOFs.

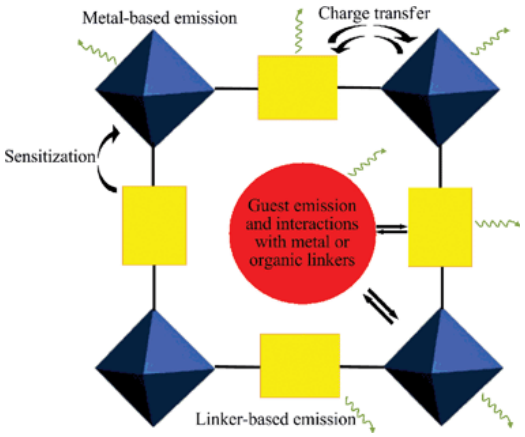

Figure 4.2 Representation of emission possibilities in a porous MOF, wherein metal clusters (blue octahedra) are linked by organic linkers (yellow rectangles) with an incorporated guest (red circle).[202]

This chapter will in part focus on the synthesis and characterisation of MOFs with potential emissive proprieties. In particular, a linker derived from the small molecule **3.3**, successfully used in the fabrication of OLEDs (Chapter 3), will be herein included in two MOFs containing two different metallic scaffolds. MOFs offer a unique platform for the development of SSL materials as they have a degree of structural predictability, in addition to well-defined environments for lumophores in their crystalline form. This can play an important role by providing a rigid multidimensional scaffold able to decrease the quenching effects associated with the aggregation of the emissive linkers. For example, isonicotinic acid is a weak blue fluorophore, but including it as ligand in a mixed-metal complex containing Zn(II) and Cu(I), the resulting [Zn_3Cu_2(isonicotinate)$_8$] MOF emits strong blue luminescence.[203] This is the combined effect of the size of the metals and of the structure and orientation of the linkers. Both factors affect the degree of isolation of the linkers from each other in the structure, this decreases the non-radiative decay rate and increases the fluorescence intensity of the linker.[205, 206, 202]

Martin *et al.* demonstrated that including the same organic linker system (a combination of isophthalate dianion and N,N′-bis(4-pyridylmethyl)piperazine) in two different MOF geometries results in changes in the emission profile. This should be related directly to the degree of π-overlap of the organic linkers in the structure of the framework.[207]

More recently Li and co-workers were able to incorporate the ligand 4′,4‴,4⁗,4⁗′-(ethene-1,1,2,2-tetrayl)tetrakis ([1,10-biphenyl]-4-carboxylic acid) (H_4tcbpe) in the framework [Zn_2(tcbpe)·*x*DMA, DMA = *N*,*N*-dimethylacetamide]. This evacuated (activated) MOF is a yellow emitter with maximum internal quantum

yield of 95.1 % and external quantum yield (expressed as % of internal quantum yield) of 96.5 % that has been included in white emitting devices as the yellow-emitting down-converting material in combination with a blue LED.[208]

4.1.2. Porous organic polymers (POPs)

POPs refers to a class of organic polymers that manifest porosity.[209, 210] Organic polymers in general are composed of organic molecules that act as monomers linked together through strong covalent bonds. The robustness of the covalent bonds used confers chemical and thermal stability on POPs, which is useful for post synthetic treatments required to thoroughly empty the voids (high temperatures and pressures) or to introduce functionalities (strong chemical treatments).[209] Furthermore POPs are generally amorphous and easy to process; they can be moulded into monolithic forms[211-213] or produced in thin films.[214, 215] Through the introduction of solubilising groups they can be dissolved in solvents and then processed directly using solvent based techniques (*e.g.* spin coating) without destroying the porosity.[216, 217] Due to their organic nature, the polymeric frameworks are composed of light organic compounds providing a weight advantage in many applications.[218, 219]

According to the IUPAC recommendation,[220] the POPs are classified with the pore dimensions:

- microporous: pore size smaller than 2 nm in diameter;
- mesoporous: pore size in the range of 2−50 nm, and
- macroporous pore size larger than 50 nm.

Depending on the pore sizes and geometries POPs can have different proprieties and then find particular applications. For example materials with high surface area generally have a smaller pore size (micropores).

The diversity of the synthetic techniques that can be used for POPs allows functionalised materials to be obtained with applications in various fields, including gas storage,[212, 218, 221] separation materials,[222-224] drug delivery,[225, 226] catalysis (both as catalysts[227] and as support for catalysts)[228, 229] and organic electronics.[230-232]

Several methodologies have been currently adapted to synthesise POPs but only few have been widely used.[209] The direct template methodology involves a casting or moulding process similar to the concept used to fabricate plastic bottles, but scaled down to the nano scale (Figure 4.3).[233, 234]

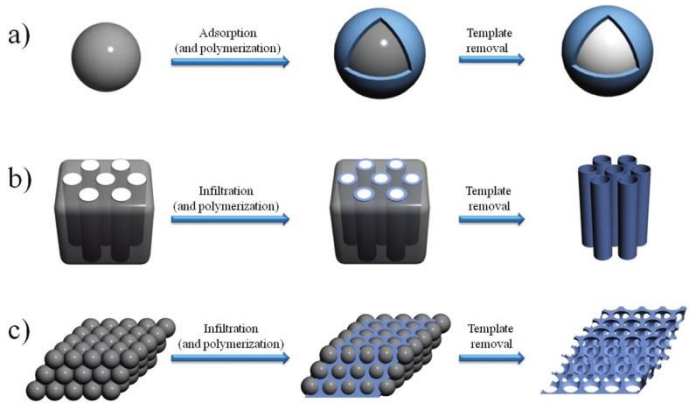

Figure 4.3 Schematic illustration of fabrication of (a) individual spherical porous polymers from solid spherical nanoparticle templates, (b) tubular porous polymers from tubular porous templates, such as AAO, and (c) ordered macroporous polymers from colloidal crystal templates.

For example, Akashi and co-workers demonstrated that hollow capsules of a poly(methyl methacrylate) (PMMA) stereocomplex can be fabricated by a combination of the layer-by-layer assembly technique and the silica template method (Figure 4.4; it = isotactic, st = syndiotactic). As result, a hollow nanostructure composed of non-ionic multilayers is constructed through van der Waals interactions.[235]

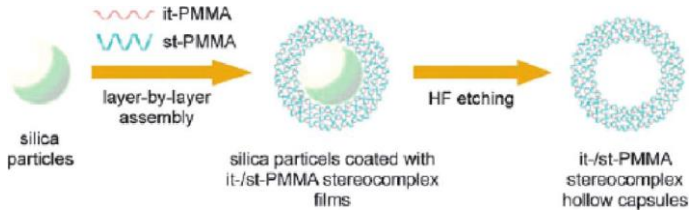

Figure 4.4 Fabrication process of it-/st-PMMA stereocomplex hollow capsules.[235]

POPs with well-defined meso- and macro- porosity can be synthesised by self-assembly using block copolymers (BCPs). [214, 236] BCPs are hybrid macromolecules consisting of two or more chemically immiscible homopolymers that are covalently linked together. They can act as a pore template or as a source of the polymer framework, with the latter being the most successful strategy. Cylindrical pores with a larger diameter (about 55 nm) have been constructed by Bolton *et al.* through the self-assembly of asymmetric PS−poly(lactic acid) (PS-PLA) bottlebrush BCPs (Figure 4.5).[237]

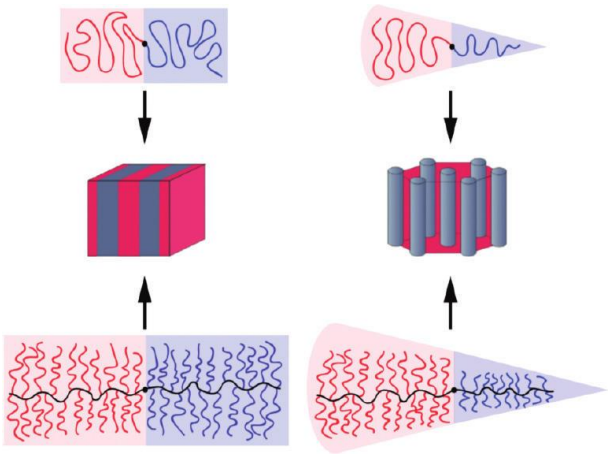

Figure 4.5 Control of the interfacial curvature during self-assembly of linear (top) and bottlebrush (bottom) block copolymers.

The direct synthesis methodology can directly generate pores during solution polymerization, followed by removal of the solvent from the pores.[238, 239] This allows direct preparation through specific polymeric reactions with the advantage of not using sacrificial components. The resulting polymers generally do not have a pore size predilection. This allows a complete synthetic flexibility; the pore size can range from the small microporous to the largest macroporous. A typical microporous polymer called porous aromatic framework (PAF-1), with an ultrahigh BET surface area, 5600 m^2g^{-1} was prepared by Zhu and co-workers using the Yamamoto coupling reaction of tetrahedral tetrakis(4-bromophenyl)methane (Figure 4.6).[240] Replacing this monomer with tetrakis(4-bromophenyl)silane, Zhou *et al.* synthesized a disordered microporous polymer with one of the highest BET surface areas recorded for POPs, of up to 6461 $m^2\ g^{-1}$.[241]

Figure 4.6 Synthesis scheme of a disordered microporous polymer PAF-1.[240]

The high internal phase emulsion (HIPE) polymerization approach can be applied for the preparation of macroporous polymers. HIPE is realised when the volume fraction of the internal phase (dispersed phase) in a conventional emulsion is increased above 74% (maximum packing fraction of uniform spherical droplets). In this situation the droplets deform to create polyhedra that can polymerise.[242, 243] PolyHIPEs usually have a very low BET surface area, typically less than 50 $m^2\ g^{-1}$.[209]

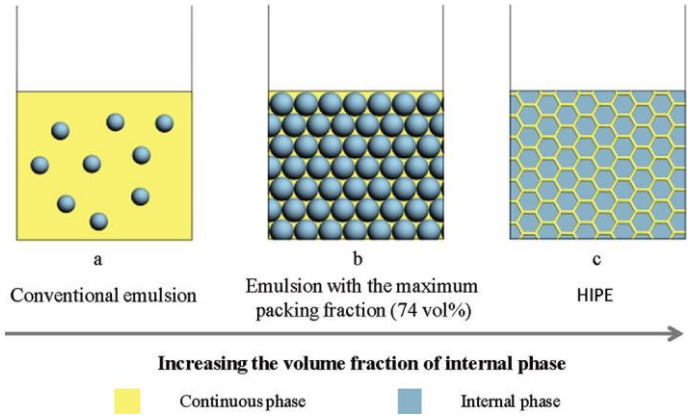

Figure 4.7 Schematic representation for the change from conventional emulsion, through emulsion with the maximum packing fraction (74 vol%), to HIPE when increasing the volume fraction of internal phase. For simplicity, surfactants at the interface between the continuous phase and the internal phase are not shown.

4.1.2.1. Light emitting POPs

Different luminescent application for POPs have been reported and the mechanisms that can be involved for the emission of visible light are theoretically the same as those described for MOFs in Section 4.1.1.2. One of the biggest advantages of POPs when compared with MOFs is their generally higher hydrothermal stability as result of the presence of covalent bonds.[209, 244] Furthermore, due to the potential for micropores, different POP materials have been synthesized and used as luminescent probes for the detection of reactive gases such as NOx,[245] hazardous explosives,[246] oxidative ions and TNT.[247]

Recently, several POPs with emission in the visible range of the electromagnetic spectrum have been synthesised through use of pyrene derivatives as building blocks. Cooper and co-workers prepared a series of microporous (BET surface areas between 303 and 1508 m^2 g^{-1}) and luminescent POPs based on pyrene. The introduction of different co-monomers results in a fine tuning of the band gap and consequently of the luminescent proprieties (Figure 4.8).[248]

Through manipulation of the ratio between 1,3,6,8-tetrabromopyrene (TBP) and 1,3,5-tris(4-bromophenyl)benzene (TBB), Cao and Guo synthesised a series of five POPs (BET specific surface areas of between 716 and 1302 m^2 g^{-1}) with emission in the range of 533 to 815 nm and very high selectivity (and sensitivity) for the detection of picric acid (<1 ppm) and Fe^{3+} (< 1 mM) ions at low concentrations (Figure 4.9).[249]

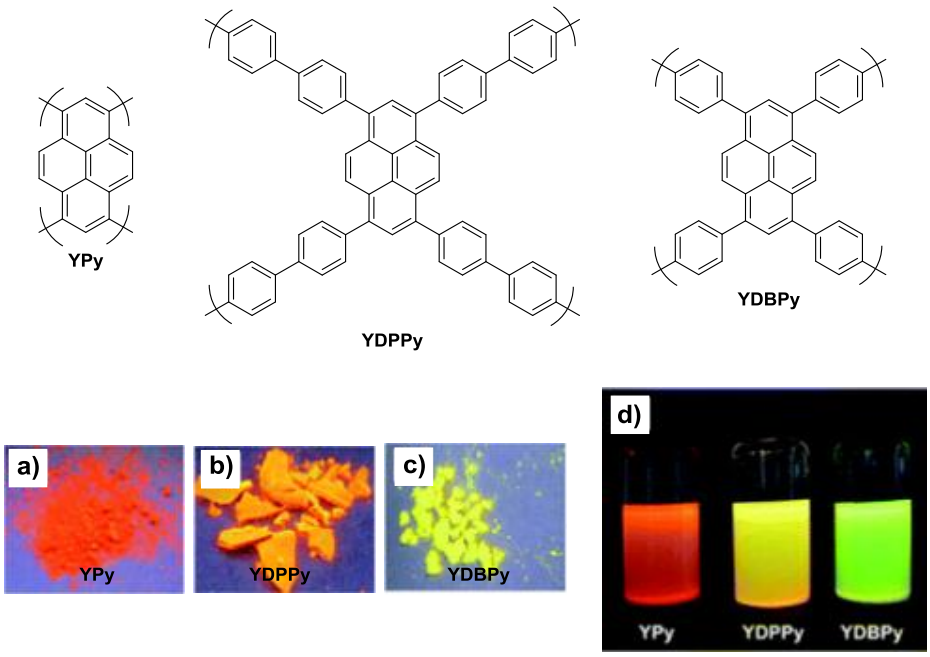

Figure 4.8 (Top) The structures of the polymers synthesised from Cooper *et al.*. (Bottom) Photographs of the polymers under irradiation with UV light (λ_{excit} = 365 nm) in the solid state, (a) YPy, (b) YDPPy and (c) YDBPy; (d) photographs of suspensions of the polymers in THF (1 mg/mL).[248]

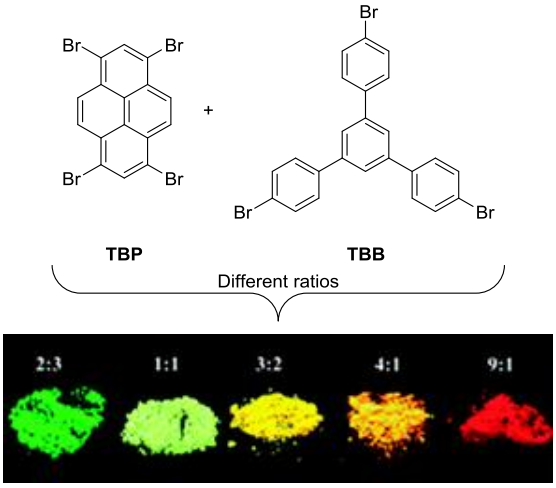

Figure 4.9 (Top) Synthetic route to the five different polymers TBP and TBB as co-monomers *via* the nickel-catalyzed Yamamoto-type Ullmann cross-coupling reaction. (Bottom) The emitted colourful luminescence of five polymers in the solid state under irradiation with UV light (λ_{excit} = 365 nm).[249]

Liu *et al.* reported a POP with a BET surface area of 680 m^2 g^{-1} obtained via Heck coupling between cubic octavinylsilsequioxane (OVS) and halogenated triphenylamine (TPA). The polymer emits in the yellow portion of the visible spectrum and its luminescence can be quenched by nitroaromatic explosives such as 4-nitrotoluene, 2,4-dinitrotoluene and 2,4,6-trinitrotoluene, indicating its potential as a chemical sensor for explosives detection.[250]

4.1.3. Adsorption isotherms and relative theories

Adsorption is the accumulation of atoms, ions, or molecules (the adsorbate) from a gas, liquid, or dissolved solid to a surface (the adsorbent).[140] It differs from absorption, in which a substance diffuses into a liquid or solid to form a solution. The term sorption encompasses both processes, while desorption is the reverse process of adsorption.

The process of adsorption is usually studied through graphs know as adsorption isotherms. These are graphs between the amounts of adsorbate (x) adsorbed on the surface of an adsorbent (m) as a function of its pressure (if gas) or concentration (if liquid) at constant temperature. Typical adsorption isotherms are those derived from the Langmuir and BET theory (Figure 4.10).[140]

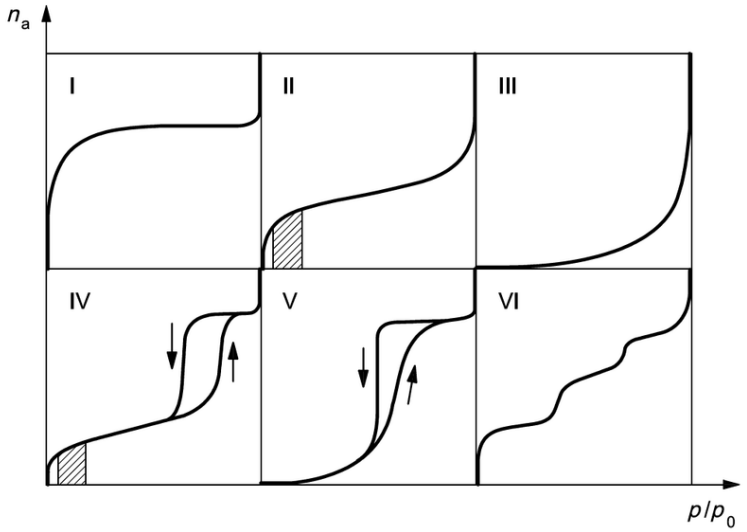

Figure 4.10 IUPAC classification of adsorption isotherms (typical BET range is indicated in types II and IV by the hatched area).[251]

The isotherm of type I is typical of the Langmuir monolayer adsorption (microporous), whereas type II describes a multilayer adsorption of a non-porous or macroporous adsorbent, with the intermediate flat region that indicates the completion of a monolayer coverage. A non-porous or macroporous adsorbent with weak adsorbent-adsorbate interaction shows an isotherm of type III where a monolayer coverage cannot be identified. Type IV is similar to type II, but indicates the presence of mesopores. The initial monolayer–multilayer coverage on the external and mesopore surface is followed by capillary condensation in mesopores; different types of hysteresis loops are observed depending on the shape of pores. Type V and VI isotherms are rarely observed. The first indicates a mesoporous

adsorbent with weak adsorbent-adsorbate interaction, whereas the latter indicates a layer-by-layer adsorption on a highly uniform surface.[252]

The Langmuir adsorption theory is based on the following assumptions:

- a fixed number of vacant or adsorption sites are available on the surface of solid;
- all the vacant sites are of equal size and shape on the surface of adsorbent,
- each site can hold a maximum of one gaseous molecule and a constant amount of heat energy is released during this process;
- a dynamic equilibrium exists between adsorbed gaseous molecules and the free gaseous molecules.

$$A(g) + B(s) \underset{\text{Desorption}}{\overset{\text{Adsorption}}{\rightleftharpoons}} AB \qquad \text{Equation 4.1}$$

Where A(g) is an unadsorbed gaseous molecule, B(s) is an unoccupied metal surface and AB is an adsorbed gaseous molecule A in the surface B. This equilibrium is described with the equation:

$$\theta = \frac{KP}{1 + KP} \qquad \text{Equation 4.2}$$

Where θ is the number of sites of the surface which are covered with gaseous molecule, P represents the pressure and K is the equilibrium constant for the distribution of adsorbate between the surface and the gas phase.

The main limitation of the Langmuir adsorption equation is that it is only valid at medium-low pressures. In fact at very low pressures, KP is so small, that the denominator $(1 + KP)$ can be ignored, reducing the Langmuir equation to

$$\theta = KP \qquad \text{Equation 4.3}$$

Conversely at high pressures KP is much bigger than one, reducing the equation to

$$\theta = \frac{KP}{KP} = 1 \qquad \text{Equation 4.4}$$

BET theory[251] tries to surpass these limitations by introducing the assumption that the molecules can be adsorbed in multilayers. The method is applicable only to adsorption isotherms of type II (disperse, nonporous or macroporous solids) and type IV (mesoporous solids, pore diameter between 2 nm and 50 nm) (Figure 4.10). Inaccessible pores are not detected. BET theory usually adopts non-corrosive gases (*e.g.* nitrogen, argon, carbon dioxide) as adsorbates to determine the surface area data.[220, 251] The gas, that is pumped into the sample tube at constant temperature, covers the external and the accessible internal pore surfaces of the solid sample. The theory uses the follow equation to determine the surface area of the sample:

$$\frac{1}{\left[V_a\left(\frac{P_0}{P}-1\right)\right]}=\frac{C-1}{V_mC}\frac{P}{P_0}+\frac{1}{V_mC} \qquad \text{Equation 4.5}$$

P is the partial vapour pressure of adsorbate gas in equilibrium with the surface at 77.4 K (boiling point of liquid nitrogen), $P_0$is the saturated pressure of adsorbate gas, V_a is the volume of gas adsorbed at standard temperature and pressure (STP, 273.15 K and atmospheric pressure of 100 kPa), V_m volume of gas adsorbed at STP to produce an apparent monolayer on the sample surface and C is a dimensionless constant that is related to the enthalpy of adsorption of the adsorbate gas on the powder sample.

This is a linear equation $f(x)=kx+i$ where

$$k=\frac{C-1}{V_mC} \qquad \text{Equation 4.6}$$

and

$$i=\frac{1}{V_mC} \qquad \text{Equation 4.7}$$

Measuring the value of V_a at each of not less than three values of P/P_0, it will be possible to obtain a linear plot of

$$\frac{1}{\left[V_a\left(\frac{P_0}{P}-1\right)\right]} \qquad \text{Equation 4.8}$$

against P/P_0, according to Equation 4.5, for a range of relative pressures usually between 0.05 and 0.3. Then the capacity of a monolayer (in $mmol/g$), is defined as

$$W_m = \frac{1}{i+k} \qquad \text{Equation 4.9}$$

can be used for the determination of the total surface area S_t as

$$S_t = \frac{W_m N \sigma}{M} \qquad \text{Equation 4.10}$$

where N is the Avogadro's number ($6.023 \cdot 10^{23}$ mol^{-1}), σ is the average area occupied by each molecule in a complete monolayer (0.162 nm^2 for nitrogen) and M is the molecular weight of the adsorbate. The specific surface area (S) is then obtained as the ratio between the total surface area and the sample weight (w).

$$S = \frac{S_t}{w} \qquad \text{Equation 4.11}$$

4.2. Results and discussion

4.2.1. Synthesis of the ligands

The final geometry of a MOF originates from the contribution of the metal preferential coordination geometries and of the geometry of the ligand at the donating extensions. The use of a linear ligand should result in the simplest and most predictable final geometry. For this reasons the 4,7-bis(2-methoxyphenyl)benzo[c][1,2,5]thiadiazole core of compounds **3.3** is an ideal candidate to be used as a MOF ligand due to its linear conjugated backbone. In order to make it a suitable and more accessible ligand the ester functional groups of **3.3** were hydrolysed with an aqueous solution of sodium hydroxide and then acidified with hydrochloric acid to form the analogous carboxylic acid **4.1** in high yields (Scheme 4.1).

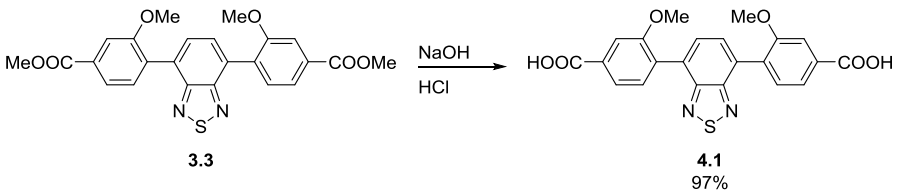

Scheme 4.1 Synthesis of **4.1**.

Compound **4.1** was then used as a ligand for the synthesis of metalorganic frameworks. Compound **3.15** (4,7-dibromobenzothiadiazole) was used as starting material for three different ligands (**3.13**, **4.2** and **4.3**). The synthesis of **3.13** (4,7-bis(5-(trimethylstannyl)thiophen-2-yl)benzo[c][1,2,5]thiadiazole) is reported in Section 3.2, while **4.2** and **4.3** were synthesised from 3-bromothiophene using a multistep procedure as shown in Scheme 4.2.

3-(2-Ethylhexyl)thiophene (**4.4**) and 3-(2-octyldodecyl)thiophene (**4.5**) were obtained in good yields *via* Kumada cross coupling between 3-bromothiophene and the corresponding *in situ* formed Grignard reagents. Controlled lithiation with TEMED and n-BuLi followed by reaction with trimethyltin chloride gave 2-trimethylstannyl-4-(2-ethylhexyl)-thiophene (**4.6**) and 2-trimethylstannyl-4-(2-octyldodecyl)-thiophene (**4.7**). Compounds **4.8** and **4.9** were synthesised *via* Stille cross coupling between 4,7-dibromobenzothiadiazole (**3.15**) and **4.6** and **4.7** respectively using $Pd(PPh_3)_4$ as catalyst. Lithiation followed by reaction with trimethyltin chloride gave the ligands **4.2** and **4.3** in good yields.

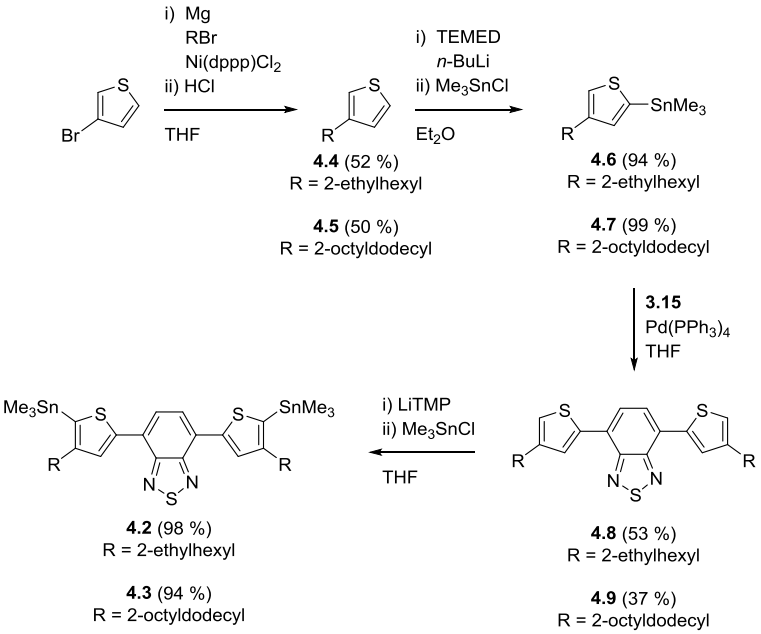

Scheme 4.2 Synthesis of the ligand **4.10** and **4.11**.

4.2.2. Synthesis and characterisation of the MOFs

Two MOFs were synthesised using compound **4.1** as the main ligand. **MOF-4.1.A** was obtained by solvothermal synthesis using $Zn(NO_3)_2 \cdot 6\ H_2O$, 4,4′-bipyridine (bipy) and **4.1** dissolved in the molecular ratio of 3:1:2 in *N*,*N*-dimethylformamide. Yellow block shaped crystals were formed. Single crystal X-ray diffraction analysis was performed and the typical pillared structure of zinc MOFs $[Zn_2\mathbf{L}_2(bipy)]_n$ (**L** = **4.1** in **MOF-4.1.A**) was identified (Figure 4.11).

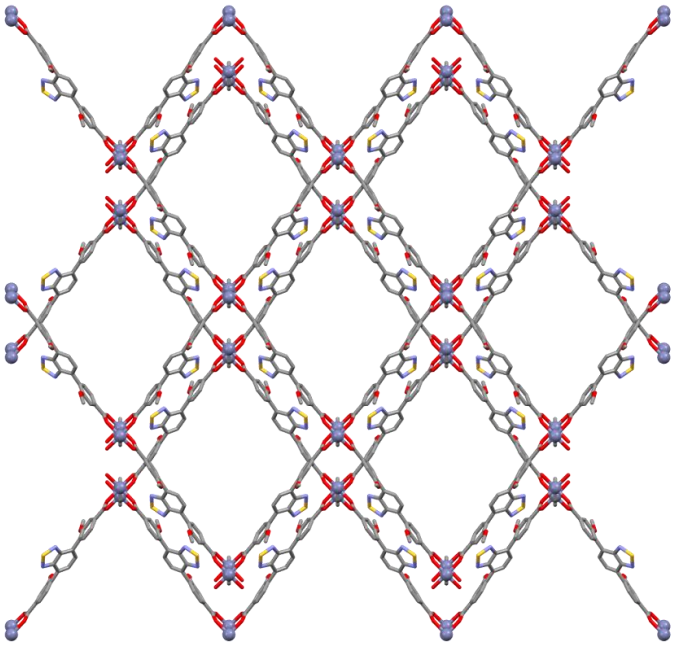

Figure 4.11 Packing of the **MOF-4.1.A**.

The full crystallographic data are reported in the appendix (Table 7.16-Table 7.18).The structure is connected by dimeric Zinc paddlewheel secondary building units, where four carboxylate groups of four different **4.1** units are coordinated to two Zn (II) centres in a square plane fashion to form two dimensional sheets of the **4.1** ligand. The axial positions are occupied by the nitrogen donor atoms of the 4,4′-bipyridine ligands which connect the sheets in the third dimension(Figure 4.12).

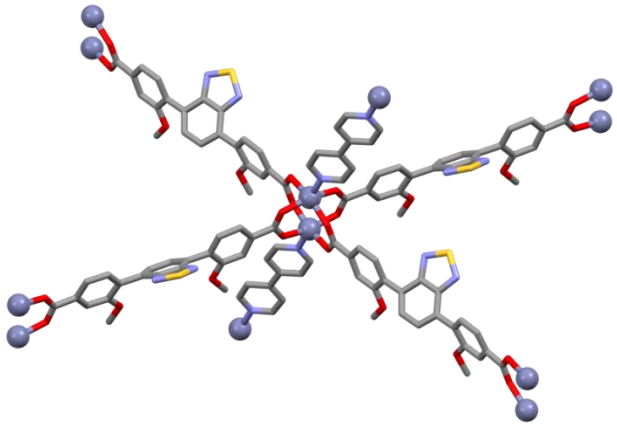

Figure 4.12 Dimeric cluster of the **MOF-4.1.A**.

MOF-4.1.A is two-fold interpenetrated, with the two sub-units represented in red and blue in Figure 4.13 (see also Figure 4.11). However it still exhibits considerable channels down the crystallographic *c* axis that are filled with disordered molecules of solvent in the crystal structure, but which suggest significant porosity upon removal (Figure 4.13).

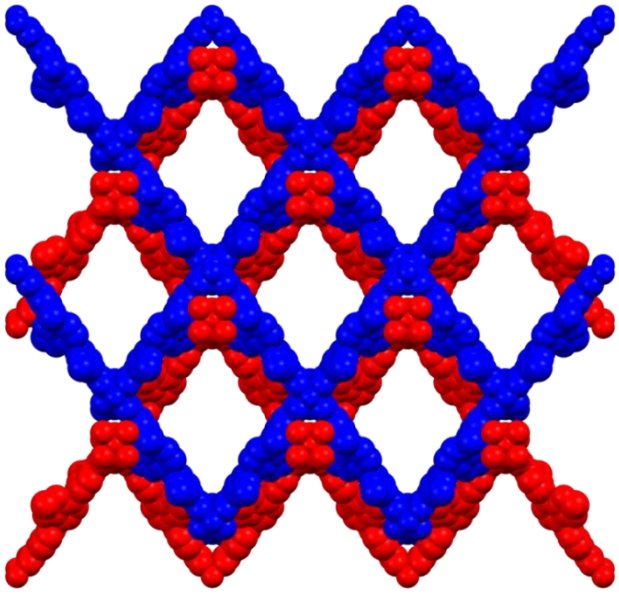

Figure 4.13 The pores of the **MOF-4.1.A** are available after removal of the solvent.

The individual units of compound **4.1** are separated considerably from one another, which suggests that MOFs are indeed a useful matrix for isolation of individual benzothiadiazole units. The methoxy groups of the ligand act as buffers between layers in the MOF, with possible short CH···O contacts between adjacent methoxy groups (C···O = 3.7 Å; CH···O = 2.9 Å) ensuring that the **BT** moieties are separated with a minimum intermolecular distance of 8.0 Å between sulphur atoms. Indeed, the closest intramolecular contact between molecules of **4.1** is between adjacent molecules coordinated to the same Zn dimer, with S···S distances of approximately 6.8 Å. The distance between the intramolecular planes of bipy units is 18.4 Å and the distance between intramolecular planes of **4.1** ligands is 13.0 Å. Intermolecular (between the two sub-units, red and blue) distance between the planes of the **4.1** ligands are 3.9 Å and between the planes of bipy 6.5 Å (Table 7.17 and Table 7.18).

As Zn (II) linked MOFs can be prone to hydrolysis, the synthesis of a MOF linked by Zr(IV) in the **UiO-66** topology ($[Zr_6O_4(OH)_4L_6]_n$) was attempted, using L-proline and hydrochloric acid as crystallisation promoters. **MOF-4.1.B** was obtained as a yellow precipitate and inspection under optical microscopy suggested the presence of microcrystalline octahedrons up to 10 micron in diameter. The precipitate was examined by powder X-ray diffraction analysis, and compared with a pattern predicted from the single crystal structure of **UiO-68-NH_2**, an analogous MOF with a similar terphenyl based ligand.[253] The close correlation between the patterns confirms the formation of a similar **UiO-66** topology MOF with the benzothiadiazole ligand (Figure 4.14). The linkers are again expected to be significantly separated from one another.

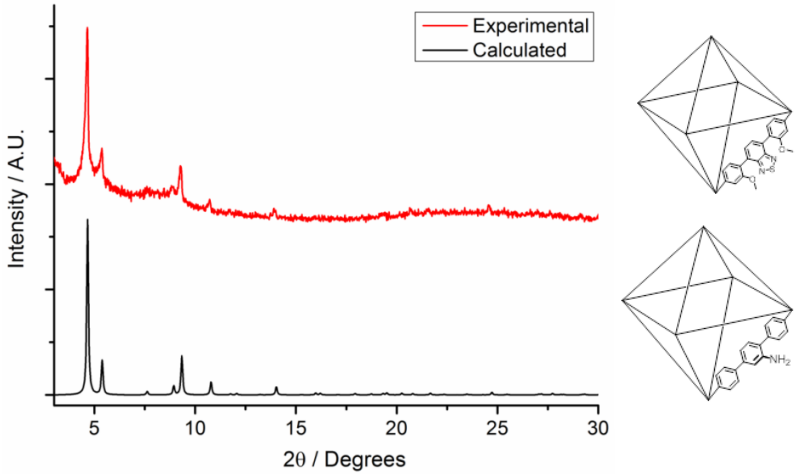

Figure 4.14 Experimental (red) and calculated (black) X-ray powder diffraction patterns for **MOF-4.1.B** and **UiO-68-NH_2** respectively.

4.2.3. Synthesis and characterisation of the porous polymers

In order to include the BT based ligands **3.13**, **4.2** and **4.3** in a three dimensional organic framework in a similar way to that of a MOF, tetrakis(4-bromophenyl)methane (**4.10**) and tetrakis(4-bromophenyl)adamantane (**4.11**)[254] were used as co-monomers for five new three dimension POPs (Figure 4.15).

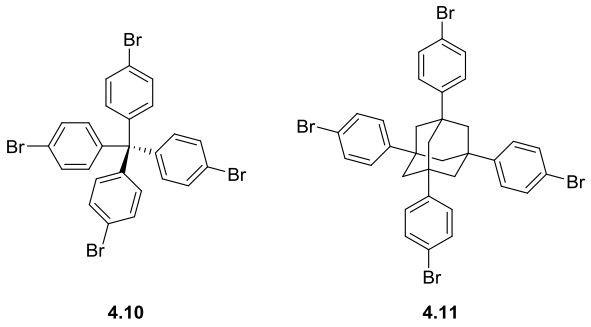

Figure 4.15 Tetrakis(4-bromophenyl)methane (**4.10**) and tetrakis(4-bromophenyl)adamantane (**4.11**).

The first polymer was synthesised by microwave assisted Stille cross coupling of compound **3.13** with compound **4.10** using the catalytic system tris(dibenzylideneacetone)dipalladium(0)/tri(o-tolyl)phosphine. The resulting precipitate was treated with hydrochloric acid in order to remove any alkyltin terminal groups and after Soxhlet extraction of the reactants, the polymer **4.12** was obtained. In similar fashion, polymer **4.13** was obtained by microwave assisted Stille cross coupling between compounds **3.13** and **4.12**. The resulting polymer (**4.13**) was further reacted with tributyltin thiophene and bromobenzene to end-cap the bromo and alkyltin terminal groups, respectively. This was used as general procedure for the synthesis of the polymers **4.14-4.16** as described in Figure 4.16. Hypothesised final structures of polymers **4.14-4.16** are presented in Figure 7.9.

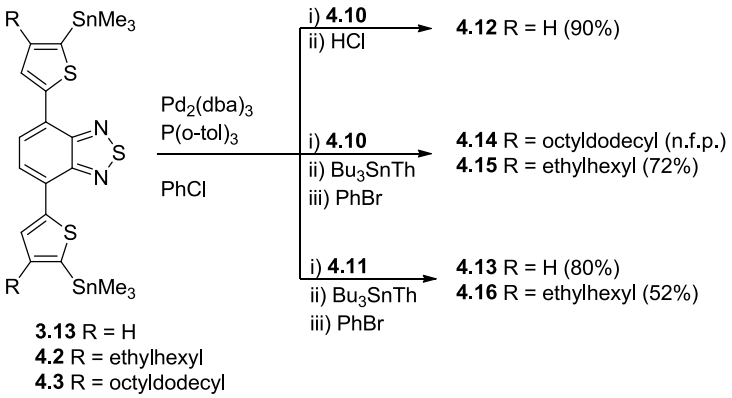

Figure 4.16 Synthesis of polymers **4.12-4.16**.

Polymers **4.12-4.13** were insoluble in common organic solvents; for this reason, in order to increase their solubility 2-octyldodecyl branched alkyl chains were adopted in the 4-position of the bis-4,7-thiophene benzothiadiazole unit using compound **4.3** as co-monomer. Polymer **4.14** was obtained through the general procedure described for **4.13** and it showed extreme solubility in common organic solvents. However, for this reason it was not possible to isolate the residual reactants and this polymer was not tested further.

In order to isolate the final product, a better balance between the solubility of the final polymer and the initial building blocks is essential. For this reason 2-ethyhexyl branched alkyl chains were adopted at the 4-position of the bis-4,7-thiophene benzothiadiazole unit using compound **4.2** as co-monomer. Polymers **4.15** and **4.16** were obtained using the general procedure adopted for polymer **4.13,** with co-monomers **4.10** and **4.11**, respectively. The polymers exhibited ideal solubility, with the reactants removed by Soxhlet extraction using in sequence methanol, acetone and hexane.

Polymers **4.15** and **4.16** were soluble in dichloromethane and their absorption and emission spectra were recorded in this medium (Figure 4.17). They show similar spectral profiles with three maxima at 485, 327, 260 nm for polymer **4.15** and 486, 328, 259 nm for polymer **4.16**. The typical absorption band of the BT unit (*ca*. 300 nm)[95, 100, 153, 154] is red shifted depending on the electron character of the thiophene substituents and to the extended conjugation through the scaffolds units. The less energetic band, attributable to the interaction between the peripheral aromatic rings and the BT core is red shifted in dependence with the extended conjugation when compared with the mother compound (**3.16**, λ_{max} = 444 and 308 nm).

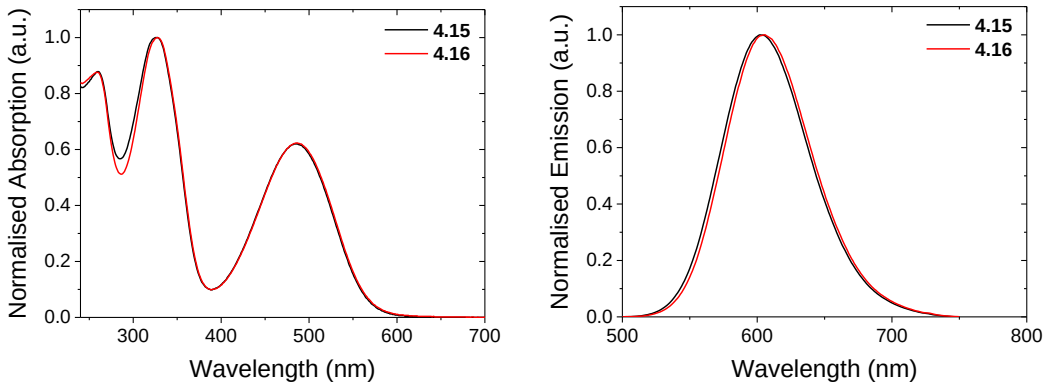

Figure 4.17 UV-Vis absorption (left) and fluorescence (right) spectra of **4.15** and **4.16**.

The fluorescence spectra show similar emission profiles with maxima at 602 and 605 nm for polymers **4.15** and **4.16**, respectively. The HOMO-LUMO gap obtained from the onset of the lowest energetic band is 2.2 eV for both the compounds. Cyclic voltammograms were recorded and they show similar profiles for both polymers with three reversible oxidations ($E_{½}$ = 0.56, 0.80, 0.98 V) and one reversible reduction ($E_{½}$ = −1.76 V) observed (Figure 4.18).

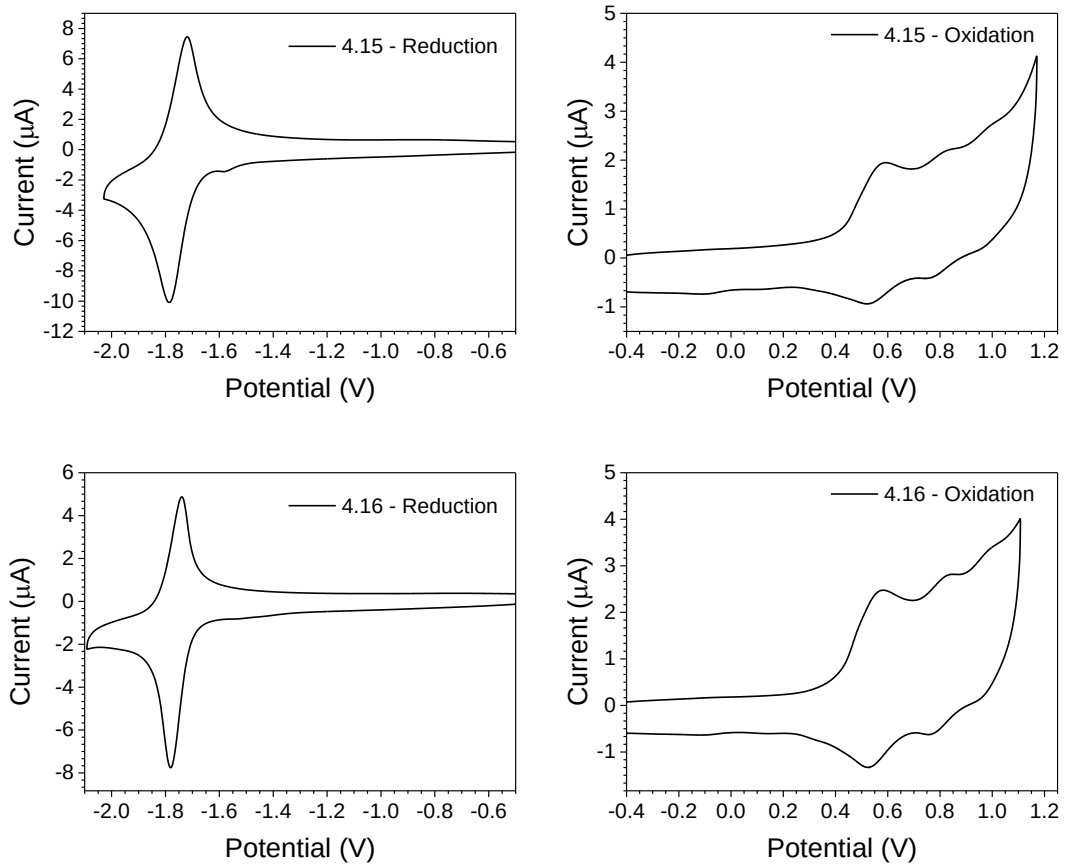

Figure 4.18 Cathodic (left) and anodic (right) waves from cyclic voltammetry of **4.15** (up) and **4.16** (down) referenced against the $E_{½}$ of the Fc/Fc^{+} redox couple; 1×10^{-4} M solution in 0.1 M n-Bu_4NPF_6 (dichloromethane); scan rate 0.1 V s^{-1}.

The reduction is attributable to the BT core as discussed in previous chapters. The three oxidations can be assigned to the thiophene and phenyl groups of the polymers that extend the π-conjugation of the POPs.

The values of the HOMO and LUMO obtained from the onset of the first oxidation and reduction waves are − 5.2 and − 3.1 eV for both polymers, with a gap of 2.1 eV in close agreement with the data obtained with the absorption profiles.

The crystallinity of the polymers **4.12**, **4.13**, **4.15**, **4.16** was measured by powder X-ray diffraction (Figure 4.19).

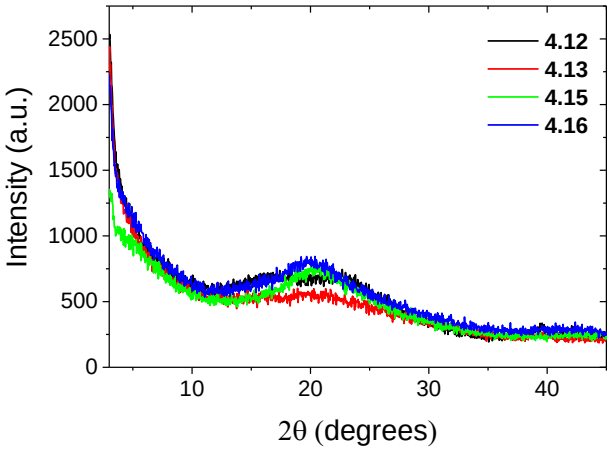

Figure 4.19 Powder X-ray diffraction patterns of the polymers **4.12**, **4.13**, **4.15** and **4.16**.

The polymers have similar diffraction patterns without any relevant crystalline peak, confirming the amorphous character of the compounds.

The porosities of the four polymers were experimentally studied *via* nitrogen and hydrogen sorption at 77 K and carbon dioxide sorption at 273 K (Figure 4.20).

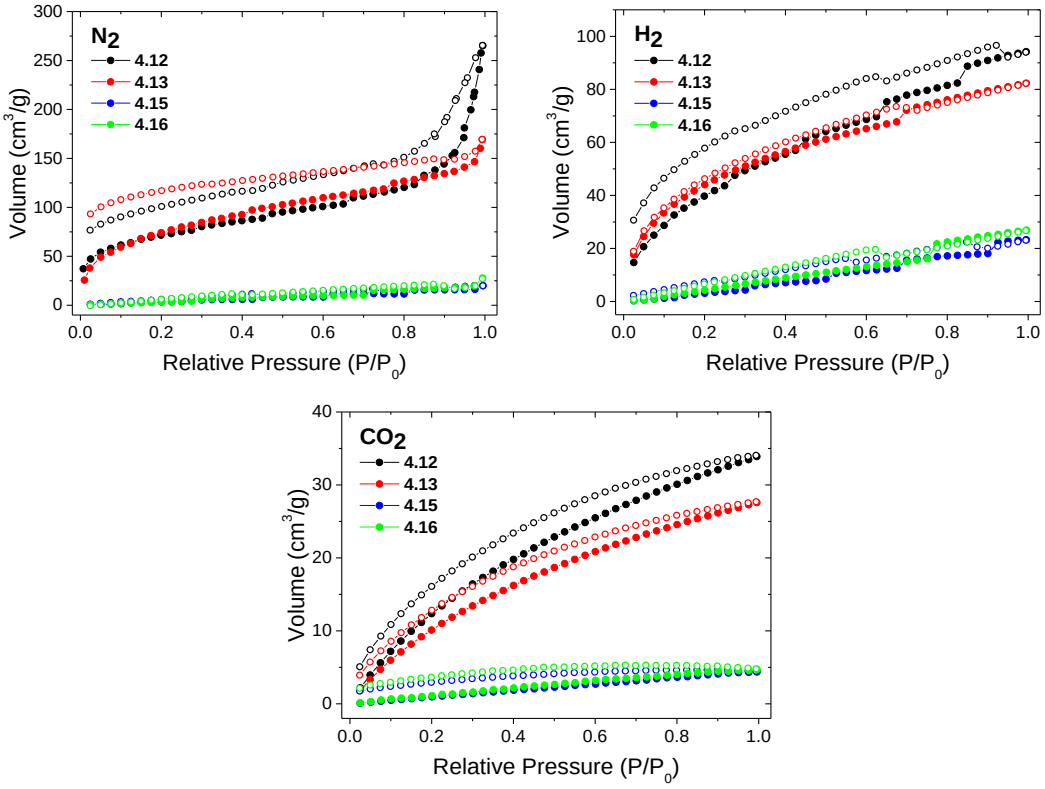

Figure 4.20 Nitrogen (top), hydrogen (bottom left) and carbon dioxide (bottom right) sorption isotherms for **4.12** (black), **4.13** (red), **4.15** (blue) and **4.16** (green); adsorption (filled circle)/desorption (open circle).

Polymers **4.12** and **4.13** show type II nitrogen sorption isotherms, with some type IV character at high relative pressures, based on the IUPAC classification.[220] These

indicate microporous solids having relatively small external surfaces. The limiting uptake is governed by the accessible micropore volume rather than by the internal surface area. The hysteresis loop is associated with the capillary condensation taking place in the pores. Furthermore there is a limited uptake at high relative pressures. This was confirmed by their respective pore size distributions calculated using the Quenched Solid Density Functional Theory (QSDFT) model (Figure 4.21).[255] In the simulation there is a contribution of macropores (half pore width > 50) likely due to the voids between submicrometer agglomerates, which is rather common in porous organic polymers.[256]

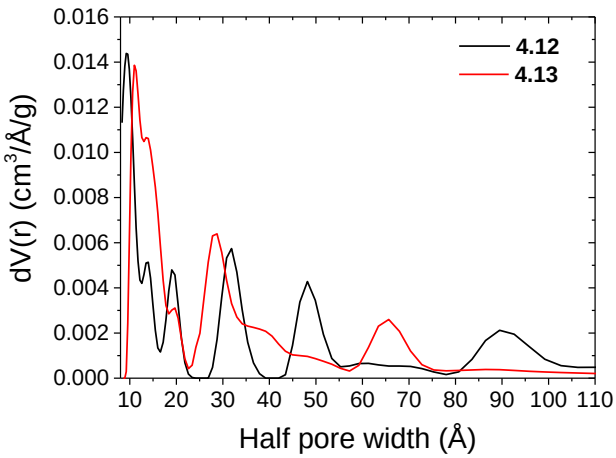

Figure 4.21 Pore size distribution of **4.12** (black) and **4.13** (red) calculated with the QSDFT adsorption branch model.

The isotherms obtained from the nitrogen sorption were used to calculate the surface area, resulting in values of 260 and 279 $m^2\ g^{-1}$ for POPs **4.12** and **4.13**, respectively. BET surface area calculations were carried out by using the ASAP 2020 software. The isotherm points chosen to calculate the BET surface area were subject to the three consistency criteria detailed by Walton and Snurr.[257] First, the pressure range selected has values of $V(P_0 - P)$ increasing with P/P_0. Second, the points used to calculate the BET surface area are linear with an upward slope. Third, the line has a positive y-intercept (Figure 4.22).

The hydrogen and carbon dioxide sorption isotherms of **4.12** and **4.13** are both type I. These are typical of microporous solids having relatively small external surfaces; using hydrogen and carbon dioxide, the limiting uptake is governed by the available and accessible micropore volume.

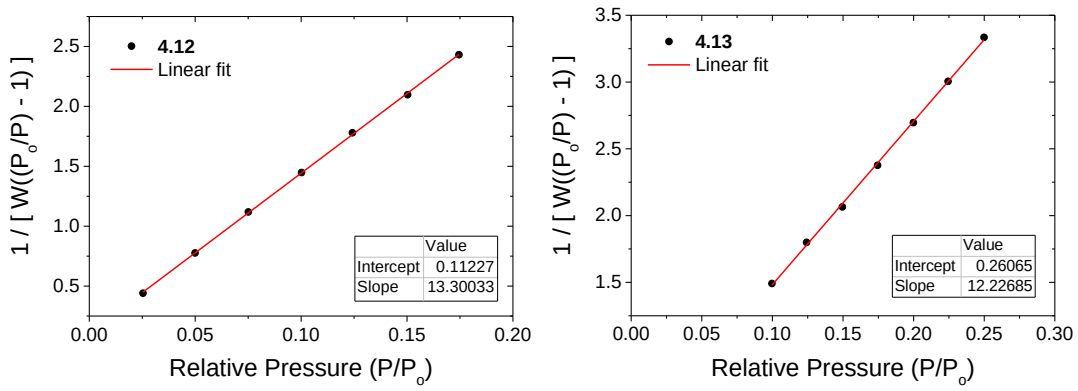

Figure 4.22 Plot of the linear region for the BET equation for **4.12** (left) and **4.13** (right).

All the sorption isotherms studied for POPs **4.15** and **4.16** are of the type I. They present very low volumes of uptake gas and for this reason they were not studied further. This behaviour is likely due to the bulky alkyl branched chains of these polymers (derived from the monomers **4.2** and **4.3** used for their synthesis) that do not allow the adsorption of the studied gas through obstructing the pores.

4.3. Conclusions

Two new MOFs (**MOF-4.1.A** and **MOF-4.1.B**) were synthesised and characterised by X-ray techniques. An X-ray structure was obtained for **MOF-4.1.A** from a single crystal. The regularity of the BT containing emissive linker without significant interactions between each other was confirmed. This allows prediction of the porosity of the MOF after removal of the incorporated solvent. The X-ray powder pattern of **MOF-4.1.B** is closely correlated to that of the square bipyramidal structure of **UiO-68-NH$_2$**.[253] The three dimensional location of the emissive linkers was confirmed. This should lead to improved absorption and emission proprieties when compared with compound **4.1**. At this stage, unfortunately, it was not possible to confirm this experimentally due to the crystalline nature of the obtained MOFs. The physical properties of the new MOFs could not be further studied due to a lack of solubility; new iterations of these MOFs should carefully consider processing solvents to promote their applicability.

Four new POPs (**4.12**, **4.13**, **4.15** and **4.16**) were synthesised and characterised. POPs **4.12** and **4.13** resulted in materials that were insoluble in common organic solvents with intrinsic (mesoporous) porosity and surface areas of 260 and 279 m^2/g,

respectively. Polymers **4.15** and **4.16** resulted in soluble materials with emissive proprieties. All the POPs incorporated emissive BT based linkers.

4.4. Future work

The synthesis of MOFs and POPs that involve highly fluorescent/phosphorescent ligands is commonly adopted in order to achieve elevated PLQY and ELQY. In fact, the integration of luminescent ligands in rigid, well defined structures is able to limit the collisional quenching that results from molecular aggregation, one of the most efficient non-radiative quenching mechanisms.[39]

The preliminary results described in this chapter can be explored further. The porosity and luminescent properties of the MOFs can be measured. In particular different strategies can be adopted to register the absorption and emission profiles and the quantum yields. Examples can be the incorporation of the MOFs in a non-absorptive and non-emissive matrix as has been done for compounds **2.1**-**2.5** (chapter 2). The incorporation in polymeric membranes or fibres through physical or chemical adsorption can be a difficult but feasible option. In this way the MOFs and POPs described can be included in luminescent devices; for example as emissive down converters or as emissive layers in LEDs.

Furthermore the main theme can be strengthened further; new organic emitters can be adopted as ligands/co-monomers and new architectures can be developed. These new compounds could show an intrinsic porosity that can be exploited for application as luminescent sensors with an ON-OFF mechanism for the detection of gases in the solid state, or ions in solution, or when dispersed.

Chapter 5. Non-covalent heteroatom interactions and their role in dictating conformation and planarity in a series of BBT based donor-acceptor small molecules

5.1. Introduction

In recent decades we have witnessed the advent of the first generation of organic electronic materials. As previously discussed, they were initially constituted chiefly of extended conjugated carbon-based structures (*e.g.* polyacetylene)[4] and preceded organic electronics that incorporate heterocycle based conjugated molecules as building blocks (*e.g.* poly(3-hexylthiophene)).[28] Recently the trend in organic electronics is to obtain extended conjugated molecular systems using the so-called "donor-acceptor" design strategy, involving the use of electron-rich and electron-poor moieties that are able to create local electron density gradients along the backbone, with low energy charge-transfer transitions.[31, 33] This allows materials with small optical and electronic band gaps to be obtained that can be used for a wide range of applications in the field of organic electronics (*e.g.* OLEDs, OFETs, OPVs).[258]

Different components containing heteroatoms and pendant units are often used along the backbone of highly conjugated materials in order to obtain different structures capable of tuning the properties of the materials.[259-261] The wide use of this strategy increases the possibility of through-space intra- and intermolecular interactions between different atoms. Many papers have been recently published ascribing these interactions as capable of stabilizing particular molecular geometries or configurations.[261-267] In particular, the possibility of weak non-bonding interactions occurring between the second and third row of elements (*e.g.* nitrogen, oxygen, sulphur) has been discussed. This is a desirable prospect in order to allow easy control and engineering of molecular geometries, as well as proprieties, of organic electronic compounds.[7]

However the presence of a vast range of heteroatom and substituent combinations makes it challenging to predict the most stable conformations. Even with the help of crystal structures it is only possible to speculate the most favourable conformations and arrangements.

The aim of this chapter is to provide a means to help the synthetic chemist to understand and predict conformational preferences. Herein, seven 4,8-disubstituted benzo[1,2-d:4,5-d']bis(thiazole) (BBT) molecules and the interactions between their building blocks have been studied using computational methods.

5.1.1. Non covalent interactions

In this chapter non classical interactions will be discussed, such as oxygen-sulphur and nitrogen-sulphur. For this reason, several literature examples of oxygen-sulphur and nitrogen-sulphur interactions will be discussed.

5.1.1.1. Oxygen-sulphur interactions

The oxygen-sulphur interaction has been postulated in many recent papers. It has been considered to occur between the sulphur of thiophenes and oxygen of carboxylic or ether functionalities. Yang and Pomerantz studied different bis-thiophene derivatives with Hartree−Fock calculations and Mulliken partial charge data suggesting a large electrostatic interaction between partial negatively charged carboxyl oxygen and partial positively charged thiophene sulphur.[268, 269]

This interaction has been predicted in other works because the stable conformations (theoretic and experimental) considered had an interatomic distance between sulphur and oxygen shorter than the sum of their respective van der Waals radii.[29, 262, 270] Additionaly, such interactions are considered to "lock" highly planar conformations of organic materials.[263, 264, 271]

5.1.1.2. Nitrogen-Sulphur interactions

In a similar fashion, nitrogen-sulphur interactions have been proposed as a locking interaction for different polymers and small molecules. In 1996, Chivers *et al.* postulated that these interactions were present in a series of sulphur-containing diazenes, as a combination of donation from the nitrogen lone pair into the σ* orbital of the sulphur and a π-"back-donation" of the chalcogen lone pair into a π* orbital of the diazene system.[272]

Özen and co-workers studied nitrogen-sulphur and oxygen-sulphur interactions in a series of thiophene substituted monomers (Figure 5.1). By means of atoms-in molecules (AIM) theory they show evidence in terms of the electron density topology for both nitrogen-sulphur and oxygen-sulphur interactions.[261]

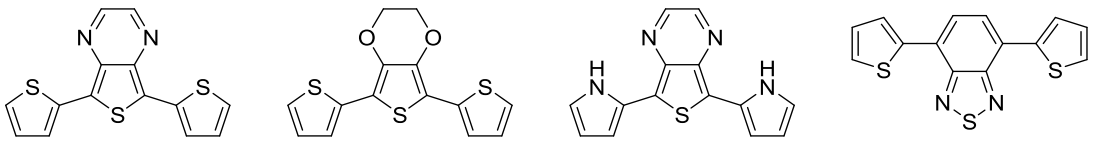

Figure 5.1 The monomers studied from Özen and co-workers.[261]

Nitrogen-sulphur interactions have been observed successively in other systems including donor-acceptor small molecules based on [1,2,5]thiadiazolo[3,4-c]pyridine and dithieno(3,2-*b*;2′,3′-*d*)silole,[265, 266] and in a set of ladderlike pyrazine polymers.[273] In these works the authors demonstrated that nitrogen-sulphur interactions are able to lock preferential geometries.

5.1.2. Computational methods

Density functional theory (DFT) has been used in this chapter to determine the properties of the organic materials studied, such as the optimal conformations and vibrations. DFT is generally used for its relative accurate capacity to describe ground-state properties with low computational cost. As a drawback, it suffers from a self-interaction error (SIE) by generally overestimating the delocalisation of the wave functions and then fostering planar conformations.[274, 275] When torsional barriers are calculated this deficiency results in a general overestimation of the energies.[276-278]

For these reasons, in this work the torsional barriers are calculated using the second-order Moller−Plesset perturbation wave function theory (MP2). This does not suffer from SIE, includes pairwise correlation and provides a better estimation of the barriers energies and relative conformation energies in simple organic molecules.[276, 279, 280] However it suffers from a basis set superposition error (BSSE) that can be limited using a large basis set, such as the cc-pVTZ basis set, that provides an accurate representation of long-range dispersion and hydrogen-bonding interactions.[281, 282] This method usually requires a very high computational cost that can be decreased using the resolution of identity (RI) MP2 method featured in the software QCHEM 4.1.2.[283, 284] This is proven to produce reliable results for relative energies as torsional potential energies, closely reproducing torsional potentials generated by highly accurate coupled cluster methods with the advantage of being significantly less expensive computationally.[285, 286] In this chapter the torsional barriers have been calculated at the RI-MP2/cc-pVTZ level of theory that generate results very close to those of the full MP2 method.[286]

5.1.3. Previous work

Jackson *et al.* performed an extensive computational study where potential interactions (including oxygen-sulphur and nitrogen-sulphur) were studied using accurate quantum-chemical wave function methods and noncovalent interaction

(NCI) analysis. The conjugated donor-acceptor polymers and small molecules selected for the study have not shown dominant oxygen-sulphur and nitrogen-sulphur interactions able to dictate preferential geometries.[287] These conclusions were mainly achieved using two different approaches: calculating the torsional potentials between the donor-acceptor moieties of the monomers and analysing the fundamental through-space interactions that occur between pairs of atoms in different molecular systems of reference. The first part of the study was performed on monomers of polymers chosen *ad hoc* from the literature. Nevertheless, all the molecular systems chosen presented the major drawback of having always potential hydrogen bonding contacts as well as non-conventional interactions. This alters the final purpose of the study. Hydrogen bonds[288, 289] are strong non-covalent interactions between a hydrogen atom in a molecule or a molecular fragment X–H, in which X is more electronegative than H, and an atom or a group of atoms in the same (or a different) molecule. They can perform important locking mechanisms when heteroatoms such as oxygen, sulphur or nitrogen are nearby. In general, their role is difficult to distinguish in the calculation of the torsional potentials where all the possible interactions are considered together. Jackson *et al.*[287] have not always considered the role of hydrogen bonding, even when it is fundamentally important in stabilising particular configurations. Furthermore, in the second part of the study, only a limited number of representative molecules were used to calculate possible contacts.

In order to explore the heteroatom interactions and have a better estimation of their role in conjugated molecular arrangements, a systematic approach to design and synthesise novel conjugated molecules was necessary. The benzo[1,2-d:4,5-d']bis(thiazole) (BBT) was chosen as a core unit in order to synthesise a series of small molecules rich in heteroatoms. Compounds **5.1**-**5.7** (Figure 5.2) were synthesised as π-extended derivatives of BBT with a range of heteroaromatic rings that were chosen as potential candidates for planarising non-covalent interactions: thiophene, thiazole, furan, benzothiophene, benzofuran, benzothiazole and benzothiaoxazole.[290]

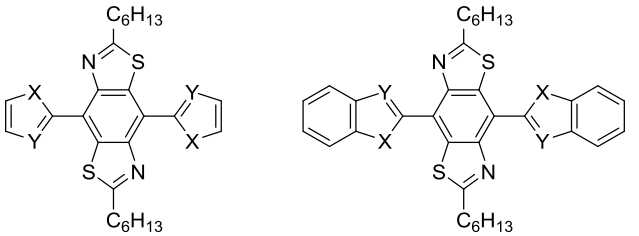

5.1 - X = O, Y = CH
5.2 - X = S, Y = CH
5.3 - X = S, Y = N

5.4 - X = O, Y = CH
5.5 - X = S, Y = CH
5.6 - X = S, Y = N
5.7 - X = O, Y = N

Figure 5.2 The seven molecules based on the BBT core **5.1-5.7**.

The BBT core was chosen due to its inherent rigidity and the presence of four heteroatoms. Non-covalent short contacts are typically observed between a wide variety of p-block elements, but very rarely between atoms if they are both from the first row of the p-block. The combination of sulphur and nitrogen atoms in the BBT unit can therefore support interactions with heteroatoms commonly found in aromatic heterocycles (*e.g.* O, N, S). Extension of the conjugated unit through the 2,6-sites has been well studied, but investigating the attachment of conjugated units at the 4,8-positions has been limited.[291-294] The latter approach provides a better template for intramolecular non-covalent contacts, resulting in extended π-systems. The substituents were chosen in order to have both potential heteroatom to heteroatom and heteroatom to hydrogen atom interactions. In this way the importance of non-traditional interactions can be isolated from common and well known hydrogen bonds. The synthesis and characterisation of the **5.1-5.7** is detailed in the PhD thesis of Gary Conboy, a former student in the Professor Peter Skabara group.[290] Single crystal X-ray structures were obtained for **5.3**, **5.4**, **5.5** and **5.7** (Figure 5.3).

The crystal structure of compound **5.4** shows a highly planar molecule with a maximum torsion angle of 4.7° between the furan ring and the benzene unit of the BBT molecule. The planar architecture could be due to the interaction of the S···O atoms (2.801 Å), but there is an alternative possibility that rigidification arises from hydrogen bonding between the C-H group of the furan ring and the N atom of the BBT unit, which are positioned perfectly for such an interaction.

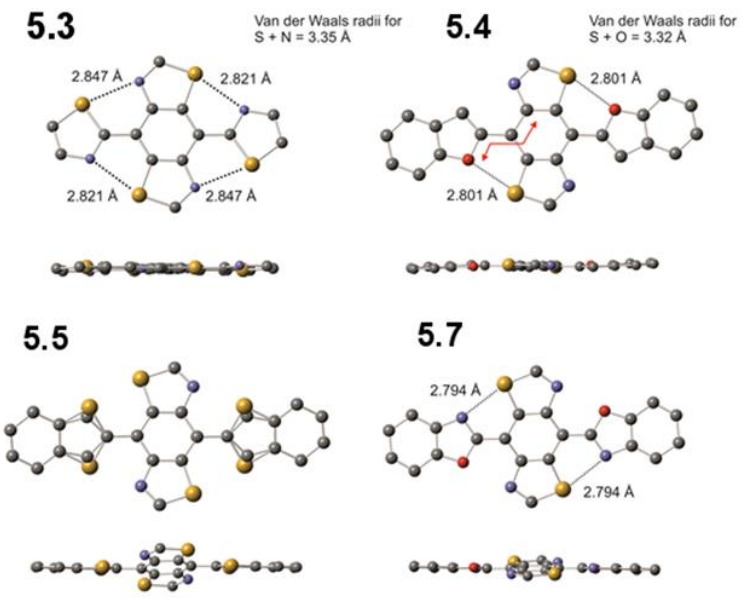

Figure 5.3 Crystal structures of **5.3**, **5.4**, **5.5** and **5.7**.[290]

However, in the thiazole analogue **5.3**, there is no opportunity for hydrogen bonding, yet the molecule is also highly planar with a maximum torsion angle of 5.1° between the thiazoles and the central benzene ring. In this case, there is only the possibility of S···N interactions and the corresponding non-covalent bond lengths are significantly shorter (0.5 Å) than the sum of the van der Waals radii for the corresponding atoms. Whilst this observation points strongly towards heteroatomic interactions dictating rigidification in the series of molecules under study, there is yet another possible reason for planarisation in these compounds – the molecules adopt a flat geometry simply due to extended conjugation and the structures observed for compounds **5.3** and **5.4** merely represent the lowest energy conformers as a function of efficient delocalisation of π electrons. In compound **5.5**, in contrast to **5.4**, the molecule is frustrated with respect to the positioning of the benzothiophene unit. There is a 72:28 probability of finding the sulfur atom of the thiophene ring adjacent to the nitrogen or sulfur atoms of the BBT unit, respectively. This is accompanied by a twisting between the benzothiophenes and the BBT benzene ring, with a maximum torsion angle of 19.5°. Considering that the only difference between compounds **5.4** and **5.5** is benzofuran *vs* benzothiophene, the variance in conformation is provided by the change in non-covalent interactions. In compound **5.5**, CH···N hydrogen bonding is off-set by the unfavourable S···S interaction in one conformer, whereas the S···N close contact in the alternative geometry is presumably deterred by steric hindrance between the C-H and S species. It is relevant to point out here that sulphur is a

significantly weaker proton acceptor than nitrogen,[295] so the argument of steric repulsion is a feasible one. Compound **5.5** therefore provides some evidence that noncovalent interactions can disrupt planarity in certain circumstances, and that a flat geometry within this series is not simply a consequence of conjugation. In compound **5.7** a planar conformation is resumed to some degree. Of the two possible non-covalent interactions, S···N or S···O, the molecule exclusively prefers short contacts between the sulphur and nitrogen atoms. However, the maximum torsion angle between the benzene unit and the benzoxazole rings observed in this molecule is 11°, which is significantly larger than that of compounds **5.3** and **5.4**. Having four intramolecular connections in these molecules (four S···N contacts in compound **5.3**; two S···O contacts plus two C-H···N hydrogen bonds in **5.4**), clearly provides a more planar molecule than two short contacts in **5.7** (recall that N···O interactions are assumed to be weak or negligible).

From these experimental conclusions, a computational study has been performed on compounds **5.1**-**5.7** to try to better understand the reasons that lead to these non-covalent interactions.

5.2. Result and discussion

5.2.1. Non-covalent interactions providing rigidification in a new class of BBT containing molecules

In order to select the best density functional method able to describe the ground state geometry properties of the seven BBT small molecules **5.1-5.7**, fifteen levels of theory combining five functionals (B3LYP, CAM-B3LYP, M06-2X, mPW1PW, wB97xD) and three basis sets (6-311G, 6-311G(d, p), Ahlrichs pVDZ) were tested for compound **5.7**. The distances, angles and torsional angles of the geometries obtained were compared with the experimental data from the crystal structure of compound **5.7** (Table 5.1-5.3 and Figure 5.4).

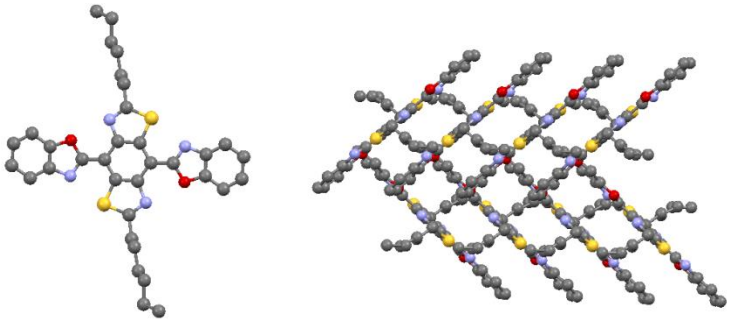

Figure 5.4 Crystal structure image of **5.7** as reported in Gary Conboy's Phd thesis, 2014.[290]

Table 5.1 Mean signed and absolute errors (MSE and MAE, Angstroms), maximal deviations (Max, Angstroms), obtained by comparing experimental and theoretical distance values.

	B3LYP			CAM-B3LYP		
	6-311G	6-311G(d, p)	Ahlrichs pVDZ	6-311G	6-311G(d, p)	Ahlrichs pVDZ
MAE	0.0345	0.0148	0.0136	0.0336	0.0175	0.0152
MSE	-0.0212	0.0073	0.0056	-0.0102	0.0165	0.0147
Max(+)	0.0155	0.0241	0.0262	0.0308	0.0420	0.0400
Min(-)	-0.0905	-0.0122	-0.0104	-0.0687	-0.0030	-0.0014

	mPW1PW			wB97xD		
	6-311G	6-311G(d, p)	Ahlrichs pVDZ	6-311G	6-311G(d, p)	Ahlrichs pVDZ
MAE	0.8894	0.0185	0.0190	0.0331	0.0159	0.0174
MSE	0.8458	0.0185	0.0190	-0.0106	0.0152	0.0170
Max(+)	2.8010	0.0314	0.0410	0.0400	0.0314	0.0319
Min(-)	-0.0717	0.0026	0.0026	-0.0699	-0.0022	-0.0013

	M06-2X		
	6-311G	6-311G(d,p)	Ahlrichs pVDZ
MAE	0.0329	0.0153	0.0157
MSE	-0.0108	0.0148	0.0157
Max(+)	0.0292	0.0292	0.0333
Min(-)	-0.0710	-0.0014	0.0003

Table 5.2 Mean signed and absolute errors (MSE and MAE, Angstroms), maximal deviations (Max, Angstroms), obtained by comparing experimental and theoretical meaning angle values.

	B3LYP			**CAM-B3LYP**		
	6-311G	6-311G(d, p)	Ahlrichs pVDZ	6-311G	6-311G(d, p)	Ahlrichs pVDZ
MAE	2.44	0.93	1.05	2.14	0.71	0.85
MSE	0.15	-0.19	-0.25	0.07	-0.22	-0.28
Max(+)	2.10	1.07	1.19	1.78	0.74	0.85
Min(-)	-3.44	-1.69	-1.89	-3.11	-1.39	-1.59

	mPW1PW			**wB97xD**		
	6-311G	6-311G(d, p)	Ahlrichs pVDZ	6-311G	6-311G(d, p)	Ahlrichs pVDZ
MAE	2.16	0.78	0.95	2.05	0.65	0.78
MSE	0.14	-0.19	-0.25	0.12	-0.16	-0.26
Max(+)	1.91	0.88	1.04	1.65	0.67	0.79
Min(-)	-3.03	-1.32	-1.60	-2.90	-1.22	-1.48

	M06-2X		
	6-311G	6-311G(d, p)	Ahlrichs pVDZ
MAE	1.99	0.58	0.68
MSE	0.14	-0.14	-0.22
Max(+)	1.63	0.54	0.69
Min(-)	-2.77	-1.07	-1.35

Table 5.3 Mean signed and absolute errors (MSE and MAE, Angstroms), maximal deviations (Max, Angstroms), obtained by comparing experimental and theoretical dihedral values.

	B3LYP			**CAM-B3LYP**		
	6-311G	6-311G(d, p)	Ahlrichs pVDZ	6-311G	6-311G(d, p)	Ahlrichs pVDZ
MAE	1.79	1.61	1.81	1.81	1.66	1.78
MSE	1.11	0.83	1.03	1.04	0.85	0.96
Max(+)	4.36	3.66	4.26	4.27	3.76	4.11
Min(-)	-0.70	-0.91	-0.84	-0.94	-0.96	-0.97

	mPW1PW			**wB97xD**		
	6-311G	6-311G(d, p)	Ahlrichs pVDZ	6-311G	6-311G(d, p)	Ahlrichs pVDZ
MAE	1.80	1.68	1.91	1.59	1.31	1.80
MSE	0.96	0.87	1.13	0.67	0.42	1.12
Max(+)	4.14	3.82	4.56	3.40	2.60	4.38
Min(-)	-0.83	-0.96	-0.84	-0.91	-1.00	-0.59

	M06-2X		
	6-311G	6-311G(d, p)	Ahlrichs pVDZ
MAE	0.87	0.71	0.45
MSE	0.48	0.30	-0.05
Max(+)	1.99	1.51	0.59
Min(-)	-0.59	-0.56	-0.67

The M06-2X/6-311G(d, p) level of theory was chosen to compute the properties of compounds **5.1-5.7** as it showed the smallest mean signed and absolute errors. When not stated the following calculations have been performed at this level of theory and

by replacing the alkyl chains with methyl groups. This is a general practice used in order to significantly reduce the computational cost of the calculations without compromising the general electronic structure of the compounds analysed.

The total energies of the BBT core and of compounds **5.1-5.7** in the singlet and triplet states were calculated in order to verify the possible biradical or "biradicaloid" character of the compounds, following the definition of J. Wirz and co-authors.[296] This states that a biradical is a molecule whose lowest singlet and triplet state energies do not differ by more than 10 kJ/mol and a "biradicaloid" would extend this range to 100 kJ/mol. The singlet-triplet energy differences in the series of the seven molecules and for the BBT core resulted in values well beyond the 100 kJ/mol limit of the "biradicaloid" character (Table 5.4), indicating a good stabilisation of the singlet ground state.

Table 5.4 Singlet and triplet energies and singlet-triplet energy differences computed for the BBT core and the **5.1-5.7** molecules calculated at the M06-2X/6-311G(d, p) level of theory.

Energy (kJ/mol)	Singlet	Triplet	Difference
BBT	−3391350	−3391040	311
5.1	−4592838	−4592628	210
5.2	−6288771	−6288551	220
5.3	−6373076	−6372857	220
5.4	−5399516	−5399315	200
5.5	−7095439	−7095224	215
5.6	−7179754	−7179533	221
5.7	−5483794	−5483567	227

The HOMO and the LUMO wave functions of the seven BBT derivatives show a complete and similar delocalisation of the electronic clouds in all the molecules (Figure 5.5). This excludes the efficient delocalisation of π electrons as the major and only reason for the degree of planarity observed experimentally by X-ray crystallography. In fact, despite the large torsional twist of the thiophene/benzothiophene units, compounds **5.1** and **5.4** show the same highly delocalised nature as the planar compounds. The HOMO and LUMO energies and associated gaps are summarised and compared with the experimentally obtained values (electrochemical *via* cyclic voltammetry and optical *via* UV-vis absorption)[290] in Table 5.5 and Figure 5.6. Note that materials with a twisted backbone that contain electron rich and poor units tend to exhibit donor-acceptor behaviour.[18]

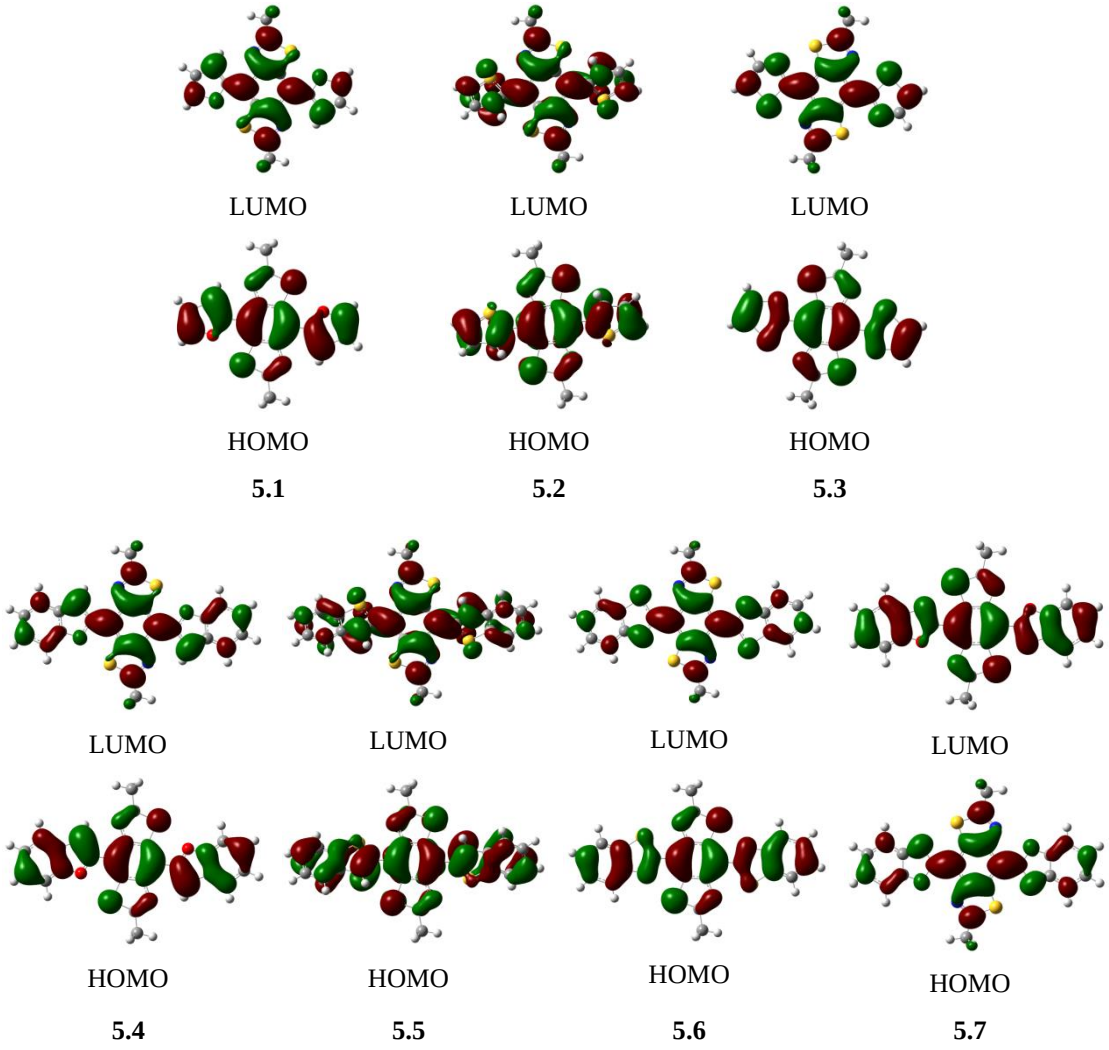

Figure 5.5 HOMO and LUMO wave function of the seven BBT derivatives **5.1**-**5.7** (isosurface 0.02) calculated at the M06-2X/6-311G(d, p) level of theory.

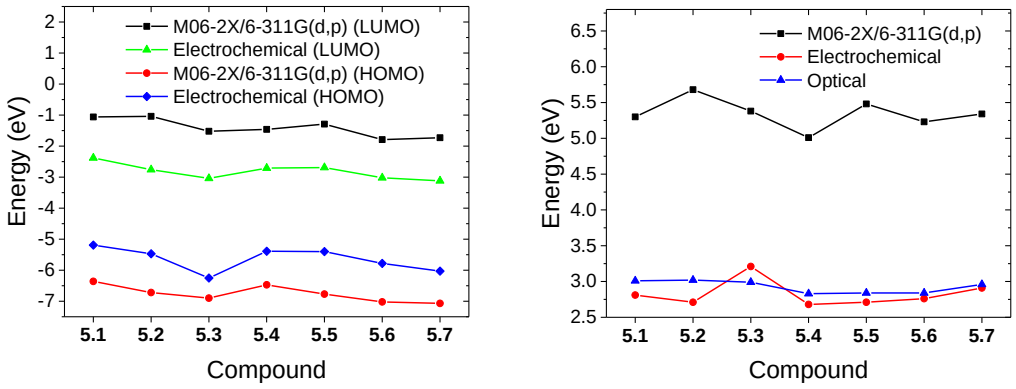

Figure 5.6 Electrochemical and calculated (at the M06-2X/6-311G(d, p) level of theory) HOMO and LUMO energies for **5.1**-**5.7** (left). Electrochemical, optical and calculated (at the M06-2X/6-311G(d, p) level of theory) HOMO-LUMO gap energies for **5.1**-**5.7** (right).

Table 5.5 HOMO-LUMO electrochemical, optical, theoretical (at the M06-2X/6-311G(d, p) level of theory) gaps and optical, theoretical HOMO and LUMO values for **5.1**-**5.7**.

	5.1	**5.2**	**5.3**	**5.4**	**5.5**	**5.6**	**5.7**
HOMO-LUMO GAP (eV) (Electrochemical)	2.81	2.71	3.21	2.68	2.71	2.76	2.91
HOMO-LUMO GAP (eV) (Optical)	3.01	3.02	2.99	2.83	2.84	2.84	2.96
HOMO-LUMO GAP (eV) (M06-2X/6-311G)**	5.30	5.68	5.38	5.01	5.48	5.23	5.34
LUMO (eV) (Electrochemical)	-2.38	-2.76	-3.04	-2.71	-2.69	-3.02	-3.12
HOMO (eV) (Electrochemical)	-5.19	-5.47	-6.25	-5.39	-5.4	-5.78	-6.03
LUMO (eV) (M06-2X/6-311G)**	-1.06	-1.04	-1.52	-1.46	-1.29	-1.79	-1.73
HOMO (eV) (M06-2X/6-311G)**	-6.36	-6.72	-6.90	-6.47	-6.77	-7.02	-7.07

5.2.2. Non-binding interactions

To further investigate the reason that leads to the complete planar rigidification in compounds **5.1**, **5.3**, **5.4**, **5.6** and **5.7**, fragments of the BBT derivatives **5.1s-5.7s** (obtained by replacing one heterocyclic substituent of the BBT core with a hydrogen atom and limiting the side-chains to methyl groups), were used to calculate the torsional potentials between the BBT core and the heterocyclic substituents, in a similar approach to that used by Ratner *et al.*.[287] The dihedral angle between the BBT core and the heterocyclic substituent was fixed (from 0° to 180°, at 10° intervals) and a geometry optimisation on all remaining degrees of freedom was performed using the M06- 2X/6-311G(p, d) level of theory. These geometries were then used as the inputs for single-point energy calculations at the RI-MP2/cc-pVTZ[286] level of theory using the QCHEM 4.1.2 package.[283] Furthermore, in order to analyse the electrostatic influence present in these systems the atomic partial charges of **5.1s-5.7s** at the 0 and 180°configurations were calculated using the Natural Population Analysis at the RI-MP2/cc-pVTZ level of theory (Figure 5.7).

These values will be discussed later together with the interaction distances between heteroatoms of interest.

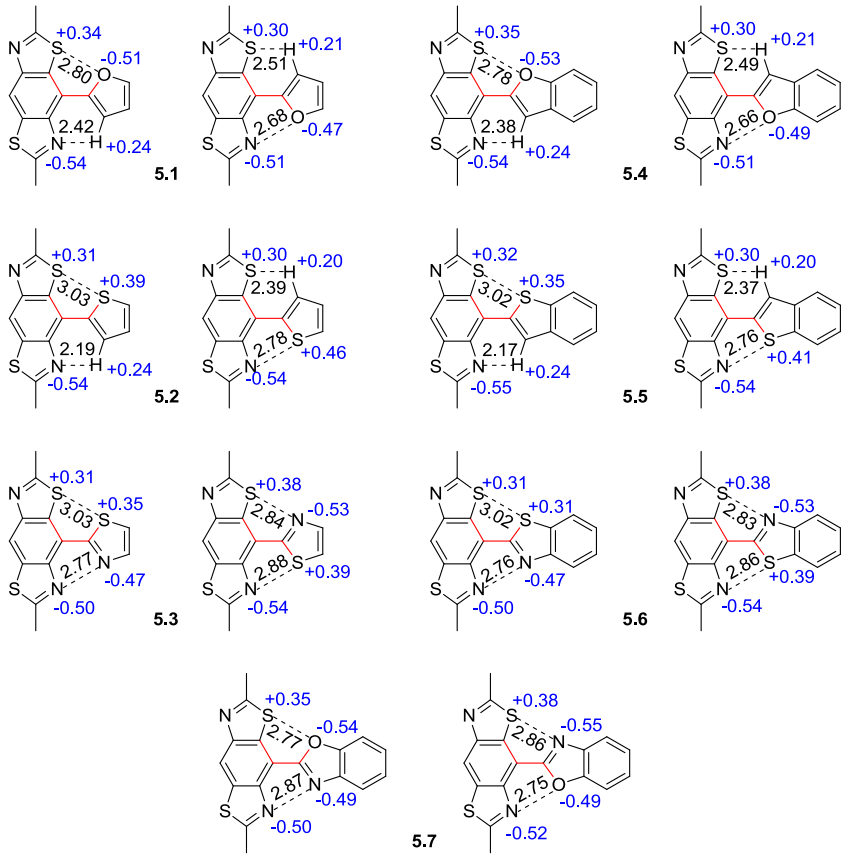

Figure 5.7 Natural Bond Orbital partial charges (blue) and selected distances (black, Å) for the fragments **5.1s-5.7s** in the 0° and 180° configuration, calculated at the RI-MP2/cc-pVTZ level of theory.

The potential energy surfaces (PESs) obtained at the RI-MP2/cc-pVTZ level of theory are presented in Figure 5.8, which suggests planar geometries for **5.1s**, **5.3s**, **5.4s**, **5.6s**, **5.7s** and twisted geometries for **5.2s** and **5.5s**, in agreement with the crystallographic data.[290]

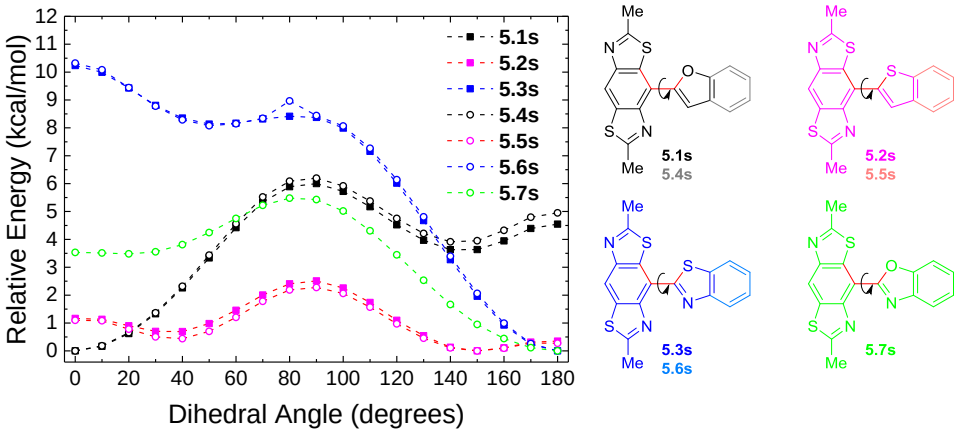

Figure 5.8 Torsional potential surfaces for the fragments **5.1s-5.7s** calculated at the RI-MP2/cc-pVTZ levels of theory (left). Rotation occurs around the inter-ring C−C bond marked in red, starting from the conformation shown (0°) (right). The colour code of the compounds on the right corresponds in the graph. Benzoheterocycles are represented with empty circles in the graph.

The PESs of **5.2s** and **5.5s** show two energy minima that differ by only 0.4-0.7 kcal/mol at 150° (S···HC 2.62-2.44 Å, N···S 2.95-2.96 Å) and 40° (N···HC 2.58-2.59 Å, S···S 3.27 Å). This energy, similar to *kT* at room temperature (*ca.* 0.6 kcal/mol), is fully consistent with the 72:28 probability of finding the sulphur atom of the thiophene (or benzothiophene) ring adjacent to the nitrogen or sulphur atoms of the BBT unit, as observed experimentally in the crystal structure of **5.5**.[287] This is also supported by the partial charges of the molecules in the 0 and 180° configurations. On one hand the 0° configuration shows the sulphur atoms with no polarisation and a constructive interaction between the BBT nitrogen (−0.55) and the thiophene (or benzothiophene) hydrogen (+0.24). On the other hand, at the 180° configuration, there is no electrostatic attraction between the BBT and thiophene (or benzothiophene) sulphurs; there is only a constructive electrostatic interaction between the BBT nitrogen that bears a negative charge of −0.54 and the thiophene (or benzothiophene) sulphur that bears a positive charge +0.46 (+0.41).

By replacing the thiophenyl (benzothiophenyl) substituent with the furanyl (benzofuranyl) unit in **5.1**s (and **5.4s**), the minima in the PESs is at the 0° geometry where the S···O (2.78-2.80 Å) and N···HC (2.38-2.42 Å) interactions are stronger. In contrast to **5.2s** and **5.5s**, moving to the opposite geometry at an angle of 180° has a relatively large torsional barrier (5.5-6.0 kcal/mol) meaning that the N···O (2.66-2.68 Å) and S···HC (2.49-2.51 Å) interactions are highly unfavourable in this configuration. These interactions become less repulsive at the 140° geometry (second minimum) where the S···HC (2.92-2.93 Å) and N···O distances (2.88-2.89 Å) allow positive attractive interactions. This is in agreement with the electrostatic attraction at the 0° configuration between the sulphur (+0.34) and the oxygen (−0.52) and between the nitrogen (−0.54) and the hydrogen (+0.24). However at the 180° configuration there are electrostatic repulsive interactions between both sulphur-hydrogen and nitrogen-oxygen that destabilises this geometry.

In compounds **5.3s** and **5.6s** the sum of the repulsive N···N (2.76-2.77 Å) and S···S (3.02-3.03 Å) interactions in the planar 0° configuration leads to the largest torsional barriers in this series of molecules with maxima of 10.2 and 13.3 kcal/mol, respectively. On the other hand the absolute minimum is present at the 180°

geometry, showing that the S···N and N···S (2.83-2.88 Å) non-covalent interactions are important and that they force the molecule into this conformation. The activation energy necessary to bring the molecule into the other stable configuration (50° torsion angle) is 8.4-9.0 kcal/mol. Again this is supported with the NBO charges that show in the 0° configuration a repulsive interaction between the sulphur-sulphur and nitrogen-nitrogen couples. At the 180° configuration the electrostatic interactions become constructive with sulphurs bearing a +0.38 positive charge and nitrogen a −0.53 negative charge.

For structure **5.7s**, there is a lowest energy minimum when the planar molecule adopts a short contact between the sulphur of the BBT unit and the nitrogen atom of the benzoxazole ring. The second energy minimum, where the BBT sulphur aligns with the oxygen of the benzoxazole, is 3.1-3.5 kcal/mol higher in energy. The lowest energy conformation is in perfect agreement with the geometry observed in the molecular structure of **5.7** determined by single crystal X-ray diffraction studies.[290]

In this case the charge analysis seems not to be able to agree with the experimental data as it shows repulsion between the nitrogen-nitrogen and oxygen-nitrogen couples at the 0° and 180 configurations, respectively. At the same time is shows attractive interactions between the sulphur-oxygen and sulphur-nitrogen at the 0° and 180 configurations, respectively. Nevertheless the sulphur-oxygen contact is shorter by 0.1 Å in the 180º configuration, likely meaning a slightly stronger interaction.

5.3. Analysis of fundamental through-space interactions

The fundamental interactions observed along the conjugated backbone of the seven BBT derivatives were explored by examining the effect of atom-to-atom non-bonding interactions using ten representative molecules (**5.8-5.17**, Figure 5.9). The benzothiazole unit (**5.13**) has been chosen to represent the BBT core, while the thiazole, oxazole, thiophene, furan, benzoxazole and benzofuran units are representative of the heterocycle substituents in compounds **5.1**-**5.7**. The diketopyrrolopyrrole (DPP) moiety (**5.17**) was introduced to the study because it was employed as a copolymer unit in a series of polymers recently synthesised by Gary Conboy (along with compounds **5.1** and **5.2**).[290] Finally pyrrole (**5.12**) was included in order to broaden the range of possible interactions in the series of mono-heterocycles.

The goal of these studies is to further rationalise, and possibly energetically quantify these non-covalent interactions, creating the required chemical insight necessary to provide general synthetic conformational control in this class of systems.

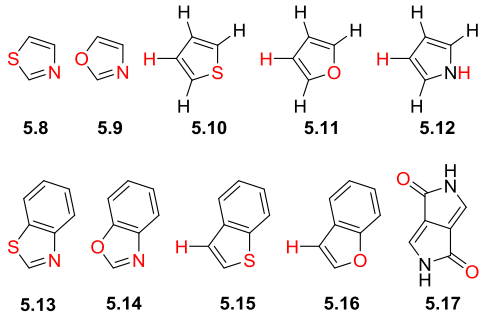

Figure 5.9 The ten representative molecules (**5.8**-**5.17**). The atoms of interest to this study are highlighted in red

The ten representative molecules were initially optimized at the M06-2X/6-311++G(d, p) level of theory. Then, by selecting them in pairs, the binding interactions were calculated: two molecules of interest were made to lie in the same plane, with the atoms of interest facing each other, and their separation distance was varied. At each chosen separation distance single-point energy calculations with Boys-Bernardi counterpoise correction[297] were performed at the MP2/aug-cc-pVTZ level of theory. The large aug-cc-pVTZ basis set was used in order to attempt to reduce basis set superposition error (BSSE) at small intermolecular distances, which will result in an overbinding of the two molecules. Another correction made in this direction is the Boys-Bernardi counterpoise correction. In addition to the standard single-point calculation, E_{AB}^{AB}, two additional single-point calculations were performed: one with the molecule A isolated in a vacuum with its basis functions, as well as the basis functions of "ghost" atoms of molecule B, E_{A}^{AB}, and vice versa, E_{B}^{AB}. Then the counterpoise-corrected interaction energy was obtained as:

$$\Delta E_{int}^{CP}(AB) = E_{AB}^{AB} - E_{A}^{AB} - E_{B}^{AB} \qquad \text{Equation 5.1}$$

As such, the parametrised spin-component-scaled (SCS)-MP2/aug-cc-pVTZ[298] and optimised spin-component-scaled SCS(MI)-MP2/aug-cc-pVTZ[299] single point energies were calculated. These methods were reasoned to provide more reliable intermolecular interaction energies when compared with the classic MP2 method.[281, 299, 300] In MP2 methods, two perturbative components, the same spin (c_s) and the

opposite spin (c_o) terms are present. It was proven that scaling down to *ca.* 1.6 the sum of the perturbative terms (that is equal to 2 in the classic MP2 method) provides a correction to the general over-estimation of the intermolecular interaction energies.[281, 287, 299, 300] In the SCS-MP2 method c_s has a value of 0.33 and c_o of 1.2, whereas in the SCS(MI) variant these are 1.29 and 0.4, respectively.[299]

For each interaction, the energies were plotted as a function of intermolecular separation and fitted (*e.g.* Figure 5.10) with the Morse potential energy function:

$$y = A\left(1 - e^{-b(x-x_0)}\right)^2 \qquad \text{Equation 5.2}$$

In Equation 5.2, x is the distance between the atoms, x_0 is the equilibrium distance, A is the well depth (defined relative to the dissociated atoms) and b controls the "width" of the potential (the smaller b is, the larger the well). The Morse potential is a combination of a short-range repulsion term and a long-range attractive term. The binding energy for each interaction is determined by the difference of the energies at the bottom of the potential well, and at a separation distance where the molecules are no longer interacting.

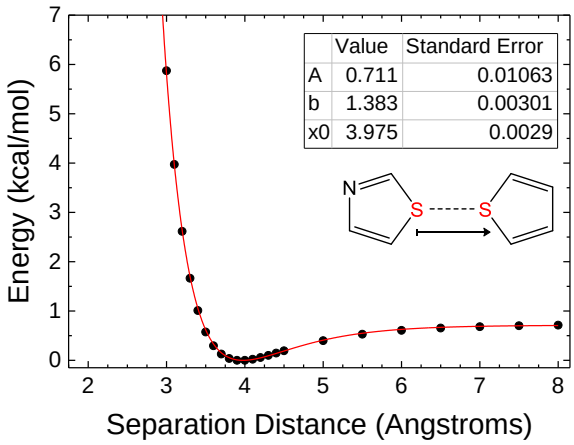

Figure 5.10 Binding potentials for S-S (thiazole-thiophene) calculated at MP2/aug-cc-pVTZ level of theory (black dots) and the fitting curve obtained with the Morse potential energy function (red curve). The atoms that interact are marked in red and the coordinate of intermolecular separation is indicated with the black arrow.

The data obtained are summarised in Figure 5.11 and the average energies of the same kinds of interaction are reported in Table 5.6. For complete comparison, all the three calculated energies are reported (the complete table with the energies and equilibrium distance of each interaction are reported in the appendices, Table 7.19,

Table 7.20 and Table 7.21) but for the following discussion only the most reliable energies, calculated at the SCS(MI)-MP2/aug-cc-pVTZ level of theory, are considered.[281, 300]

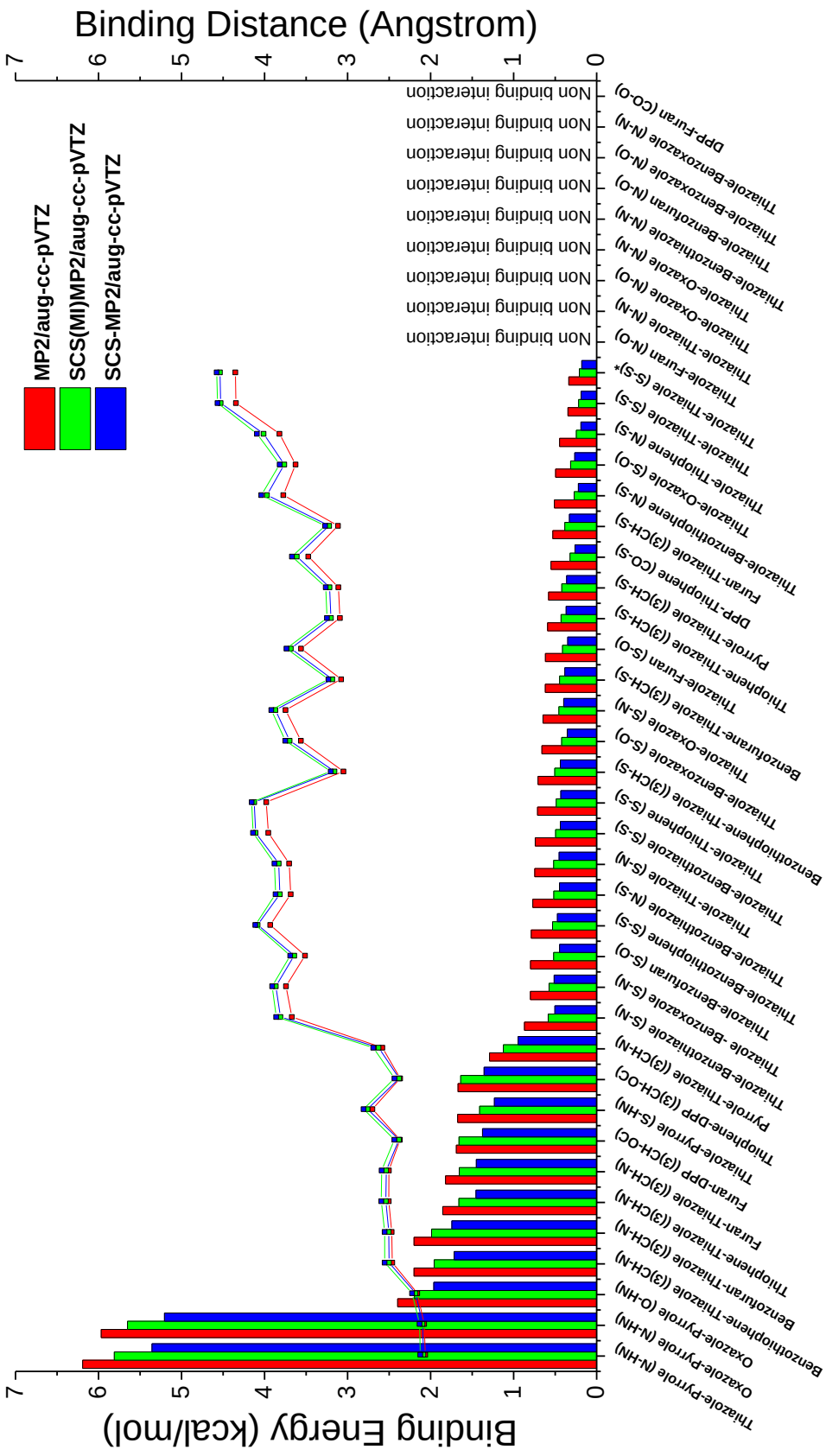

Figure 5.11 Binding potential energies (kcal/mol, bars) and relative interaction distances (Angstrom, squares connected with black lines) for selected combination of the ten representative molecules. Calculated at the MP2/aug-cc-pVTZ (red), SCS-MP2/aug-cc-pVTZ (green) and SCS(MI)-MP2/aug-cc-pVTZ (blu) levels of theory. * Inverse configuration.

Table 5.6 Average binding potential energies (*kT*) for the main interactions calculated at the MP2/aug-cc-pVTZ, SCS-MP2/aug-cc-pVTZ and SCS(MI)-MP2/aug-cc-pVTZ levels of theory. *nb* = non-binding interaction

Interaction	Binding potential energies (*kT*)		
	MP2/aug-cc-pVTZ	SCS-MP2/aug-cc-pVTZ	SCS(MI)-MP2/aug-cc-pVTZ
N-HN	10.25	8.91	9.66
O-HN	4.04	3.31	3.70
(3)CH-N	3.16	2.47	2.83
(3)CH-OC	2.84	2.31	2.78
S-HN	2.82	2.08	2.38
S-N	1.15	0.66	0.76
S-O	1.08	0.60	0.70
S-S	0.99	0.58	0.65
(3)CH-S	1.02	0.63	0.74
CO-S	0.93	0.44	0.54
N-O	*nb*	*nb*	*nb*
N-N [E]	*nb*	*nb*	*nb*
CO-O	*nb*	*nb*	*nb*

Interactions involving an acidic hydrogen atom, *e.g.* N···H, O···H and S···H, are, as expected, dominant over alternative interactions. The pyrrolic hydrogen gives the strongest interaction when interacting with nitrogen, oxygen and sulphur. This ranged from a maximum of 5.8 kcal/mol (9.8 *kT*) for N···HN in the thiazole-pyrrole system at a distance of 2.1 Å, to 2.2 kcal/mol (3.7 *kT*) for O···HN in the oxazole-pyrrole system at a distance of 2.2 Å, with a minimum of 1.4 kcal/mol (2.4 *kT*) for S···HN in the thiazole-pyrrole system at a distance of 2.8 Å. These are classic interactions and are so strong due to the stronger acidity (in the series) of the pyrrolic hydrogen at the N-H position (pKa = 17.5); the following trend was observed, N···HN >> O···HN > S···HN. It is generally accepted that hydrogen interactions depend on the electronegativity and on the dimension/polarizability of the interacting atom.[301]

Lower in energy are the hydrogen interactions between the hydrogen bonded at the 3-position [$^{(3)}$CH] in thiophene, furan, pyrrole, benzofuran and benzothiophene with either nitrogen, oxygen and sulphur of the thiophene, furan, thiazole, oxazole, benzofuran, benzothiazole, benzoxazole, benzothiophene and DPP units. In this case, due principally to the lower acidity of the $^{(3)}$CH hydrogen, the values of these interactions range from 1.9 kcal/mol (3.3 kT) for the benzothiophene-thiazole $^{(3)}$CH···N interaction to 0.4 kcal (0.7 kT) for the furan-thiazole $^{(3)}$CH···S interaction. The trend is $^{(3)}$CH···N > $^{(3)}$CH···OC >> $^{(3)}$CH···S at distances that range from 2.4-2.6

Å for the $^{(3)}$CH···N and $^{(3)}$CH···OC interactions to a maximum of 3.2 Å for the $^{(3)}$CH···S ones. N···N, N···O and CO···S contacts do not show any bound state. They interactions are limited to a repulsion at close distances, generally for values smaller than 3-4 Å (deduced by a purely exponential decay of the interaction energy). Thus they should not be a motive for any conformational stabilisation in donor−acceptor type units.

Contrarily, the non-traditional S···N, S···O and S···S contacts do show binding interactions. The maximum binging energy is 0.58 kcal/mol (1.0 kT) at 3.8 Å for the S···N interaction in the thiazole-benzothiazole system. Considering all similar interactions and averaging them, the trend is S···N > S···O > S···S for these molecular systems in contrast with previous results.[287] These energies, that can partially be attributed to the *d* orbitals of sulfur,[302] are smaller than 2 *kT*, which is the lower limit generally considered for conformational control.[287] Nevertheless they are able to form bound states, although such states are very weak in agreement with previous studies.[287, 303]

In the crystal structures these weak (<0.6 kcal/mol) non-bonding interactions may be of greater importance, but in a thermally fluctuating environment at room temperature, as is always the case for small molecules and polymers in organic electronic devices, these interactions are likely insignificant if considered individually. However in molecular systems, where two or more of these interactions can operate together, they can play a crucial cooperative role in rigidifying a particular conformation. This is supported from the PES and the torsional potentials discussed in the previous section. In fact, a combination of these non-covalent interactions, with the addition of strong electrostatic attractions, can lead to rigidification in predictable conformations.

5.4. Conclusions

In summary, the experimental and computational data obtained for seven BBT derivatives (**5.1**-**5.7**) corroborates well with each other in the conclusion that planar rigidification is dictated by interactions between specific heteroatoms in these molecular systems. Since the calculations were performed in the gas phase and the results correlate very closely with the crystal structures, one can assume that packing forces have little effect on the planarization within this series of BBT molecules.

From the PESs and the partial charges calculated it can be inferred that the strength of the interactions is of the order:

$$S\cdots N > S\cdots O >> S\cdots S \qquad \text{Equation 5.3}$$

This is on the basis of S···N dominating over S···O in the conformation of compound **5.7**. Interpreting the role of H bonding is still elusive, since such interactions can still have a role to play in compounds **5.1**, **5.3**, **5.4**, **5.6**. However, the influential character of non-covalent heteroatom interactions on the conformations of the BBT series of compounds is unambiguous.

The analysis of the fundamental through-space interactions confirms further that the hydrogen non-covalent interactions are the strongest in this series of BBT molecules with the trends:

$$N\cdots HN >> O\cdots HN > S\cdots HN \qquad \text{Equation 5.4}$$

$$^{(3)}CH\cdots N > {}^{(3)}CH\cdots OC >> {}^{(3)}CH\cdots S \qquad \text{Equation 5.5}$$

The energy of traditionally reported hydrogen bonds can range from 38 to few kcal/mol,[304] with large differences even between hydrogen bonds of the same type.[305] The hydrogen binding energies calculated for the model molecules studied (between 0.4 and 5.8 kcal/mol) can range from weak to significant.

Non-traditional S···N, S···O and S···S contacts showed binding interactions in agreement with the results obtained through the PESs and partial charge data, with a trend:

$$S\cdots N > S\cdots O > S\cdots S \qquad \text{Equation 5.6}$$

They show weak, non-influential binding tendencies when consider singularly with average binding energies of 0.45, 0.41 and 0.38 kcal/mol, respectively. However, a simultaneous cooperation of two or more of these weak interactions can lead to the rigidification of the BBT based molecular systems, as confirmed from the torsional studies.The other contacts studied (N···O, N···N, CO···O) do not show any binding interactions and they have strong repulsion up to 4-5 Å.Finally, the energies of the

binding interactions at the equilibrium distances are reported in order to provide a general guide for predict molecular preferential geometries.

Part of this chapter has been included in a peer reviewed paper where the role of non-covalent heteroatom interactions have been explored extensively from different points of view.[306]

5.5. Future work

The role of non-covalent interactions to dictate particular molecular conformations can be explored further. The bond orders, the electrostatic interactions, and the role of dispersion (*e.g.* electron correlation) can be measured for these interactions. The π-bond order between the conjugated rings can be measured in order to understand if one effect of the heteroatoms is to alter the strength of the partial double bonds between adjacent rings. The heterocycle substituents can be replaced with non-conjugated rings (*e.g.* THF instead of furane) and the length of the C-C bonds between adjacent rings, as well as the shape of the orbitals involved in the interactions, analysed. Furthermore it would be helpful to measure three-dimensionally the binding potential curves in order to further understand the origin of these non-traditional interactions.

General conclusions

The general theme of this thesis is the experimental and theoretical exploration of light-emissive compounds and their properties, with the common goal of employing such materials in various functioning emissive devices. Such devices include hybrid organic/inorganic LEDs, that combine the flexibility of organic materials with the high performance of blue inorganic LEDs, and OLEDs, where organic materials can be deposited either using vacuum or solution processing to provide emissive devices that employ a variety of mechanisms to achieve light output. The results presented above show that this was achieved to a greater or lesser extent across the four chapters of results that have been presented.

In **chapter 2**, five new bBT emissive derivatives (compounds **2.1**-**2.5**) have been synthesised and characterised. They are able to adsorb blue light in the blue region (430-463 nm) and re-emit in the yellow region of the electromagnetic spectrum (530-604 nm). In particular, compound **2.3** has been successfully employed as a co-emitting down-converting material in hybrid white LEDs. The combination of the partially transmitted blue light emitted from a commercial inorganic blue LED and the yellow-orange light re-emitted from encapsulated compound **2.3** in an inert polymer matrix produced white light with different colour tonalities. However, the numerous variables involved in the fabrication of these hybrid devices (*e.g.* deposition method, curing process, morphology of the films) did not allow precise prediction of the colour properties of the white light in respect to the concentration of the down-converting material.

In **chapter 3**, five new emissive esters bases on the benzothiadiazole core (compounds **3.1**-**3.5**) were synthesised and characterised. Compound **3.3** was successfully employed as a single emitting layer for the fabrication of white OLED devices. The white emission was proven to be generated by the combination of the exciton fluorescence/electromer emission of compound **3.3** and of the exciplex/electroplex emission at the heterojunction between compound **3.3** and the hole transporting material **TPD.** The devices showed excellent colour quality with C.I.E. 1931 coordinates in the range (0.34, 0.40) to (0.42, 0.45) and a colour temperature in the range of 4800 - 3800K.

In **chapter 4**, the possibility of using MOF and POP architectures in order to decrease the emission collisional quenching caused by solid state aggregation was explored. Fluorophores based on the BT core have been included in well-ordered 3-dimensional systems where aggregation is restricted by rigid bonds. Two new MOFs (**MOF-4.1.A** and **MOF-4.1.B**) and four new POPs (**4.12**, **4.13**, **4.15** and **4.16**) have been synthesised and characterised using different techniques. In the MOFs, the regularity of the BT containing emissive linker without significant interactions between close BT units was confirmed by X-ray diffraction. Additionally, the regularity and the presence of pores in POPs were confirmed through study of their gas sorption isotherms. These preliminary studies confirmed the possible implementation of these materials in light emitting devices, though it was clear that solubility of the final network material was an issue. As such, new iterations of these materials should carefully consider processing solvents to promote their applicability.

In **chapter 5**, non-covalent heteroatom interactions and their role in dictating conformation and planarity in a series of BBT based donor-acceptor small molecules was explored by theoretical methods. Experimental data, together with calculated potential energy surfaces and binding energies, corroborated well with each other in the conclusion that planar rigidification is dictated by interactions between specific heteroatoms in these molecular systems. The analysis of the theoretical data provides general trends for using non-covalent heteroatom interactions to design organic semiconductor materials. For example, hydrogen non-covalent interactions are the strongest in this series of BBT molecules with the trends: N···HN >> O···HN > S···HN and $^{(3)}$CH···N > $^{(3)}$CH···OC >> $^{(3)}$CH···S. The hydrogen binding energies calculated for the model molecules studied (between 5.8 and 0.4 kcal/mol) can be considered of medium to weak entity when compared with similar hydrogen interactions. On the other hand, the non-traditional contacts present in this series of BBT molecules showed binding interactions with a trend: S···N > S···O > S···S. These are weak, non-influential binding tendencies when consider singularly with average binding energies of 0.45, 0.41 and 0.38 kcal/mol, respectively. However, a simultaneous cooperation of two or more of these weak interactions can lead to the rigidification of the BBT based molecular systems, as confirmed from the torsional and experimental studies (X-ray diffraction). While this chapter is distinctly more fundamental than others within this thesis, the results detailed within provide a guide

in the design of organic semiconductor for example as materials for emissive applications.

Overall, this work highlights the variety of materials and methods available for achieving white light emission, ranging from organic down-converter molecules suitable for hybrid LED applications (chapter 2), to a design strategy for constructing organic semiconductors (chapter 5). This strategy is evident throughout chapter 3 where the speculated planar structure of compounds **3.1**, **3.2**, **3.4** and **3.5** indicated that they were unsuitable for light emission (due to S···N, N···H and O···H interactions), while the twisted structure of compound **3.3** provided a material more suitable for light emission. As such, one aspect of future work is the role of non-covalent interactions to dictate particular molecular conformations with a view to providing improved molecular materials for light emission. Further studies should include measurement of the bond order, electrostatic interactions and the role of dispersion. Additionally, it is clear from the results of **chapters 2** and **3** that further investigation of device architecture is important to improve device performance through improved reproducibility (**chapter 2**) and enhanced efficiency (**chapter 3**). This can be done through selection of different processing techniques, including blade-coating, or employment of alternative layers within the device architecture. In **chapter 3**, design and synthesis of alternative emissive or charge transport layers would provide a means to systematically optimise the device architecture to improve device efficiency. Finally, in each of experimental chapters, device optimisation was limited by solubility of the organic material. Adjusting molecular structures to incorporate solubilising groups for device processing is key, and would likely improve the networked materials disclosed in **chapter 4** for example.

Chapter 6. Experimental

All reactions were performed using vacuum Schlenk lines, in an inert atmosphere of nitrogen or argon. Dry solvents were obtained from a solvent purification system (SPS 400 from Innovative Technologies) using alumina as the drying agent.

n-Butyllithium and lithium diisopropylamide (LDA) solutions were purchased from Sigma Aldrich and titrated either against (+)-menthol (with 2,2-bipyridyl as an indicator) or against diphenylacetic acid before use.

Tetrakis(triphenylphosphine)palladium(0) was synthesised prior to use and stored under Ar. Unless otherwise stated all the other reagents were purchased from Sigma Aldrich or Alfa Aesar and used without further purification.

Microwave syntheses were conducted using a Biotage Initiator Classic microwave heating apparatus. Commercial TLC plates (Silica gel 60 F254) were used for thin-layer chromatography and column chromatography was performed on silica gel Zeoprep 60 Hyd (40- 63 μm mesh). Solvents were removed using a rotary evaporator (vacuum supplied by low vacuum pump) and, when necessary, a high vacuum pump was used to remove residual volatiles. Distillation of high boiling liquids was performed on a Kugelrohr Z24 with a high vacuum pump.

^{1}H and ^{13}C NMR spectra were recorded on a Bruker Avance DPX400 or on a Bruker AV400 apparatus at 400.13 and 100.6 MHz, respectively, or on a Bruker DRX500 apparatus at 500.13 and 125.76 MHz, respectively. ^{1}H and ^{13}C NMR chemical shifts are reported as δ values in ppm relative to the deuterated solvents used.[307] Data are presented as follows: chemical shift, integration, multiplicity (s = singlet, d = doublet, t = triplet, q = quartet, m = multiplet), and coupling constant(s) (J) are in Hz. Multiplets are reported over the range (in ppm) they appeared.

MS MALDI-TOF spectra were run on a Shimadzu Axima-CFR spectrometer (mass range 1-150000 Da). The high resolution mass measurements were performed on the Thermo Scientific LTQ ORBITRAP XL instrument, using the nano-electrospray ionisation (nano-ESI) technique. Thermogravimetric analyses (TGA) were performed using a Perkin-Elmer Thermogravimetric Analyser TGA7 under a constant flow of Argon (20 mL/min). The temperature was raised to 50 °C followed by an isothermal period of 5 minutes. The temperature was raised again at a rate of 10 °C/min until the desired temperature, at which point, the material was left for an isothermal period of 30 minutes. The percentage weight loss over time was recorded at this temperature and the data was processed using the Pyris Series Software. Melting points were taken using a Stuart Scientific instrument SMP1. Differential

Scanning Calorimetry was conducted on a TA Instruments DSC QC1000 with a RC-90 refrigerated cooling unit attached. The calibration was conducted using Indium (melt temperature 156.42°C, ΔH_f 28.42 J/g). The test procedure used was a standard Heat-Cool- Reheat, which allows the removal of thermal history on the first heat allowing examination of any thermal processes on the cooling and second heat scan. The temperature range was from -50 °C to 300 °C at 10 °C/min unless otherwise stated.

The electronic absorption spectra in the UV-Vis-NIR region were performed in solution using a Shimadzu UV 2700 spectrometer. The samples spectra were recorded against a white spectrum in quartz cuvettes with 0.1 cm path length. Luminescence emission spectra were recorded on a Perkin-Elmer LS45, on a Jasco FP-6500 or on an Edinburgh Instruments FLS980 spectrometer, either in solution at 77K or at room temperature in quartz cuvettes (path length 10 mm). Alternatively spectra were recorded as thin films prepared by thermovacuum deposition onto clean quartz substrates or spin coating *ca.* 2M solution of the required compound onto clean quartz slices (10 × 10 × 1 mm). Luminescence decay curves of thin films (prepared by thermovacuum deposition onto clean quartz substrates or spin coating ca. 2M solution of the required compound onto clean quartz slices, 10 × 10 × 1 mm) were recorded with an Edinburgh Instruments FLS980 spectrometer using a low repetition rate μF920H Xenon Flashlamp as the excitation source. The emission was measured twice: immediately after excitation and with a delay after the pulse was turned off (the delay time was set to be ca. 30 μs). Absolute photoluminescence quantum yield measurements were measured according to the method of de Mello,[308] by using a calibrated integrating sphere attached to a USB 2000 spectrometer and Gooch & Housego spectrometer. The excitation light was chosen from a Quartz Tungsten Halogen lamp by using a Gooch & Housego spectrometer and the emission light was collected by Ocean optics USB 2000 spectrometer. Measurements were performed in air.

Cyclic voltammetry (CV) measurements were performed on a CH Instruments 660A electrochemical workstation with *iR* compensation at a scan rate of 0.1 V s^{-1} using anhydrous dichloromethane as the solvent. The electrodes were glassy carbon, platinum wire and silver wire as the working, counter and reference electrodes, respectively. All solutions were degassed (Ar) and contained the substrate in concentrations of *ca.* 10^{-4} M, together with n-Bu_4NPF_6 (0.1M) as the supporting

electrolyte. All measurements are referenced against the E1/2 of the Fc/Fc^+ redox couple. The ionisation potentials reported in Chapter 3 were measured by the electron photoemission method in air.[309] The samples were fabricated by means of vacuum deposition of the compound onto an indium tin oxide (ITO) coated glass substrate. The experimental setup consists of the deep-UV deuterium light source ASBN-D130-CM, the CM110 1/8m monochromator, and the 6517B Keithley electrometer. The characteristics of the current density−voltage and luminance−voltage dependences were measured with a semiconductor parameter analyser (HP 4145A) in air without passivation immediately after fabrication of the device. The measurement of brightness was performed using a calibrated photodiode.[310] Calibration of the photodetector was carried out using a radiometer RTN 20 (accuracy ± 2%). The photodiode was placed in front of the OLED in a dark room and the calibration was performed according to the method described earlier.[311] The external quantum efficiency (EQE) values were determined using a literature procedure.[312] The OLED electroluminescence and photoluminescence (PL) spectra of the solid films were recorded with an Ocean Optics USB2000 spectrometer.

The chromaticity coordinates (CIE 1931) and correlated colour temperatures (CCT) were calculated from the response-corrected spectra.

X-ray diffraction measurements at grazing incidence (XRDGI) were performed for compound **3.3** using a D8 Discover diffractometer (Bruker) with Cu Kα (λ = 1.54 Å) X-ray source. Parallel beam geometry with a 60 mm Göbel mirror (X-ray mirror on a high precision parabolic surface) was used. This configuration enables transforming the divergent incident X-ray beam from a line focus of the X-ray tube into a parallel beam that is free of Kβ radiation. The primary side also had a Soller slit with an axial divergence of 2.5º. The secondary side had a LYNXEYE (0D mode) detector with an opening angle of 1.275º and slit opening of 9.5 mm. The sample stage was a Centric Eulerian cradle mounted to a horizontal D8 Discover with a vacuum chuck (sample holder) fixed on the top of the stage. X-ray generator voltage and current was 40.0 kV and 40 mA, respectively. XRDGI scans were performed in the range of 5.0-135.0º with a step size of 0.066º, time per step of 0.2 s and auto-repeat function enabled. Powder X-ray diffraction measurements for the POPs and the MOFs were performed at 298 K using a PANalytical X′Pert PRO diffractometer (λ (CuKα) = 1.4505 Å) on a mounted bracket sample stage. Data were collected over the range 3

– 45°. The resultant diffractograms were processed with the software DIFFRAC.EVA.

AFM experiments were carried out in air at room temperature using a NanoWizardIII atomic force microscope (JPK Instruments), while data were analysed using SurfaceXplorer and JPKSPM Data Processing software. AFM images were collected using a V-shaped silicon cantilever (spring constant of 3 N/m, tip curvature radius of 10.0 nm and the cone angle of 20º) operating in contact mode.

The space-charge-limited current (SCLC) measurements were adopted for the estimation of charge drift mobility of compound **3.3**. Hole-only and electron-only devices were fabricated as described in Paragraph 3.2.4. The current density vs. voltage characteristics of the hole-only and electron-only devices were recorded and fitted using the Mott-Gurney law:[313]

$$J_{SCLC} = \mu_0 \frac{9}{8} \frac{V^2}{d^3} \varepsilon\varepsilon_0 (0.891\gamma\sqrt{V/d}) \qquad \text{Equation 6.1}$$

J_{SCLC} is the steady-state current density; μ_0 is the zero field mobility; V is applied voltage; d is the film thickness, ε is the permittivity of the film (~3); ε_0 is the vacuum permittivity and γ is the field dependence parameter. The ITO-coated glass substrates had a sheet resistance of 15 Ω/sq and the organic layers were deposited in top of it at a rate < 0.1Å/s, using a MB EcoVap4G vacuum deposition system build in a Kurt J. Lesker glove box. The sample area was of 6 mm^2. The charge drift mobility of compound **3.3** was estimated as previously described from J. C. Blakesley *et al.*[169]

Gas adsorption analyses were performed with nitrogen and hydrogen at 77 K and with carbon dioxide at 273 K on a Quantachrome Autosorb iQ gas sorption analyser. The samples were degassed under vacuum at 393 K for 20 hours using a turbo pump. BET surface areas were calculated from the isotherms using the Micropore BET Assistant software. Pore-size distribution analyses were carried out using the QSDFT model (N_2 on carbon at 77 K, slit/cylindrical pore model) implemented in the Quantachrome ASiQwin operating software.[255]

The density functional theory (DFT) calculations were performed either with the software package Gaussian09 (Revision A.02)[134] or with QCHEM 4.1.2.

Tetrakis(triphenylphosphine) palladium(0)

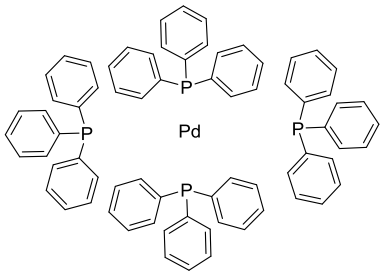

Palladium (II) chloride (1.00 g, 5.64 mmol) and triphenylphosphine (7.40 g, 28.20 mmol) were charged under nitrogen in a round bottom flask. Dry DMSO (80 mL) was added and the suspension was heated with rapid stirring to *ca.* 140 °C where upon complete dissolution occurred. Hydrazine monohydrate (1.13 mL, 22.56 mmol) was then added rapidly via syringe (vigorous reaction) to produce a dark solution. The solution was cooled with the aid of a water bath until crystallisation began to occur (*ca.* 125 °C). The water bath was removed and the solution was then allowed to cool to room temperature without external cooling. The mixture was filtered under nitrogen and the precipitate washed with anhydrous methanol (3 × 20 mL) and diethyl ether (3 × 20 mL) to give the product as a bright yellow solid (6.45 g, 5.58 mmol, 99 %).[314]

7,7'-Bis(5-(9,9-dihexyl-7-(trimethylsilyl)-9H-fluoren-2-yl)-3-hexylthiophen-2-yl)-4,4'-bibenzo[c][1,2,5]thiadiazole (**2.1**)

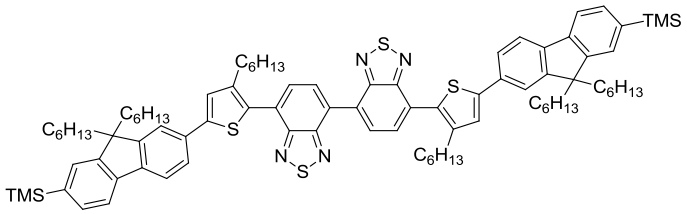

7,7'-Bis(3-hexyl-5-(trimethylstannyl)thiophen-2-yl)-4,4'-bibenzo[c][1,2,5]thiadiazole (**2.12**) (130 mg, 0.112 mmol) and (7-bromo-9,9-dihexyl-9H-fluoren-2-yl)trimethylsilane (**2.16**) (163 mg, 0.336 mmol) were dissolved in dry toluene (10 mL) under nitrogen. Tetrakis(triphenylphosphine)palladium(0) (25.9 mg, 0.022 mmol) was added and the mixture was stirred at reflux for 70 h. After this time brine (50 mL) was added and the mixture was extracted with dichloromethane (3 × 50 mL). The combined organic layers were washed with brine (2 × 50 mL), water (2 × 50 mL), dried over $MgSO_4$, filtered and concentrated under reduced pressure.

Purification on silica gel, eluting 20 % dichloromethane in hexane afforded the title compound as a red solid (50 mg, 0.035 mmol, 31.6 %); ^{1}H NMR δ_{H} (400 MHz, Chloroform-*d*): 8.52 (2H, d, *J* = 7.4 Hz, Ar*H*), 7.89 (2H, d, *J* = 7.4 Hz, Ar*H*), 7.74 – 7.66 (6H, m, Ar*H*), 7.65 – 7.62 (2H, m, Ar*H*), 7.53 – 7.47 (4H, m, Ar*H*), 7.42 (2H, s, Ar*H*), 2.83 – 2.74 (4H, m, CH_2), 2.02 (8H, t, *J* = 8.4 Hz, CH_2), 1.76 (4H, p, *J* = 7.6 Hz, CH_2), 1.40 – 1.32 (4H, m, CH_2), 1.31 – 1.24 (8H, m, CH_2), 1.16 – 1.04 (24H, m, CH_2), 0.89 – 0.83 (6H, m, CH_3), 0.78 (12H, t, *J* = 6.9 Hz, , CH_3), 0.75 – 0.60 (8H, m, CH_2), 0.33 (18H, s, Si(CH_3)$_3$); ^{13}C NMR δ_{C} (101 MHz, Chloroform-*d*): 154.8, 154.0, 151.9, 150.2, 143.3, 141.4, 141.1, 139.3, 133.3, 132.0, 131.6, 131.2, 130.0, 128.9, 128.4, 127.7, 125.4, 124.8, 120.3, 119.1, 55.3, 40.4, 31.8, 31.5, 31.0, 30.0, 29.7, 29.4, 23.8, 22.8, 22.7, 14.2, -0.7; *m/z* (%) (MALDI-TOF) 1410.34 (100), 1411.46 (70), 1412.47 (60), 1413.46 (40), 1414.42 (15); Anal. Calculated for $C_{88}H_{114}N_4S_4Si_2$: C, 74.84; H, 8.14; N, 3.97; found C, 74.47; H, 7.90; N, 4.16; TGA: 5% mass loss at 367 ºC, 10 % mass loss at 403 ºC; T_m = 67 ºC; M.P.: 102-104ºC.

7,7'-Bis(9,9-dihexyl-7-(trimethylsilyl)-9H-fluoren-2-yl)-4,4'-bibenzo[c][1,2,5]thiadiazole (**2.2**)

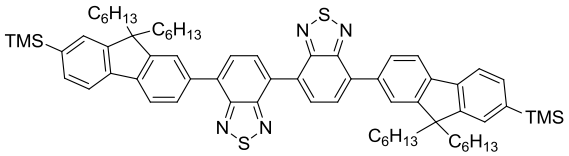

7,7'-Diiodo-4,4'-bibenzo[c][1,2,5]thiadiazole (**2.8**) (240 mg, 0.409 mmol) and potassium carbonate (226 mg, 1.636 mmol) were dissolved in toluene (10 mL) under argon. (9,9-Dihexyl-7-(trimethylsilyl)-9h-fluoren-2-yl)boronic acid (**2.17**) (700 mg, 1.555 mmol) in toluene (10 mL) was added, tetrakis(triphenylphosphine)palladium(0) (95 mg, 0.082 mmol) was added and the mixture was heated at reflux for 70 h. After this time brine (50 mL) was added and the mixture was extracted with dichloromethane (3 × 50 mL). The combined organic layers were washed with brine (2 x 50 mL), water (2 × 50 mL), died over $MgSO_4$, filtered and concentrated under reduced pressure. Purification on silica gel, eluting with 20% dichloromethane in hexane afforded a yellow solid that was recrystallised from hot ethanol to afford the title compound as yellow powder (274 mg, 0.254 mmol, 62.0 %); ^{1}H NMR δ_{H} (400 MHz, Chloroform-*d*): 8.49 (2H, d, *J* = 7.4 Hz, Ar*H*), 8.06 (2H, dd, *J* = 7.9, 1.6 Hz, Ar*H*), 8.03 – 7.97 (4H, m, Ar*H*), 7.90 (2H, d, *J*

= 7.9 Hz, Ar*H*), 7.77 (2H, dd, *J* = 7.3, 0.9 Hz, Ar*H*), 7.53 (4H, dd, *J* = 8.6, 1.1 Hz, Ar*H*), 2.04 (8H, dq, *J* = 12.9, 7.4, 6.5 Hz, CH_2), 1.19 – 1.05 (24H, m, CH_2), 0.88 – 0.73 (20H, m, CH_3), 0.34 (18H, s, SiCH_3); ^{13}C NMR δ_C (101 MHz, Chloroform-*d*) 154.6, 154.4, 151.5, 150.7, 141.7, 141.4, 139.6, 136.3, 135.1, 132.1, 131.4, 128.7, 128.4, 127.9, 127.8, 124.3, 120.0, 119.4, 76.8, 55.3, 40.2, 31.6, 29.8, 24.0, 22.7, -0.7; m/z (%) (MALDI-TOF) 1078.31 (70), 1079.31 (100), 1080.32 (50), 1081.34 (30), 1082.33 (10); Anal. Calculated for $C_{68}H_{86}N_4S_2Si_2$: C, 75.64; H, 8.03; N, 5.19; Found: C, 75.43; H, 7.80; N, 5.27; TGA: 5% loss of mass at 401 ºC, 10% loss of mass at 412 ºC; T_m' = 197 ºC; T_m'' = 223 ºC; M.P.: 218-220ºC.

4,4'-([4,4'-Bisbenzo[c][1,2,5]thiadiazole]-7,7'-diylbis(9,9-dihexyl-9H-fluorene-7,2-diyl))bis(N,N-diphenylaniline) (**2.3**)

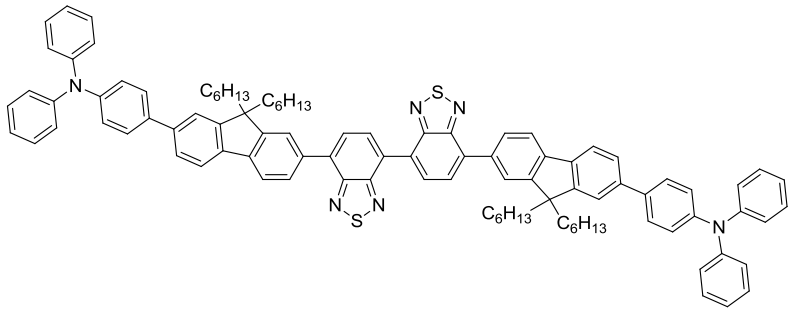

7,7'-Bis(7-bromo-9,9-dihexyl-9H-fluoren-2-yl)-4,4'-bibenzo[c][1,2,5]thiadiazole (**2.4**) (84 mg, 0.077 mmol), (4-(diphenylamino)phenyl)boronic acid (67 mg, 0.231 mmol), tetrakis(triphenylphosphine)palladium(0) (18 mg, 0.015 mmol), barium hydroxide octa hydrate (49 mg, 0.154 mmol) and tetrabutylammonium bromide (25 mg, 0.077 mmol) were dissolved in a THF (9 mL) and degassed water (2 mL) and the mixture was heated at reflux for 44 h. After this time brine (50 mL) was added and the mixture was extracted with dichloromethane (3 × 50 mL). The combined organic layers were washed with water (3 × 50 mL), dried over $MgSO_4$, filtered and concentrated under reduced pressure. A first purification on silica gel, eluting with 50 % dichloromethane in hexane afforded an orange residue. A second purification on silica gel, first eluting with 25 % dichloromethane in hexane to remove by-products and then 33% dichloromethane in hexane afforded the title compound as orange powder. (70 mg, 0.049 mmol, 64.1 %); ^{1}H NMR δ_H (400 MHz, Chloroform-*d*): 8.51 (2H, d, *J* = 7.4 Hz, Ar*H*), 8.10 (2H, dd, *J* = 7.8, 1.6 Hz, Ar*H*), 8.05 – 8.00 (4H, m, Ar*H*), 7.91 (2H, d, *J* = 7.9 Hz, Ar*H*), 7.83 (2H, d, *J* = 8.4 Hz, Ar*H*), 7.63 –

7.57 (8H, m, Ar*H*), 7.33 – 7.27 (8H, m, Ar*H*), 7.22 – 7.15 (12H, m, Ar*H*), 7.09 – 7.03 (4H, m, Ar*H*), 2.20 – 2.01 (8H, m, CH_2), 1.19 – 1.09 (24H, m, , CH_2), 0.91 – 0.82 (8H, m, CH_2), 0.79 (12H, t, *J* = 6.9 Hz, CH_3); ^{13}C NMR δ_C (101 MHz, Chloroform-*d*): 151.5, 147.8, 141.5, 140.0, 139.6, 136.0, 135.7, 135.1, 131.4, 129.4, 128.7, 128.5, 128.0, 127.8, 125.8, 124.5, 124.2, 124.2, 123.1, 121.2, 120.4, 119.9, 55.5, 40.6, 31.7, 29.9, 24.1, 22.8, 14.2; m/z (%) (MALDI-TOF) 1420.18 (90), 1421.19 (100), 1422.19 (80), 1423.24 (30), 1424.32 (10); Anal. Calculated for $C_{98}H_{96}N_6S_2$: C, 82.78; H, 6.81; N, 5.91; Found: C, 83.10; H, 6.82; N, 5.83; TGA: 5% loss of mass a 418 ºC, 10% loss of the mass at 436 ºC; T_m' = 216 ºC, T_m'' = 221ºC. T_g' = 166 ºC; T_g'' = 337 ºC; M.P.: 224-226ºC.

7,7'-Bis(7-bromo-9,9-dihexyl-9H-fluoren-2-yl)-4,4'-bibenzo[c][1,2,5]thiadiazole (**2.4**)

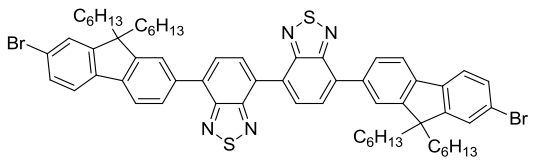

7,7'-Bis(9,9-dihexyl-7-(trimethylsilyl)-9H-fluoren-2-yl)-4,4'-bibenzo[c][1,2,5]thiadiazole (**2.2**) (0.220 g, 0.204 mmol) and sodium acetate (0.033 g, 0.408 mmol) were dissolved in dry THF (30 mL) under argon. The mixture was cooled to 0°C, dibromine (2M solution in dichloromethane, 0.48 mL, 0.949 mmol) was added dropwise and the mixture was stirred for 20 h at room temperature. After this time triethylamine (0.23 mL, 1.630 mmol) was added and the mixture stirred for 30 minutes. Sodium sulfate (100 mL, saturated aqueous solution) was added and the mixture was extracted with dichloromethane (3 × 50 mL). The combined organic layers were washed with water (3 × 50 mL), dried over $MgSO_4$, filtered and concentrated under reduced pressure. The orange solid obtained was filtered through a silica gel plug eluting with dichloromethane and then concentrated under reduced pressure to afford a solid that was dissolved in the minimum volume of boiling dichloromethane. Cold methanol was added and the title compound was reprecipitated as an orange powder (201 mg, 0.184 mmol, 90 % yield); ^{1}H NMR δ_H (400 MHz, Chloroform-*d*): 8.49 (2H, d, *J* = 7.4 Hz, Ar*H*), 8.07 (2H, dd, *J* = 7.8, 1.5 Hz, Ar*H*), 8.03 – 7.97 (4H, m, Ar*H*), 7.86 (2H, d, *J* = 7.9 Hz, Ar*H*), 7.64 (2H, d, *J* = 7.9 Hz, Ar*H*), 7.56 – 7.46 (4H, m, Ar*H*), 2.13 – 1.93 (8H, m, CH_2), 1.19 – 1.07

(24H, m, CH_2), 0.84 – 0.72 (20H, m, CH_3); ^{13}C NMR δ_C (101 MHz, Chloroform-*d*): 154.6, 154.3, 153.7, 150.9, 140.6, 136.6, 134.9, 131.3, 130.2, 128.8, 128.6, 127.9, 126.4, 124.2, 121.6, 121.5, 120.0, 55.7, 40.4, 31.6, 29.8, 24.0, 22.7, 14.2; *m/z* (%) (MALDI-TOF) 1090.87 (50), 1091.91 (100), 1092.88 (100), 1093.92 (100), 1094.90 (80), 1095.94 (30), 1096.91 (20); Anal. Calculated for $C_{62}H_{68}Br_2N_4S_2$: C, 68.12; H, 6.27; N, 5.13; Found: C, 68.36; H, 6.13; N, 5.15; TGA: 5% loss of mass a 412 ºC, 10% loss of the mass at 428 ºC; T_m' = 70 ºC; T_m'' = 170 ºC; T_g = 116 ºC; M.P.: 166-168ºC.

4,4'-([4,4'-Bisbenzo[c][1,2,5]thiadiazole]-7,7'-diylbis(9,9-dihexyl-9H-fluorene-7,2-diyl))bis(N,N-diethylaniline) (**2.5**)

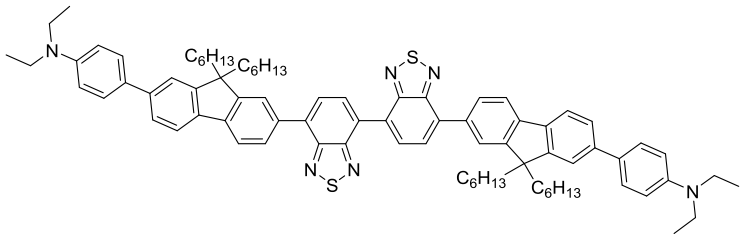

7,7'-Bis(7-bromo-9,9-dihexyl-9H-fluoren-2-yl)-4,4'-bibenzo[c][1,2,5]thiadiazole (**2.4**) (92 mg, 0.084 mmol), (4-(diethylamino)phenyl)boronic acid (49 mg, 0.252 mmol), tetrakis(triphenylphosphine)palladium(0) (19 mg, 0.017 mmol), barium hydroxide octa hydrate (53 mg, 0.168 mmol) and tetrabutylammonium bromide (27 mg, 0.084 mmol) were dissolved in dry THF (9 mL) and degassed water (2 mL), and the mixture was heated at reflux for 70 h. After this time, brine (50 mL) was added and the mixture was extracted with dichloromethane (3 × 50 mL). The combined organic layers were washed with brine (2 × 50 mL), water (2 × 50 mL), dried over $MgSO_4$, filtered and concentrated under reduced pressure. Purification on silica gel, eluting with 50 % dichloromethane in hexane afforded the title compound as an orange powder (78 mg, 0.063 mmol, 75.0 %); ^{1}H NMR δ_H (400 MHz, Chloroform-*d*): 8.50 (2H, d, *J* = 7.4 Hz, Ar*H*), 8.08 (2H, dd, *J* = 7.9, 1.6 Hz, Ar*H*), 8.05 – 7.99 (4H, m, Ar*H*), 7.89 (2H, d, *J* = 7.9 Hz, Ar*H*), 7.79 (2H, d, *J* = 7.8 Hz, Ar*H*), 7.63 – 7.54 (8H, m, Ar*H*), 6.86 – 6.77 (4H, m, Ar*H*), 3.44 (8H, q, *J* = 7.1 Hz, CH_2), 2.18 – 1.99 (8H, m, CH_2), 1.23 (12H, t, *J* = 7.0 Hz, CH_3), 1.19 – 1.08 (24H, m, CH_2), 0.91 – 0.82 (8H, m, CH_2), 0.79 (12H, t, *J* = 6.9 Hz, CH_3); ^{13}C NMR δ_C (101 MHz, Chloroform-*d*): 154.6, 154.4, 152.1, 151.4, 147.3, 141.8, 140.8, 138.6, 135.7, 135.1, 131.4, 128.6, 128.4, 128.1, 127.8, 125.2, 124.2, 120.7, 120.3, 119.7, 112.2, 55.4,

44.6, 40.6, 31.7, 30.0, 24.1, 22.8, 14.2, 12.8; *m/z* (%) (MALDI-TOF) 1228.80 (85), 1229.81 (100), 1230.85 (50), 1231.82 (20); Anal. Calculated for $C_{82}H_{96}N_6S_2$: C, 80.08; H, 7.87; N, 6.68; Found: C, 79.60; H, 7.78; N, 6.90; TGA: 5% loss of mass a 423 ºC, 10% loss of the mass at 441 ºC; T_m = 302 ºC; M.P.: 284-286ºC.

4,4'-Bibenzo[c][1,2,5]thiadiazole (**2.7**)

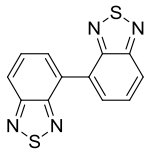

4-Bromobenzo[c][1,2,5]thiadiazole (**2.6**) (590 mg, 2.74 mmol), palladium (II) acetate (30.8 mg, 0.137 mmol), potassium carbonate (379 mg, 2.74 mmol) and PEG 4000 (2.743 g, 0.686 mmol) were dissolved in dry DMF (10 mL) under nitrogen and the mixture was stirred at 120 °C for 20 h. After this time water was added and the obtained solid was filtered, washed with water and dissolved in chloroform to obtain a solution. The solution was washed with brine (3 × 50 mL), dried over $MgSO_4$, filtered and concentrated under reduced pressure. Purification on silica gel, eluting with 70 to 100%dichloromethane in petroleum ether afforded the title compound as a yellow solid (298 mg, 1.102 mmol, 80 %); ^{1}H NMR δ_H (400 MHz, Chloroform-*d*): 8.26 (2H, dd, *J* = 7.0, 1.1 Hz, Ar*H*), 8.11 (2H, dd, *J* = 8.8, 1.1 Hz, Ar*H*), 7.81 (2H, dd, *J* = 8.8, 7.0 Hz, Ar*H*); ^{13}C NMR δ_H (101 MHz, Chloroform-*d*): 155.7, 153.8, 130.9, 130.2, 129.6, 121.8. *m/z* (%) (MALDI-TOF) 270.02 (100), 271.03 (70), 272.02 (30), 273.03 (15); Anal. Calculated for $C_{12}H_6N_4S_2$: C, 53.32; H, 2.24; N, 20.73; found C, 53.91; H, 2.38; N, 20.70. M.P.: 236-240ºC. This was consistent with the previously published data.[122]

7,7'-Diiodo-4,4'-bibenzo[c][1,2,5]thiadiazole (**2.8**)

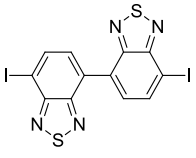

Silver sulfate (2.971 mg, 9.53 mmol) was dissolved in sulfuric acid (9 mL). Iodine (789 mg, 3.11 mmol) was added and the solution was stirred for 3 h at room temperature until the iodine had dissolved. The mixture was then added to 4,4'-bibenzo[c][1,2,5]thiadiazole (**2.7**) (280 mg, 1.036 mmol) at 110°C. The resulting

mixture was stirred at 110°C for 1 h. After this time water (100 mL) was added and the mixture was extracted with chloroform (4 × 100 mL). The combined chloroform extracts were filtered in a glass fritted funnel and the solution was concentrated under reduced pressure to afford a yellow solid that was recrystallized from boiling toluene to afford the title compound as a yellow powder (244 mg, 0.467 mmol, 45.1 %); ^{1}H NMR δ_{H} (400 MHz, Chloroform-*d*): 8.30 (2H, d, *J* = 7.5 Hz, Ar*H*), 8.06 (2H, d, *J* = 7.5 Hz, Ar*H*); *m/z* (%) (MALDI-TOF) 520.40 (30), 521.40 (60), 522.41 (100). M.P.: 108-112ºC. This was consistent with the previously published data.[97]

2-(3-Hexylthiophen-2-yl)-4,4,5,5-tetramethyl-1,3,2-dioxaborolane (**2.10**)

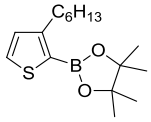

2-Bromo-3-hexylthiophene (2.5 g, 10.11 mmol) was dissolved in dry THF (15 mL) under nitrogen. The solution was cooled to −78 °C and *n*-butyllithium (2.30 M, 4.62 mL, 10.62 mmol) was added dropwise. The mixture was stirred at −78 °C for 1 h and then triisopropyl borate (2.58 mL, 11.12 mmol) was added at −78 °C. The mixture was allowed to reach room temperature and stirred for 2 h. 2,3-Dimethylbutane-2,3-diol (1.434 g, 12.14 mmol) was added and the mixture was stirred for 20 h. After this time the mixture was concentrated under reduced pressure and then re-dissolved in petroleum ether (50 mL). The white precipitate was filtered in a glass fritted funnel, and the resulting solution was filtered over neutral aluminium oxide and the solution was concentrated under reduced pressure. Purification on silica gel, eluting with 15 % dichloromethane in hexane afforded the title compound as a mixture with 2-bromo-3-hexylthiophene and unknown by-product (980 mg). The compound was used without further purification; ^{1}H NMR δ_{H} (400 MHz, Chloroform-*d*): 7.48 (1H, d, *J* = 4.7 Hz, Ar*H*), 7.01 (1H, d, *J* = 4.7 Hz, Ar*H*), 2.91 – 2.85 (2H, m), 1.64 – 1.55 (2H, m),1.33 (12H, s, CH_3), 1.31 – 1.22 (6H, m), 0.91 – 0.85 (3H, m). This was consistent with the previously published data.[315]

7,7'-Bis(3-hexylthiophen-2-yl)-4,4'-bibenzo[c][1,2,5]thiadiazole (**2.11**)

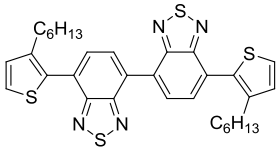

7,7'-Diiodo-4,4'-bibenzo[c][1,2,5]thiadiazole (**2.8**) (580 mg, 1.111 mmol), 2-(3-hexylthiophen-2-yl)-4,4,5,5-tetramethyl-1,3,2-dioxaborolane (**2.10**) (981 mg, 3.33 mmol), barium hydroxide octahydrate (701 mg, 2.222 mmol) and tetrabutylammonium bromide (357 mg, 1.111 mmol) were dissolved under nitrogen in a mixture of degassed water (2 mL), THF (9 mL) and dry toluene (9 mL). Tetrakis(triphenylphosphine)palladium(0) (257 mg, 0.222 mmol) was added and the mixture was heated at 70 °C for 70 h. After this time brine (50 mL) was added and the mixture was extracted with dichloromethane (3 × 50 mL). The combined organic layers were washed with brine (2 × 50 mL), water (2 × 50 mL), dried over $MgSO_4$, filtered and concentrated over reduced pressure. Purification on silica gel, eluting with 1 % ethyl acetate in hexane afforded an orange residue that was purified *via* recycling gel permeation chromatography (eluting with THF) to afford the title compound as an orange solid (122 mg, 0.202 mmol, 18.2 %). The compound was used without further purification; ^{1}H NMR δ_H (400 MHz, Chloroform-*d*): 8.46 (2H, d, *J* = 7.3 Hz), 7.82 (2H, d, *J*=7.4 Hz), 7.47 (2H, d, *J*=5.2 Hz), 7.13 (2H, d, *J*=5.2 Hz), 2.76 – 2.67 (4H, m), 1.66 (4H, s), 1.23 (12H, td, *J*=4.7, 2.6 Hz), 0.86 – 0.78 (6H, m). This was consistent with the previously published data.[96]

7,7'-Bis(3-hexyl-5-(trimethylstannyl)thiophen-2-yl)-4,4'-bibenzo[c][1,2,5]thiadiazole (**2.12**)

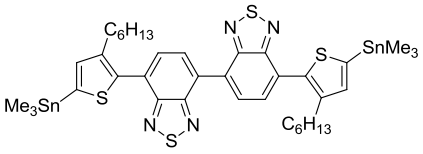

2,2,6,6-Tetramethylpiperidine (0.073 mL, 0.431 mmol) was dissolved in dry THF (5 mL) under nitrogen and *n*-butyllithium (2.3 M in hexane, 0.19 mL, 0.431 mmol) was added to the solution at −78 °C. The resulting mixture was stirred for 30 min at −78°C and then was allowed to reach room temperature and stirred for additional 15 min to afford LiTMP. 7,7'-Bis(3-hexylthiophen-2-yl)-4,4'-bibenzo[c][1,2,5]thiadiazole (**2.11**) (100 mg, 0.166 mmol) was dissolved in dry THF (10 mL) under nitrogen and then added to the LiTMP solution. The mixture was stirred for 45 min at −78 °C. Trimethyltin chloride (86 mg, 0.431 mmol) was then added dropwise at −78 °C, then the mixture was allowed to reach room temperature and stirred for 20 h. Brine (50 mL) was added and the mixture was extracted with

dichloromethane (3 × 50 mL). The combined organic layers were washed with brine (3 × 50 mL), water (2 × 50 mL), dried over $MgSO_4$, filtered and concentrated under reduced pressure to afford the title compound as an orange solid (135 mg, 0.145 mmol, 88 %). The compound was used without further purification; ^{1}H NMR δ_H (400 MHz, Chloroform-d): 8.47 – 8.43 (2H, m, Ar*H*), 7.78 (2H, d, *J* = 7.4 Hz, Ar*H*), 7.19 (2H, s, Ar*H*), 2.76 – 2.70 (4H, m, CH_2), 1.69 – 1.65 (4H, m, CH_2), 1.27 – 1.19 (12H, m, CH_2), 0.85 – 0.81 (6H, m, CH_3), 0.42 (18H, s, SnCH_3).

9,9-Dihexyl-9H-fluorene (**2.14**)

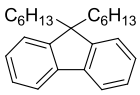

9*H*-fluorene (12 g, 70.8 mmol) was dissolved in dry THF (80 mL) under nitrogen and 1-bromohexane (37.8 ml, 269 mmol) was added. The mixture was cooled in an ice bath; a solution of potassium *tert*-butoxide (20.64 g, 184 mmol) in THF (80 mL) was added dropwise and the mixture was stirred at room temperature for 20 h. The mixture was filtered through a silica plug eluting with THF to remove the white precipitate. The filtrate was evaporated under reduced pressure and a yellow oil was obtained. The excess of 1-bromohexane was removed by KugelRohr distillation at 4.5 mmHg and 85°C. The obtained oil was recrystallised from ethanol and then from hexane to afford the title compound as white crystals (19.0 g, 56.8 mmol, 80 %); ^{1}H NMR, δ_H (400 MHz, Chloroform-*d*): 7.78 – 7.72 (2H, m, Ar*H*), 7.41 – 7.31 (6H, m, Ar*H*), 2.07 – 1.96 (4H, m, CH_2), 1.20 – 1.04 (12H, m, CH_2), 0.81 (6H, t, *J* = 7.1 Hz, CH_3), 0.75 – 0.63 (4H, m, CH_2). This was consistent with the previously published data.[316]

2,7-Dibromo-9,9-dihexyl-9H-fluorene (**2.15**)

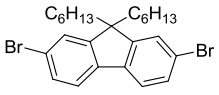

9,9-Dihexyl-9H-fluorene (19.1 g, 57.1 mmol) and diiodine (0.145 g, 0.571 mmol) were dissolved under nitrogen in dry dichloromethane (150 mL). Bromine (6.70 ml, 131 mmol) was added dropwise and the mixture was stirred at room temperature for 20 h. The mixture was cooled in an ice bath and a Na_2SO_3 aqueous saturated solution was added (100 mL). The mixture was extracted with dichloromethane (3 × 50 mL)

and the combined organic layers were washed with $NaHCO_3$ (3 × 50 mL), water (3 × 50 mL), then dried over $MgSO_4$, filtered and concentrated under reduced pressure. The obtained solid was recrystallised from hot ethanol and then from hot hexane (22.91 g, 46.5 mmol, 82 %); ^{1}H NMR, δ_H (400 MHz, Chloroform-*d*): 7.52 (2H, dd, *J* = 7.4, 1.2 Hz, Ar*H*), 7.45 (4H, dd, *J* = 8.1, 1.8 Hz, Ar*H*), 1.95 – 1.87 (4H, m, CH_2), 1.18 – 0.98 (12H, m, CH_2), 0.78 (6H, t, *J* = 7.1 Hz, CH_3), 0.63 – 0.53 (4H, m, CH_2). M.P.: 58-60ºC. This was consistent with the previously published data.[317]

(7-Bromo-9,9-dihexyl-9H-fluoren-2-yl)trimethylsilane (**2.16**)

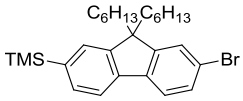

2,7-Dibromo-9,9-dihexyl-9H-fluorene (**2.15**) (5 g, 10.16 mmol) was dissolved in dry THF (100 mL) under nitrogen. The solution was cooled to −90°C, *n*-butyllithium (2.3 M in hexane, 4.44 ml, 10.21 mmol) was added dropwise and the mixture was stirred for 30 min. The temperature was further reduced to −100 °C and chlorotrimethylsilane (1.29 ml, 10.16 mmol) was added dropwise. The mixture was allowed to reach room temperature and stirred for 20 h. After this time water (100 mL) was added and the mixture was extracted with diethyl ether (3 × 100 mL). The combined organic layers were washed with water (3 × 100 mL), dried over $MgSO_4$, filtered and concentrated under reduced pressure. Purification on silica gel, eluting with 5% ethyl acetate in hexane afforded the title compound as a colourless solid (3.73 g, 7.68 mmol, 76 %). The compound was used without further purification; ^{1}H NMR δ_H (400 MHz, Chloroform-*d*): 7.64 (1H, dd, *J* = 7.5, 0.8 Hz, Ar*H*), 7.55 (1H, dd, *J* = 7.9, 0.6 Hz, Ar*H*), 7.48 (1H, dd, *J* = 7.4, 0.9 Hz, Ar*H*), 7.46 – 7.42 (3H, m, Ar*H*), 2.00 – 1.86 (4H, m, CH_2), 1.14 – 1.02 (12H, m, CH_2), 0.77 (6H, t, *J* = 7.0 Hz, CH_3), 0.70 – 0.56 (4H, m, CH_2), 0.31 (9H, s, Si(CH_3)$_3$). This was consistent with the previously published data.[318]

(9,9-Dihexyl-7-(trimethylsilyl)-9H-fluoren-2-yl)boronic acid (**2.17**)

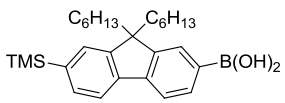

2,7-Dibromo-9,9-dihexyl-9H-fluorene (**2.16**) (4.2 g, 8.53 mmol) was dissolved in dry THF (100 mL) under nitrogen. The solution was cooled to −90°C, *n*-butyllithium

(2.44 M in hexane, 3.50 mL, 8.53 mmol) was added dropwise and the mixture was stirred for 30 min. The temperature was reduced to −100 °C, chlorotrimethylsilane (1.08 mL, 8.53 mmol) was then added dropwise and the reaction mixture stirred until it reached room temperature. The mixture was then cooled to −90 °C, *n*-butyllithium (2.44 M, 3.67 mL, 8.96 mmol) was added and the mixture stirred for 30 min. The temperature was further reduced to −100 °C, triisopropyl borate (5.94 mL, 25.6 mmol) was added dropwise and then the mixture was stirred at room temperature for 20 h. After this time water (100 mL) was added and the mixture was extracted with diethyl ether (3 × 100 mL). The combined organic layers were washed with water (3 × 100 mL), dried over $MgSO_4$, filtered and concentrated under reduced pressure. Purification on silica gel, eluting first with toluene to remove the by-products then with 50 % to 100% diethyl ether in toluene afforded the title compound as a colourless solid (3.00 g, 6.66 mmol, 78 %); ^{1}H NMR δ_H (400 MHz, Chloroform-*d*): 8.30 (1H, d, *J* = 7.6 Hz, Ar*H*), 8.22 (1H, s, Ar*H*), 7.89 (1H, d, *J* = 7.6 Hz, Ar*H*), 7.80 (1H, d, *J* = 7.7 Hz, Ar*H*), 7.57 – 7.51 (2H, m, Ar*H*), 2.19 – 2.01 (4H, m, CH_2), 1.18 – 0.99 (12H, m, CH_2), 0.81 – 0.64 (10H, m, CH_2CH_3), 0.34 (9H, s, SiCH_3). This was consistent with the previously published data.[107]

Di-*tert*-butyl 2,2'-(benzo[c][1,2,5]thiadiazole-4,7-diyl)bis(thiazole-5-carboxylate) (**3.1**)

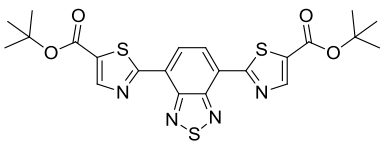

2,2,6,6-Tetramethylpiperidine (0.174 mL, 1.032 mmol) was dissolved in dry THF (10 mL) under nitrogen and *n*-butyllithium (2.4 M in hexane, 0.43 mL, 1.032 mmol) was added to the solution at −78 °C. The resulting mixture was stirred 30 min at −78 °C and then was allowed to reach room temperature and stirred for additional 15 min to afford LiTMP. 4,7-Di(thiazol-2-yl)benzo[c][1,2,5]thiadiazole (**3.21**) (120 mg, 0.397 mmol) was dissolved in dry THF (55 mL) under nitrogen and the solution was cooled to −78 °C. The LiTMP solution was then added dropwise and the resulting solution was stirred for 45 min at −78 °C. Di-*tert*-butyl dicarbonate (2 M in THF, 2.98 mL, 5.95 mmol) was added dropwise at −78 °C, then the mixture was allowed to reach room temperature and stirred for 20 h. Brine (50 mL) was added and the mixture was extracted with dichloromethane (3 × 50 mL). The combined organic

layers were washed with water (3 × 100 mL), dried over $MgSO_4$, filtered and concentrated under reduced pressure to afford a dark red residue. Purification on silica gel, eluting with 20% ethyl acetate in hexane, afforded the title compound as a yellow solid (8 mg, 0.016 mmol, 4.0 %); ^{1}H NMR δ_H (400 MHz, Chloroform-*d*): 8.82 (2H, s, Ar*H*), 8.52 (2H, s, Ar*H*), 1.64 (18H, s, COOC(CH_3)$_3$); ^{13}C NMR δ_H (101 MHz, Chloroform-*d*): 165.7, 160.9, 152.0, 148.4, 134.1, 128.3, 127.1, 83.1, 29.9, 28.4; *m/z* (%) (MALDI-TOF) 502.87 (70), 503.88 (100), 504.89 (30), 505 (20); HRMS (LSI-TOF) m/z: $[M + H]^+$ Calcd for $C_{22}H_{22}N_4O_4S_3$ 503.0881; Found 503.0881. Since the mass of the title compound obtained was very little, the M.P. was not measured.

Di-tert-butyl 5,5'-(benzo[c][1,2,5]thiadiazole-4,7-diyl)bis(thiophene-2-carboxylate) (**3.2**)

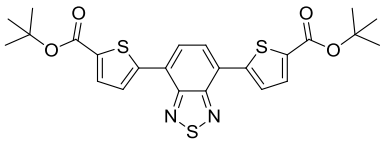

2,1,3-Benzothiadiazole-4,7-bis(boronic acid pinacol ester) (**3.12**) (400 mg, 1.031 mmol), *tert*-butyl-5-bromothiophene-2-carboxylate (**3.7**) (814 mg, 3.09 mmol), [1,1′-bis(diphenylphosphino)ferrocene]dichloropalladium(II) dichloromethane adduct (168 mg, 0.206 mmol) and tripotassium phosphate (43.8 mg, 0.206 mmol) were dissolved in degassed water (3 mL) and DMF (27 mL) under nitrogen. The mixture was stirred at 70°C for 68 h. After this time the mixture was diluted with brine (100 mL) and extracted with dichloromethane (3 × 50 mL). The recombined organic layers were washed with brine (2 × 50 mL), water (3 × 50 mL), dried over $MgSO_4$ and concentrated under reduced pressure to afford a dark orange residue. Purification on silica gel, eluting with 50% dichloromethane in hexane afforded the title compound as an orange powder (398 mg, 0.795 mmol, 77 %); 1H NMR, δ_H (400 MHz, Chloroform-*d*): 8.06 (2H, d, *J* = 4.0 Hz, Ar*H*), 7.96 (2H, s, Ar*H*), 7.79 (2H, d, *J* = 4.0 Hz, Ar*H*), 1.63 (18H, s, COOC(CH_3)$_3$); 13C NMR δ_C (101 MHz, Chloroform-*d*): 161.6, 152.5, 144.7, 136.6, 133.4, 127.9, 126.4, 126.4, 82.2, 28.4. m/z (%) (MALDI-TOF) 500.04 (100), 501.05 (30), 502.02(20); HRMS (LSI-TOF) m/z: $[M - t\text{-Butyl} + H + H]^+$ Calcd for $C_{20}H_{17}N_2O_4S_3$ 445.0345; Found 445.0344. Anal. Calculated for $C_{24}H_{24}N_2O_2$: C, 57.58; H, 4.83; N, 5.60; Found: C, 57.57; H, 4.64; N, 5.63; M.P.: 198-202°C.

Dimethyl 4,4'-(benzo[c][1,2,5]thiadiazole-4,7-diyl)bis(3-methoxybenzoate) (**3.3**)

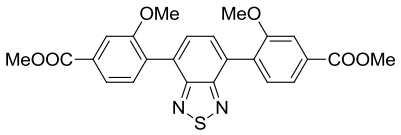

2,1,3-Benzothiadiazole-4,7-bis(boronic acid pinacol ester) (**3.12**) (100 mg, 0.258 mmol), potassium phosphate (109 mg, 0.515 mmol), [1,1′-bis(diphenylphosphino)ferrocene]-dichloropalladium(II) dichloromethane adduct (21 mg, 0.026 mmol) and methyl 4-iodo-3-methoxybenzoate (**3.11**) (226 mg, 0.773 mmol) were dissolved in degassed water (1 mL) and N,N-dimethylformamide (9 mL) under nitrogen. The mixture was stirred at 60°C for 18 h. After this time the mixture was diluted with brine (50 mL) and extracted with dichloromethane (3 × 50 mL). The recombined organic layers were washed with brine (2 × 50 mL), water (3 × 50 mL), dried over $MgSO_4$ and concentrated under reduced pressure to afford a dark yellow solid. Purification on silica gel, eluting with dichloromethane to wash off the impurities and then chloroform afforded a dark yellow powder. The title compound was obtained after recrystallisation from hot acetone as a bright yellow powder (69 mg, 58%); ^{1}H NMR δ_H (400 MHz, 7.81 (2H, dd, *J* = 7.9, 1.5 Hz, Ar*H*), 7.78 – 7.74 (4H, m, Ar*H*), 7.65 (2H, d, *J* = 7.8 Hz, Ar*H*), 3.98 (6H, s, ArOCH_3), 3.88 (6H, s, COOCH_3); ^{13}C NMR δ_C (101 MHz, Chloroform-*d*): 166.9, 157.2, 154.1, 131.9, 131.5, 131.2, 130.5, 129.9, 122.1, 112.4, 56.1, 52.4; m/z (%) (MALDI-TOF) 464.15 (100), 465.12 (75), 466.14 (30); HRMS (LSI-TOF) *m/z* [M + H]$^+$ calcd for $C_{24}H_{21}N_2O_6S$ 465.1115, found 465.1117; TGA: 5% mass loss at 311 °C; T_m = 227 °C, T_c = 147 °C; M.P.: 230-232 °C.

Di-*tert*-butyl-5',5'''-(benzo[c][1,2,5]thiadiazole-4,7-diyl)bis([2,2'-bithiophene]-5-carboxylate) (**3.4**)

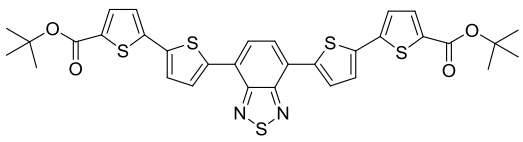

4,7-Bis(5-(trimethylstannyl)thiophen-2-yl)benzo[c][1,2,5]thiadiazole (**3.13**) (94 mg, 0.150 mmol) and tert-butyl 5-bromothiophene-2-carboxylate (**3.7**) (138 mg, 0.526 mmol) were dissolved under nitrogen in dry toluene (15 mL). Tetrakis(triphenylphosphine) palladium(0) (39.9 mg, 0.035 mmol) was added and

the reaction was stirred at 70°C for 96 h. After this time the mixture was diluted with dichloromethane, washed with water (3 × 50mL), dried over $MgSO_4$ and concentrated under reduced pressure to afford a dark red residue. Purification on silica gel initially eluting with 50% dichloromethane in hexane, before switching gradually to 100% dichloromethane afforded the title compound as a dark red solid (61 mg, 0.092 mmol, 61.1 %); ^{1}H- NMR δ_H (400 MHz, Chloroform-*d*): 8.06 (2H, d, *J* = 4.0 Hz, Ar*H*), 7.89 (2H, s, Ar*H*), 7.66 (2H, d, *J* = 3.9 Hz, Ar*H*), 7.37 (2H, d, *J* = 4.0 Hz, Ar*H*), 7.24 (2H, d, *J* = 3.9 Hz, Ar*H*), 1.60 (18H, s, C*H*$_3$); ^{13}C NMR δ_C (151 MHz, Chloroform-*d*): 161.4, 152.5, 143.2, 138.2, 134.3, 133.7, 128.5, 125.9, 125.7, 125.5, 124.2, 82.1, 29.9, 28.4; *m/z* (%) (MALDI-TOF) 664.13 (100), 665.15 (50), 666.16 (20); Anal. Calculated for $C_{32}H_{28}N_2O_4S_5$: C, 57.81; H, 4.24; N, 4.21; Found: C, 57.64; H, 4.19; N, 4.05; M.P.: 310°C (dec.).

Di-*tert*-butyl-7,7'-(benzo[c][1,2,5]thiadiazole-4,7-diyl)bis(2,3-dihydrothieno[3,4-b][1,4]dioxine -5-carboxylate) (**3.5**)

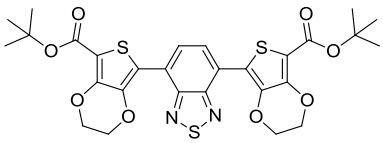

2,2,6,6-Tetramethylpiperidine (0.13 mL, 0.749 mmol) was dissolved in dry THF (10 mL) under nitrogen and *n*-butyllithium (2.4 M in hexane, 0.31 mL, 0.749 mmol) was added to the solution at −78 °C. The resulting mixture was stirred for 30 min at −78 °C and then was allowed to reach room temperature and was stirred for additional 15 min to afford LiTMP. 4,7-Di(3,4-ethylenedioxythiophen-2-yl)benzo[c][1,2,5]thiadiazole (**3.22**) (0.120 g, 0.288 mmol) was dissolved in dry THF (55 mL) under nitrogen and the solution was cooled to −78 °C. LiTMP solution was then added dropwise and the mixture was stirred for 45 min at −78 °C. Di-*tert*-butyl dicarbonate (2M in THF, 2.88 mL, 5.76 mmol) was then added dropwise at −78 °C and then the mixture was allowed to reach room temperature and was stirred for 20 h. Brine (50 mL) was added and the mixture was extracted with dichloromethane (3 × 50 mL). The combined organic layers were washed with water (3 × 100 mL), dried over $MgSO_4$, filtered and concentrated under reduced pressure to afford a dark red residue. Purification on silica gel, first eluting with dichloromethane to wash off the starting compound, then with 50% to 70% ethyl acetate in hexane, afforded the title compound as a dark red solid (30 mg, 0.049

mmol, 16.9 % yield); ^{1}H NMR, δ_{H} (400 MHz, Chloroform-*d*): 8.46 (2H, s, Ar*H*), 4.50 – 4.44 (4H, m, CH_2), 4.44 – 4.39 (4H, m, CH_2), 1.61 (18H, s, CH_3); ^{13}C NMR δ_C (101 MHz, Chloroform-*d*): 161.1, 152.3, 145.5, 140.3, 128.3, 124.2, 118.5, 110.3, 82.0, 65.1, 64.8, 28.5; *m/z* (%) (MALDI-TOF) 616.10 (100), 617.13 (25), 618.11 (18), 619.08 (5); HRMS (LSI-TOF) *m/z*: $[M + H]^+$ Calcd for $C_{28}H_{29}N_2O_6S_3$ 617.1081; Found 617.1076; M.P.: 280°C (dec.).

Tert-butyl 5-bromothiophene-2-carboxylate (**3.7**)

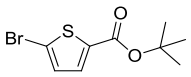

n-Butyllithium (2.4 M in hexane, 3.0 mL, 7.17 mmol) was added under nitrogen to a flask containing toluene (9 mL) at −10°C (liquid nitrogen/acetonitrile bath). Butylmagnesium chloride (1.908 ml, 3.63 mmol) was added dropwise at such a rate as to keep the temperature under -5°C. The resulting white opaque mixture was stirred at −10°C for 30 min, then 2,5-dibromothiophene (0.4 M in toluene, 21 mL, 8.43 mmol), as a solution in toluene (20 mL), was added at such a rate as to keep the temperature under −5°C. After the addition was complete the mixture was stirred at -10°C for 1.5 h and di-*tert*-butyl dicarbonate (0.86 M in toluene, 12.5 mL, 10.79 mmol) was added at such a rate as to keep the temperature under −5 °C. After the addition was completed the mixture was stirred at -10°C for 2 h. The mixture was quenched by the addiction of citric acid (10% aqueous solution, 50 mL) which resulted in an exothermic generation of CO_2. The compound was extracted with dichloromethane, washed with citric acid (10% aqueous solution, 2 × 50 mL), water (2 × 50 mL), dried over $MgSO_4$, filtered and concentrated under vacuum to afford a yellow oil. Purification on silica gel, eluting with 40% dichloromethane in hexane, afforded the title compound as a light yellow oil (1.86 g, 7.05 mmol, 84 %); ^{1}H-NMR δ_{H} (400 MHz, Chloroform-*d*): 7.46 (1H, d, *J* = 3.9 Hz, Ar*H*), 7.03 (1H, d, *J* = 4.0 Hz, Ar*H*), 1.56 (9H, s, CH_3). This was consistent with the previously published data.[319]

3-Hydroxy-4-iodobenzoic acid (**3.9**)

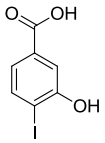

3-Hydroxybenzoic acid (25 g, 181 mmol) was dissolved in dry methanol (250 mL), then sodium hydroxide (7.52 g, 188 mmol) and sodium iodide (28.2 g, 188 mmol) were added and stirred until dissolved. The mixture was cooled to −10 °C and sodium hypochlorite (112 g, 188 mmol) was added dropwise over 1 hour at such a rate as to keep the temperature under 3°C. The resulting dark orange solution was stirred for 1 hour at 0°C and then at room temperature overnight to give a pale yellow suspension. The solvent was evaporated under reduced pressure, water was added (150 mL) and the solution acidified to pH 1 with concentrated hydrochloric acid. The precipitate was collected by filtration under reduced pressure, and washed with water. The solid was recrystallised from 20% ethanol in water to afford the title compound as a white solid (21.37 g, 81 mmol, 44.8 %); ^{1}H NMR δ_H (500 MHz, Dimethyl sulfoxide-d_6): 12.95 (1H, s, COO*H*), 10.67 (1H, s, ArO*H*), 7.79 (1H, d, *J* = 8.1 Hz, Ar*H*), 7.43 (1H, d, *J* = 1.9 Hz, Ar*H*), 7.13 (1H, dd, *J* = 8.1, 1.9 Hz, Ar*H*); ^{13}C NMR δ_C (126 MHz, Dimethyl sulfoxide-d_6): 166.9, 156.8, 139.1, 132.1, 121.6, 115.1, 90.9. This was consistent with the previously published data.[149]

Methyl 3-hydroxy-4-iodobenzoate (**3.10**)

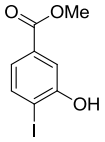

3-Hydroxy-4-iodobenzoic acid (**3.9**) (21.1 g, 80 mmol) was dissolved in methanol (250 mL). Concentrated sulfuric acid (7.3 mL, 129 mmol) was added and the mixture was heated at reflux for 20 h. The solution was cooled to 0°C and brought to pH 7 with $NaHCO_3$ (saturated aqueous solution). Methanol was removed under reduced pressure and the aqueous mixture was extracted with ethyl acetate (3 × 60 mL). The combined organic extracts were washed with brine (2 × 80 mL), water (2 × 80 mL), dried over $MgSO_4$, filtered and concentrated under reduced pressure to afford the title compound as a white solid (21.73 g, 78 mmol, 98 %); ^{1}H NMR δ_H (500 MHz, Chloroform-*d*): 7.75 (1H, d, *J* = 8.2 Hz, Ar*H*), 7.63 (1H, d, *J* = 2.0 Hz,

Ar*H*), 7.33 (1H, dd, *J* = 8.2, 2.0 Hz, Ar*H*), 5.63 (1H, s, ArO*H*), 3.91 (3H, s, $COOCH_3$). M.P.: 158-160ºC. This was consistent with the previously published data.[149]

Methyl 4-iodo-3-methoxybenzoate (**3.11**)

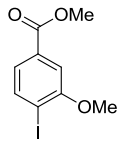

Methyl 3-hydroxy-4-iodobenzoate (**3.10**) (4 g, 14.39 mmol), potassium carbonate (2.58 g, 18.70 mmol) and dimethyl sulfate (1.65 mL, 17.26 mmol) were dissolved in acetone (170 mL) and then heated at reflux for 20 h under a nitrogen atmosphere. After this time water (100 mL) was added and the acetone was evaporated under reduced pressure. The product was then extracted with dichloromethane (3 × 70 mL), dried over $MgSO_4$, filtered and concentrated under reduced pressure to a yellow oil, which solidified upon standing to afford the title compound as a white solid (4.11 g, 14.07 mmol, 98 %); ^{1}H NMR δ_H (400 MHz, Chloroform-*d*): 7.84 (1H, d, *J* = 8.1 Hz, Ar*H*), 7.44 (1H, d, *J* = 1.8 Hz, Ar*H*), 7.35 (1H, dd, *J* = 8.1, 1.8 Hz, Ar*H*), 3.93 (3H, s, ArOCH_3), 3.91 (3H, s, COOCH_3); ^{13}C NMR δ_C (101 MHz, Chloroform-*d*): 166.6, 158.2, 139.5, 131.6, 123.3, 111.2, 92.7, 56.6, 52.4. M.P.: 48-50ºC. This was consistent with the previously published data.[149]

4,7-Bis(5-(trimethylstannyl)thiophen-2-yl)benzo[c][1,2,5]thiadiazole (**3.13**)

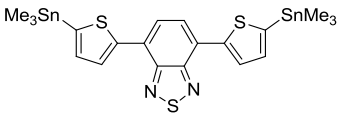

2,2,6,6-Tetramethylpiperidine (0.23 ml, 1.298 mmol) was dissolved in dry THF (10 mL) under nitrogen and *n*-butyllithium (2.28 M in hexane, 0.57 mL, 1.298 mmol) was added rapidly at −78 °C. The resulting solution was stirred at −78 °C for 30 min, then allowed to reach room temperature and stirred for an additional 10 min, to afford lithium 2,2,6,6-tetramethylpiperidide (LiTMP). The solution was cooled to −78 °C and 4,7-di(thiophen-2-yl)benzo[c][1,2,5]thiadiazole (**3.16**) (0.150 g, 0.499 mmol) in THF (15 mL) was added dropwise (during this time the colourless solution turned purple). The resulting solution was stirred at −78 °C for 45 min and trimethiltin chloride (1M in THF, 1.62 mL, 1.298 mmol) was added dropwise at - 78

°C (during this time the solution turned from purple to orange). The solution was then allowed to reach room temperature and stirred for 20 h. After this time the mixture was diluted with brine (20 mL) and extracted with dichloromethane (3 × 30 mL). The combined organic layers were washed with brine (3 × 60 mL), dried over $MgSO_4$, filtered and concentrated under reduced pressure. The dark orange residue was recrystallized from hot ethanol to give orange needle-like crystals (192 mg, 0.307 mmol, 61.4 %); ^{1}H- NMR δ_H (400 MHz, Chloroform-*d*): 8.21 – 8.17 (2H, m, Ar*H*), 7.88 (2H, s, Ar*H*), 7.30 (2H, d, *J* = 3.5 Hz, Ar*H*), 0.44 (18H, s, Ar*H*). This was consistent with the previously published data.[320]

4,7-Dibromobenzo[c][1,2,5]thiadiazole (**3.15**)

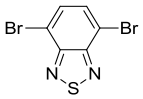

Benzo[c][1,2,5]thiadiazole (10 g, 73.4 mmol) was dissolved in hydrobromic acid (150 mL) and heated at reflux while a solution of bromine (11.35 mL, 220 mmol) in hydrochloric acid (80 mL) was added dropwise over 2 h. The mixture was heated at reflux for an additional 4 h, then was allowed to reach room temperature and stirred for 18 h. After this time the reaction was quenched by addiction of sodium thiosulfate (600 mL, saturated aqueous solution) and the precipitate was collected by filtration. The solid was recrystallised firstly from hot acetone and then from hot ethanol to afford the title compound as yellow needle shaped crystals (12.92 g, 44.0 mmol, 59.8 %); ^{1}H NMR, δ_H (400 MHz, Chloroform-*d*): 7.73 (2H, s). M.P.: 184-186. This was consistent with the previously published data.[321]

4,7-Di(thiophen-2-yl)benzo[c][1,2,5]thiadiazole (**3.16**)

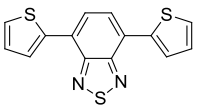

4,7-Dibromo-2,1,3-benzothiadiazole (**3.15**) (1.0 g, 3.40 mmol) and 2-(tributhylstannyl)thiophene (3.41 mL, 10.21 mmol) were dissolved under nitrogen in dry THF (15 mL) in a microwave vial. Tetrakis(triphenylphosphine) palladium(0) (0.786 g, 0.680 mmol) was added, the vial was sealed and the mixture was heated to 100 ºC in the microwave for 2 h. After this time a second portion of tetrakis(triphenylphosphine) palladium(0) (0.786 g, 0.680 mmol) was added and the

mixture was heated to 100 ºC in the microwave for an additional 2 h. Dichloromethane (20 mL) was added and the mixture was washed with water (3 × 100 mL), brine (2 ×100 mL), dried over MgSO4, filtered and concentrated under reduced pressure do afford a dark orange solid. Purification on silica gel, eluting with 20% dichloromethane in hexane, afforded the title compound as an orange solid (778 mg, 2.59 mmol, 76 %); ^{1}H NMR, δ_{H} (400 MHz, Chloroform-*d*): 8.12 (2H, dd, *J* = 3.7, 1.2 Hz, Ar*H*), 7.88 (2H, s, Ar*H*), 7.46 (2H, dd, *J* = 5.1, 1.2 Hz, Ar*H*), 7.22 (2H, dd, *J* = 5.1, 3.7 Hz, Ar*H*). M.P.: 112-114ºC. This was consistent with the previously published data.[100]

2-(Tributylstannyl)thiazole (**3.19**)

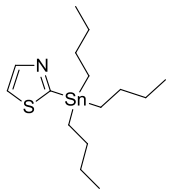

Thiazole (1.0 mL, 14.10 mmol) was dissolved under nitrogen in diethyl ether (80 mL). The solution was cooled to −78 °C, *n*-butyllithium (2.41 M, 6.43 mL, 15.51 mmol) was added dropwise and the solution was stirred at -50 °C for 1 h. Tributyltin chloride (4.59 mL, 16.92 mmol) was added dropwise at −78 °C, the mixture was allowed to reach room temperature and then was stirred for 20 h. After this time the mixture was washed with sodium hydrogen carbonate (3 × 50 mL), brine (3 × 50 mL), water (3 × 50 mL), dried over $MgSO_4$, filtered and concentrated under reduced pressure to afford a dark yellow oil. The oil was distilled (Kugelrohr, at 0.4 mbar and 170 °C) and then it was used without further purification (3.95 g) as a mixture with tributyltin chloride and unknown by-products; ^{1}H NMR, δ_{H} (400 MHz, Chloroform-*d*): 8.17 (1H, d, *J* = 3.0 Hz, Ar*H*), 7.54 (1H, d, *J* = 3.0 Hz, Ar*H*), aliphatic proton are difficult to integrate because they appear in the same region of tributyltin chloride (see Appendix).[155]

2-(Trimethylstannyl)-3,4-ethylenedioxythiophene (**3.20**)

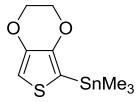

3,4-Ethylenedioxythiophene (0.5 g, 3.52 mmol) was dissolved in dry THF (20 mL) under nitrogen and the mixture was cooled to −78 °C. *n*-Butyllithium (2.39 M in hexane, 1.6 mL, 3.87 mmol) was added dropwise at −78 °C and the mixture stirred for 1 h at the same temperature. Trimethyltin chloride (1M in THF, 4.2 mL, 4.22 mmol) was added dropwise and the mixture was allowed to reach room temperature and stirred for 20 h. After this time, ammonium chloride (saturated aqueous solution, 100 mL) was added and the mixture was extracted with dichloromethane (3 × 50 mL). The combined organic layers were washed with water (3 × 100 mL), dried over $MgSO_4$, filtered and concentrated under reduced pressure to afford the title compound as a lightly pink solid (1.01 g) as a mixture with trimethyltin chloride and unknown by-products. The compound was used without further purification; ^{1}H NMR δ_H (400 MHz, Chloroform-*d*): 6.58 (1H, s, Ar*H*), 4.17 (4H, s, CH_2), 0.35 (9H, s, Sn(CH_3)$_3$). This was consistent with the previously published data.[322]

4,7-Di(thiazol-2-yl)benzo[c][1,2,5]thiadiazole (**3.21**)

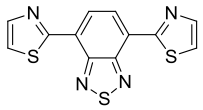

4,7-Dibromo-2,1,3-benzothiadiazole (**3.15**) (0.650 g, 2.211 mmol) and 2-(tributylstannyl)thiazole (**3.19**) (2.90 g, 7.74 mmol) were dissolved under nitrogen in dry DMF (10 mL) in a microwave vial. Tetrakis(triphenylphosphine) palladium(0) (0.639 g, 0.553 mmol) was added, the vial was sealed and the mixture was heated to 110 ºC in the microwave for 3 h. After this time chloroform (30 mL) was added and the mixture was washed with brine (3 × 50 mL), water (3 × 50 mL), dried over $MgSO_4$, filtered and concentrated under reduced pressure do afford a dark yellow solid. Purification on silica gel, eluting with 2% to 5% ethyl acetate in toluene, afforded a dark yellow solid. Recrystallisation from hot chloroform afforded the title compound as a yellow solid (94 mg, 0.311 mmol, 14.1 %); ^{1}H NMR δ_H (400 MHz, Chloroform-*d*): 8.76 (2H, s, Ar*H*), 8.07 (2H, d, *J* = 3.2 Hz, Ar*H*), 7.63 (2H, d, *J* = 3.2 Hz, Ar*H*); ^{13}C NMR δ_H (101 MHz, Chloroform-*d*): 162.0, 152.1, 143.6, 127.5, 126.7,

122.5; *m/z* (%) (MALDI-TOF) 301.81 (100), 302.82 (80), 303.81 (30). This was consistent with the previously published data.[156]

4,7-Di(3,4-ethylenedioxythiophen-2-yl)benzo[c][1,2,5]thiadiazole (**3.22**)

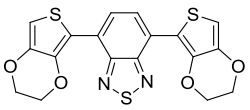

4,7-Dibromo-2,1,3-benzothiadiazole (**3.15**) (1 g, 3.40 mmol) and 2-(trimethylstannyl)-3,4-ethylenedioxythiophene (**3.20**) (3.11 g, 10.21 mmol) were dissolved under nitrogen in dry DMF (15 mL) in a microwave vial. Tetrakis(triphenylphosphine) palladium(0) (0.197 g, 0.170 mmol) was added, the vial was sealed and the mixture was heated to 140 ºC in the microwave for 2 h. After this time a second portion of tetrakis(triphenylphosphine) palladium(0) (0.590 g, 0.510 mmol) was added and the mixture was heated to 160 ºC in the microwave for an additional 2 h. Dichloromethane (20 mL) was added and the mixture was washed with water (3 × 100 mL), brine (2 ×100 mL), dried over $MgSO_4$, filtered and concentrated under reduced pressure to afford a dark orange solid. Purification on silica gel, eluting with 30% to 60% dichloromethane in hexane, afforded the title compound as a dark red solid (477 mg, 1.145 mmol, 33.7 %); ^{1}H NMR, δ_H (400 MHz, Chloroform-*d*): 8.39 (2H, s, Ar*H*), 6.56 (2H, s, Ar*H*), 4.42 – 4.38 (4H, m, CH_2), 4.33 – 4.29 (4H, m, CH_2). This was consistent with the previously published data.[323]

4,4'-(Benzo[c][1,2,5]thiadiazole-4,7-diyl)bis(3-methoxybenzoic acid) (**4.1**)

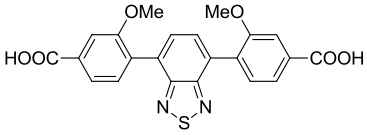

Dimethyl 4,4'-(benzo[c][1,2,5]thiadiazole-4,7-diyl)bis(3-methoxybenzoate) (**3.3**) (0.385 g, 0.829 mmol) was dissolved in THF (150 mL) under nitrogen. Sodium hydroxide (2M aqueous, 14.9 mL, 29.8 mmol) was added and the mixture was heated to 75°C for 20 h. After this time the obtained yellow suspension was dissolved in sodium hydroxide (2M aqueous solution, 100 mL) and the organic solvent was evaporated under reduced pressure. The resulting basic solution was acidified with concentrated hydrogen chloride until pH 1, stirred at room temperature

for 1 h and then cooled (or stored) at −20°C for 20 h. The mixture was filtered under reduced pressure, washed with water (3 × 50 mL) and dried under reduced pressure to obtain a yellow powder (350 mg, 0.802 mmol, 97 %); ^{1}H NMR δ_H (400 MHz, DMSO-d_6): 13.16 (2H, s, COO*H*), 7.79 (2H, s, Ar*H*), 7.72 – 7.68 (4H, m, Ar*H*), 7.63 (2H, d, *J* = 8.1 Hz, Ar*H*), 3.81 (6H, s, OCH_3); ^{13}C NMR δ_H (101 MHz, DMSO-d_6): 167.1, 156.8, 153.3, 132.3, 131.7, 130.4, 130.0, 129.8, 121.5, 111.9, 55.7; *m/z* (%) (MALDI-TOF) 436.15 (90), 437.17 (100), 438.16 (60), 439.19 (15); HRMS (LSI-TOF) *m/z*: $[M - H]^-$ Calcd for $C_{22}H_{15}N_2O_6S$ 435.0656; Found 435.0649; TGA: 5% loss of mass at 324 ºC, 10% loss of the mass at 351 ºC; T_m = 239 ºC; M.P.: 352-354ºC.

4,7-Bis(4-(2-ethylhexyl)-5-(trimethylstannyl)thiophen-2-yl)benzo[c][1,2,5]thiadiazole (**4.2**)

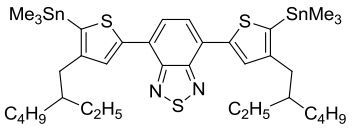

2,2,6,6-Tetramethylpiperidine (0.27 mL, 1.553 mmol) was dissolved in dry THF (10 mL) under nitrogen. *n*-Butyllithium (2.42 M in hexane, 0.64 mL, 1.553 mmol) was added to the solution rapidly at −78 °C. The resulting mixture was stirred at −78 °C for 30 min, then was allowed to reach room temperature and stirred for 10 min, to afford lithium 2,2,6,6-tetramethylpiperidide (LiTMP). The solution was further cooled to −78 °C and 4,7-bis(4-(2-ethylhexyl)thiophen-2-yl)benzo[c][1,2,5]thiadiazole (**4.8**) (0.330 g, 0.597 mmol) in THF (15 mL) was added dropwise. The resulting solution was stirred at - 78 °C for 45 min, followed by by trimethyltin chloride (1.55 mL, 1.553 mmol) dropwise. The mixture was then allowed to reach room temperature and stirred overnight. After this time brine (50 mL) was added and the mixture was extracted into dichloromethane (3 × 50 mL), washed with brine (3 × 50 mL), dried over $MgSO_4$, filtered and concentrated under reduced pressure to afford an orange residue. The residue was recrystallized from boiling ethanol to give the title compound as orange needle-like crystals (497 mg, 0.584 mmol, 98 %), which were used without further purification; ^{1}H NMR δ_H (400 MHz, Chloroform-*d*): 8.04 (2H, s, Ar*H*), 7.82 (2H, s, Ar*H*), 2.62 (4H, d, *J* = 7.5 Hz, CH_2), 1.71 – 1.65 (2H, m, C*H*), 1.42 – 1.30 (16H, m, CH_2), 0.92 – 0.88 (12H, m, CH_3), 0.51 – 0.37 (18H, m, Sn(CH_3)$_3$).

4,7-Bis(4-(2-octyldodecyl)-5-(trimethylstannyl)thiophen-2-yl)benzo[c][1,2,5]thiadiazole (**4.3**)

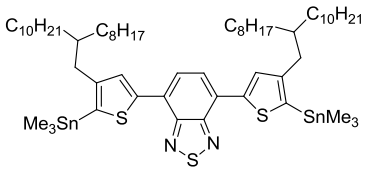

2,2,6,6-Tetramethylpiperidine (0.183 ml, 1.056 mmol) was dissolved into dry THF (25 mL) under nitrogen. *n*-Butyllithium (2.3 M in hexane, 0.46 mL, 1.056 mmol) was added into the solution rapidly at −78 °C. The resulting solution was stirred at −78 °C for 30 min, and was then allowed to reach room temperature and stirred for 10 min, to afford lithium 2,2,6,6-tetramethylpiperidide (LiTMP). The solution was cooled to −78 °C and 4,7-bis(4-(2-octyldodecyl)thiophen-2-yl)benzo[c][1,2,5]thiadiazole (**4.9**) (0.350 g, 0.406 mmol) in THF (15 mL) was added in a dropwise manner. The resulting solution was stirred at −78 °C for 45 min and trimethyltin chloride (1.06 mL, 1.056 mmol) was then added dropwise. The solution was then allowed to reach room temperature and stirred overnight. After this time brine (50 mL) was added and the mixture was extracted into dichloromethane (3 × 50 mL), washed with brine (3 × 50 mL), dried over $MgSO_4$, filtrated and concentrated under reduced pressure to afford the title compound (454 mg, 0.382 mmol, 94 % yield), which was used without further purification; ^{1}H NMR δ_H (400 MHz, Chloroform-*d*): 8.05 (2H, s, Ar*H*), 7.82 (2H, s, Ar*H*), 2.65 – 2.57 (4H, m, CH_2), 1.77 – 1.69 (2H, m, C*H*), 1.33 – 1.20 (64H, m, CH_2), 0.89 – 0.83 (12H, m, CH_3), 0.43 (18H, s, Sn(CH_3)$_3$).

3-(2-Ethylhexyl)thiophene (**4.4**)

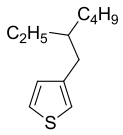

Magnesium turnings (1.349 g, 55.5 mmol) were suspended in dry THF (10 mL) under nitrogen. 2-Ethylhexyl bromide (9.11 ml, 51.2 mmol) was added dropwise at a rate sufficient to maintain reflux. The reflux was then maintained for 2 h and the mixture was allowed to reach room temperature. The resulting mixture was added *via* cannula under nitrogen to a mixture of 3-bromothiophene (4 mL, 42.7 mmol) and 1,3-bis(diphenylphosphino)propane-nickel(II) chloride (0.231 g, 0.427 mmol) in dry

THF (20 mL). The resulting mixture was stirred at reflux for 20 h. After this time the reaction was quenched with concentrated hydrochloric acid (10 mL) and then extracted with dichloromethane (3 × 50 mL). The combined organic layers were washed with brine (2 × 50 mL), water (2 × 50 mL), dried over $MgSO_4$, filtered and concentrated under reduced pressure. Purification on silica gel, eluting with hexane afforded the title compound as colourless oil (4.39 g, 22.36 mmol, 52.4 %), which was used without further purification; ^{1}H NMR δ_H (400 MHz, Chloroform-*d*): 7.23 (1H, dd, *J* = 4.9, 2.9 Hz, Ar*H*), 6.93 – 6.87 (2H, m, Ar*H*), 2.56 (2H, d, *J* = 6.9 Hz, CH_2), 1.63 – 1.54 (1H, m, C*H*), 1.29 – 1.25 (8H, m, CH_2), 0.90 – 0.87 (6H, m, CH_3). This was consistent with previously published data.[324]

3-(2-Hexyldodecyl)thiophene (**4.5**)

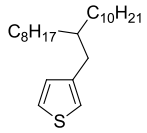

Magnesium turnings (0.506 g, 20.81 mmol) were suspended in dry THF (5 mL) under nitrogen. 9-(Bromomethyl)nonadecane (6.94 g, 19.21 mmol) in dry THF (15 mL) was added dropwise at a rate sufficient to maintain reflux. The reflux was then maintained for 2 h and the mixture was allowed to reach room temperature. The resulting mixture was added *via* cannula under nitrogen to a mixture of 3-bromothiophene (1.5 mL, 16.01 mmol) and 1,3-bis(diphenylphosphino)propane-nickel(II) chloride (0.087 g, 0.160 mmol) in dry THF (30 mL). The resulting mixture was stirred at reflux for 20 h. After this time the reaction was quenched with concentrated hydrochloric acid (10 mL) and then extracted with dichloromethane (3 × 50 mL). The combined organic layers were washed with brine (2 × 50 mL), water (2 × 50 mL), dried over $MgSO_4$, filtered and concentrated under reduced pressure. Purification on silica gel, eluting with hexane, afforded the title compound as a light yellow oil (2.69 g, 7.99 mmol, 49.9 %), which was used without further purification; ^{1}H NMR δ_H (400 MHz, Chloroform-*d*): 7.22 (1H, dd, *J* = 4.9, 2.9 Hz, Ar*H*), 6.91 – 6.87 (2H, m, Ar*H*), 2.56 (2H, d, *J* = 6.8 Hz, CH_2), 1.63 – 1.56 (1H, m, C*H*), 1.28 – 1.21 (32H, m, CH_2), 0.88 (6H, t, *J* = 6.8 Hz, CH_3). This was consistent with the previously published data.[325]

(4-(2-Ethylhexyl)thiophen-2-yl)trimethylstannane (**4.6**)

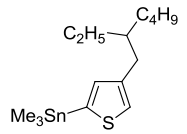

3-(2-Ethylhexyl)thiophene (**4.4**) (2.0 g, 10.19 mmol) and N,N,N',N'-tetramethylethylenediamine (1.70 mL, 11.20 mmol) were dissolved in dry diethyl ether (20 mL) under nitrogen. *n*-Butyllithium (2.30 M in hexane, 4.45 mL, 10.24 mmol) was added and the mixture was heated at reflux for 1 h. The mixture was cooled at 0°C, trimethyltin chloride (15.28 ml, 15.28 mmol) was added dropwise and the mixture was stirred at room temperature for 20 h. After this time brine (50 mL) was added and the mixture was extracted with diethyl ether (3 × 50 mL). The combined organic layers were washed with water (3 × 50 mL), dried over $MgSO_4$, filtered and concentrated under reduced pressure to afford a light yellow oil (3.44 g, 9.58 mmol, 94 %), which was used without further purification; ^{1}H NMR δ_H (400 MHz, Chloroform-*d*): 7.16 (1H, s, Ar*H*), 6.96 (1H, s, Ar*H*), 2.59 (2H, d, *J* = 6.9 Hz, CH_2), 1.60 – 1.55 (1H, m, C*H*), 1.29 – 1.25 (8H, m, CH_2), 0.90 – 0.87 (6H, m, CH_3), 0.35 (9H, s, Sn(CH_3)$_3$). This was consistent with the previously published data.[326]

Trimethyl(4-(2-octyldodecyl)thiophen-2-yl)stannane (**4.7**)

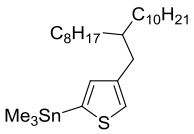

3-(2-Octyldodecyl)thiophene (**4.5**) (2.65 g, 7.27 mmol) and N,N,N',N'-tetramethylethylenediamine (1.21 mL, 7.99 mmol) were dissolved in dry diethyl ether (25 mL) under nitrogen. *n*-Butyllithium (2.3 M in hexane, 3.18 mL, 7.30 mmol) was added, the mixture was heated at reflux for 1 h and then cooled at 0°C. Trimethyltin chloride (10.90 mL, 10.90 mmol) was added dropwise and the mixture was stirred at room temperature for 20 h. After this time brine (50 mL) was added and the mixture was extracted with diethyl ether (3 × 50 mL). The combined organic layers were washed with water (3 × 50 mL), dried over $MgSO_4$, filtered and concentrated under reduced pressure to afford a light yellow oil (3.79 g, 7.19 mmol, 99 %), which was used without further purification; ^{1}H NMR δ_H (400 MHz, Chloroform-*d*): 7.15 (1H, d, *J* = 0.9 Hz, Ar*H*), 6.95 (1H, d, *J* = 1.0 Hz, Ar*H*), 2.58

(2H, d, J = 6.7 Hz, CH_2), 1.65 – 1.57 (1H, m, CH_2), 1.27 – 1.24 (32H, m, CH_2), 0.90 – 0.87 (6H, m, CH_3), 0.35 (9H, s, Sn(CH_3)$_3$).

4,7-Bis(4-(2-ethylhexyl)thiophen-2-yl)benzo[c][1,2,5]thiadiazole (**4.8**)

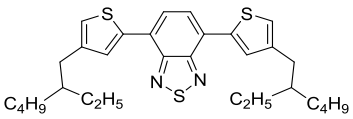

4,7-Dibromo-2,1,3-benzothiadiazole (**3.15**) (0.35 g, 1.191 mmol), and (4-(2-ethylhexyl)thiophen-2-yl)trimethylstannane (**4.6**) (1.425 g, 3.57 mmol) were dissolved under nitrogen in THF (10 mL) in a microwave vial. Tetrakis(triphenylphosphine)palladium(0) (0.275 g, 0.238 mmol) was added and the solution was heated at 100 °C for 2 h in the microwave. After this time, a second portion of tetrakis(triphenylphosphine)palladium(0) (0.275 g, 0.238 mmol) was added. The mixture was heated at 110 °C for 3.5 h in the microwave and then stirred at room temperature for 18 h. After this time the mixture was diluted with dichloromethane (50 mL), washed with water (3 × 50 mL), brine (50 mL), dried over $MgSO_4$, filtered and concentrated under reduced pressure. Purification on silica gel, eluting with 20% dichloromethane in hexane, afforded an orange residue that was recrystallised from boiling ethanol to afford the title compound as an orange powder (330 mg, 0.629 mmol, 52.8 %). The compound was used without further purification; ^{1}H NMR δ_H (400 MHz, Chloroform-*d*): 7.95 (2H, d, J = 1.4 Hz, Ar*H*), 7.83 (2H, s, Ar*H*), 7.02 (2H, d, J = 1.3 Hz, Ar*H*), 2.64 (4H, d, J = 6.9 Hz, CH_2), 1.73 – 1.60 (2H, m, C*H*), 1.39 – 1.29 (16H, m, CH_2), 0.94 – 0.88 (12H, m, CH_3). This was consistent with the previously published data.[327]

4,7-Bis(4-(2-octyldodecyl)thiophen-2-yl)benzo[c][1,2,5]thiadiazole (**4.9**)

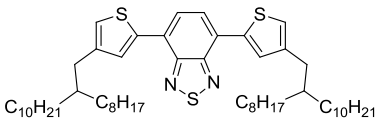

4,7-Dibromo-2,1,3-benzothiadiazole (**3.15**) (0.35 g, 1.191 mmol), and trimethyl(4-(2-octyldodecyl)thiophen-2-yl)stannane (**4.7**) (1.88 g, 3.57 mmol) were dissolved under nitrogen in THF (10 mL) in a microwave vial. Tetrakis(triphenylphosphine) palladium(0) (0.275 g, 0.238 mmol) was added and the solution was heated at 100 °C for 2 h in the microwave. After this time, a second portion of

tetrakis(triphenylphosphine) palladium(0) (0.275 g, 0.238 mmol) was added. The mixture was heated at 110 °C for 3.5 h in the microwave and then stirred at room temperature for 18 h. After this time the mixture was diluted with dichloromethane, washed with water (3 × 50 mL), brine (50 mL), dried over $MgSO_4$, filtered and concentrated under reduced pressure. Purification on silica gel, eluting with 10% dichloromethane in hexane, afforded an orange residue that was recrystallised from ethanol to afford the title compound as an orange powder (379 mg, 0.440 mmol, 37.0 % yield); ^{1}H NMR δ_H (400 MHz, Chloroform-*d*): 7.95 (2H, d, *J* = 1.4 Hz, Ar*H*), 7.83 (2H, s, Ar*H*), 7.01 (2H, d, *J* = 1.3 Hz, Ar*H*), 2.63 (4H, d, *J* = 6.7 Hz, CH_2), 1.75 – 1.65 (2H, m, C*H*), 1.35 – 1.22 (64H, m, CH_2), 0.91 – 0.84 (12H, m, CH_3). This was consistent with the previously published data.[93]

MOF-**4.1.A**

$Zn(NO_3)_2 \cdot 6\ H_2O$ (23 mg, 0.075 mmol), 4,4'-(benzo[c][1,2,5]thiadiazole-4,7-diyl)bis(3-methoxybenzoic acid) (**4.1**) (11 mg, 0.025 mmol) and 4,4'-bipyridine (7.5 mg, 0.05 mmol) were combined in N,N-dimethylformamide (8 mL) and then sonicated. The solution was filtered, decanted into two 20 mL screw-top scintillation vials and sealed. On heating in an oven at 80 °C for 48 h, yellow block shaped crystals of **$[Zn_2L_2(bipy)]_n$** formed. The yield was not recorded.

MOF-**4.1.B**

$ZrCl_4$ (12 mg, 0.05 mmol), 4,4'-(benzo[c][1,2,5]thiadiazole-4,7-diyl)bis(3-methoxybenzoic acid) (**4.1**) (22 mg, 0.05 mmol) and L-proline (23 mg, 0.2 mmol) were dissolved in N,N-dimethylformamide (20 ml) assisted by sonication (10 min). Hydrochloric acid (6 M aqueous, 0.01 mL) was added and the resulting solution was sonicated for a further 10 min. The solution was added to a 50 ml screw-top pyrex jar, sealed, and placed in an oven at 100 °C for 16 h. The yellow precipitate obtained was isolated by centrifugation, washed with DMF (20 mL), acetone (2 × 20 mL) and dried under vacuum to yield **$[Zr_6O_4(OH)_4L_6]_n$** (55 mg, 77%).

POP-**4.12**

4,7-Bis(5-(trimethylstannyl)thiophen-2-yl)benzo[c][1,2,5]thiadiazole (**3.13**) (197 mg, 0.314 mmol), tris(dibenzylideneacetone)dipalladium(0) (7 mg, 7.86 μmol), tetrakis(4-bromophenyl)methane (**4.10**) (100 mg, 0.157 mmol) and tri-o-tolylphosphine (10 mg, 0.031 mmol) were dissolved in chlorobenzene (3 mL) under

nitrogen in a microwave vial. The mixture was heated in the microwave at 160 °C for 2 h, then poured in hydrochloric acid (5% in methanol, 25 mL) and stirred for 30 min. After this time the mixture was filtered and the collected dark red solid was purified by Soxhlet extraction with methanol, acetone, hexane and dichloromethane successively for 48 h each. The dark red solid obtained was then dried under vacuum to afford the title compound (138 mg, 0.142 mmol, 90 %). The compound was insoluble in the common organic solvents. Anal. Calculated for $C_{53}H_{32}N_4S_6$: C, 69.40; H, 3.52; N, 6.11; Found: C, 65.60; H, 2.84; N, 5.62; TGA: 5% loss of mass a 505 ºC, 10% loss of the mass at 578 ºC; M.P.: not revealed until 320ºC.

POP-**4.13**

4,7-Bis(5-(trimethylstannyl)thiophen-2-yl)benzo[c][1,2,5]thiadiazole (**3.13**) (166 mg, 0.264 mmol), tris(dibenzylideneacetone)dipalladium(0) (6.05 mg, 6.61 µmol), 1,3,5,7-tetrakis(4-bromophenyl)adamantane (**4.11**) (100 mg, 0.132 mmol) and tri-o-tolylphosphine (8.05 mg, 0.026 mmol) were dissolved in chlorobenzene (5 mL) under nitrogen in a microwave vial. The mixture was heated in the microwave at 160 °C for 2 h. After this time tributyl(thiophen-2-yl)stannane (49.3 mg, 0.132 mmol) was added and the mixture was heated in the microwave at 160 °C for 10 min. Bromobenzene (20.76 mg, 0.132 mmol) was then added and the mixture was heated in the microwave at 160 °C for 10 min. After this time the mixture was filtered and the collected dark red solid was purified by Soxhlet extraction with methanol, acetone, hexane and dichloromethane successively for 48 h each. The dark red solid obtained was then dried under vacuum to afford the title compound (140 mg, 0.106 mmol, 80 %). The compound was insoluble in common solvents; Anal. Calculated for $C_{84}H_{60}N_4S_6$: C, 76.56; H, 4.59; N, 4.25; Found: C, 67.92; H, 3.76; N, 4.77; TGA: 5% loss of mass at 392 ºC, 10% loss of the mass at 472 ºC; M.P.: not revealed until 320ºC.

POP-**4.14**

4,7-Bis(4-(2-octyldodecyl)-5-(trimethylstannyl)thiophen-2-yl)benzo[c][1,2,5] thiadiazole (**4.3**) (249 mg, 0.292 mmol), tris(dibenzylideneacetone)dipalladium(0) (6.7 mg, 7.31 µmol), tetrakis(4-bromophenyl)methane (**4.10**) (93 mg, 0.146 mmol) and tri-*o*-tolylphosphine (8.9 mg, 0.029 mmol) were dissolved in chlorobenzene (5 mL) under nitrogen in a microwave vial. The mixture was heated in the microwave

at 160 °C for 2 h. After this time tributyl(thiophen-2-yl)stannane (33 mg, 0.088 mmol) was added and the mixture was heated in the microwave at 160 °C for 10 min. Bromobenzene (13.8 mg, 0.088 mmol) was then added and the mixture was heated in the microwave at 160 °C for 10 min. After this time dichloromethane (30 mL) was added and the mixture was washed with water (3 × 50 mL), dried over $MgSO_4$, filtrated and concentrated under reduced pressure. The title compound was obtained as a mixture with the reactants and unknown by-products (247 mg). Purification was not possible; in fact the mixture obtained showed excellent solubility in common organic solvents that did not allow the isolation of the residual reactants. This polymer was not tested further.

POP-**4.15**

4,7-Bis(4-(2-ethylhexyl)-5-(trimethylstannyl)thiophen-2-yl)benzo[c][1,2,5]thiadiazole (**4.2**) (249 mg, 0.292 mmol), tris(dibenzylideneacetone)dipalladium(0) (7 mg, 7.31 µmol), tetrakis(4-bromophenyl)methane (**4.10**) (93 mg, 0.146 mmol) and tri-o-tolylphosphine (9 mg, 0.029 mmol) were dissolved in dry chlorobenzene (5 mL) under nitrogen in a microwave vial. The mixture was heated in the microwave at 160 °C for 2 h. After this time tributyl(thiophen-2-yl)stannane (33 mg, 0.088 mmol) was added and the mixture was heated in the microwave at 160 °C for 10 min. Bromobenzene (13.77 mg, 0.088 mmol) was then added and the mixture was heated in the microwave at 160 °C for 10 min. After this time the mixture was concentrated under reduced pressure. The residue was dissolved in 1 mL of boiling dichloromethane, cold methanol (30 mL) was added and the mixture was cooled to −30°C for one hour. The mixture was filtered and the collected dark red solid was purified by Soxhlet extraction with methanol, acetone and hexane successively for 24 h each. The dark red solid obtained was then dried under vacuum to afford the title compound (177 mg, 0.105 mmol, 71.9 %); Anal. Calculated for $C_{105}H_{108}N_4S_8$: C, 74.95; H, 6.47; N, 3.33; Found: C, 63.47; H, 5.51; N, 2.52; TGA: 5% loss of mass at 415 ºC, 10% loss of the mass at 481 ºC; M.P.: not revealed until 320ºC.

POP-**4.16**

4,7-Bis(4-(2-ethylhexyl)-5-(trimethylstannyl)thiophen-2-yl)benzo[c][1,2,5]thiadiazole (**4.2**) (225 mg, 0.264 mmol), tris(dibenzylideneacetone)dipalladium(0) (6 mg, 6.61 µmol), 1,3,5,7-tetrakis(4-bromophenyl)adamantine (**4.11**) (100 mg, 0.132

mmol) and tri-*o*-tolylphosphine (8 mg, 0.026 mmol) were dissolved in chlorobenzene (5 mL) under nitrogen in a microwave vial. The mixture was heated in the microwave at 160 °C for 2 h. After this time tributyl(thiophen-2-yl)stannane (29.6 mg, 0.079 mmol) was added and the mixture was heated in the microwave at 160 °C for 10 min. Bromobenzene (12.46 mg, 0.079 mmol) was then added and the mixture was heated in the microwave at 160 °C for 10 min. After this time the mixture was concentrated under reduced pressure. The residue was dissolved in 1 mL of boiling dichloromethane, cold methanol (30 mL) was added and the mixture was cooled at −30°C for 1 h. The mixture was filtered and the collected dark red solid was purified by Soxhlet extraction with methanol, acetone and hexane successively for 24 h each. The dark red solid obtained was then dried under vacuum to afford the title compound (122 mg, 0.069 mmol, 52.2 %); Anal. Calculated for $C_{116}H_{124}N_4S_6$: C, 78.87; H, 7.08; N, 3.17; Found: C, 70.46; H, 6.08; N, 3.07; TGA: 5% loss of mass at 379 ºC, 10% loss of the mass at 421 ºC; M.P.: not revealed until 320ºC.

Chapter 7. Appendix

a)

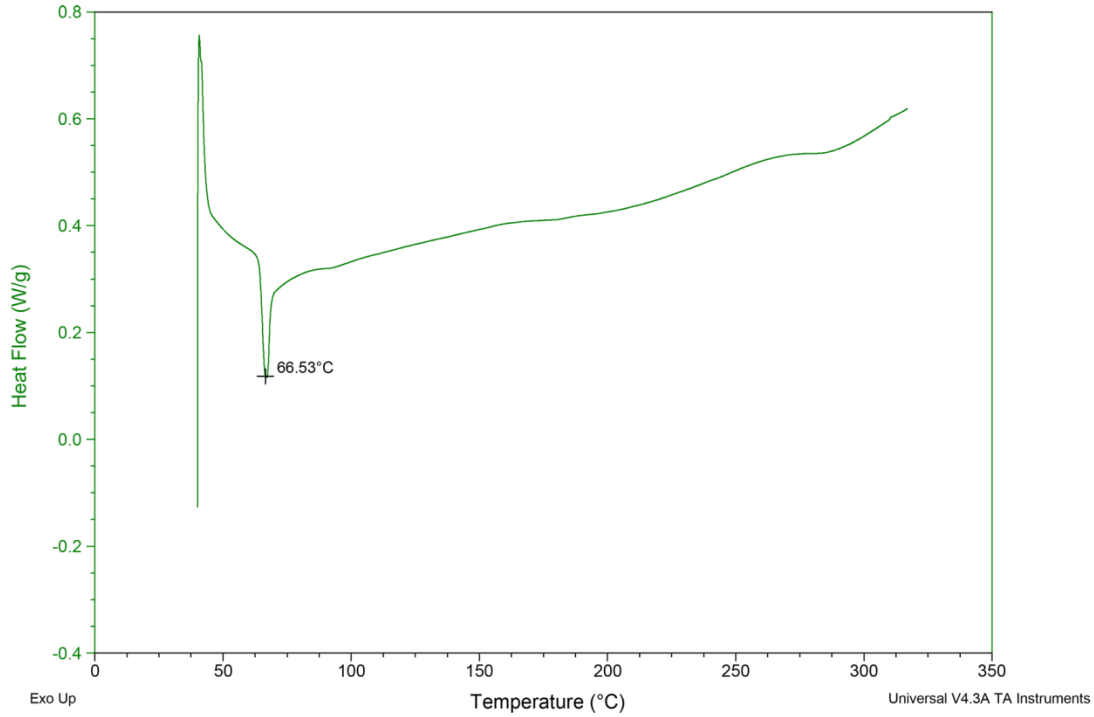
0.8
0.6
0.4
0.2
0.0
-0.2
-0.4
Heat Flow (W/g)
66.53°C
0
50
100
150
200
250
300
350
Exo Up
Temperature (°C)
Universal V4.3A TA Instruments

b)

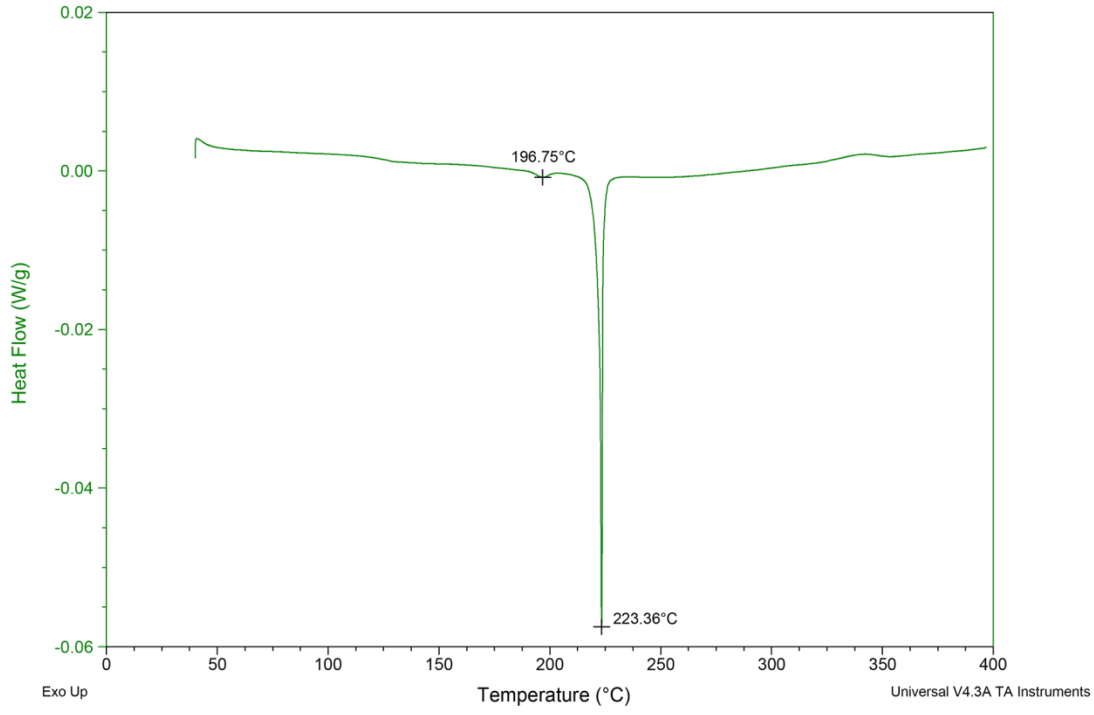
0.02
0.00
-0.02
-0.04
-0.06
Heat Flow (W/g)
196.75°C
223.36°C
0
50
100
150
200
250
300
350
400
Exo Up
Temperature (°C)
Universal V4.3A TA Instruments

c)

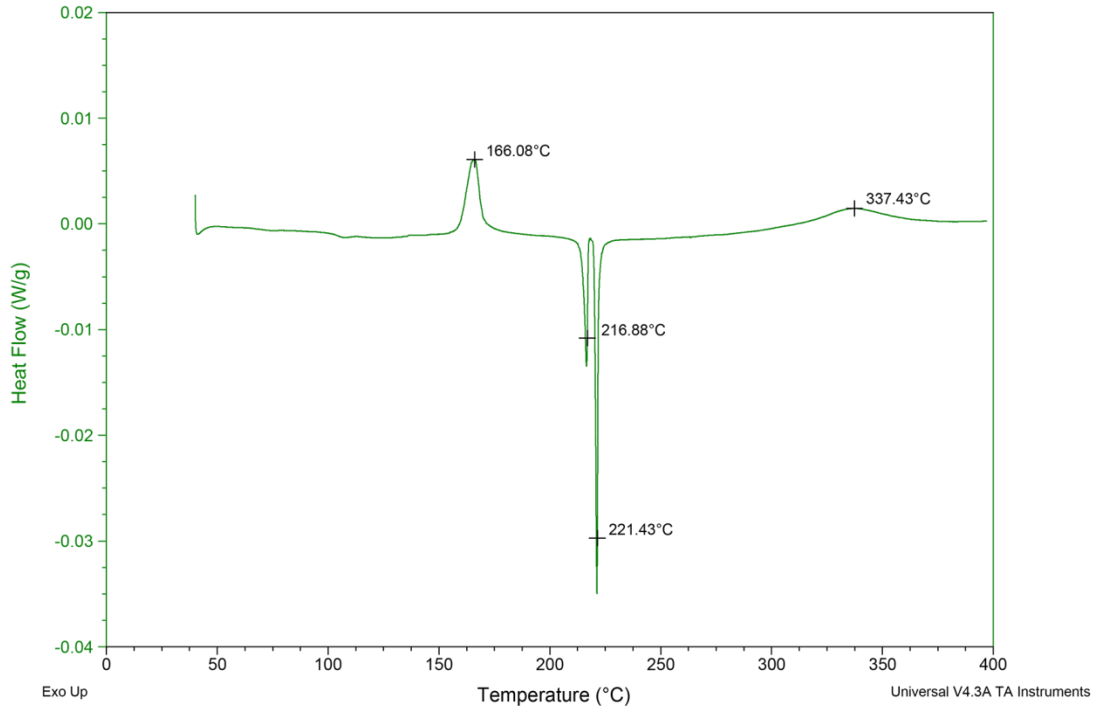
0.02
0.01
0.00
-0.01
-0.02
-0.03
-0.04
Heat Flow (W/g)
166.08°C
337.43°C
216.88°C
221.43°C
0
50
100
150
200
250
300
350
400
Exo Up
Temperature (°C)
Universal V4.3A TA Instruments

d)

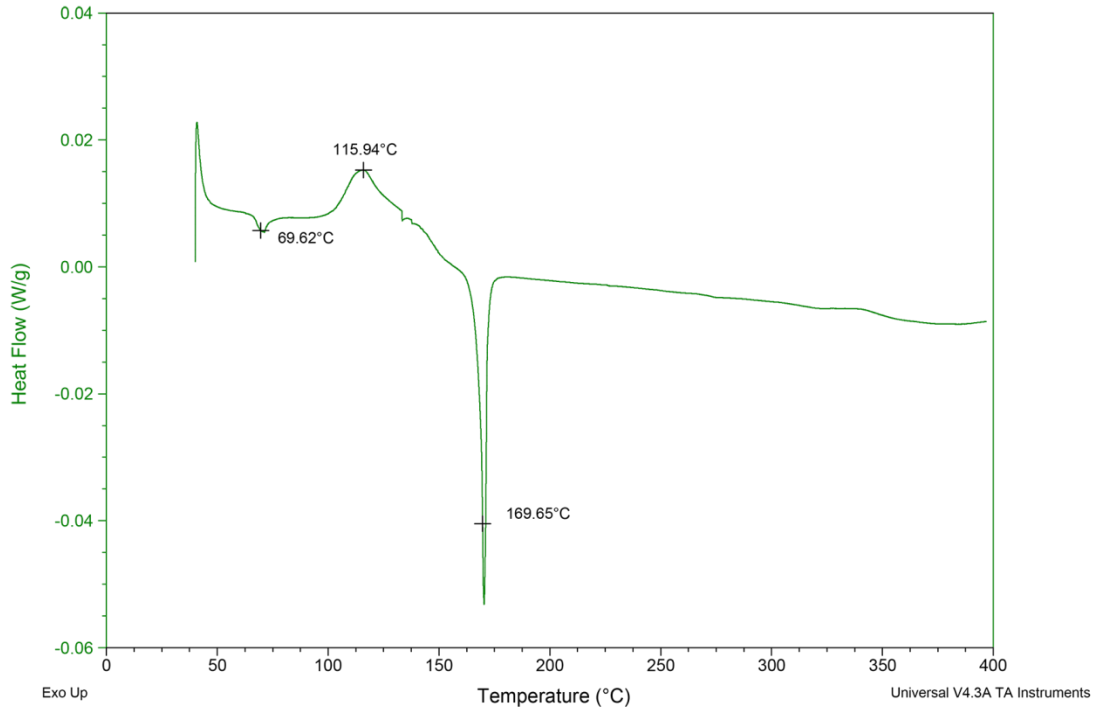
0.04
0.02
0.00
-0.02
-0.04
-0.06
Heat Flow (W/g)
115.94°C
69.62°C
169.65°C
0
50
100
150
200
250
300
350
400
Exo Up
Temperature (°C)
Universal V4.3A TA Instruments

e)

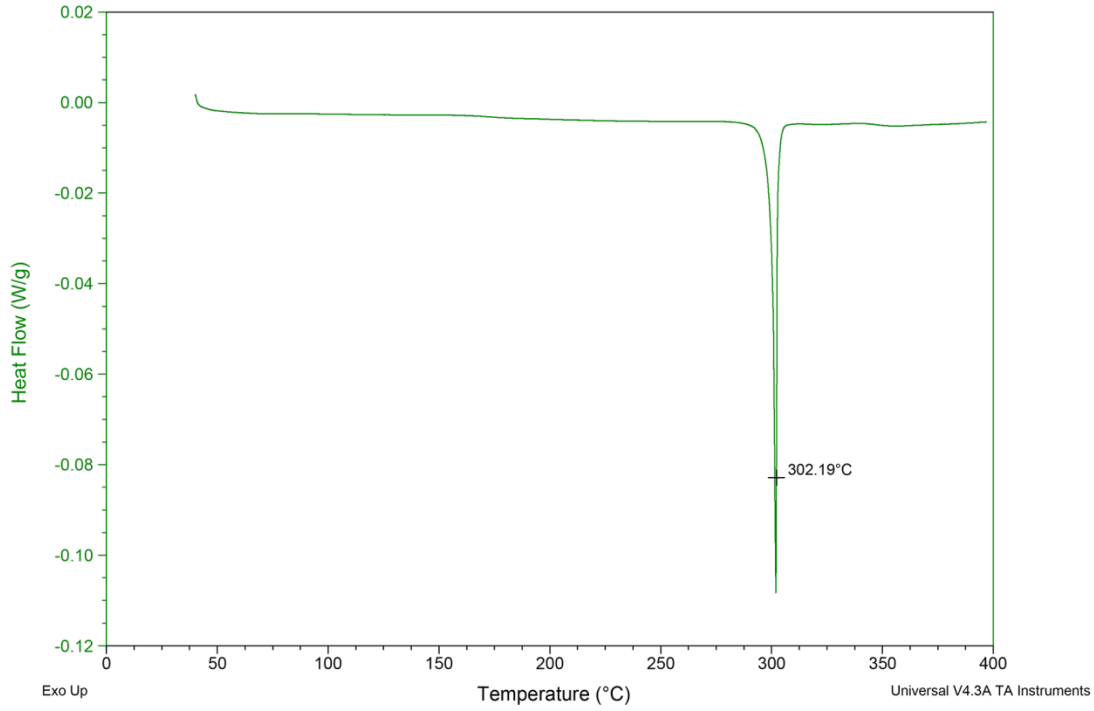

Figure 7.1 DSC spectra of compounds **2.1** (a), **2.2** (b), **2.3** (c) **2.4** (d) and **2.5** (e).

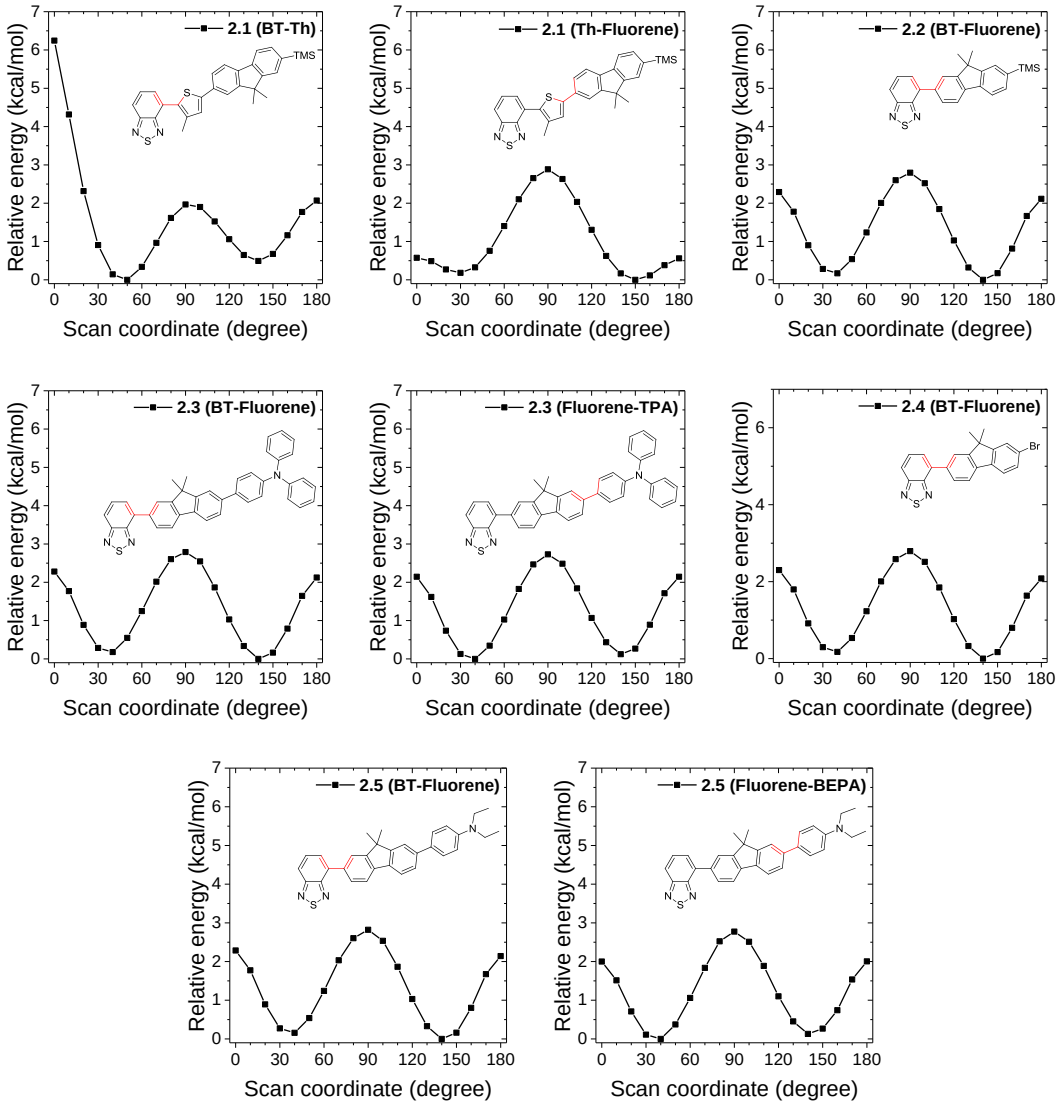

Figure 7.2 Torsional potential surfaces for the fragments of compounds **2.1**-**2.5** calculated at the CAM-B3LYP/6-311(d,g) level of theory. Rotation occurs around the inter-ring C−C bond marked in red, starting from the conformation shown (0°) in the respective graph.

Table 7.1 Torsional potential relative energies for the fragments of compounds **2.1-2.5** calculated at the CAM-B3LYP/6-311(d,g) level of theory.

Torsional angle	2.1		2.2	2.3		2.4	2.5	
	BT-Th	Th-Fluorene	BT-Fluorene	BT-Fluorene	Fluorene-TPA	BT-Fluorene	BT-Fluorene	Fluorene-BEPA
	Relative energy (kcal/mol)							
0	6.25	0.57	2.29	2.28	2.15	2.30	2.29	2.00
10	4.32	0.49	1.78	1.77	1.62	1.80	1.77	1.51
20	2.31	0.27	0.90	0.89	0.74	0.91	0.89	0.71
30	0.91	0.18	0.28	0.29	0.13	0.30	0.27	0.11
40	0.14	0.32	0.17	0.18	0.00	0.18	0.16	0.00
50	0.00	0.76	0.54	0.55	0.35	0.54	0.54	0.37
60	0.34	1.40	1.24	1.25	1.03	1.23	1.24	1.06
70	0.97	2.10	2.01	2.02	1.83	2.00	2.03	1.84
80	1.61	2.65	2.60	2.60	2.47	2.58	2.60	2.52
90	1.97	2.88	2.80	2.79	2.73	2.79	2.82	2.77
100	1.90	2.63	2.52	2.54	2.49	2.51	2.53	2.51
110	1.52	2.03	1.85	1.87	1.84	1.85	1.86	1.89
120	1.06	1.30	1.03	1.03	1.07	1.03	1.03	1.10
130	0.65	0.62	0.32	0.34	0.43	0.33	0.33	0.45
140	0.49	0.17	0.00	0.00	0.12	0.00	0.00	0.13
150	0.68	0.00	0.17	0.16	0.27	0.17	0.16	0.27
160	1.16	0.11	0.81	0.79	0.89	0.80	0.80	0.74
170	1.77	0.38	1.67	1.65	1.71	1.64	1.67	1.54
180	2.07	0.56	2.11	2.12	2.14	2.08	2.14	2.00

Table 7.2 Energies, wavelengths, oscillator strengths, symmetry and orbital assignments of the first 20 singlet vertical electronic transitions for **2.1** (vacuum) calculated at the TD-DFT/CAM-B3LYP/6-31G(d,p) level of theory.

Wavelength (nm)	Energy (eV)	Oscillation Strength	Major contributions
426.5	2.91	1.447	H-2->LUMO (14%), HOMO->LUMO (74%)
375.2	3.30	0.031	H-1->LUMO (39%), HOMO->L+1 (42%)
328.4	3.78	0.015	H-2->L+1 (22%), H-1->LUMO (36%), HOMO->L+1 (26%)
313.2	3.96	0.152	H-4->LUMO (13%), H-2->LUMO (39%), H-1->L+1 (19%)
300.7	4.12	1.882	H-1->L+3 (34%), HOMO->L+2 (43%)
297.4	4.17	0.308	H-1->L+2 (39%), HOMO->L+3 (43%)
281.4	4.41	0.043	H-3->L+1 (10%), H-2->LUMO (14%), H-1->L+1 (45%), HOMO->LUMO (19%)
273.3	4.54	0.026	H-7->LUMO (33%), H-5->LUMO (16%), H-4->L+1 (20%)
271.6	4.56	0.037	H-8->LUMO (12%), H-7->L+1 (11%), H-4->LUMO (47%)
270.7	4.58	0.000	H-12->L+1 (16%), H-11->LUMO (59%)
268.3	4.62	0.217	H-12->LUMO (58%), H-11->L+1 (17%)
268.0	4.63	0.004	H-13->LUMO (19%), H-3->LUMO (18%), H-2->L+1 (17%), HOMO->L+1 (16%)
262.4	4.72	0.000	H-23->L+1 (21%), H-22->LUMO (17%), H-20->LUMO (11%), H-3->LUMO (11%)
260.2	4.77	0.006	H-1->L+5 (16%), HOMO->L+6 (13%)
259.3	4.78	0.000	H-9->L+2 (10%), H-1->L+6 (22%), HOMO->L+5 (18%)
258.0	4.81	0.017	H-23->LUMO (33%), H-22->L+1 (17%), H-20->L+1 (11%)
252.5	4.91	0.011	H-2->L+2 (13%), HOMO->L+4 (17%)
251.9	4.92	0.001	H-23->L+1 (10%), H-3->LUMO (25%)
246.2	5.04	0.000	H-6->L+3 (15%), H-5->L+2 (11%)
245.7	5.05	0.011	H-6->L+2 (16%), H-5->L+3 (15%)

Table 7.3 Energies, wavelengths, oscillator strengths, symmetry and orbital assignments of the first 20 singlet vertical electronic transitions for **2.2** (vacuum) calculated at the TD-DFT/CAM-B3LYP/6-31G(d,p) level of theory.

Wavelength (nm)	Energy (eV)	Oscillation Strength	Major contributions
410.3	3.02	1.316	HOMO->LUMO (85%)
355.2	3.49	0.000	H-1->LUMO (18%), HOMO->L+1 (69%)
310.2	4.00	0.000	H-2->L+1 (13%), H-1->LUMO (65%), HOMO->L+1 (12%)
288.7	4.29	0.476	H-2->LUMO (49%), H-1->L+1 (22%)
274.3	4.52	1.026	H-1->L+1 (19%), H-1->L+3 (18%), HOMO->L+2 (44%)
273.1	4.54	0.011	H-9->L+1 (11%), H-8->LUMO (32%), H-1->L+2 (12%), HOMO->L+3 (21%)
269.3	4.60	0.003	H-8->LUMO (18%), H-5->LUMO (24%)
267.6	4.63	0.118	H-9->LUMO (42%), H-8->L+1 (10%), H-6->LUMO (11%)
266.3	4.66	0.170	H-9->LUMO (18%), H-8->L+1 (11%), H-6->LUMO (18%)
263.7	4.70	0.020	H-8->LUMO (18%), H-1->L+2 (16%), HOMO->L+3 (20%)
261.4	4.74	0.092	H-7->L+1 (13%), H-2->LUMO (18%), H-1->L+1 (27%)
258.8	4.79	0.000	H-19->L+1 (10%), H-16->LUMO (11%), H-7->LUMO (19%)
255.0	4.86	0.094	H-19->LUMO (27%), H-16->L+1 (18%)
251.8	4.92	0.000	H-19->L+1 (13%), H-16->LUMO (14%), H-7->LUMO (23%), H-2->L+1 (12%)
248.5	4.99	0.034	H-4->LUMO (14%), H-3->L+3 (11%), H-1->L+5 (14%)
247.9	5.00	0.001	H-4->L+3 (11%), H-3->LUMO (14%), HOMO->L+5 (12%)
235.4	5.27	0.001	H-5->LUMO (20%), HOMO->L+5 (11%)
235.3	5.27	0.006	H-6->LUMO (22%), H-4->L+2 (10%), H-3->L+3 (10%), HOMO->L+4 (13%)
234.1	5.30	0.022	H-2->L+2 (24%), H-1->L+3 (15%), HOMO->L+6 (24%)
234.0	5.30	0.001	H-7->LUMO (18%), H-2->L+1 (42%)

Table 7.4 Energies, wavelengths, oscillator strengths, symmetry and orbital assignments of the first 20 singlet vertical electronic transitions for **2.3** (vacuum) calculated at the TD-DFT/CAM-B3LYP/6-31G(d,p) level of theory.

Wavelength (nm)	Energy (eV)	Oscillation Strength	Major contributions
415.8	2.98	1.770	H-2->LUMO (61%), HOMO->LUMO (22%)
360.4	3.44	0.000	H-3->LUMO (16%), H-2->L+1 (44%), H-1->LUMO (11%), HOMO->L+1 (16%)
326.0	3.80	0.003	H-4->L+1 (10%), H-3->LUMO (12%), H-2->L+1 (19%), H-1->LUMO (41%)
317.1	3.91	1.172	H-4->LUMO (13%), H-2->LUMO (12%), H-1->L+3 (13%), HOMO->LUMO (29%), HOMO->L+2 (14%)
300.4	4.13	0.018	H-3->LUMO (11%), H-1->L+2 (24%), HOMO->L+3 (27%)
298.1	4.16	1.493	H-1->L+3 (17%), HOMO->LUMO (36%), HOMO->L+2 (20%)
290.0	4.27	0.000	H-3->LUMO (38%), H-1->LUMO (41%)
285.0	4.35	0.011	H-4->LUMO (14%), H-3->L+1 (28%), H-1->L+1 (26%), HOMO->LUMO (11%)
279.4	4.44	0.014	H-1->L+5 (30%), H-1->L+6 (11%), HOMO->L+5 (37%)
279.4	4.44	0.026	H-1->L+5 (11%), H-1->L+6 (30%), HOMO->L+6 (38%)
274.6	4.51	0.141	H-4->LUMO (11%), H-3->L+3 (11%), H-2->L+2 (21%), H-1->L+1 (20%)
271.3	4.57	0.025	H-20->L+1 (12%), H-19->LUMO (40%)
270.4	4.59	0.010	H-19->LUMO (13%), HOMO->L+1 (27%)
270.3	4.59	0.243	H-1->L+8 (24%), HOMO->L+8 (24%)
270.2	4.59	0.246	H-1->L+8 (14%), H-1->L+9 (20%), HOMO->L+8 (13%), HOMO->L+9 (18%)
268.1	4.63	0.127	H-20->LUMO (22%), H-6->LUMO (12%)
267.6	4.63	0.000	H-11->LUMO (10%), HOMO->L+1 (37%)
266.4	4.65	0.205	H-20->LUMO (31%), H-19->L+1 (15%)
263.2	4.71	0.036	H-4->LUMO (22%), H-1->L+1 (17%)
262.9	4.72	0.007	H-19->LUMO (11%), H-3->L+2 (15%), H-2->L+3 (18%)

Table 7.5 Energies, wavelengths, oscillator strengths, symmetry and orbital assignments of the first 20 singlet vertical electronic transitions for **2.4** (vacuum) calculated at the TD-DFT/CAM-B3LYP/6-31G(d,p) level of theory.

Wavelength (nm)	Energy (eV)	Oscillation Strength	Major contributions
403.9	3.07	1.293	HOMO->LUMO (84%)
350.4	3.54	0.008	H-1->LUMO (16%), HOMO->L+1 (69%)
308.3	4.02	0.008	H-2->L+1 (14%), H-1->LUMO (62%), HOMO->L+1 (10%)
289.2	4.29	0.363	H-2->LUMO (47%), H-1->L+1 (22%)
273.5	4.53	0.974	H-1->L+1 (13%), H-1->L+3 (20%), HOMO->L+2 (44%)
272.3	4.55	0.046	H-9->L+1 (13%), H-8->LUMO (36%), H-1->L+2 (11%), HOMO->L+3 (19%)
267.9	4.63	0.260	H-9->LUMO (57%), H-8->L+1 (19%)
266.2	4.66	0.000	H-8->LUMO (30%), H-1->L+2 (14%), HOMO->L+3 (15%)
264.9	4.68	0.015	H-15->L+1 (11%), H-14->LUMO (14%), H-4->L+1 (11%), H-3->LUMO (31%)
263.3	4.71	0.002	H-4->LUMO (36%), H-3->L+1 (12%)
259.1	4.78	0.207	H-5->L+1 (14%), H-2->LUMO (17%), H-1->L+1 (30%), HOMO->LUMO (11%)
256.5	4.83	0.003	H-15->L+1 (11%), H-14->LUMO (18%), H-3->LUMO (11%)
255.2	4.86	0.030	H-15->LUMO (28%), H-14->L+1 (26%)
254.0	4.88	0.008	H-11->LUMO (11%), H-5->LUMO (30%), HOMO->L+3 (13%)
248.5	4.99	0.006	H-1->L+5 (22%), HOMO->L+4 (17%)
248.4	4.99	0.000	H-1->L+4 (22%), HOMO->L+5 (19%)
233.8	5.30	0.000	H-2->L+1 (16%)
233.8	5.30	0.015	H-2->L+2 (27%), H-1->L+3 (17%), HOMO->L+6 (26%)
233.0	5.32	0.003	H-4->LUMO (15%), H-4->L+2 (13%), H-3->L+3 (12%), H-1->L+7 (12%), HOMO->L+8 (13%)
232.5	5.33	0.002	H-2->L+1 (28%)

Table 7.6 Energies, wavelengths, oscillator strengths, symmetry and orbital assignments of the first 20 singlet vertical electronic transitions for **2.5** (vacuum) calculated at the TD-DFT/CAM-B3LYP/6-31G(d,p) level of theory.

Wavelength (nm)	Energy (eV)	Oscillation Strength	Major contributions
417.8	2.97	1.637	H-2->LUMO (43%), HOMO->LUMO (37%)
362.6	3.42	0.000	H-3->LUMO (12%), H-2->L+1 (30%), H-1->LUMO (15%), HOMO->L+1 (26%)
326.4	3.80	0.002	H-2->L+1 (20%), H-1->LUMO (39%)
311.8	3.98	0.598	H-4->LUMO (19%), H-2->LUMO (26%), HOMO->LUMO (19%)
289.3	4.28	1.456	HOMO->LUMO (13%), HOMO->L+2 (18%), HOMO->L+3 (37%)
288.3	4.30	0.595	H-1->L+2 (39%), HOMO->L+3 (10%)
283.4	4.38	0.016	H-3->L+1 (22%), H-1->L+1 (39%), HOMO->LUMO (15%)
278.9	4.45	0.007	H-11->LUMO (11%), H-3->LUMO (42%), H-1->LUMO (24%)
269.9	4.59	0.013	H-12->LUMO (40%)
269.4	4.60	0.032	H-13->LUMO (15%), H-9->LUMO (12%)
268.6	4.62	0.021	H-12->LUMO (20%)
266.5	4.65	0.227	H-13->LUMO (44%), H-12->L+1 (17%)
265.6	4.67	0.002	H-4->L+1 (12%), H-2->L+1 (14%), HOMO->L+1 (34%)
262.5	4.72	0.019	HOMO->L+6 (11%), HOMO->L+8 (35%)
261.5	4.74	0.026	H-4->LUMO (29%), H-2->L+2 (10%)
259.5	4.78	0.023	H-1->L+5 (12%), H-1->L+7 (25%)
257.9	4.81	0.007	H-19->LUMO (11%), H-18->LUMO (10%), H-18->L+1 (10%), HOMO->L+6 (10%)
257.7	4.81	0.004	H-19->L+1 (10%), H-18->LUMO (11%)
255.0	4.86	0.001	H-5->LUMO (12%), H-5->L+3 (10%), HOMO->L+6 (10%)
254.5	4.87	0.002	H-6->LUMO (11%), H-1->L+5 (12%)

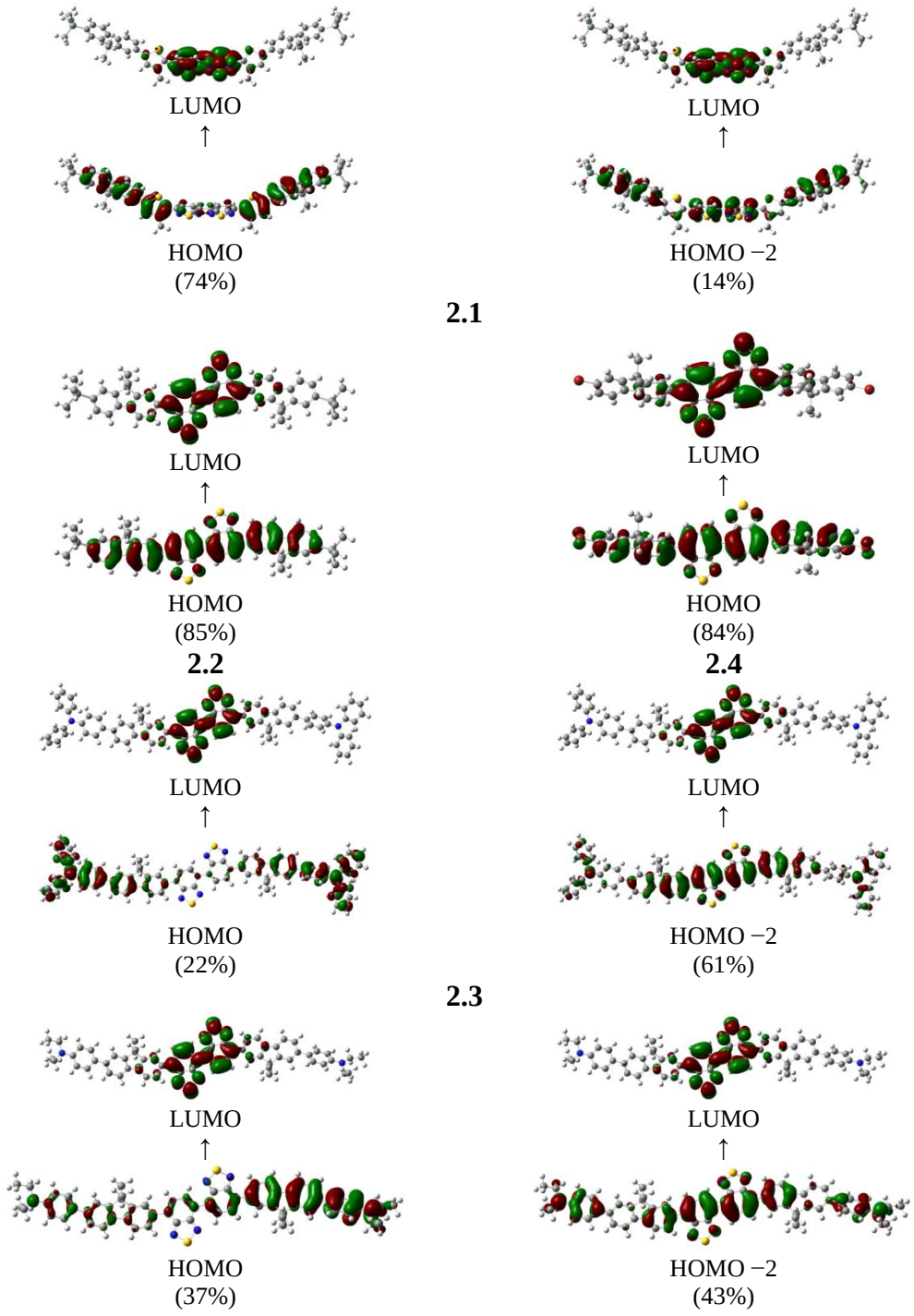

Figure 7.3 Graphical representation (isosurface 0.2) of the orbitals involved in the first transition (main contributions) for **2.1**-**2.5** calculated at the TD-DFT/CAM-B3LYP/6-31G(d,p) level of theory.

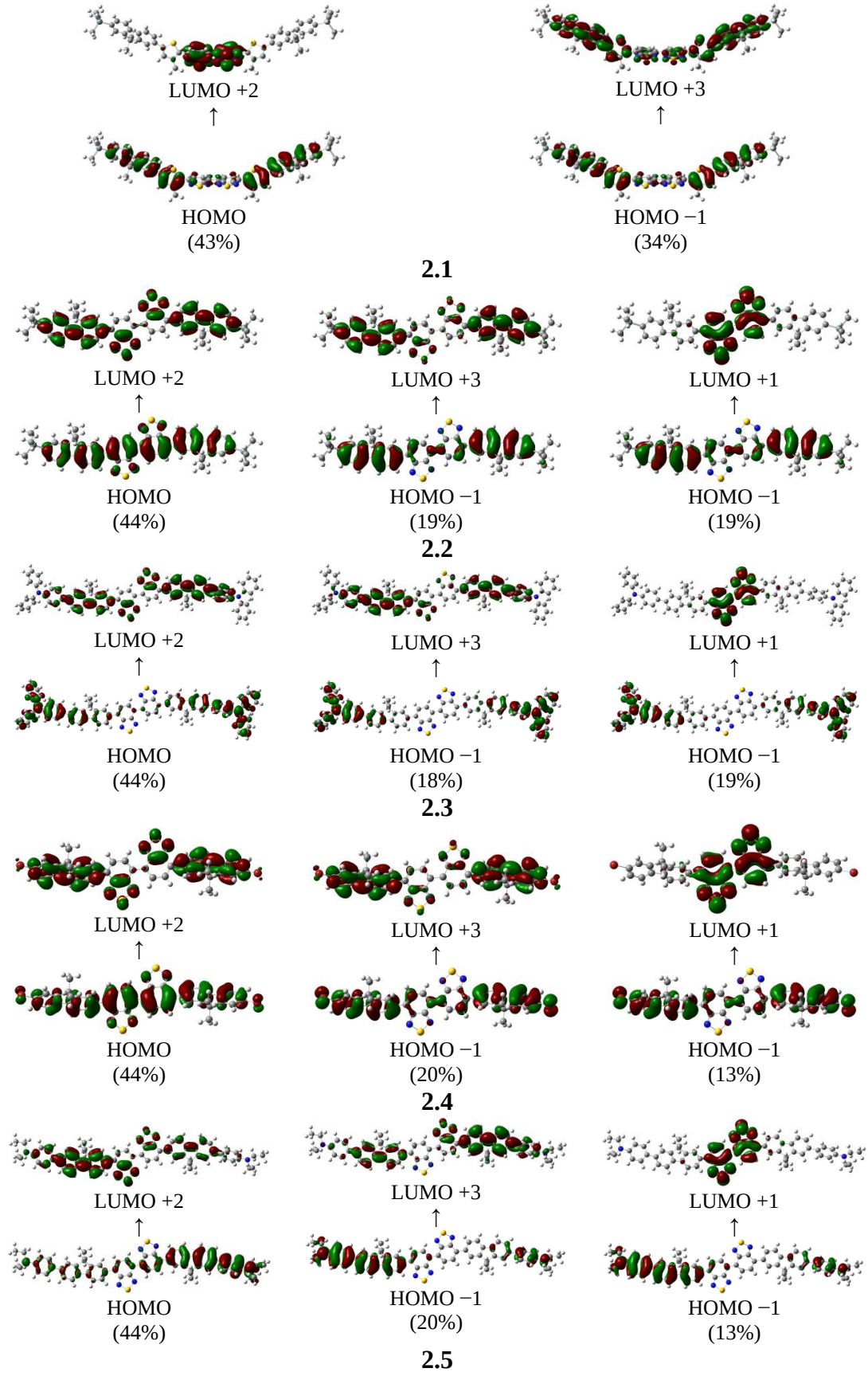

Figure 7.4 Graphical representation (isosurface 0.2) of the orbitals involved in the second relevant transitions (main contributions) for **2.1**-**2.5** calculated at the TD-DFT/CAM-B3LYP/6-31G(d,p) level of theory.

Table 7.7 Mean signed and mean square errors (MSiE and MSqE, eV) and maximal deviations (Max-Min, eV), obtained by comparing experimental and theoretical meaning maximum absorption values of **3** (4,7-dithiophenyl-benzothiadiazole).

	B3LYP			
	6-31G	**6-311G(d,p)**	**6-311+G(2d,p)**	**DGDZVP**
MSiE	-0.323	-0.281	-0.319	-0.397
MSqE	0.113	0.087	0.109	0.166
Max(+)	-0.228	-0.190	-0.236	-0.306
Min(-)	-0.418	-0.372	-0.402	-0.488

	wB97X-D			
	6-31G	**6-311G(d,p)**	**6-311+G(2d,p)**	**DGDZVP**
MSiE	0.463	0.475	0.436	0.436
MSqE	0.231	0.241	0.199	0.202
Max(+)	0.593	0.601	0.531	0.546
Min(-)	0.334	0.349	0.341	0.326

	CAM-B3LYP			
	6-31G	**6-311G(d,p)**	**6-311+G(2d,p)**	**DGDZVP**
MSiE	0.363	0.405	0.359	0.316
MSqE	0.155	0.182	0.139	0.117
Max(+)	0.515	0.539	0.461	0.446
Min(-)	0.210	0.272	0.256	0.186

	M06-2X			
	6-31G	**6-311G(d,p)**	**6-311+G(2d,p)**	**DGDZVP**
MSiE	0.363	0.421	0.351	0.335
MSqE	0.160	0.197	0.134	0.130
Max(+)	0.531	0.562	0.453	0.469
Min(-)	0.194	0.279	0.248	0.202

	PBE0			
	6-31G	**6-311G(d,p)**	**6-311+G(2d,p)**	**DGDZVP**
MSiE	-0.153	-0.114	-0.153	-0.153
MSqE	0.037	0.025	0.032	0.034
Max(+)	-0.035	-0.004	-0.058	-0.050
Min(-)	-0.271	-0.224	-0.248	-0.255

Table 7.8 Torsional potential surface energies for **3.1sh**-**3.5sh** calculated at the PBE0/6-311G(d,p) level of theory.

Dihedral angle (degree)	Relative energy (kcal/mol)				
	3.1sh	**3.2sh**	**3.3sh**	**3.4sh**	**3.5sh**
0	5.551	0.000	3.500	0.144	7.355
10	5.429	0.003	2.711	0.000	5.709
20	5.185	0.077	1.508	0.117	4.075
30	5.030	0.350	0.543	0.461	2.970
40	5.097	0.882	0.038	1.092	2.448
50	5.409	1.660	0.064	1.972	2.450
60	5.909	2.566	0.487	2.956	2.860
70	6.460	3.405	1.000	3.893	3.524
80	6.892	3.987	1.276	4.576	4.228
90	7.023	4.168	1.237	4.832	4.690
100	6.668	3.928	0.832	4.598	4.641
110	5.801	3.327	0.317	3.964	4.116
120	4.611	2.544	0.000	3.085	3.232
130	3.346	1.778	0.135	2.221	2.239
140	2.180	1.182	0.929	1.514	1.329
150	1.232	0.852	2.549	1.055	0.614
160	0.543	0.773	5.088	0.852	0.172
170	0.131	0.838	8.533	0.824	0.000
180	0.000	0.894	12.674	0.834	0.038

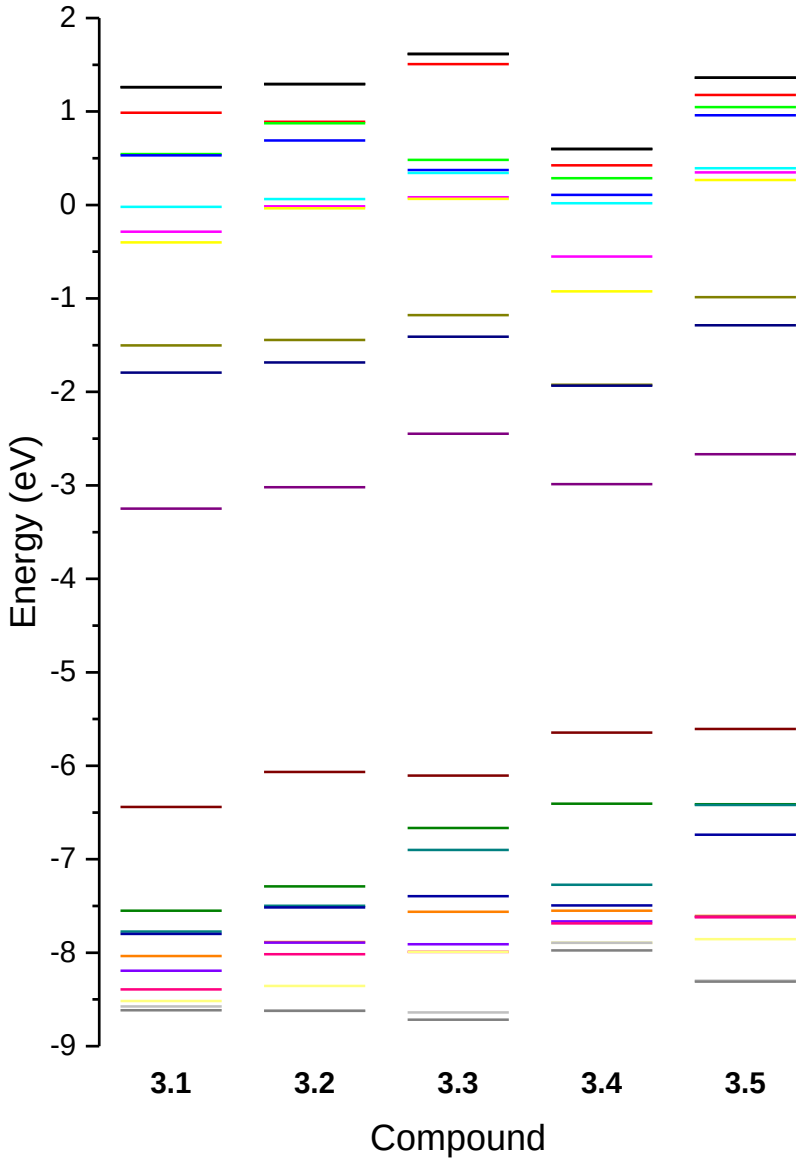

Figure 7.5 Kohn-Sham molecular orbital diagram (HOMO−9 - LUMO+9) for **3.1**-**3.5** calculated at the PBE0/6-311G(d,p) level of theory.

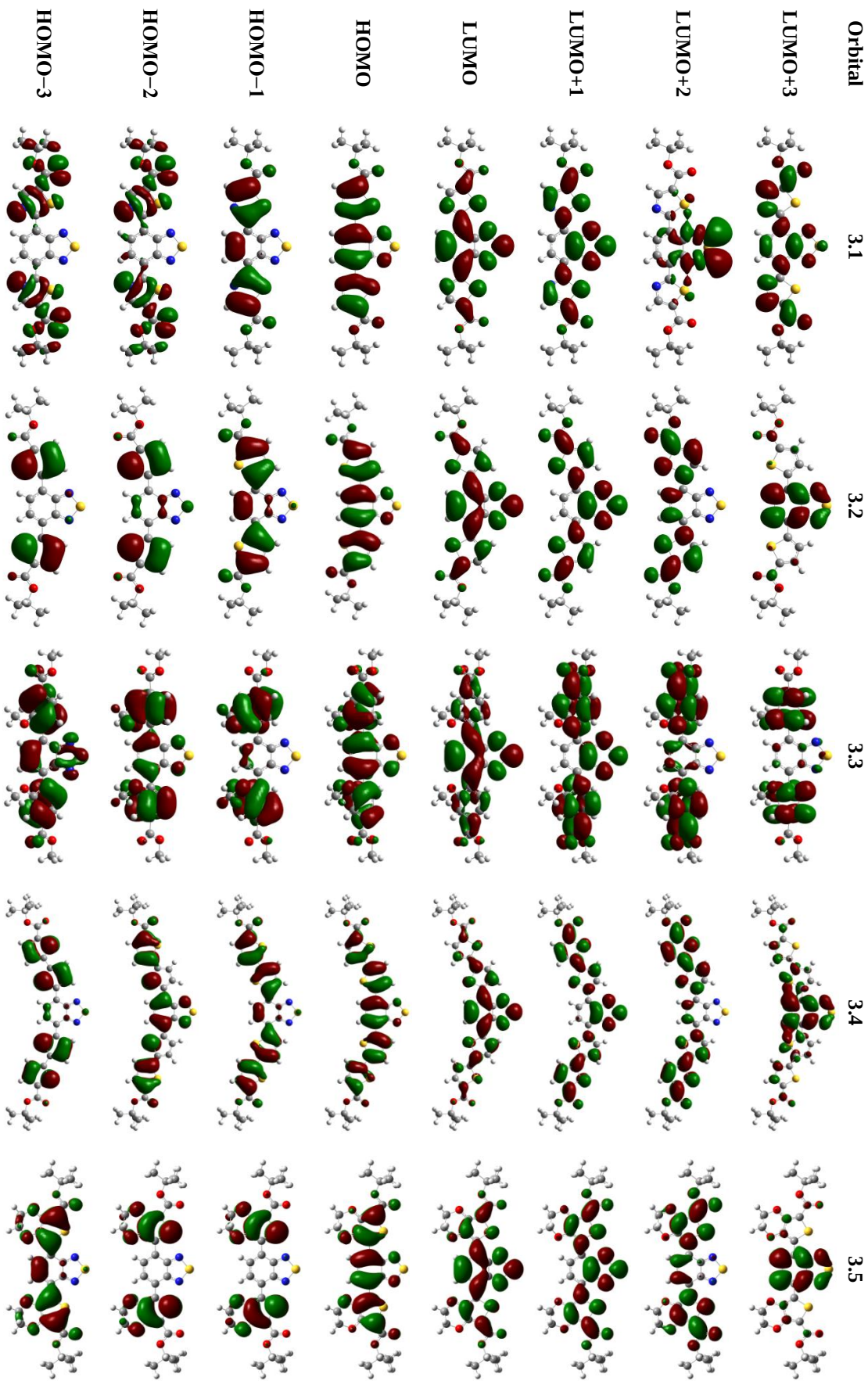

Figure 7.6 HOMO-3 to LUMO+3 graphical representation (isosurface 0.02) of **3.1**-**3.5** in the gas phase calculated at the PBE0/6-311G(d,p) level of theory.

Table 7.9 Energies, wavelengths, oscillator strengths, symmetry and orbital assignments of the first 10 singlet vertical electronic transitions for **3.1** (vacuum) calculated at the PBE0/6-311G(d,p) level of theory.

Wavelength (nm)	Energy (eV)	Oscillation Strength	Major contributions
462.1	2.68	0.690	HOMO->LUMO (99%)
339.3	3.65	0.000	H-1->LUMO (93%)
336.3	3.69	0.000	H-2->LUMO (90%)
332.1	3.73	0.000	H-3->LUMO (90%)
315.9	3.93	0.724	HOMO->L+1 (95%)
301.9	4.11	0.054	H-4->LUMO (80%), HOMO->L+2 (12%)
293.5	4.22	0.001	H-5->LUMO (96%)
281.6	4.40	0.000	H-6->LUMO (37%), HOMO->L+2 (43%)
280.7	4.42	0.000	H-12->LUMO (19%), H-7->LUMO (58%)
277.8	4.46	0.000	H-12->LUMO (69%), H-7->LUMO (22%)
277.1	4.47	0.000	H-8->LUMO (87%)
275.4	4.50	0.075	H-6->LUMO (56%), HOMO->L+2 (31%)
264.0	4.70	0.017	H-9->LUMO (92%)
255.0	4.86	0.000	H-3->L+2 (35%), H-2->L+1 (49%)
254.8	4.87	0.000	H-3->L+1 (46%), H-2->L+2 (38%)
249.5	4.97	0.005	H-10->LUMO (97%)
249.4	4.97	0.011	H-11->LUMO (93%)
243.3	5.10	0.005	H-1->L+1 (93%)
239.7	5.17	0.000	H-15->LUMO (60%), H-13->LUMO (33%)
232.8	5.33	0.003	HOMO->L+3 (76%)

Table 7.10 Energies, wavelengths, oscillator strengths, symmetry and orbital assignments of the first 10 singlet vertical electronic transitions for **3.2** (vacuum) calculated at the PBE0/6-311G(d,p) level of theory.

Wavelength (nm)	Energy (eV)	Oscillation Strength	Major contributions
490.5	2.53	0.633	HOMO->LUMO (98%)
343.3	3.61	0.007	H-1->LUMO (89%), HOMO->L+2 (10%)
336.7	3.68	0.692	HOMO->L+1 (95%)
329.0	3.77	0.000	H-2->LUMO (96%)
326.8	3.79	0.030	H-3->LUMO (97%)
304.9	4.07	0.128	H-6->LUMO (14%), HOMO->L+2 (73%)
299.1	4.14	0.000	H-4->LUMO (86%)
297.8	4.16	0.000	H-5->LUMO (87%)
282.2	4.39	0.045	H-6->LUMO (72%), HOMO->L+2 (14%), HOMO->L+3 (10%)
272.0	4.56	0.000	H-10->LUMO (86%)
266.7	4.65	0.018	H-7->LUMO (94%)
249.9	4.96	0.039	H-1->L+1 (95%)
244.3	5.08	0.000	H-11->LUMO (20%), H-5->L+1 (34%), H-4->L+2 (29%)
244.2	5.08	0.055	H-3->L+1 (65%), H-2->L+2 (18%), HOMO->L+4 (10%)
243.5	5.09	0.016	H-3->L+2 (14%), H-2->L+1 (70%)
242.9	5.11	0.000	H-5->L+2 (36%), H-4->LUMO (13%), H-4->L+1 (41%)
242.6	5.11	0.009	H-8->LUMO (98%)
242.4	5.11	0.007	H-9->LUMO (89%)
239.5	5.18	0.001	H-11->LUMO (70%)
234.4	5.29	0.092	H-1->L+2 (85%), HOMO->L+4 (13%)

Table 7.11 Energies, wavelengths, oscillator strengths, symmetry and orbital assignments of the first 10 singlet vertical electronic transitions for **3.3** (vacuum) calculated at the PBE0/6-311G(d,p) level of theory.

Wavelength (nm)	Energy (eV)	Oscillation Strength	Major contributions
415.0	2.99	0.403	HOMO->LUMO (98%)
355.3	3.49	0.007	H-1->LUMO (99%)
331.3	3.74	0.027	H-2->LUMO (96%)
311.2	3.98	0.603	HOMO->L+1 (95%)
300.9	4.12	0.006	H-3->LUMO (74%), HOMO->L+2 (13%)
286.1	4.33	0.064	H-4->LUMO (25%), HOMO->L+2 (63%)
276.7	4.48	0.051	H-4->LUMO (52%), H-1->L+1 (12%), HOMO->L+2 (10%)
272.4	4.55	0.044	H-1->L+1 (64%), HOMO->L+2 (10%)
268.6	4.62	0.025	H-2->L+1 (50%), H-1->L+2 (31%)
262.2	4.73	0.018	H-5->LUMO (89%)
261.4	4.74	0.000	H-8->LUMO (43%), H-6->LUMO (32%)
259.3	4.78	0.000	H-7->LUMO (63%), H-7->L+1 (14%), H-6->L+2 (17%)
257.9	4.81	0.000	H-8->LUMO (33%), H-7->L+2 (13%), H-6->LUMO (31%), H-6->L+1 (12%)
248.0	5.00	0.047	H-2->L+1 (36%), H-1->L+2 (61%)
245.8	5.05	0.000	H-3->L+1 (11%), H-2->L+2 (59%), H-1->L+1 (17%)
237.6	5.22	0.003	H-11->LUMO (79%)
233.1	5.32	0.017	H-4->L+1 (10%), H-3->L+1 (65%), H-2->L+2 (17%)
230.5	5.38	0.000	H-7->L+2 (25%), H-6->LUMO (36%), H-6->L+1 (32%)
230.0	5.39	0.006	H-7->LUMO (33%), H-7->L+1 (25%), H-6->L+2 (21%)
228.3	5.43	0.065	H-3->L+2 (17%), HOMO->L+4 (58%)

Table 7.12 Energies, wavelengths, oscillator strengths, symmetry and orbital assignments of the first 10 singlet vertical electronic transitions for **3.4** (vacuum) calculated at the PBE0/6-311G(d,p) level of theory.

Wavelength (nm)	Energy (eV)	Oscillation Strength	Major contributions
568.6	2.18	1.098	HOMO->LUMO (99%)
424.8	2.92	0.024	H-1->LUMO (91%)
397.7	3.12	0.894	HOMO->L+1 (96%)
373.8	3.32	0.137	HOMO->L+2 (90%)
332.4	3.73	0.009	H-2->LUMO (92%)
321.2	3.86	0.002	H-5->LUMO (14%), H-3->LUMO (83%)
316.5	3.92	0.002	H-6->LUMO (21%), H-4->LUMO (60%), HOMO->L+3 (11%)
310.8	3.99	0.046	H-1->L+1 (96%)
305.7	4.06	0.290	H-1->L+2 (81%), HOMO->L+3 (14%)
298.8	4.15	0.001	H-5->LUMO (80%), H-3->LUMO (14%)
298.1	4.16	0.001	H-6->LUMO (72%), H-4->LUMO (24%)
291.4	4.25	0.003	H-4->LUMO (13%), H-1->L+2 (10%), HOMO->L+3 (68%)
290.0	4.27	0.064	H-9->LUMO (60%), HOMO->L+4 (24%)
283.8	4.37	0.000	H-8->LUMO (17%), H-8->L+2 (10%), H-7->LUMO (55%)
283.8	4.37	0.000	H-8->LUMO (55%), H-7->LUMO (17%), H-7->L+2 (10%)
275.0	4.51	0.018	H-10->LUMO (52%), H-9->LUMO (10%), HOMO->L+4 (23%)
271.7	4.56	0.000	H-14->LUMO (86%), H-14->L+1 (10%)
264.6	4.69	0.002	H-10->LUMO (42%), HOMO->L+4 (36%)
260.1	4.77	0.066	H-3->L+2 (16%), H-2->L+1 (74%)
259.8	4.77	0.000	H-4->L+2 (10%), H-3->L+1 (24%), H-2->L+2 (54%)

Table 7.13 Energies, wavelengths, oscillator strengths, symmetry and orbital assignments of the first 10 singlet vertical electronic transitions for **3.5** (vacuum) calculated at the PBE0/6-311G(d,p) level of theory.

Wavelength (nm)	Energy (eV)	Oscillation Strength	Major contributions
508.1	2.44	0.695	HOMO->LUMO (98%)
404.0	3.07	0.002	H-1->LUMO (99%)
402.7	3.08	0.025	H-2->LUMO (99%)
360.0	3.44	0.002	H-3->LUMO (93%)
340.2	3.64	0.800	HOMO->L+1 (97%)
304.3	4.07	0.006	H-6->LUMO (10%), HOMO->L+2 (74%)
294.0	4.22	0.000	H-6->LUMO (34%), H-4->LUMO (53%)
292.9	4.23	0.000	H-5->LUMO (90%)
286.1	4.33	0.054	H-6->LUMO (40%), H-4->LUMO (20%), HOMO->L+2 (14%), HOMO->L+3 (12%)
280.4	4.42	0.011	H-7->LUMO (32%), H-1->L+1 (56%)
277.2	4.47	0.051	H-10->LUMO (59%), H-2->L+1 (25%)
275.3	4.50	0.088	H-10->LUMO (28%), H-2->L+1 (58%)
272.2	4.56	0.000	H-7->LUMO (64%), H-1->L+1 (33%)
257.9	4.81	0.040	H-3->L+1 (81%), H-1->L+2 (12%)
255.1	4.86	0.013	H-2->L+2 (86%)
254.1	4.88	0.033	H-3->L+1 (12%), H-1->L+2 (78%)
244.0	5.08	0.000	H-13->LUMO (19%), H-11->LUMO (70%)
241.9	5.12	0.008	H-8->LUMO (97%)
241.6	5.13	0.017	H-9->LUMO (97%)
238.3	5.20	0.049	H-3->L+2 (76%), HOMO->L+4 (12%)

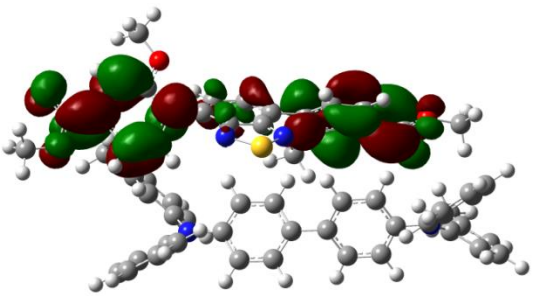

LUMO +2

(-0.046 eV)

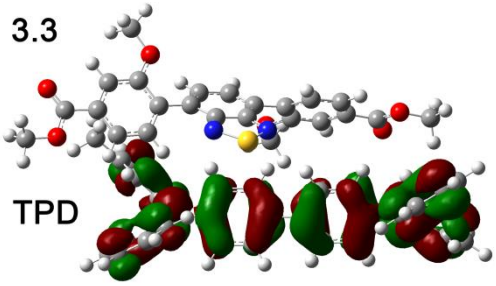

HOMO

(-0.187 eV)

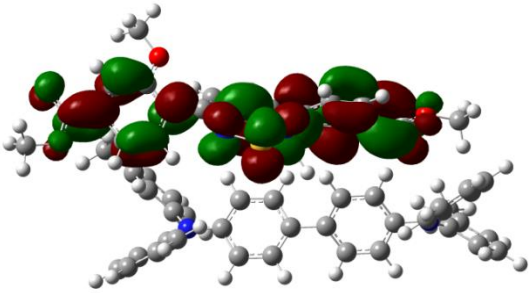

LUMO +1

(-0.055 eV)

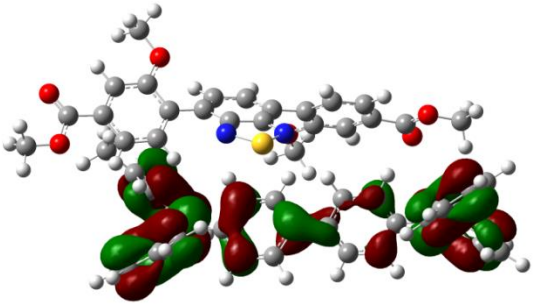

HOMO −1

(-0.200 eV)

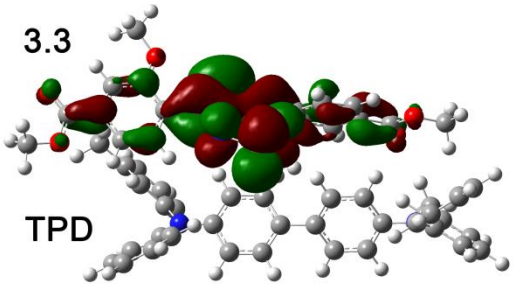

LUMO

(-0.092 eV)

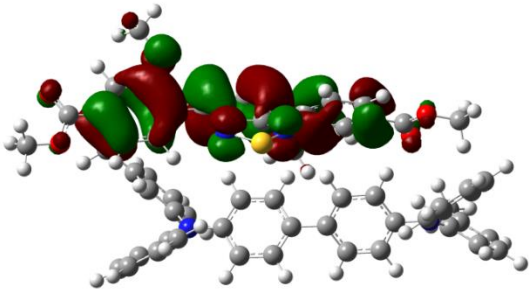

HOMO −2

(-0.227 eV)

Figure 7.7 Molecular orbital graphical representations and energies (HOMO-2 to LUMO+2) of the **TPD**:**3.3** complex calculated at the PBE0/6-311G(d,p) level of theory (isosurface 0.02).

Table 7.14 Energies, wavelengths, oscillator strengths, symmetry and orbital assignments of the first 10 singlet vertical electronic transitions for **TPD** (vacuum) calculated at the PBE0/6-311G(d,p) level of theory.

Wavelength (nm)	Energy (eV)	Oscillation Strength	Major contributions
356.0	3.48	1.069	HOMO->LUMO (96%)
328.0	3.78	0.010	H-1->L+2 (14%), HOMO->L+1 (83%)
323.3	3.84	0.019	H-1->L+1 (21%), HOMO->L+2 (75%)
313.8	3.95	0.001	H-1->LUMO (95%)
307.5	4.03	0.186	H-1->L+3 (17%), HOMO->L+3 (78%)
306.2	4.05	0.179	H-1->L+4 (16%), HOMO->L+4 (80%)
284.5	4.36	0.066	H-1->L+2 (27%), HOMO->L+6 (56%)
280.7	4.42	0.001	H-1->L+1 (72%), HOMO->L+2 (19%)
277.8	4.46	0.001	HOMO->L+5 (52%), HOMO->L+8 (13%)
277.0	4.48	0.018	H-1->L+6 (15%), HOMO->L+7 (43%), HOMO->L+8 (11%), HOMO->L+9 (10%)
275.1	4.51	0.037	H-1->L+8 (13%), HOMO->L+7 (21%), HOMO->L+9 (42%)
274.0	4.53	0.004	H-1->L+2 (49%), HOMO->L+1 (11%), HOMO->L+6 (23%)
270.3	4.59	0.000	HOMO->L+5 (35%), HOMO->L+8 (43%)
267.5	4.64	0.040	H-1->L+3 (79%), HOMO->L+3 (18%)
266.5	4.65	0.039	H-1->L+4 (81%), HOMO->L+4 (17%)
265.7	4.67	0.026	H-1->L+5 (83%)
264.4	4.69	0.001	H-1->L+6 (74%), HOMO->L+9 (11%)
263.6	4.70	0.006	H-1->L+7 (31%), H-1->L+9 (43%), HOMO->L+6 (13%)
258.2	4.80	0.020	H-2->LUMO (16%), H-1->L+8 (38%), HOMO->L+7 (11%), HOMO->L+10 (13%)
255.8	4.85	0.000	H-1->L+7 (39%), H-1->L+9 (20%), HOMO->L+8 (22%)

Table 7.15 Energies, wavelengths, oscillator strengths, symmetry and orbital assignments of the first 10 singlet vertical electronic transitions for the complex **3.3**:**TPD** (vacuum) calculated at the PBE0/6-311G(d,p) level of theory.

Wavelength (nm)	Energy (eV)	Oscillation Strength	Major contributions
600.7	2.06	0.000	HOMO->LUMO (95%)
508.7	2.44	0.000	H-1->LUMO (94%)
414.0	2.99	0.304	H-2->LUMO (98%)
401.7	3.09	0.001	HOMO->L+1 (95%)
372.9	3.33	0.002	H-1->L+1 (30%), HOMO->L+2 (67%)
355.1	3.49	0.020	H-4->LUMO (48%), H-3->LUMO (48%)
353.3	3.51	0.001	H-1->L+1 (65%), HOMO->L+2 (25%)
350.3	3.54	0.747	HOMO->L+3 (93%)
335.2	3.70	0.008	H-5->LUMO (10%), H-4->LUMO (34%), H-3->LUMO (34%)
331.8	3.74	0.014	H-7->LUMO (36%), H-1->L+2 (52%)
331.5	3.74	0.022	H-7->LUMO (40%), H-1->L+2 (30%)
330.6	3.75	0.004	H-6->LUMO (23%), H-5->LUMO (45%), HOMO->L+4 (12%)
328.4	3.78	0.012	H-1->L+4 (18%), HOMO->L+4 (53%)
325.4	3.81	0.027	H-1->L+5 (13%), HOMO->L+5 (74%)
324.8	3.82	0.006	H-1->L+3 (83%)
324.1	3.83	0.002	H-9->LUMO (26%), H-6->LUMO (28%), H-5->LUMO (24%)
321.0	3.86	0.518	H-2->L+1 (87%)
318.1	3.90	0.000	H-8->LUMO (80%)
314.9	3.94	0.001	H-9->LUMO (51%), H-6->LUMO (28%)
313.2	3.96	0.133	H-1->L+6 (23%), HOMO->L+6 (66%)

Table 7.16 Crystal data and structure refinement details of **MOF-4.1.A**.

Identification code	2015ncs0493_sq	
Empirical formula	$0.25(C_{216}H_{144}N_{24}O_{48}S_8Zn_8)$	
Formula weight	1155.75 g/mol	
Temperature	100 (2) K	
Wavelength	0.71073 Å	
Crystal system	Monoclinic	
Space group	I 2/m	
Unit cell dimensions	a = 13.87678(19) Å	α = 90°
	b = 23.2823(4) Å	β = 97.6958(13)°
	c = 29.9426(4)Å	γ = 90°
Volume	9586.83(18) Å^3	
Z	4	
Density (calculated)	0.801 Mg / m^3	
Absorption coefficient	0.336 mm^{-1}	
F(000)	2360	
Crystal	block; yellow	
Crystal size	0.25 × 0.12 × 0.10 mm^3	
θ range for data collection	1.7990 – 29.1420°	
Index ranges	$-18 \le h \le 19$, $-32 \le k \le 32$, $-41 \le l \le 41$	
Reflections total	12938	
Independent reflections	2548 [R_{int} = 0.088]	
Completeness to θ =	29.32 °	95.82 %
Absorption correction	Multi-scan using spherical harmonics	
Max. and min. transmission	1.00000 and 0.59767	
Refinement method	Full-matrix least-squares on F^2	
Data / restraints / parameters	12938 / 30 / 390	
Goodness-of-fit on F^2	1.052	
Final *R* indices [$F^2 > 2\sigma(F^2)$]	*R1* = 0.0831, *wR2* = 0.2537	
R indices (all data)	*R1* = 0.0950, *wR2* = 0.2668	
Largest diff. peak and hole	1.920 and –0.771 e Å^{-3}	

Disorder present in the ring containing C8-C13, N1, N2, S1. This was modelled over 3 partially occupied sites with occupancies 0.35, 0.35, 0.3. Disorder is also present in the OMe group O6 and C6M which was modelled over two partially occupied sites with occupancies 0.65:0.35. Distance restraints were applied and, apart from S1, partially occupied atom sites were refined with isotropic adps.

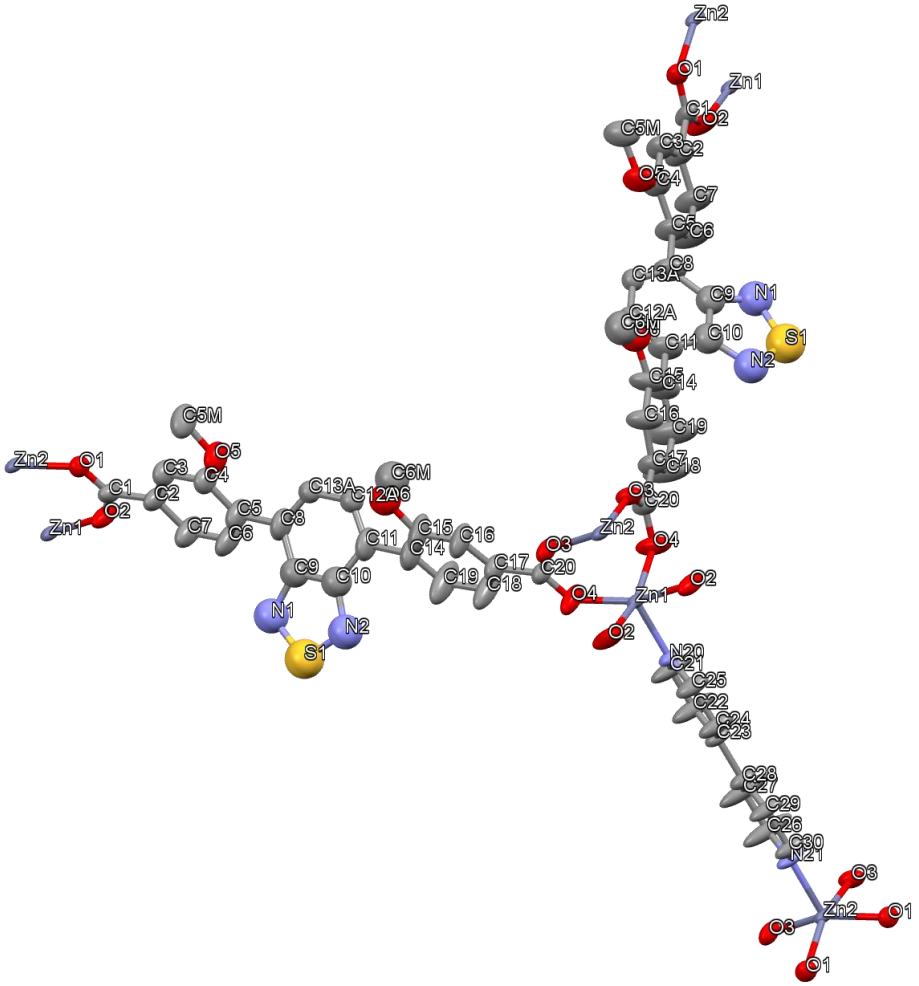

Figure 7.8 Structure details of **MOF-4.1.A**.

Table 7.17 Atomic coordinates, equivalent isotropic displacement parameters (U_{eq}) and site occupancy factors (*S. Occ. F.*). U_{eq} is defined as one third of the trace of the orthogonalized U^{ij} tensor.

Atom label	*x*	*y*	*z*	U_{eq}	*S. Occ. F.*
Zn1	0.74178(3)	0.5	0.87700(2)	0.0272	1
Zn2	1.54793(3)	0.5	0.90663(2)	0.0276	1
S1	0.5919(5)	0.1465(3)	0.6631(2)	0.136	0.35
O1	0.09837(17)	0.06045(10)	0.45258(7)	0.0409	1
O2	0.24217(18)	0.06028(14)	0.42676(10)	0.0715	1
O3	0.54896(16)	0.43929(11)	0.85691(7)	0.0445	1
O4	0.69180(18)	0.43971(14)	0.83118(10)	0.0658	1
O5	0.1525(2)	0.18856(14)	0.59052(10)	0.0694	1
O6	0.3283(5)	0.3165(4)	0.7507(2)	0.088	0.655
N1	0.4981(12)	0.1444(7)	0.6227(6)	0.105	0.35
N2	0.5704(13)	0.2018(7)	0.6930(6)	0.105	0.35
N20	0.8887(2)	0.5	0.87978(11)	0.0331	1
N21	1.4013(2)	0.5	0.90432(11)	0.0435	1
C1	0.1853(2)	0.07589(16)	0.45387(12)	0.0503	1
C2	0.2258(3)	0.1147(2)	0.49211(14)	0.0622	1
C3	0.1674(3)	0.13524(19)	0.52155(14)	0.0604	1
H3	0.1011	0.1274	0.5167	0.072	1
C4	0.2056(3)	0.16808(19)	0.55903(14)	0.0602	1
C5	0.3052(3)	0.1804(2)	0.56580(17)	0.0745	1
C6	0.3635(4)	0.1610(3)	0.5340(2)	0.0972	1
H6	0.4293	0.1703	0.5378	0.117	1
C7	0.3255(3)	0.1287(3)	0.49750(19)	0.0899	1
H7	0.3649	0.1161	0.4767	0.108	1
C8	0.3500(3)	0.2147(2)	0.60526(15)	0.0734	1
C9	0.4391(11)	0.1944(7)	0.6318(5)	0.075	0.35
C10	0.4811(13)	0.2270(6)	0.6703(6)	0.082	0.35
C11	0.4388(4)	0.2803(2)	0.68175(15)	0.0721	1
C14	0.4836(4)	0.3149(2)	0.72151(16)	0.0713	1
C15	0.4305(4)	0.3302(3)	0.75513(16)	0.0809	1
C16	0.4709(3)	0.3645(2)	0.79101(14)	0.069	1
H16	0.4343	0.3741	0.8138	0.083	1
C17	0.5639(3)	0.38398(18)	0.79265(13)	0.0562	1
C18	0.6185(4)	0.3679(3)	0.7599(2)	0.107	1
H18	0.6823	0.3807	0.7609	0.129	1
C19	0.5770(4)	0.3321(3)	0.7249(2)	0.1181	1
H19	0.615	0.3198	0.7034	0.142	1
C20	0.6055(2)	0.42428(15)	0.82992(11)	0.0435	1
C21	0.9360(4)	0.5	0.84483(19)	0.0825	1
H21	0.8999	0.5	0.8163	0.099	1
C22	1.0364(4)	0.5	0.84770(19)	0.0946	1
H22	1.0664	0.5	0.8217	0.113	1
C23	1.0911(3)	0.5	0.88974(14)	0.0393	1
C24	1.0416(3)	0.5	0.92625(16)	0.0657	1
H24	1.0757	0.5	0.9552	0.079	1
C25	0.9415(3)	0.5	0.92027(17)	0.0603	1
H25	0.9094	0.5	0.9456	0.072	1

C26	1.3470(4)	0.5	0.86421(19)	0.1136	1
H26	1.3784	0.5	0.8387	0.137	1
C27	1.2471(4)	0.5	0.85828(18)	0.1118	1
H27	1.2126	0.5	0.8294	0.134	1
C28	1.1993(3)	0.5	0.89502(14)	0.0424	1
C29	1.2553(3)	0.5	0.93558(15)	0.0601	1
H29	1.2256	0.5	0.9616	0.072	1
C30	1.3549(3)	0.5	0.93922(14)	0.0471	1
H30	1.3906	0.5	0.9678	0.057	1
C6M	0.2721(8)	0.3312(5)	0.7865(3)	0.103	0.655
H6MA	0.2059	0.3192	0.7783	0.155	0.655
H6MB	0.2989	0.3121	0.8138	0.155	0.655
H6MC	0.2741	0.372	0.7912	0.155	0.655
C12A	0.3563(7)	0.2957(5)	0.6564(3)	0.049	0.35
H12A	0.3257	0.3294	0.6634	0.059	0.35
C13A	0.3136(8)	0.2624(4)	0.6193(3)	0.044	0.35
H13A	0.2552	0.2754	0.6036	0.053	0.35
C5M	0.0488(4)	0.1779(2)	0.58385(16)	0.078	1
H5MA	0.0192	0.199	0.5581	0.117	1
H5MB	0.0213	0.1899	0.6101	0.117	1
H5MC	0.0372	0.1376	0.579	0.117	1
S1	0.5919(5)	0.8535(3)	0.6631(2)	0.136	0.35
O1	0.09837(17)	0.93955(10)	0.45258(7)	0.0409	1
O2	0.24217(18)	0.93972(14)	0.42676(10)	0.0715	1
O3	0.54896(16)	0.56071(11)	0.85691(7)	0.0445	1
O4	0.69180(18)	0.56029(14)	0.83118(10)	0.0658	1
O5	0.1525(2)	0.81144(14)	0.59052(10)	0.0694	1
O6	0.3283(5)	0.6835(4)	0.7507(2)	0.088	0.655
N1	0.4981(12)	0.8556(7)	0.6227(6)	0.105	0.35
N2	0.5704(13)	0.7982(7)	0.6930(6)	0.105	0.35
C1	0.1853(2)	0.92411(16)	0.45387(12)	0.0503	1
C2	0.2258(3)	0.8853(2)	0.49211(14)	0.0622	1
C3	0.1674(3)	0.86476(19)	0.52155(14)	0.0604	1
H3	0.1011	0.8726	0.5167	0.072	1
C4	0.2056(3)	0.83192(19)	0.55903(14)	0.0602	1
C5	0.3052(3)	0.8196(2)	0.56580(17)	0.0745	1
C6	0.3635(4)	0.8390(3)	0.5340(2)	0.0972	1
H6	0.4293	0.8297	0.5378	0.117	1
C7	0.3255(3)	0.8713(3)	0.49750(19)	0.0899	1
H7	0.3649	0.8839	0.4767	0.108	1
C8	0.3500(3)	0.7853(2)	0.60526(15)	0.0734	1
C9	0.4391(11)	0.8056(7)	0.6318(5)	0.075	0.35
C10	0.4811(13)	0.7730(6)	0.6703(6)	0.082	0.35
C11	0.4388(4)	0.7197(2)	0.68175(15)	0.0721	1
C14	0.4836(4)	0.6851(2)	0.72151(16)	0.0713	1
C15	0.4305(4)	0.6698(3)	0.75513(16)	0.0809	1
C16	0.4709(3)	0.6355(2)	0.79101(14)	0.069	1
H16	0.4343	0.6259	0.8138	0.083	1
C17	0.5639(3)	0.61602(18)	0.79265(13)	0.0562	1
C18	0.6185(4)	0.6321(3)	0.7599(2)	0.107	1

H18	0.6823	0.6193	0.7609	0.129	1
C19	0.5770(4)	0.6679(3)	0.7249(2)	0.1181	1
H19	0.615	0.6802	0.7034	0.142	1
C20	0.6055(2)	0.57572(15)	0.82992(11)	0.0435	1
C6M	0.2721(8)	0.6688(5)	0.7865(3)	0.103	0.655
H6MA	0.2059	0.6808	0.7783	0.155	0.655
H6MB	0.2989	0.6879	0.8138	0.155	0.655
H6MC	0.2741	0.628	0.7912	0.155	0.655
C12A	0.3563(7)	0.7043(5)	0.6564(3)	0.049	0.35
H12A	0.3257	0.6706	0.6634	0.059	0.35
C13A	0.3136(8)	0.7376(4)	0.6193(3)	0.044	0.35
H13A	0.2552	0.7246	0.6036	0.053	0.35
C5M	0.0488(4)	0.8221(2)	0.58385(16)	0.078	1
H5MA	0.0192	0.801	0.5581	0.117	1
H5MB	0.0213	0.8101	0.6101	0.117	1
H5MC	0.0372	0.8624	0.579	0.117	1
Zn1	0.24178(3)	0	0.37700(2)	0.0272	1
Zn1	0.24178(3)	1	0.37700(2)	0.0272	1
Zn2	0.54793(3)	0.5	0.90663(2)	0.0276	1
Zn2	0.04793(3)	0	0.40663(2)	0.0276	1
Zn2	0.04793(3)	1	0.40663(2)	0.0276	1
O1	1.59837(17)	0.56045(10)	0.95258(7)	0.0409	1
O1	1.59837(17)	0.43955(10)	0.95258(7)	0.0409	1
O2	0.74217(18)	0.56028(14)	0.92676(10)	0.0715	1
O2	0.74217(18)	0.43972(14)	0.92676(10)	0.0715	1
O3	1.54896(16)	0.43929(11)	0.85691(7)	0.0445	1
O3	1.54896(16)	0.56071(11)	0.85691(7)	0.0445	1
S1A	0.3251(5)	0.1394(2)	0.7091(2)	0.1155	0.35
N1A	0.3065(12)	0.1461(7)	0.6543(5)	0.103	0.35
N2A	0.3836(12)	0.1987(7)	0.7258(5)	0.098	0.35
C12	0.4355(15)	0.3025(8)	0.6379(4)	0.091	0.35
H12	0.4635	0.338	0.6338	0.109	0.35
C13	0.3899(12)	0.2716(6)	0.5992(5)	0.076	0.35
H13	0.3859	0.2878	0.5706	0.091	0.35
C9A	0.3475(12)	0.1973(7)	0.6467(4)	0.078	0.35
C10A	0.3899(11)	0.2283(6)	0.6845(5)	0.076	0.35
S1B	0.4940(8)	0.1240(5)	0.6954(3)	0.159	0.3
N1B	0.4199(13)	0.1305(8)	0.6484(6)	0.096	0.3
N2B	0.5003(14)	0.1908(8)	0.7146(6)	0.101	0.3
C13B	0.337(2)	0.2747(7)	0.6071(8)	0.108	0.3
H13B	0.2957	0.2931	0.5844	0.129	0.3
C9B	0.4064(10)	0.1900(5)	0.6428(4)	0.048	0.3
C12B	0.3871(18)	0.3081(9)	0.6441(6)	0.095	0.3
H12B	0.3851	0.348	0.643	0.114	0.3
C10B	0.4503(10)	0.2226(4)	0.6806(4)	0.044	0.3
O6A	0.3598(9)	0.2900(5)	0.7565(4)	0.075	0.345
C6MA	0.3129(18)	0.2977(12)	0.7963(6)	0.123	0.345
H6MD	0.2632	0.2691	0.7968	0.185	0.345
H6ME	0.36	0.2939	0.8226	0.185	0.345
H6MF	0.2841	0.3352	0.7958	0.185	0.345

Table 7.18 Bond lengths (Å) and angles (°) for the structure of **MOF-4.1.A**.

Number	Atom1	Atom2	Atom3	Length (Å) / Angle (°)
1	Zn1	O4		2.02
2	Zn1	N20		2.029
3	Zn1	O4		2.02
4	Zn1	O2		2.046
5	Zn1	O2		2.046
6	Zn2	N21		2.027
7	Zn2	O1		2.026
8	Zn2	O1		2.026
9	Zn2	O3		2.054
10	Zn2	O3		2.054
11	S1	N1		1.65(2)
12	S1	N2		1.62(2)
13	O1	C1		1.254(4)
14	O1	Zn2		2.026
15	O2	C1		1.259(5)
16	O2	Zn1		2.046
17	O3	C20		1.249(4)
18	O3	Zn2		2.054
19	O4	C20		1.246(4)
20	O5	C4		1.358(5)
21	O5	C5M		1.448(6)
22	O6	C15		1.442(9)
23	O6	C6M		1.45(1)
24	N1	C9		1.47(2)
25	N2	C10		1.45(2)
26	N20	C21		1.308
27	N20	C25		1.33
28	N21	C26		1.33
29	N21	C30		1.299
30	C1	C2		1.507(5)
31	C2	C3		1.362(6)
32	C2	C7		1.409(6)
33	C3	H3		0.93
34	C3	C4		1.402(6)
35	C4	C5		1.400(6)
36	C5	C6		1.404(8)
37	C5	C8		1.491(6)
38	C6	H6		0.93
39	C6	C7		1.372(8)
40	C7	H7		0.93
41	C8	C9		1.46(2)
42	C8	C13A		1.31(1)
43	C9	C10		1.44(2)
44	C10	C11		1.43(2)
45	C11	C14		1.502(6)
46	C11	C12A		1.34(1)
47	C14	C15		1.372(8)

48	C14	C19	1.347(8)
49	C15	C16	1.395(7)
50	C16	H16	0.931
51	C16	C17	1.363(6)
52	C17	C18	1.369(8)
53	C17	C20	1.512(5)
54	C18	H18	0.931
55	C18	C19	1.401(9)
56	C19	H19	0.93
57	C21	H21	0.931
58	C21	C22	1.384
59	C22	H22	0.931
60	C22	C23	1.38
61	C23	C24	1.367
62	C23	C28	1.489
63	C24	H24	0.93
64	C24	C25	1.377
65	C25	H25	0.93
66	C26	H26	0.929
67	C26	C27	1.374
68	C27	H27	0.931
69	C27	C28	1.359
70	C28	C29	1.351
71	C29	H29	0.929
72	C29	C30	1.372
73	C30	H30	0.93
74	C6M	H6MA	0.96
75	C6M	H6MB	0.961
76	C6M	H6MC	0.96
77	C12A	H12A	0.93
78	C12A	C13A	1.42(1)
79	C13A	H13A	0.93
80	C5M	H5MA	0.959
81	C5M	H5MB	0.96
82	C5M	H5MC	0.96
83	S1	N1	1.65(2)
84	S1	N2	1.62(2)
85	O1	C1	1.254(4)
86	O1	Zn2	2.026
87	O2	C1	1.259(5)
88	O2	Zn1	2.046
89	O3	C20	1.249(4)
90	O3	Zn2	2.054
91	O4	C20	1.246(4)
92	O5	C4	1.358(5)
93	O5	C5M	1.448(6)
94	O6	C15	1.442(9)
95	O6	C6M	1.45(1)
96	N1	C9	1.47(2)
97	N2	C10	1.45(2)

98	C1	C2		1.507(5)
99	C2	C3		1.362(6)
100	C2	C7		1.409(6)
101	C3	H3		0.93
102	C3	C4		1.402(6)
103	C4	C5		1.400(6)
104	C5	C6		1.404(8)
105	C5	C8		1.491(6)
106	C6	H6		0.93
107	C6	C7		1.372(8)
108	C7	H7		0.93
109	C8	C9		1.46(2)
110	C8	C13A		1.31(1)
111	C9	C10		1.44(2)
112	C10	C11		1.43(2)
113	C11	C14		1.502(6)
114	C11	C12A		1.34(1)
115	C14	C15		1.372(8)
116	C14	C19		1.347(8)
117	C15	C16		1.395(7)
118	C16	H16		0.931
119	C16	C17		1.363(6)
120	C17	C18		1.369(8)
121	C17	C20		1.512(5)
122	C18	H18		0.931
123	C18	C19		1.401(9)
124	C19	H19		0.93
125	C6M	H6MA		0.96
126	C6M	H6MB		0.961
127	C6M	H6MC		0.96
128	C12A	H12A		0.93
129	C12A	C13A		1.42(1)
130	C13A	H13A		0.93
131	C5M	H5MA		0.959
132	C5M	H5MB		0.96
133	C5M	H5MC		0.96
1	O4	Zn1	N20	106.2
2	O4	Zn1	O4	88.1
3	O4	Zn1	O2	159.8
4	O4	Zn1	O2	89.1
5	N20	Zn1	O4	106.2
6	N20	Zn1	O2	93.8
7	N20	Zn1	O2	93.8
8	O4	Zn1	O2	89.1
9	O4	Zn1	O2	159.8
10	O2	Zn1	O2	86.6
11	N21	Zn2	O1	106.1
12	N21	Zn2	O1	106.1
13	N21	Zn2	O3	94.6
14	N21	Zn2	O3	94.6

15	O1	Zn2	O1	87.99
16	O1	Zn2	O3	159.18
17	O1	Zn2	O3	88.79
18	O1	Zn2	O3	88.79
19	O1	Zn2	O3	159.18
20	O3	Zn2	O3	86.95
21	N1	S1	N2	104.0(9)
22	C1	O1	Zn2	117.6
23	C1	O2	Zn1	136.6
24	C20	O3	Zn2	136.7
25	Zn1	O4	C20	117.5
26	C4	O5	C5M	117.8(3)
27	C15	O6	C6M	120.0(7)
28	S1	N1	C9	104(1)
29	S1	N2	C10	106(1)
30	Zn1	N20	C21	125.2
31	Zn1	N20	C25	117.7
32	C21	N20	C25	117.1
33	Zn2	N21	C26	118.4
34	Zn2	N21	C30	125.2
35	C26	N21	C30	116.4
36	O1	C1	O2	125.5(3)
37	O1	C1	C2	117.0(3)
38	O2	C1	C2	117.4(3)
39	C1	C2	C3	120.6(4)
40	C1	C2	C7	119.1(4)
41	C3	C2	C7	120.3(4)
42	C2	C3	H3	119.5
43	C2	C3	C4	121.0(4)
44	H3	C3	C4	119.5
45	O5	C4	C3	124.4(4)
46	O5	C4	C5	116.4(4)
47	C3	C4	C5	119.2(4)
48	C4	C5	C6	118.9(4)
49	C4	C5	C8	121.6(4)
50	C6	C5	C8	119.5(4)
51	C5	C6	H6	119.2
52	C5	C6	C7	121.4(5)
53	H6	C6	C7	119.4
54	C2	C7	C6	119.0(5)
55	C2	C7	H7	120.4
56	C6	C7	H7	120.6
57	C5	C8	C9	119.5(7)
58	C5	C8	C13A	124.7(6)
59	C9	C8	C13A	115.8(8)
60	N1	C9	C8	128(1)
61	N1	C9	C10	113(1)
62	C8	C9	C10	119(1)
63	N2	C10	C9	113(1)
64	N2	C10	C11	126(1)

65	C9	C10	C11	121(1)
66	C10	C11	C14	121.0(8)
67	C10	C11	C12A	116.3(9)
68	C14	C11	C12A	122.6(6)
69	C11	C14	C15	121.0(5)
70	C11	C14	C19	120.7(5)
71	C15	C14	C19	118.3(5)
72	O6	C15	C14	119.6(5)
73	O6	C15	C16	119.1(5)
74	C14	C15	C16	120.9(5)
75	C15	C16	H16	120
76	C15	C16	C17	120.0(4)
77	H16	C16	C17	120.1
78	C16	C17	C18	119.7(4)
79	C16	C17	C20	120.0(4)
80	C18	C17	C20	120.3(4)
81	C17	C18	H18	120.3
82	C17	C18	C19	119.1(5)
83	H18	C18	C19	120.6
84	C14	C19	C18	121.9(6)
85	C14	C19	H19	119
86	C18	C19	H19	119.1
87	O3	C20	O4	125.7(3)
88	O3	C20	C17	116.1(3)
89	O4	C20	C17	118.1(3)
90	N20	C21	H21	117.9
91	N20	C21	C22	124
92	H21	C21	C22	118.1
93	C21	C22	H22	120.5
94	C21	C22	C23	118.9
95	H22	C22	C23	120.7
96	C22	C23	C24	117.1
97	C22	C23	C28	121.4
98	C24	C23	C28	121.5
99	C23	C24	H24	119.9
100	C23	C24	C25	120.2
101	H24	C24	C25	120
102	N20	C25	C24	122.8
103	N20	C25	H25	118.6
104	C24	C25	H25	118.6
105	N21	C26	H26	118.1
106	N21	C26	C27	123.8
107	H26	C26	C27	118
108	C26	C27	H27	120.3
109	C26	C27	C28	119.3
110	H27	C27	C28	120.4
111	C23	C28	C27	120.6
112	C23	C28	C29	123.1
113	C27	C28	C29	116.3
114	C28	C29	H29	119.2

115	C28	C29	C30	121.6
116	H29	C29	C30	119.3
117	N21	C30	C29	122.6
118	N21	C30	H30	118.7
119	C29	C30	H30	118.7
120	O6	C6M	H6MA	109.5
121	O6	C6M	H6MB	109.6
122	O6	C6M	H6MC	109.5
123	H6MA	C6M	H6MB	109
124	H6MA	C6M	H6MC	109
125	H6MB	C6M	H6MC	109
126	C11	C12A	H12A	118.8
127	C11	C12A	C13A	122.4(9)
128	H12A	C12A	C13A	119
129	C8	C13A	C12A	125.1(9)
130	C8	C13A	H13A	117.4
131	C12A	C13A	H13A	118
132	O5	C5M	H5MA	109.5
133	O5	C5M	H5MB	109.5
134	O5	C5M	H5MC	109.4
135	H5MA	C5M	H5MB	109.6
136	H5MA	C5M	H5MC	109.5
137	H5MB	C5M	H5MC	109.4
138	N1	S1	N2	104.0(9)
139	C1	O1	Zn2	117.6
140	C1	O2	Zn1	136.6
141	C20	O3	Zn2	136.7
142	Zn1	O4	C20	117.5
143	C4	O5	C5M	117.8(3)
144	C15	O6	C6M	120.0(7)
145	S1	N1	C9	104(1)
146	S1	N2	C10	106(1)
147	O1	C1	O2	125.5(3)
148	O1	C1	C2	117.0(3)
149	O2	C1	C2	117.4(3)
150	C1	C2	C3	120.6(4)
151	C1	C2	C7	119.1(4)
152	C3	C2	C7	120.3(4)
153	C2	C3	H3	119.5
154	C2	C3	C4	121.0(4)
155	H3	C3	C4	119.5
156	O5	C4	C3	124.4(4)
157	O5	C4	C5	116.4(4)
158	C3	C4	C5	119.2(4)
159	C4	C5	C6	118.9(4)
160	C4	C5	C8	121.6(4)
161	C6	C5	C8	119.5(4)
162	C5	C6	H6	119.2
163	C5	C6	C7	121.4(5)
164	H6	C6	C7	119.4

165	C2	C7	C6	119.0(5)
166	C2	C7	H7	120.4
167	C6	C7	H7	120.6
168	C5	C8	C9	119.5(7)
169	C5	C8	C13A	124.7(6)
170	C9	C8	C13A	115.8(8)
171	N1	C9	C8	128(1)
172	N1	C9	C10	113(1)
173	C8	C9	C10	119(1)
174	N2	C10	C9	113(1)
175	N2	C10	C11	126(1)
176	C9	C10	C11	121(1)
177	C10	C11	C14	121.0(8)
178	C10	C11	C12A	116.3(9)
179	C14	C11	C12A	122.6(6)
180	C11	C14	C15	121.0(5)
181	C11	C14	C19	120.7(5)
182	C15	C14	C19	118.3(5)
183	O6	C15	C14	119.6(5)
184	O6	C15	C16	119.1(5)
185	C14	C15	C16	120.9(5)
186	C15	C16	H16	120
187	C15	C16	C17	120.0(4)
188	H16	C16	C17	120.1
189	C16	C17	C18	119.7(4)
190	C16	C17	C20	120.0(4)
191	C18	C17	C20	120.3(4)
192	C17	C18	H18	120.3
193	C17	C18	C19	119.1(5)
194	H18	C18	C19	120.6
195	C14	C19	C18	121.9(6)
196	C14	C19	H19	119
197	C18	C19	H19	119.1
198	O3	C20	O4	125.7(3)
199	O3	C20	C17	116.1(3)
200	O4	C20	C17	118.1(3)
201	O6	C6M	H6MA	109.5
202	O6	C6M	H6MB	109.6
203	O6	C6M	H6MC	109.5
204	H6MA	C6M	H6MB	109
205	H6MA	C6M	H6MC	109
206	H6MB	C6M	H6MC	109
207	C11	C12A	H12A	118.8
208	C11	C12A	C13A	122.4(9)
209	H12A	C12A	C13A	119
210	C8	C13A	C12A	125.1(9)
211	C8	C13A	H13A	117.4
212	C12A	C13A	H13A	118
213	O5	C5M	H5MA	109.5
214	O5	C5M	H5MB	109.5

215	O5	C5M	H5MC	109.4
216	H5MA	C5M	H5MB	109.6
217	H5MA	C5M	H5MC	109.5
218	H5MB	C5M	H5MC	109.4
219	O3	Zn2	O3	86.95

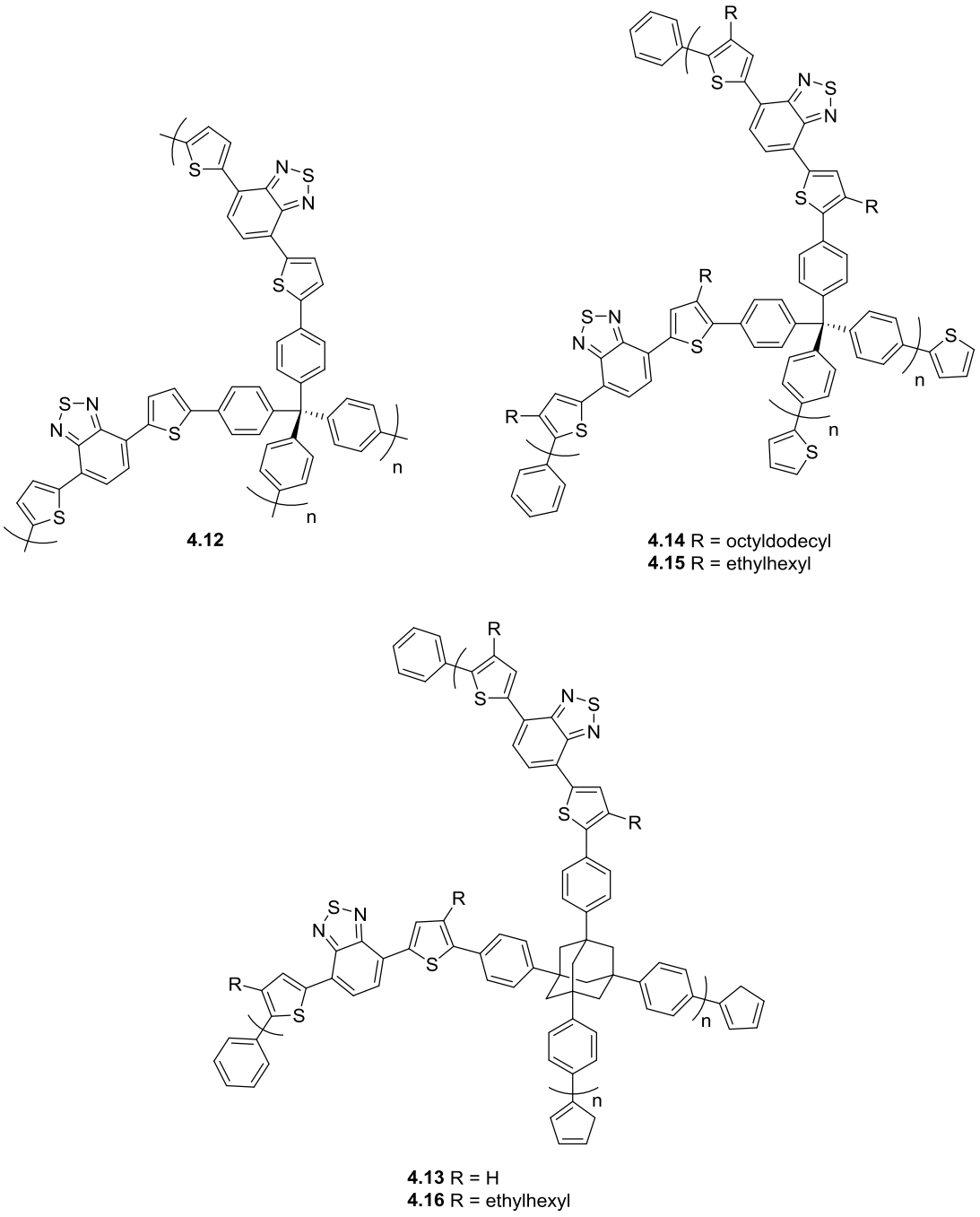

Figure 7.9 Proposed structures for polymers **4.12-4.16**.

Table 7.19 Binding potential energies and relative interaction distances for selected combinations of **TEN** calculated at the MP2/aug-cc-pVTZ level of theory. *inverse configuration.

			MP2/aug-cc-pVTZ		
Monomer A	**Monomer B**	**Interaction**	**Energy (kcal/mol)**	**Energy (kT)**	**Distance (Angstroms)**
Thiazole	Pyrrole	N-HN	6.19	10.44	2.1
Oxazole	Pyrrole	N-HN	5.97	10.06	2.1
Oxazole	Pyrrole	O-HN	2.40	4.04	2.2
Benzothiophene	Thiazole	(3)CH-N	2.20	3.71	2.5
Benzofuran	Thiazole	(3)CH-N	2.20	3.71	2.5
Thiophene	Thiazole	(3)CH-N	1.85	3.13	2.5
Furane	Thiazole	(3)CH-N	1.82	3.07	2.5
Furane	DPP	(3)CH-OC	1.69	2.85	2.4
Thiazole	Pyrrole	S-HN	1.68	2.82	2.7
Thiophene	DPP	(3)CH-OC	1.67	2.82	2.4
Pyrrole	Thiazole	(3)CH-N	1.29	2.18	2.6
Thiazole	Benzothiazole	S-N	0.87	1.47	3.7
Thiazole	Benzooxazole	S-N	0.80	1.35	3.7
Thiazole	Benzofurane	S-O	0.80	1.35	3.5
Thiazole	Benzothiophene	S-S	0.79	1.33	3.9
Thiazole	Benzothiazole	N-S	0.77	1.30	3.7
Thiazole	Thiazole	S-N	0.75	1.26	3.7
Thiazole	Benzothiazole	S-S	0.74	1.25	4.0
Thiazole	Thiophene	S-S	0.71	1.20	4.0
Benzothiophene	Thiazole	(3)CH-S	0.71	1.19	3.0
Thiazole	Benzooxazole	S-O	0.66	1.11	3.6
Thiazole	Oxazole	S-N	0.65	1.09	3.7
Benzofurane	Thiazole	(3)CH-S	0.62	1.04	3.1
Thiazole	Furane	S-O	0.62	1.04	3.6
Thiophene	Thiazole	(3)CH-S	0.59	1.00	3.1
Pyrrole	Thiazole	(3)CH-S	0.58	0.98	3.1
DPP	Thiophene	CO-S	0.55	0.93	3.5
Furane	Thiazole	(3)CH-S	0.53	0.89	3.1
Thiazole	Benzothiophene	N-S	0.51	0.86	3.8
Thiazole	Oxazole	S-O	0.50	0.83	3.6
Thiazole	Thiophene	N-S	0.45	0.75	3.8
Thiazole	Thiazole	S-S	0.35	0.58	4.3
Thiazole	Thiazole	S-S*	0.34	0.57	4.4
Thiazole	Furane	N-O	nb	nb	nb
Thiazole	Thiazole	N-N	nb	nb	nb
Thiazole	Oxazole	N-O	nb	nb	nb
Thiazole	Oxazole	N-N	nb	nb	nb
Thiazole	Benzothiazole	N-N	nb	nb	nb
Thiazole	Benzofurane	N-O	nb	nb	nb
Thiazole	Benzooxazole	N-O	nb	nb	nb
Thiazole	Benzooxazole	N-N	nb	nb	nb
DPP	Furane	CO-O	nb	nb	nb

Table 7.20 Binding potential energies and relative interaction distances for selected combinations of **TEN** calculated at the SCS-MP2/aug-cc-pVTZ level of theory. *inverse configuration.

			SCS-MP2/aug-cc-pVTZ		
Monomer A	**Monomer B**	**Interaction**	**Energy (kcal/mol)**	**Energy (kT)**	**Distance (Angstroms)**
Thiazole	Pyrrole	N-HN	5.36	9.03	2.1
Oxazole	Pyrrole	N-HN	5.21	8.78	2.1
Oxazole	Pyrrole	O-HN	1.96	3.31	2.2
Benzothiophene	Thiazole	(3)CH-N	1.72	2.89	2.6
Benzofuran	Thiazole	(3)CH-N	1.74	2.94	2.6
Thiophene	Thiazole	(3)CH-N	1.45	2.45	2.6
Furane	Thiazole	(3)CH-N	1.45	2.45	2.6
Furane	DPP	(3)CH-OC	1.38	2.32	2.4
Thiazole	Pyrrole	S-HN	1.23	2.08	2.8
Thiophene	DPP	(3)CH-OC	1.36	2.29	2.4
Pyrrole	Thiazole	(3)CH-N	0.95	1.60	2.7
Thiazole	Benzothiazole	S-N	0.50	0.85	3.9
Thiazole	Benzooxazole	S-N	0.51	0.86	3.9
Thiazole	Benzofurane	S-O	0.45	0.75	3.7
Thiazole	Benzothiophene	S-S	0.47	0.80	4.1
Thiazole	Benzothiazole	N-S	0.45	0.76	3.9
Thiazole	Thiazole	S-N	0.45	0.76	3.9
Thiazole	Benzothiazole	S-S	0.44	0.74	4.1
Thiazole	Thiophene	S-S	0.43	0.73	4.2
Benzothiophene	Thiazole	(3)CH-S	0.44	0.74	3.2
Thiazole	Benzooxazole	S-O	0.35	0.60	3.7
Thiazole	Oxazole	S-N	0.40	0.67	3.9
Benzofurane	Thiazole	(3)CH-S	0.38	0.65	3.2
Thiazole	Furane	S-O	0.35	0.59	3.7
Thiophene	Thiazole	(3)CH-S	0.37	0.62	3.2
Pyrrole	Thiazole	(3)CH-S	0.36	0.61	3.3
DPP	Thiophene	CO-S	0.26	0.44	3.7
Furane	Thiazole	(3)CH-S	0.33	0.55	3.3
Thiazole	Benzothiophene	N-S	0.22	0.37	4.0
Thiazole	Oxazole	S-O	0.26	0.44	3.8
Thiazole	Thiophene	N-S	0.19	0.32	4.1
Thiazole	Thiazole	S-S	0.19	0.32	4.6
Thiazole	Thiazole	S-S*	0.18	0.30	4.6
Thiazole	Furane	N-O	nb	nb	nb
Thiazole	Thiazole	N-N	nb	nb	nb
Thiazole	Oxazole	N-O	nb	nb	nb
Thiazole	Oxazole	N-N	nb	nb	nb
Thiazole	Benzothiazole	N-N	nb	nb	nb
Thiazole	Benzofurane	N-O	nb	nb	nb
Thiazole	Benzooxazole	N-O	nb	nb	nb
Thiazole	Benzooxazole	N-N	nb	nb	nb
DPP	Furane	CO-O	nb	nb	nb

Table 7.21 Binding potential energies and relative interaction distances for selected combinations of **TEN** calculated at the SCS(MI)-MP2/aug-cc-pVTZ level of theory. *inverse configuration.

			SCS(MI)-MP2/aug-cc-pVTZ		
Monomer A	**Monomer B**	**Interaction**	**Energy (kcal/mol)**	**Energy (kT)**	**Distance (Angstroms)**
Thiazole	Pyrrole	N-HN	5.81	9.80	2.1
Oxazole	Pyrrole	N-HN	5.65	9.53	2.1
Oxazole	Pyrrole	O-HN	2.19	3.70	2.2
Benzothiophene	Thiazole	(3)CH-N	1.96	3.30	2.5
Benzofuran	Thiazole	(3)CH-N	1.99	3.35	2.5
Thiophene	Thiazole	(3)CH-N	1.66	2.80	2.5
Furane	Thiazole	(3)CH-N	1.66	2.79	2.5
Furane	DPP	(3)CH-OC	1.66	2.80	2.4
Thiazole	Pyrrole	S-HN	1.41	2.38	2.8
Thiophene	DPP	(3)CH-OC	1.64	2.76	2.4
Pyrrole	Thiazole	(3)CH-N	1.12	1.90	2.6
Thiazole	Benzothiazole	S-N	0.58	0.99	3.8
Thiazole	Benzooxazole	S-N	0.57	0.97	3.9
Thiazole	Benzofurane	S-O	0.52	0.87	3.6
Thiazole	Benzothiophene	S-S	0.53	0.90	4.1
Thiazole	Benzothiazole	N-S	0.52	0.87	3.8
Thiazole	Thiazole	S-N	0.52	0.88	3.8
Thiazole	Benzothiazole	S-S	0.49	0.83	4.1
Thiazole	Thiophene	S-S	0.49	0.82	4.1
Benzothiophene	Thiazole	(3)CH-S	0.51	0.85	3.2
Thiazole	Benzooxazole	S-O	0.42	0.71	3.7
Thiazole	Oxazole	S-N	0.45	0.77	3.9
Benzofurane	Thiazole	(3)CH-S	0.45	0.75	3.2
Thiazole	Furane	S-O	0.41	0.70	3.7
Thiophene	Thiazole	(3)CH-S	0.43	0.72	3.2
Pyrrole	Thiazole	(3)CH-S	0.42	0.71	3.2
DPP	Thiophene	CO-S	0.32	0.54	3.6
Furane	Thiazole	(3)CH-S	0.38	0.65	3.2
Thiazole	Benzothiophene	N-S	0.27	0.46	4.0
Thiazole	Oxazole	S-O	0.31	0.53	3.8
Thiazole	Thiophene	N-S	0.25	0.41	4.0
Thiazole	Thiazole	S-S	0.22	0.37	4.5
Thiazole	Thiazole	S-S*	0.21	0.35	4.5
Thiazole	Furane	N-O	nb	nb	nb
Thiazole	Thiazole	N-N	nb	nb	nb
Thiazole	Oxazole	N-O	nb	nb	nb
Thiazole	Oxazole	N-N	nb	nb	nb
Thiazole	Benzothiazole	N-N	nb	nb	nb
Thiazole	Benzofurane	N-O	nb	nb	nb
Thiazole	Benzooxazole	N-O	nb	nb	nb
Thiazole	Benzooxazole	N-N	nb	nb	nb
DPP	Furane	CO-O	nb	nb	nb

NMR spectra of the compounds described in the experimental section.

2.1

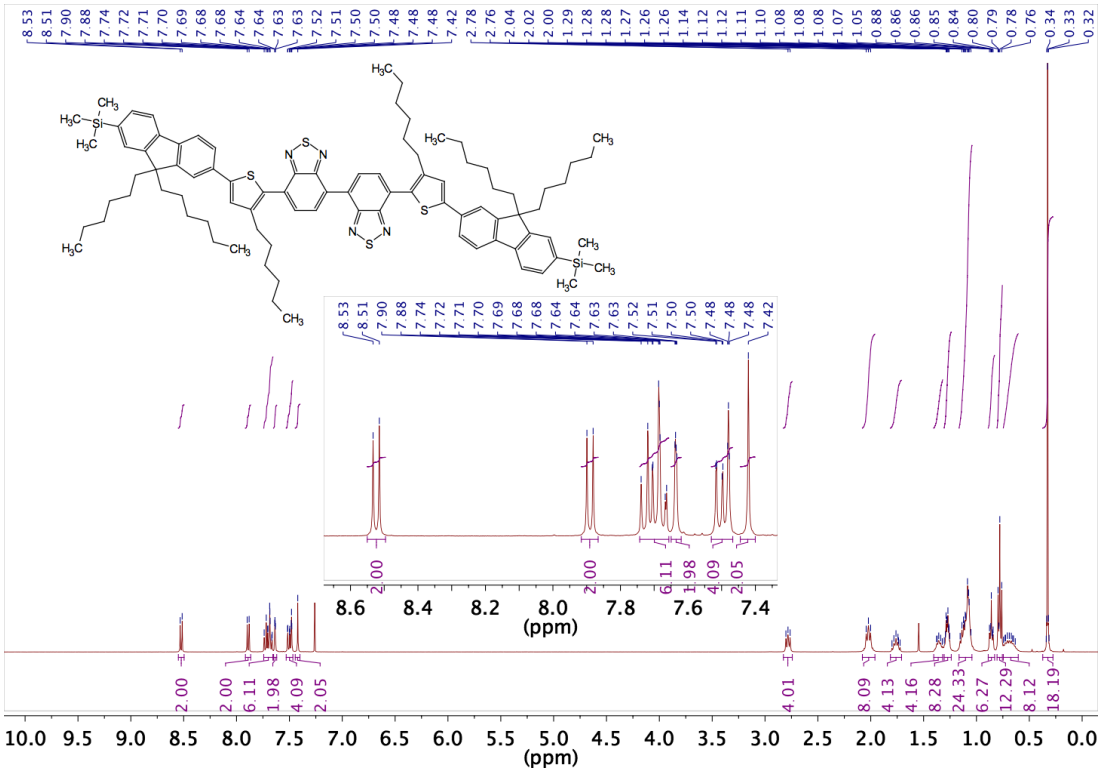

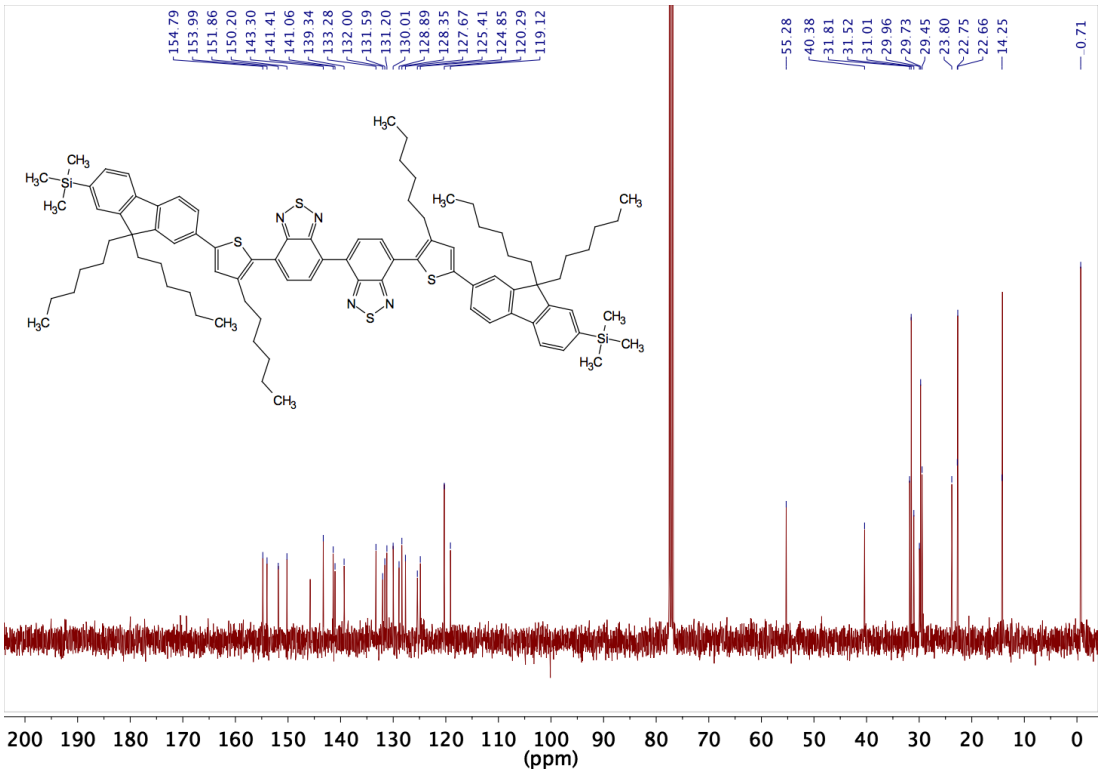

2.2

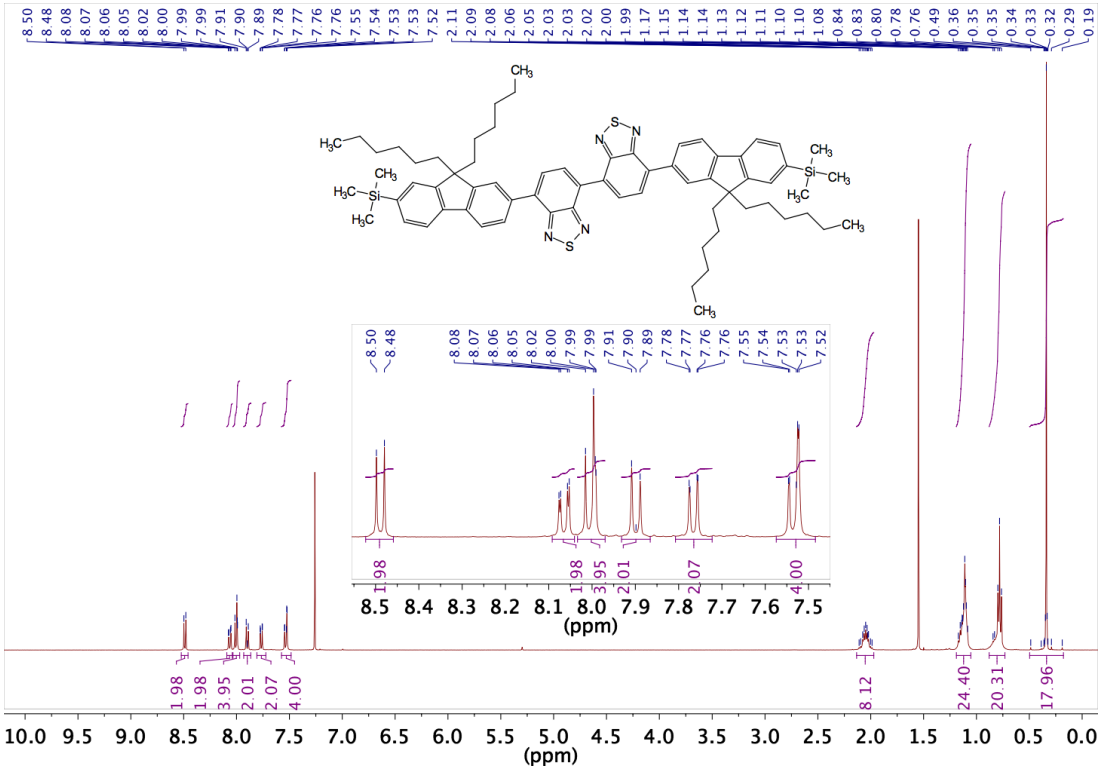
8.50 8.48 8.08 8.07 8.06 8.05 8.02 8.00 7.99 7.99 7.91 7.90 7.89 7.78 7.77 7.76 7.76 7.55 7.54 7.53 7.53 7.52 2.11 2.09 2.08 2.06 2.05 2.03 2.03 2.02 2.00 1.99 1.17 1.15 1.14 1.14 1.13 1.12 1.11 1.10 1.08 0.84 0.83 0.80 0.78 0.76 0.49 0.36 0.35 0.35 0.34 0.33 0.32 0.29 0.19
1.98 1.98 3.95 2.01 2.07 4.00 8.12 24.40 20.31 17.96
10.0 9.5 9.0 8.5 8.0 7.5 7.0 6.5 6.0 5.5 5.0 4.5 4.0 3.5 3.0 2.5 2.0 1.5 1.0 0.5 0.0
(ppm)
1.98 1.98 3.95 2.01 2.07 4.00
8.5 8.4 8.3 8.2 8.1 8.0 7.9 7.8 7.7 7.6 7.5
(ppm)

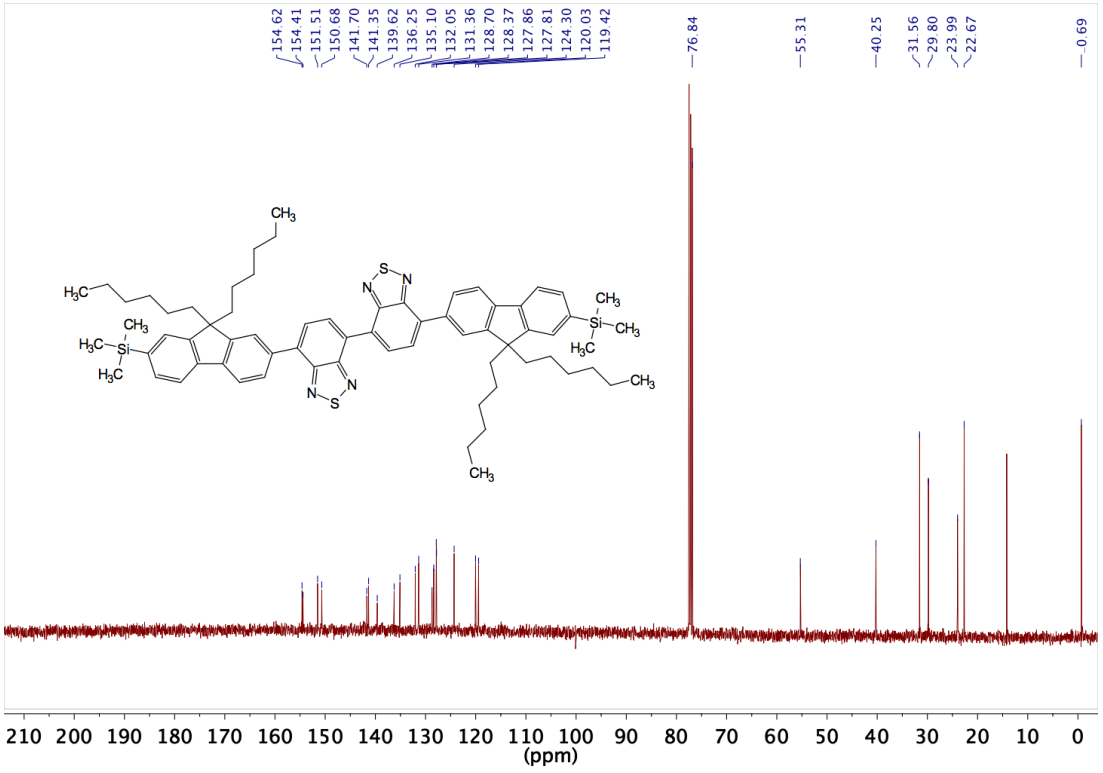
154.62 154.41 151.51 150.68 141.70 141.35 139.62 136.25 135.10 132.05 131.36 128.70 128.37 127.86 127.81 124.30 120.03 119.42
76.84
55.31
40.25
31.56 29.80 23.99 22.67
0.69
210 200 190 180 170 160 150 140 130 120 110 100 90 80 70 60 50 40 30 20 10 0
(ppm)

2.3

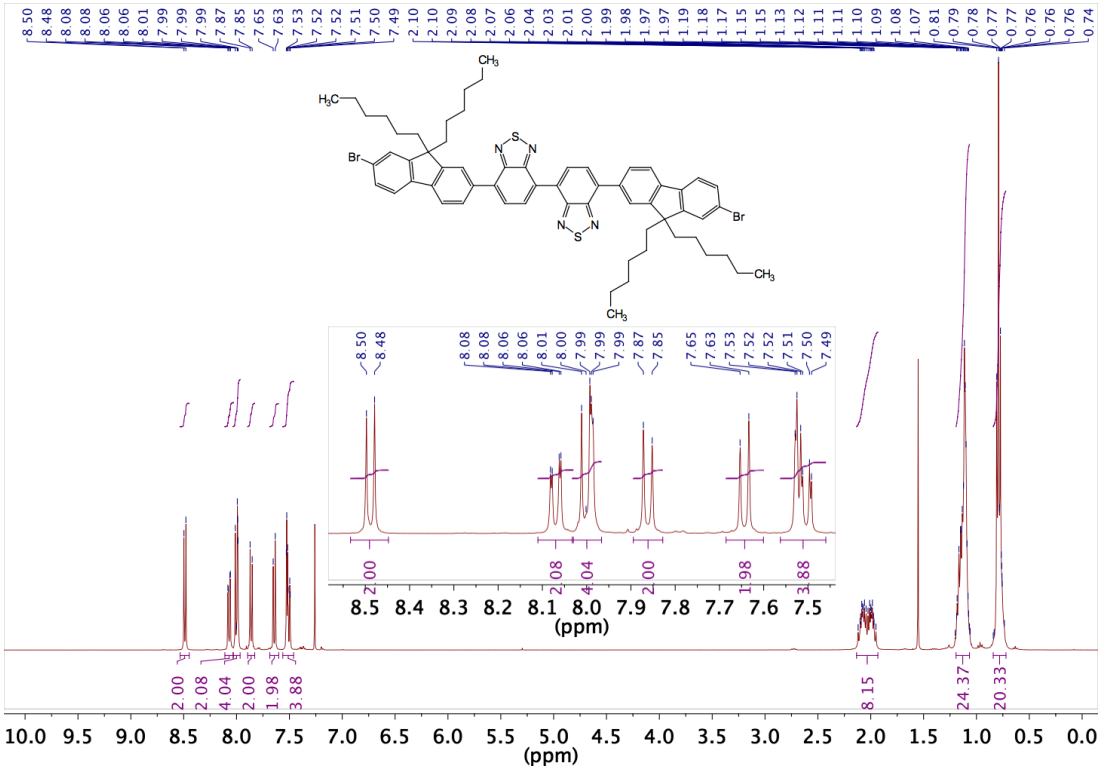
8.50 8.48 8.08 8.08 8.06 8.06 8.01 7.99 7.99 7.99 7.87 7.85 7.65 7.63 7.53 7.52 7.52 7.51 7.50 7.49 2.10 2.09 2.08 2.07 2.06 2.04 2.03 2.01 2.00 1.99 1.98 1.97 1.19 1.18 1.17 1.15 1.15 1.13 1.12 1.11 1.11 1.10 1.09 1.08 1.07 0.81 0.79 0.78 0.77 0.77 0.76 0.76 0.76 0.74
CH3
H3C
Br
S
N
N
N
S
N
Br
CH3
CH3
2.00 2.08 4.04 2.00 1.98 3.88
8.15 24.37 20.33
10.0 9.5 9.0 8.5 8.0 7.5 7.0 6.5 6.0 5.5 5.0 4.5 4.0 3.5 3.0 2.5 2.0 1.5 1.0 0.5 0.0
(ppm)
2.00 2.08 4.04 2.00 1.98 3.88
8.5 8.4 8.3 8.2 8.1 8.0 7.9 7.8 7.7 7.6 7.5
(ppm)

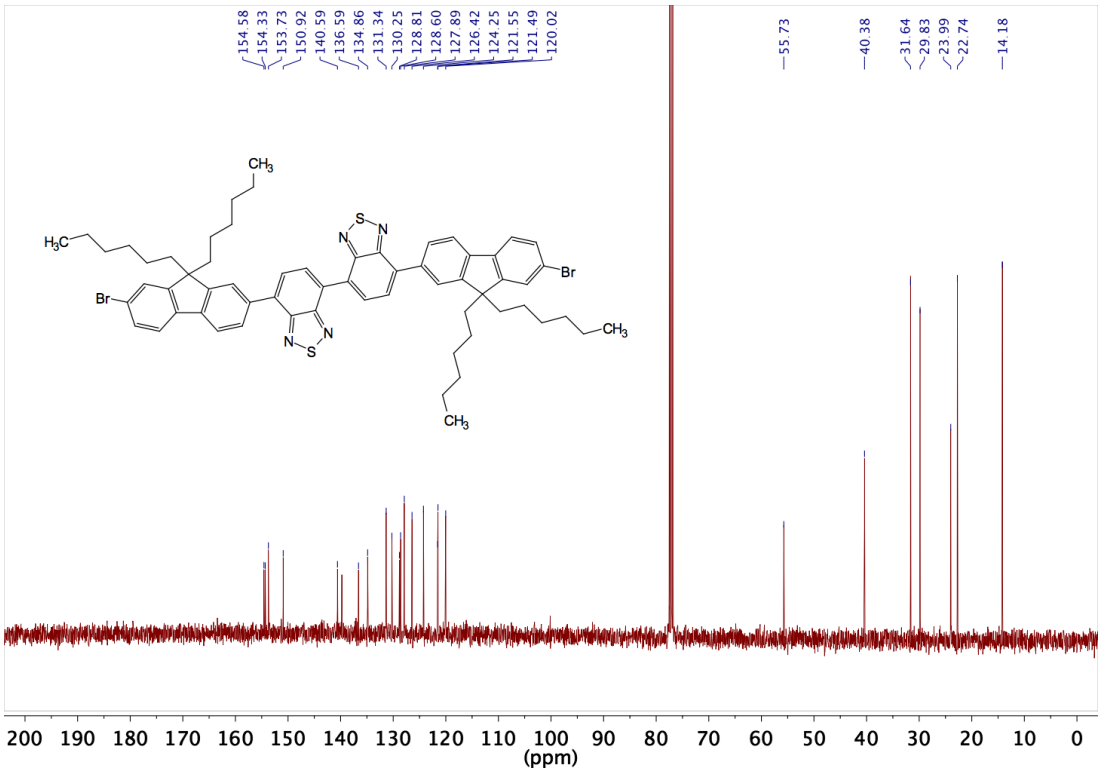
154.58 154.33 153.73 150.92 140.59 136.59 134.86 131.34 130.25 128.81 128.60 127.89 126.42 124.25 121.55 121.49 120.02
55.73 40.38 31.64 29.83 23.99 22.74 14.18
CH3
H3C
Br
S
N
N
N
S
N
Br
CH3
CH3
200 190 180 170 160 150 140 130 120 110 100 90 80 70 60 50 40 30 20 10 0
(ppm)

2.4

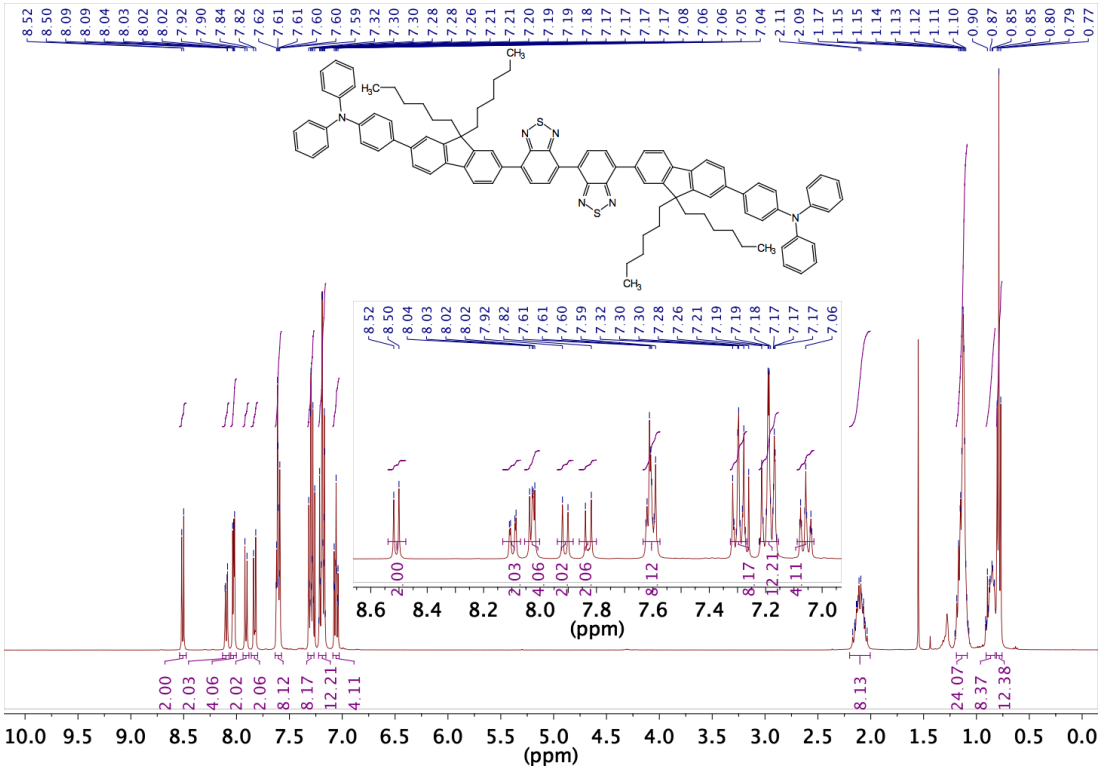

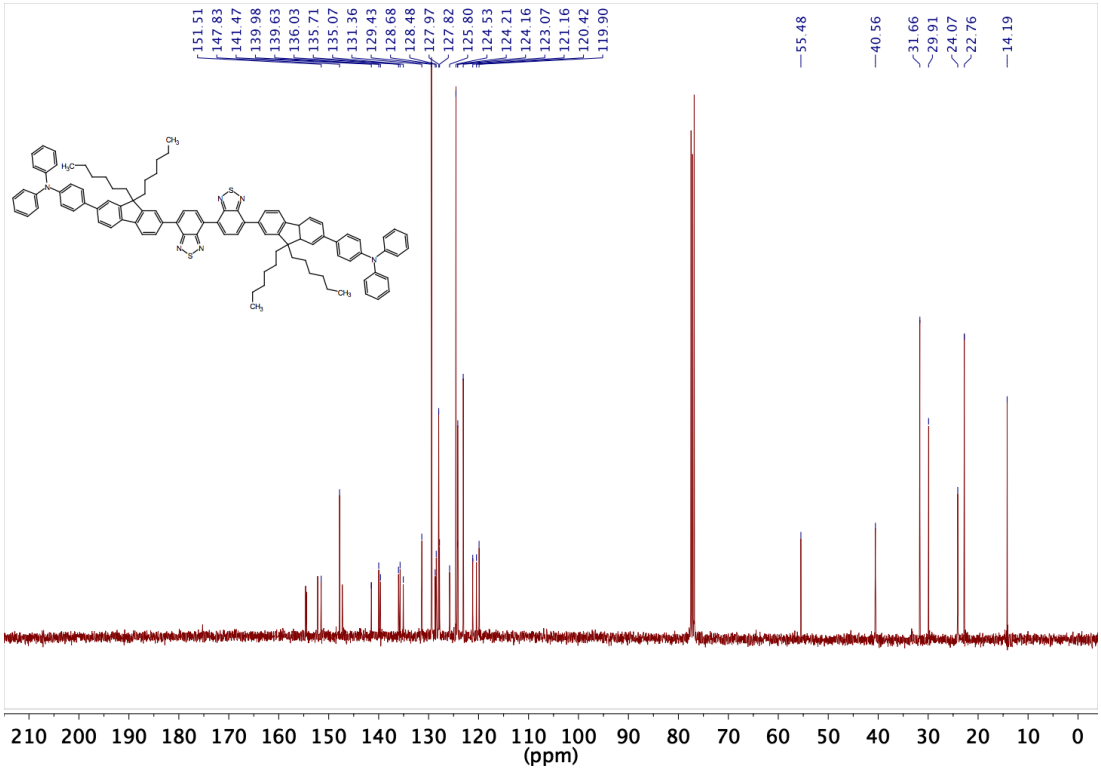

2.5

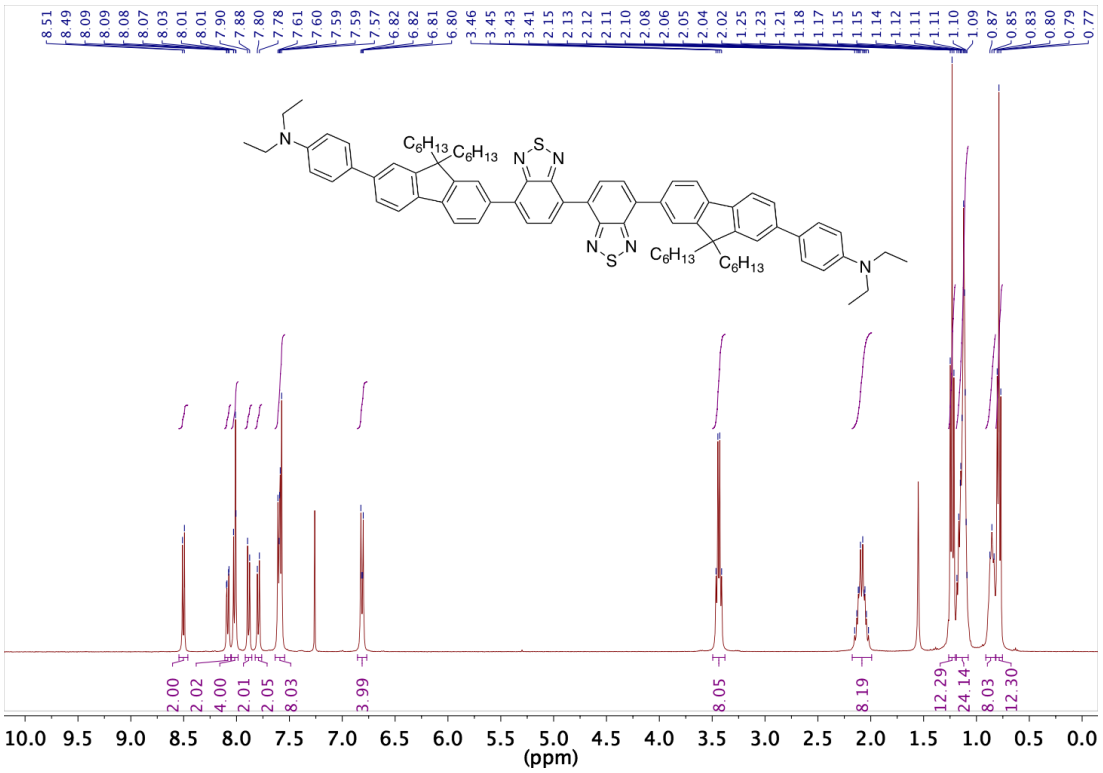
8.51 8.49 8.09 8.09 8.08 8.07 8.03 8.01 8.01 7.90 7.88 7.80 7.78 7.61 7.60 7.59 7.59 7.57 6.82 6.82 6.81 6.80 3.46 3.45 3.43 3.41 2.15 2.13 2.12 2.11 2.10 2.08 2.06 2.05 2.04 2.02 1.25 1.23 1.21 1.18 1.17 1.15 1.15 1.14 1.12 1.11 1.11 1.10 1.09 0.87 0.85 0.83 0.80 0.79 0.77
2.00 2.02 4.00 2.01 2.05 8.03 3.99 8.05 8.19 12.29 24.14 8.03 12.30
10.0 9.5 9.0 8.5 8.0 7.5 7.0 6.5 6.0 5.5 5.0 4.5 4.0 3.5 3.0 2.5 2.0 1.5 1.0 0.5 0.0
(ppm)

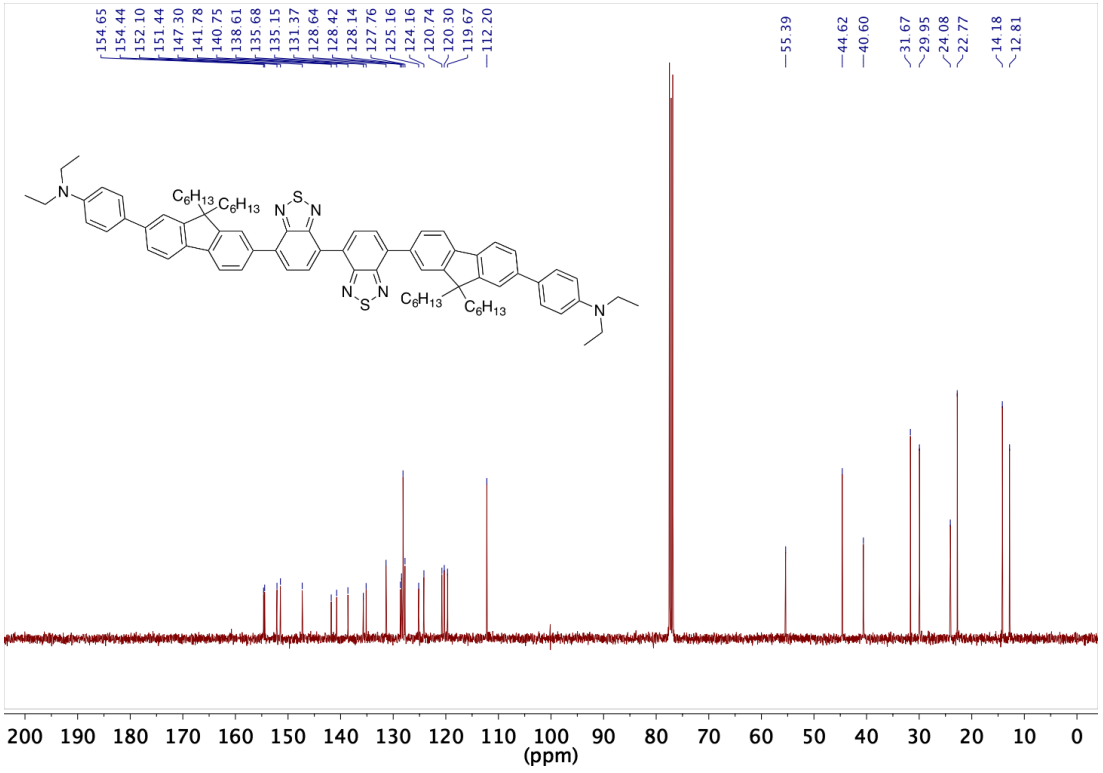
154.65 154.44 152.10 151.44 147.30 141.78 140.75 138.61 135.68 135.15 131.37 128.64 128.42 128.14 127.76 125.16 124.16 120.74 120.30 119.67 112.20
55.39 44.62 40.60 31.67 29.95 24.08 22.77 14.18 12.81
200 190 180 170 160 150 140 130 120 110 100 90 80 70 60 50 40 30 20 10 0
(ppm)

2.7

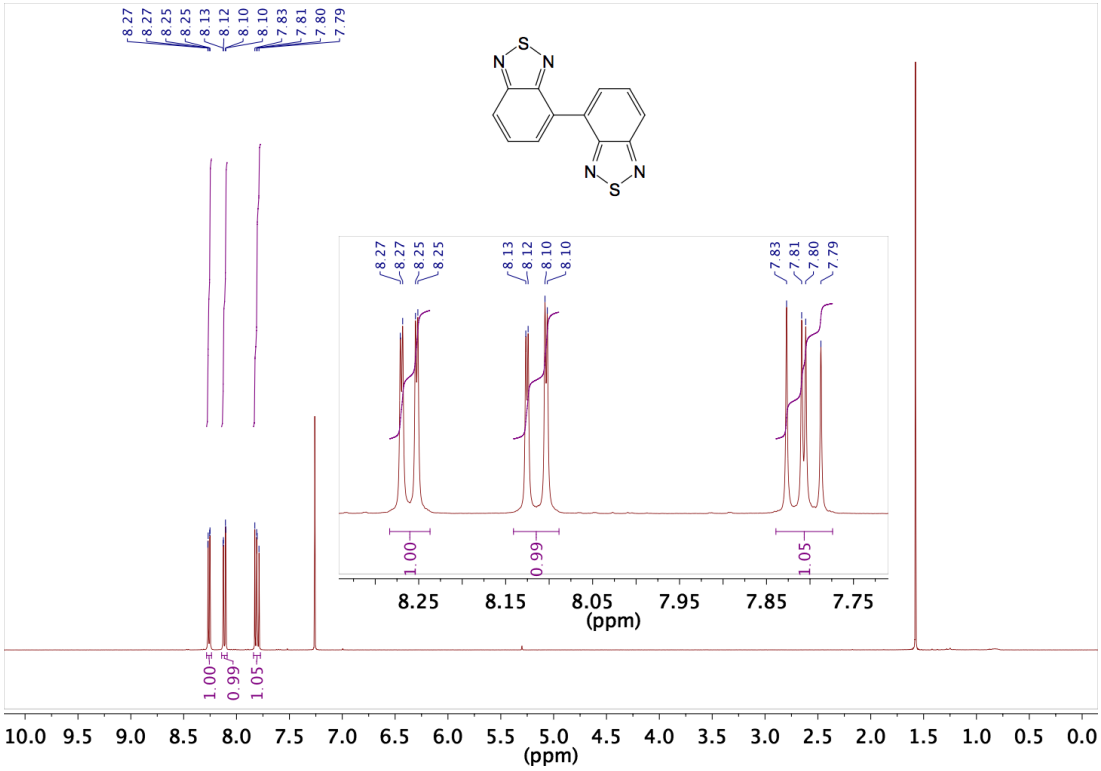
8.27
8.27
8.25
8.25
8.13
8.12
8.10
8.10
7.83
7.81
7.80
7.79
1.00
0.99
1.05
(ppm)

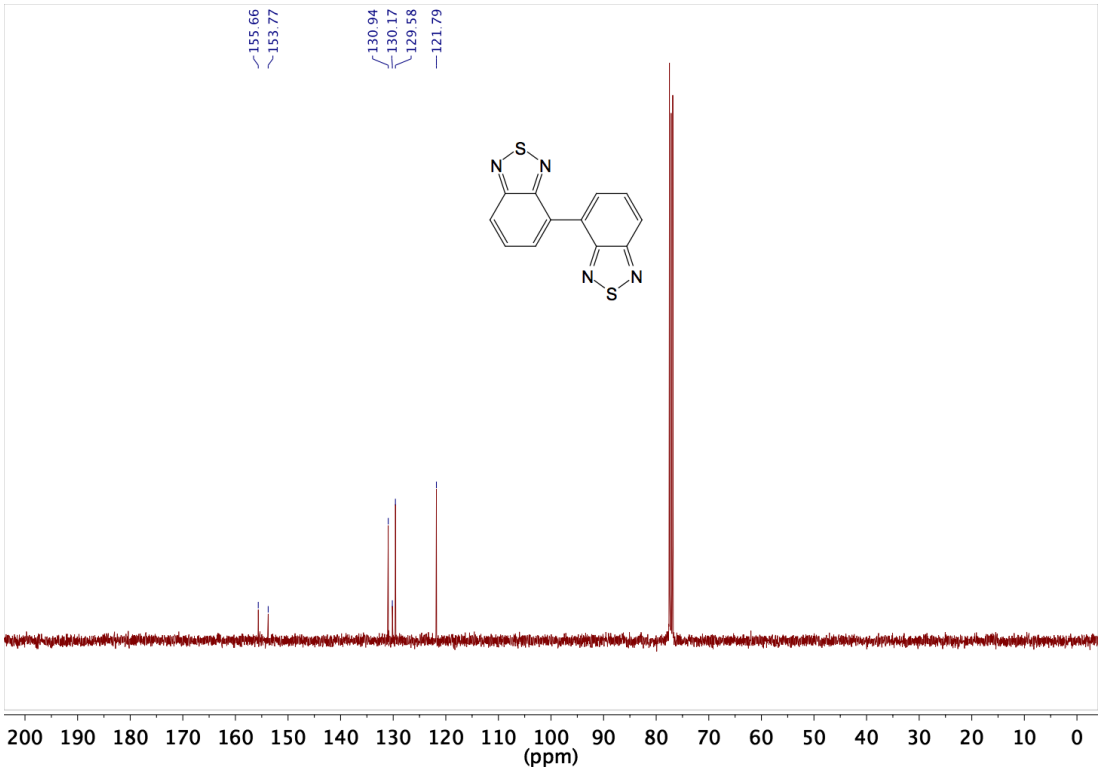
155.66
153.77
130.94
130.17
129.58
121.79
(ppm)

2.8

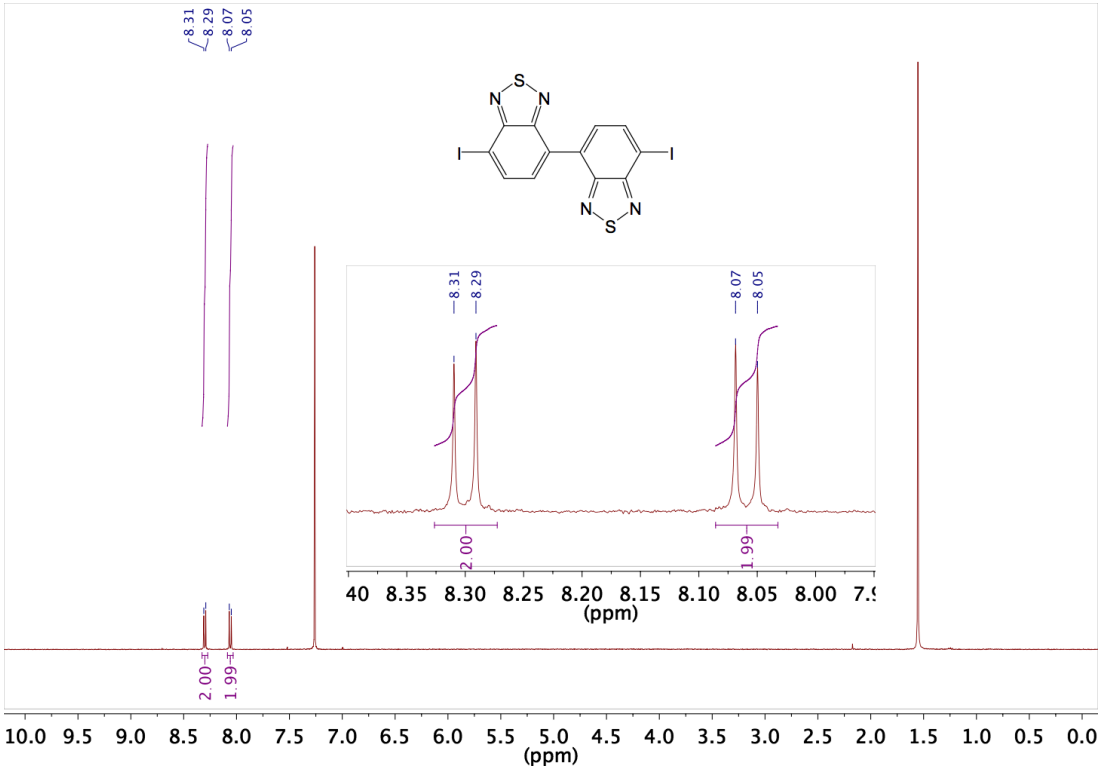
8.31
8.29
8.07
8.05
S
N
N
I
I
N
S
N
2.00
1.99
40 8.35 8.30 8.25 8.20 8.15 8.10 8.05 8.00 7.9
(ppm)
10.0 9.5 9.0 8.5 8.0 7.5 7.0 6.5 6.0 5.5 5.0 4.5 4.0 3.5 3.0 2.5 2.0 1.5 1.0 0.5 0.0
(ppm)

2.10

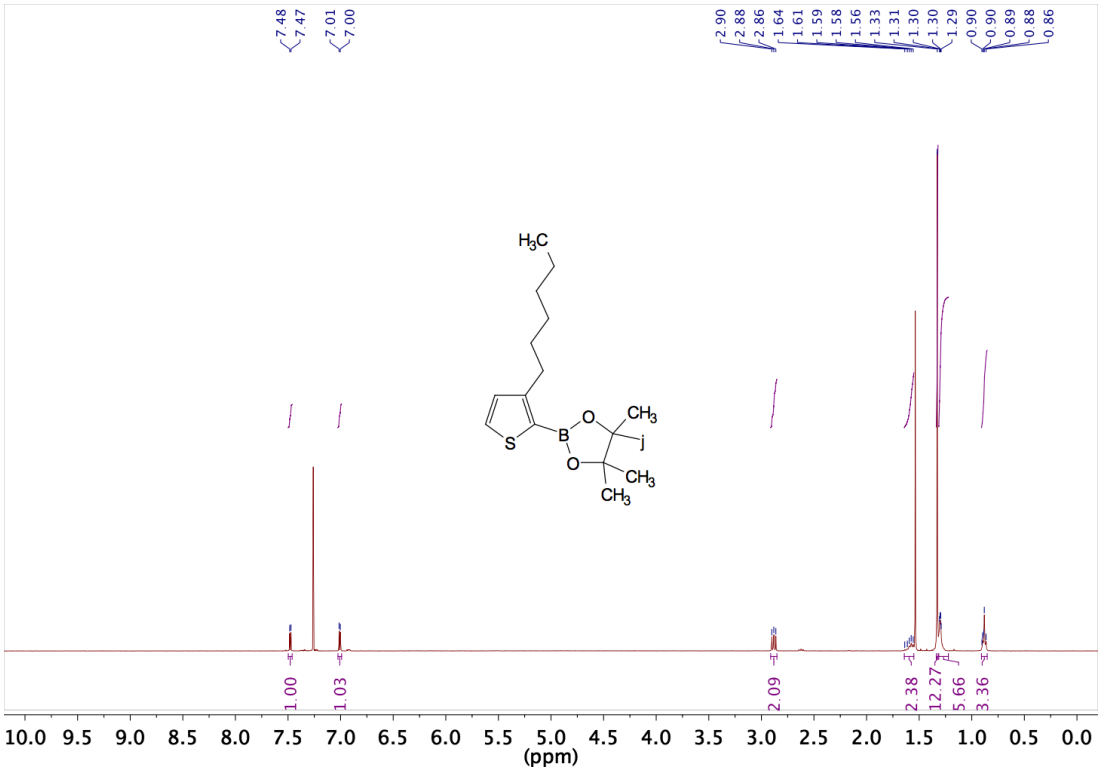
7.48
7.47
7.01
7.00
2.90
2.88
2.86
1.64
1.61
1.59
1.58
1.56
1.33
1.31
1.30
1.30
1.29
0.90
0.90
0.89
0.88
0.86
H3C
S
B
O
O
CH3
CH3
CH3
1.00
1.03
2.09
2.38
12.27
5.66
3.36
10.0 9.5 9.0 8.5 8.0 7.5 7.0 6.5 6.0 5.5 5.0 4.5 4.0 3.5 3.0 2.5 2.0 1.5 1.0 0.5 0.0
(ppm)

2.11

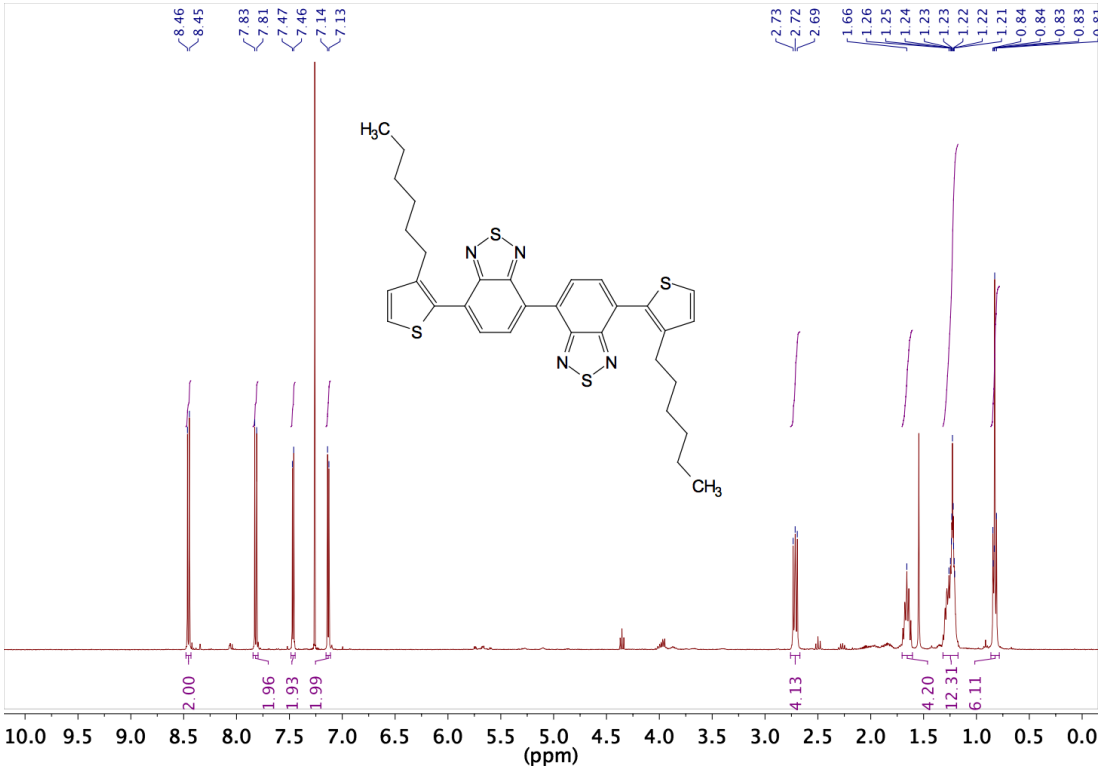
8.46
8.45
7.83
7.81
7.47
7.46
7.14
7.13
2.73
2.72
2.69
1.66
1.26
1.25
1.24
1.23
1.23
1.22
1.22
1.21
0.84
0.84
0.83
0.83
2.00
1.96
1.93
1.99
4.13
4.20
12.31
6.11
10.0 9.5 9.0 8.5 8.0 7.5 7.0 6.5 6.0 5.5 5.0 4.5 4.0 3.5 3.0 2.5 2.0 1.5 1.0 0.5 0.0
(ppm)

2.12

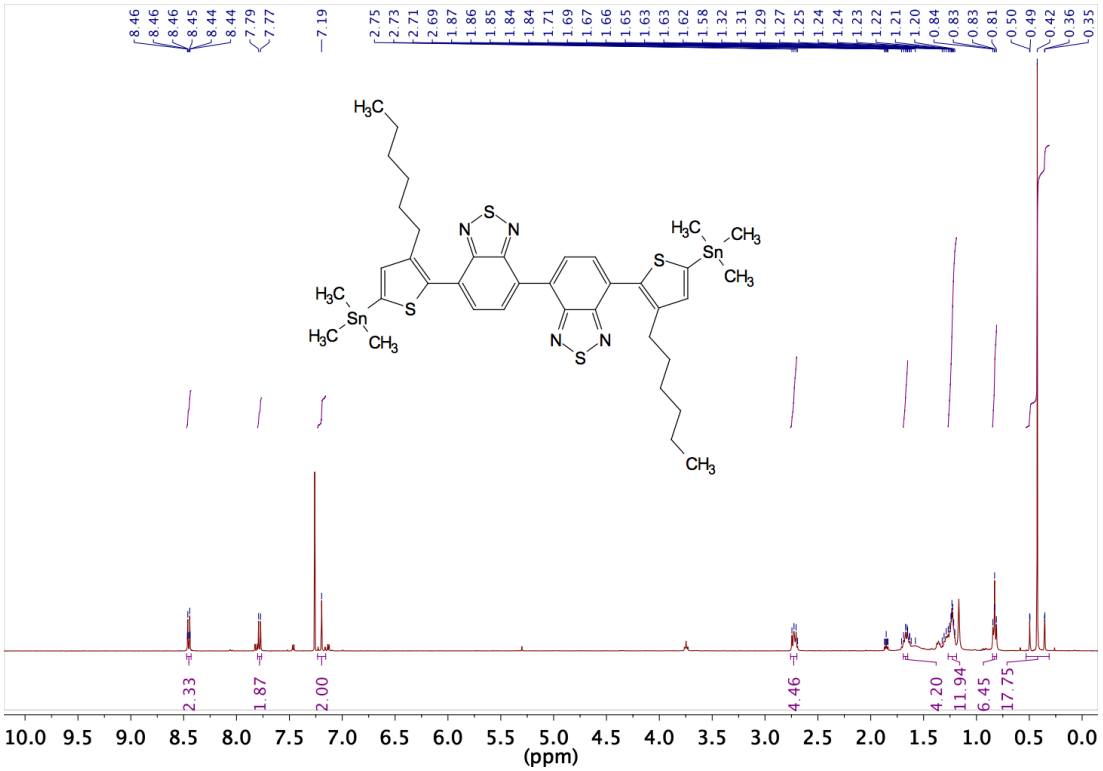
8.46
8.46
8.46
8.45
8.44
8.44
7.79
7.77
7.19
2.75
2.73
2.71
2.69
1.87
1.86
1.85
1.84
1.84
1.71
1.69
1.67
1.66
1.65
1.63
1.63
1.62
1.58
1.32
1.31
1.29
1.27
1.25
1.24
1.24
1.23
1.22
1.21
1.20
0.84
0.83
0.83
0.81
0.50
0.49
0.42
0.36
0.35
2.33
1.87
2.00
4.46
4.20
11.94
6.45
17.75
10.0 9.5 9.0 8.5 8.0 7.5 7.0 6.5 6.0 5.5 5.0 4.5 4.0 3.5 3.0 2.5 2.0 1.5 1.0 0.5 0.0
(ppm)

2.14

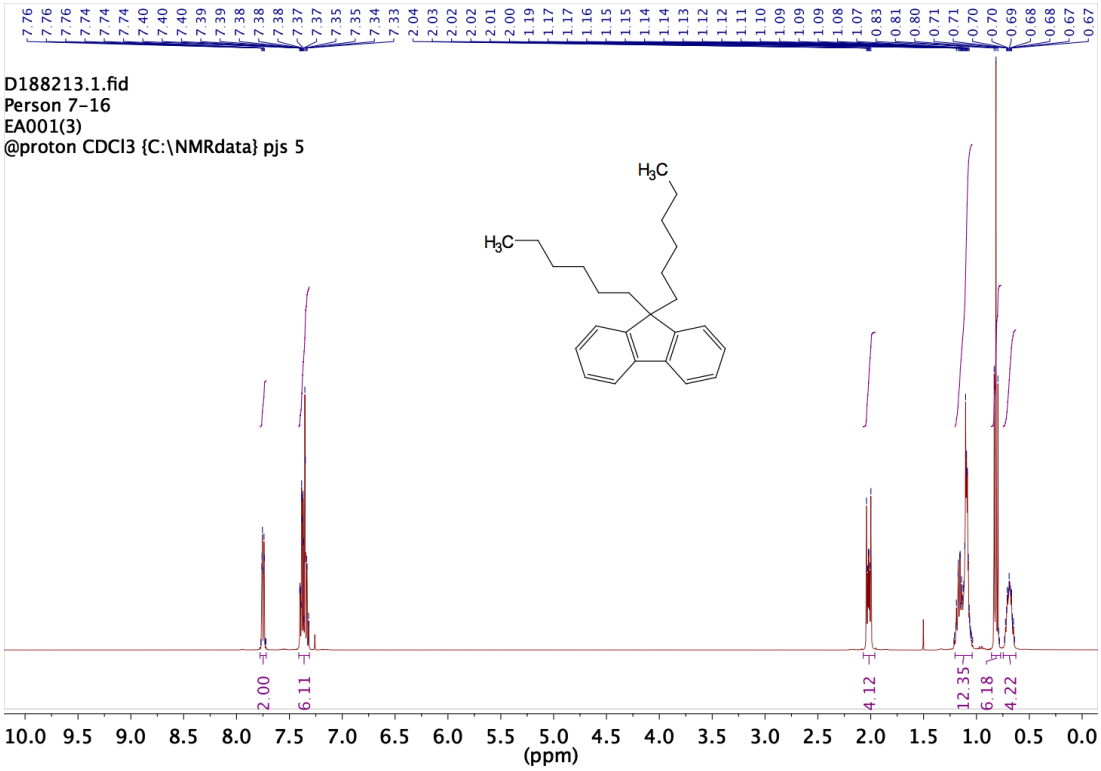
D188213.1.fid
Person 7-16
EA001(3)
@proton CDCl3 {C:\NMRdata} pjs 5
H3C
H3C
2.00
6.11
4.12
12.35
6.18
4.22
10.0 9.5 9.0 8.5 8.0 7.5 7.0 6.5 6.0 5.5 5.0 4.5 4.0 3.5 3.0 2.5 2.0 1.5 1.0 0.5 0.0
(ppm)

2.15

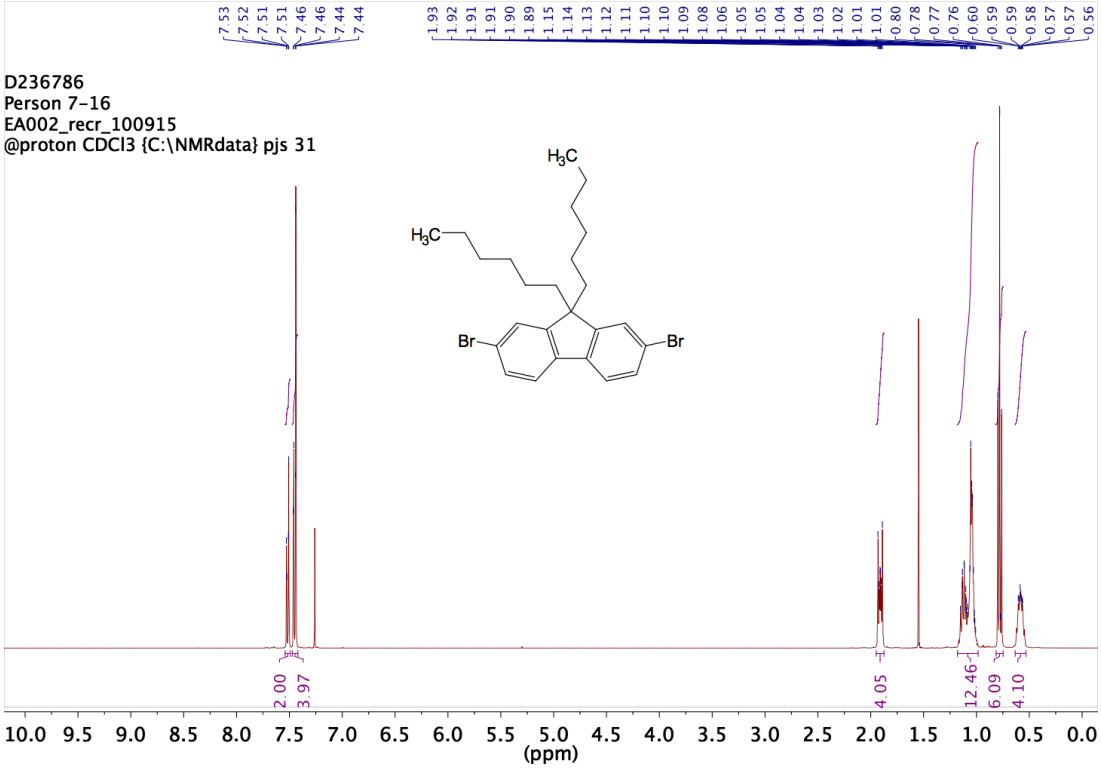
D236786
Person 7-16
EA002_recr_100915
@proton CDCl3 {C:\NMRdata} pjs 31
H3C
H3C
Br
Br
2.00
3.97
4.05
12.46
6.09
4.10
10.0 9.5 9.0 8.5 8.0 7.5 7.0 6.5 6.0 5.5 5.0 4.5 4.0 3.5 3.0 2.5 2.0 1.5 1.0 0.5 0.0
(ppm)

2.16

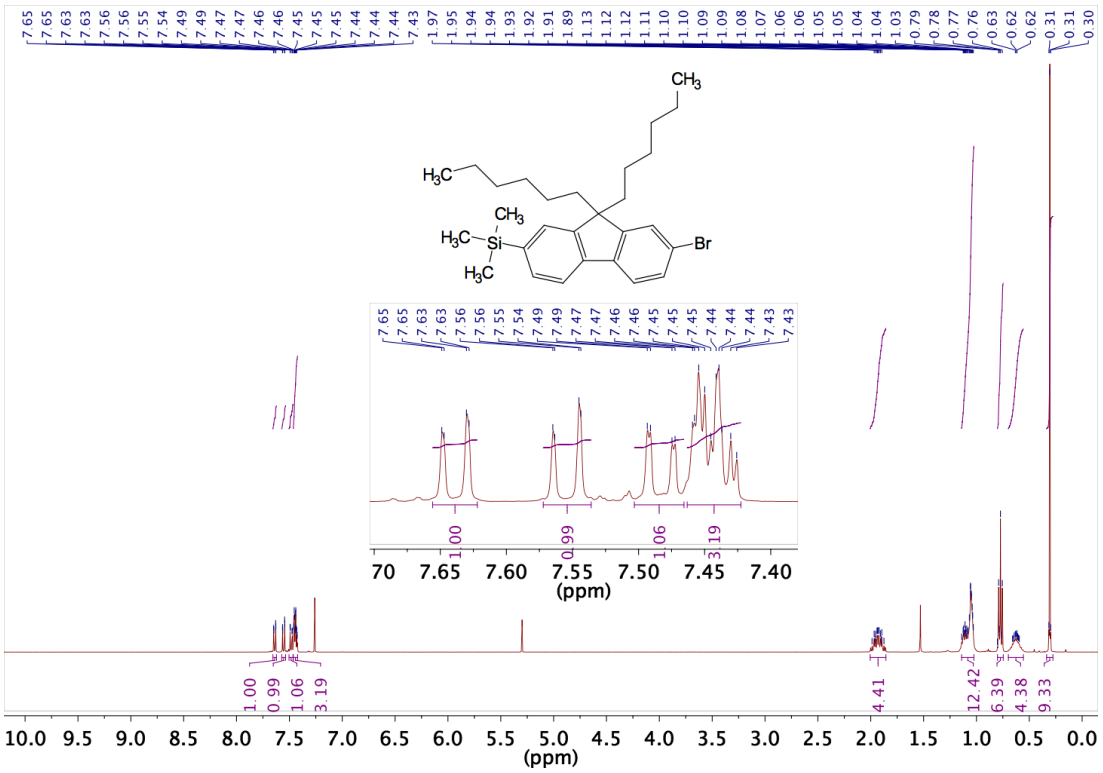

2.17

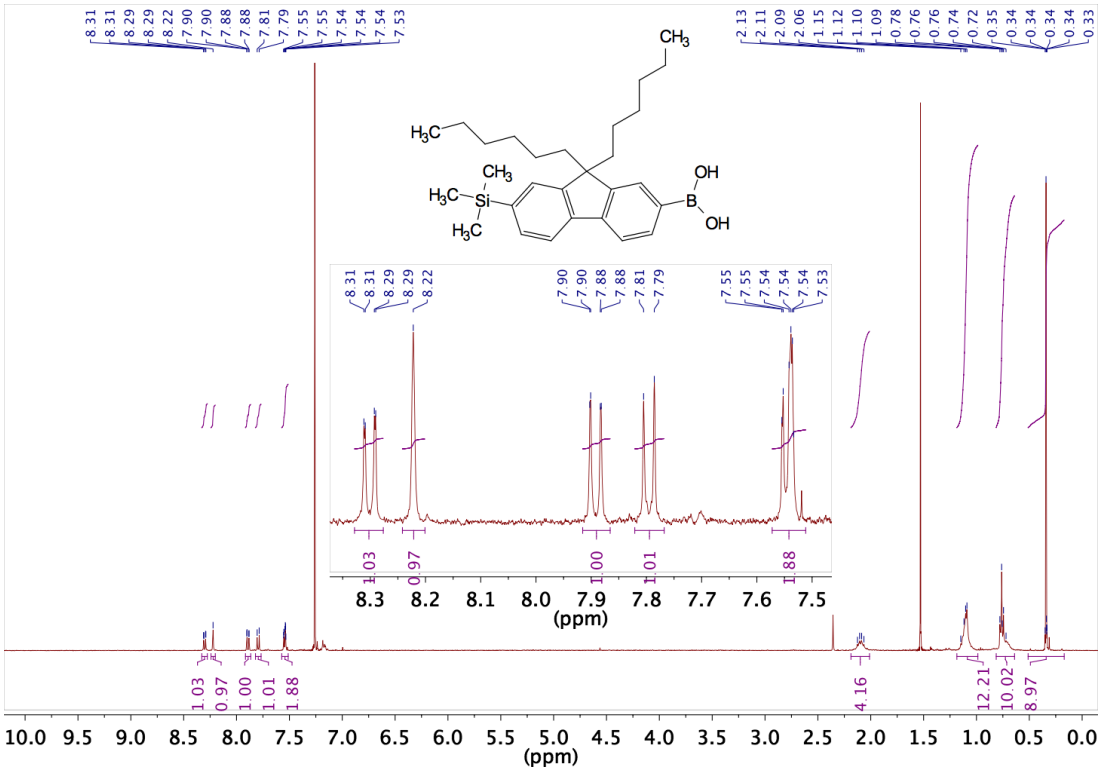

3.1

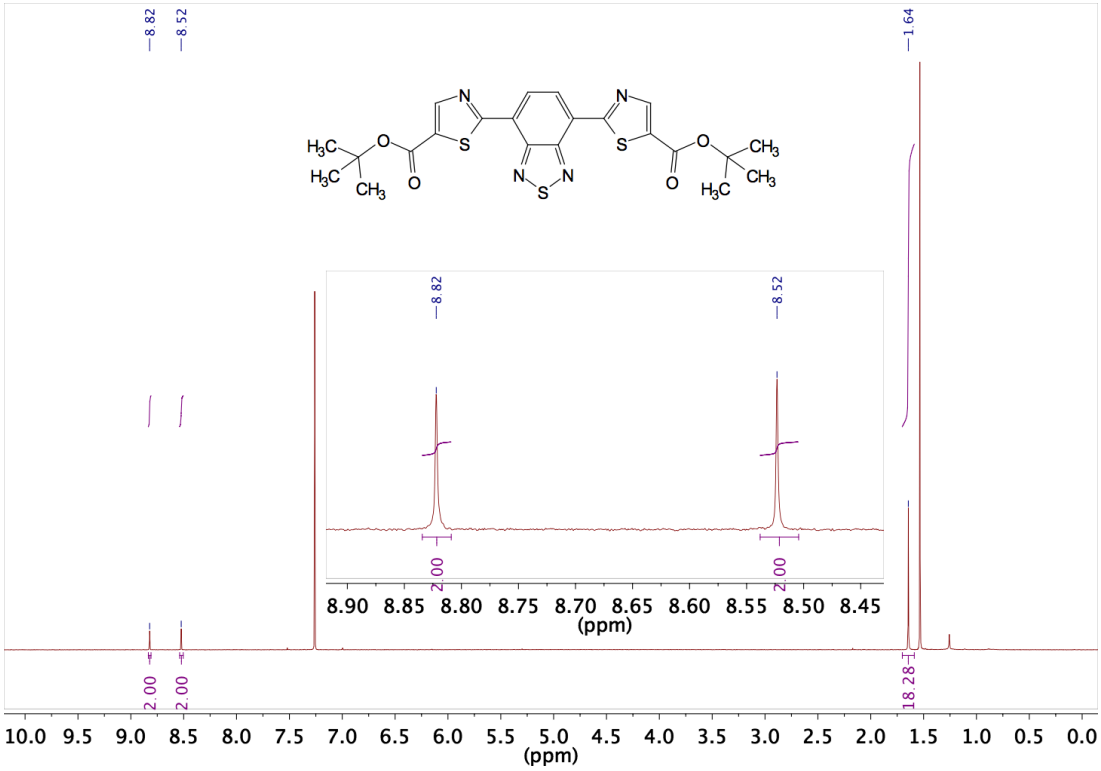
8.82
8.52
1.64
2.00
2.00
18.28
10.0 9.5 9.0 8.5 8.0 7.5 7.0 6.5 6.0 5.5 5.0 4.5 4.0 3.5 3.0 2.5 2.0 1.5 1.0 0.5 0.0
(ppm)
8.90 8.85 8.80 8.75 8.70 8.65 8.60 8.55 8.50 8.45
(ppm)

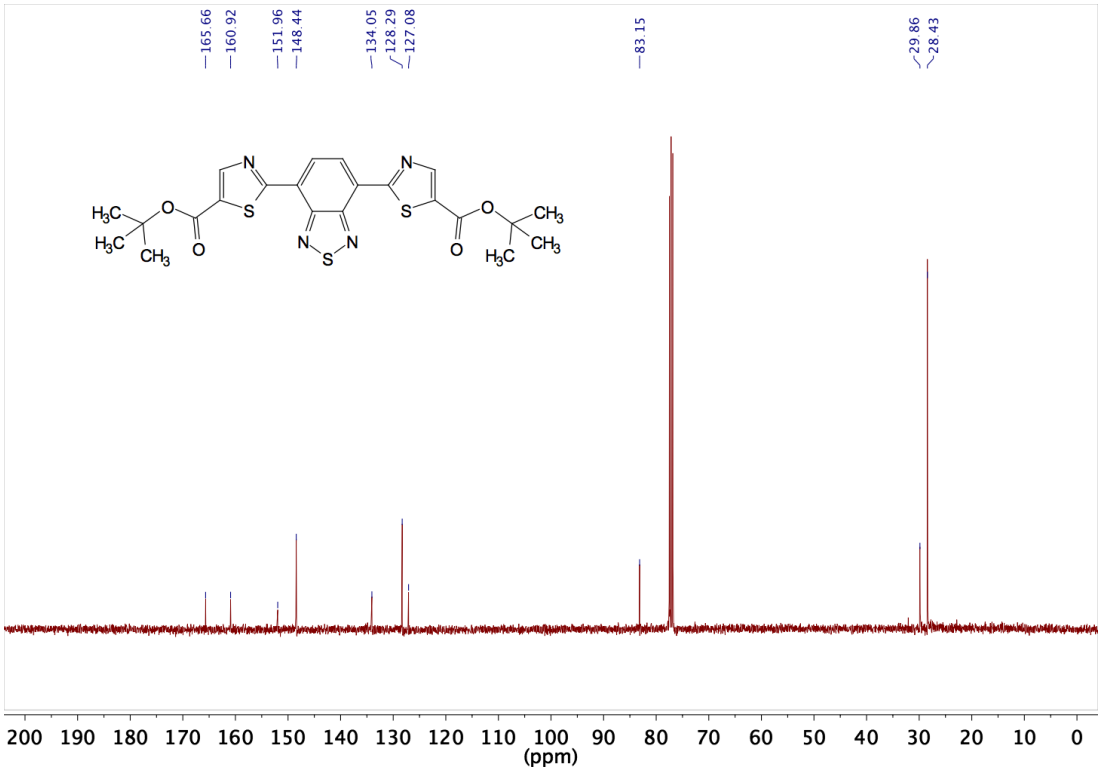
165.66
160.92
151.96
148.44
134.05
128.29
127.08
83.15
29.86
28.43
200 190 180 170 160 150 140 130 120 110 100 90 80 70 60 50 40 30 20 10 0
(ppm)

3.2

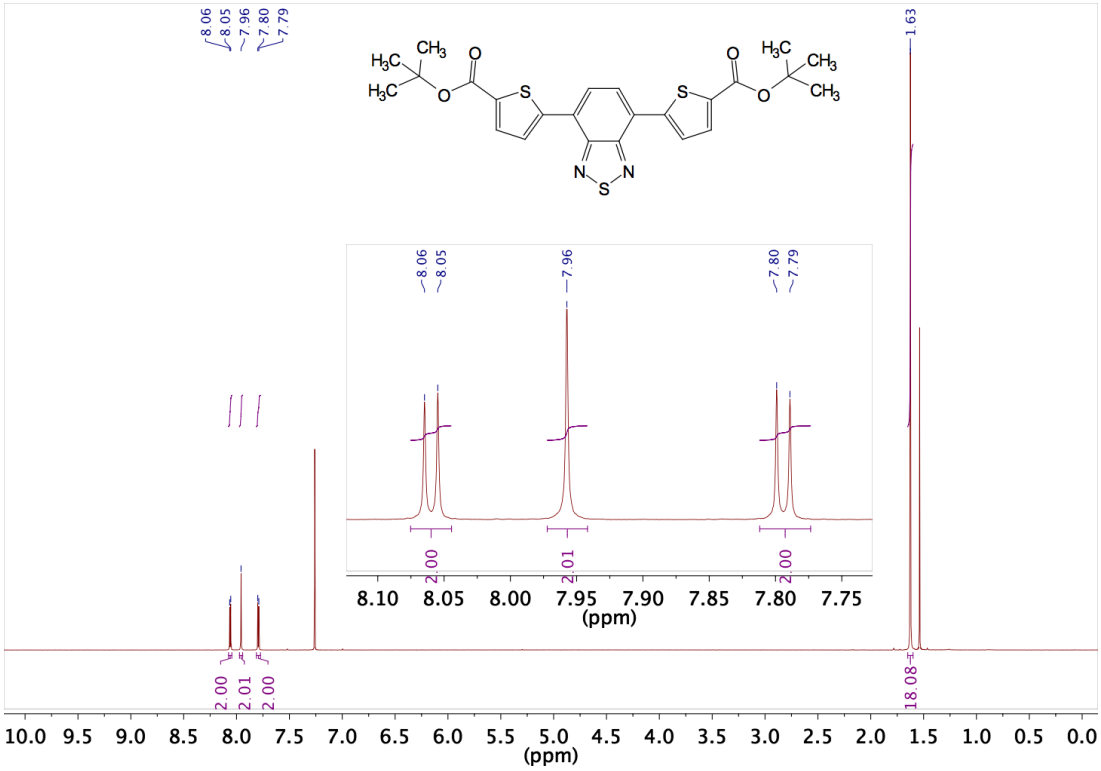
8.06
8.05
7.96
7.80
7.79
1.63
2.00
2.01
2.00
18.08
10.0 9.5 9.0 8.5 8.0 7.5 7.0 6.5 6.0 5.5 5.0 4.5 4.0 3.5 3.0 2.5 2.0 1.5 1.0 0.5 0.0
(ppm)
8.10 8.05 8.00 7.95 7.90 7.85 7.80 7.75
(ppm)

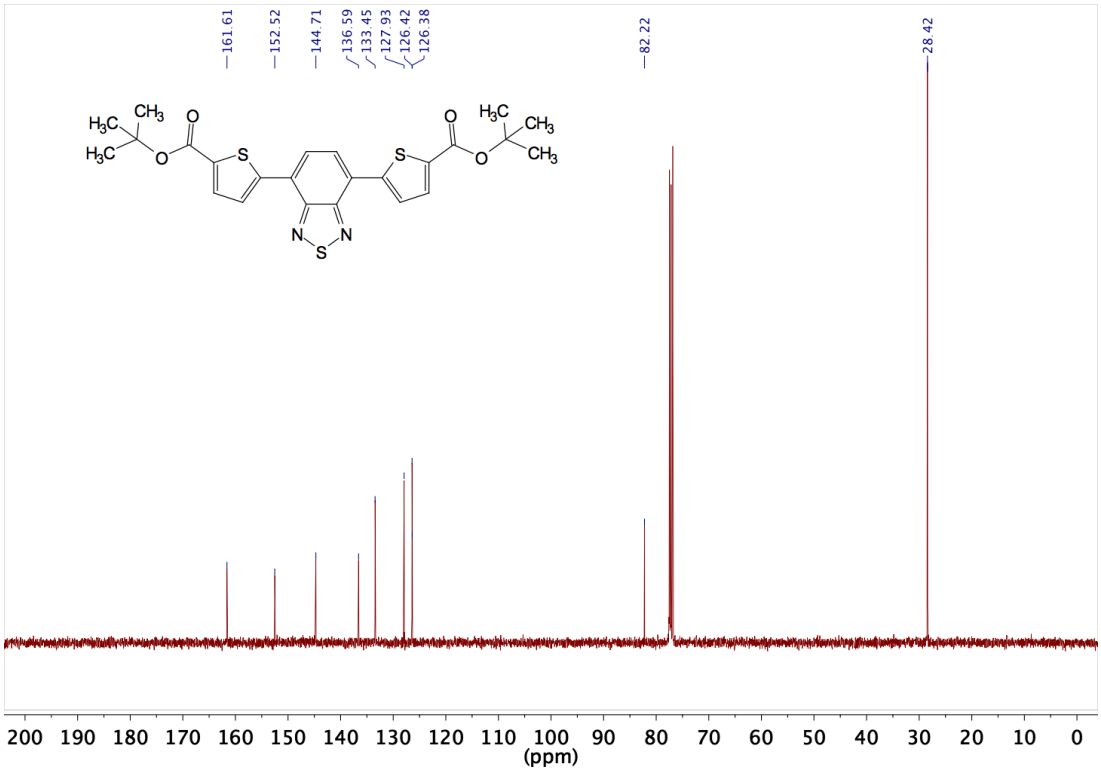
161.61
152.52
144.71
136.59
133.45
127.93
126.42
126.38
82.22
28.42
200 190 180 170 160 150 140 130 120 110 100 90 80 70 60 50 40 30 20 10 0
(ppm)

3.3

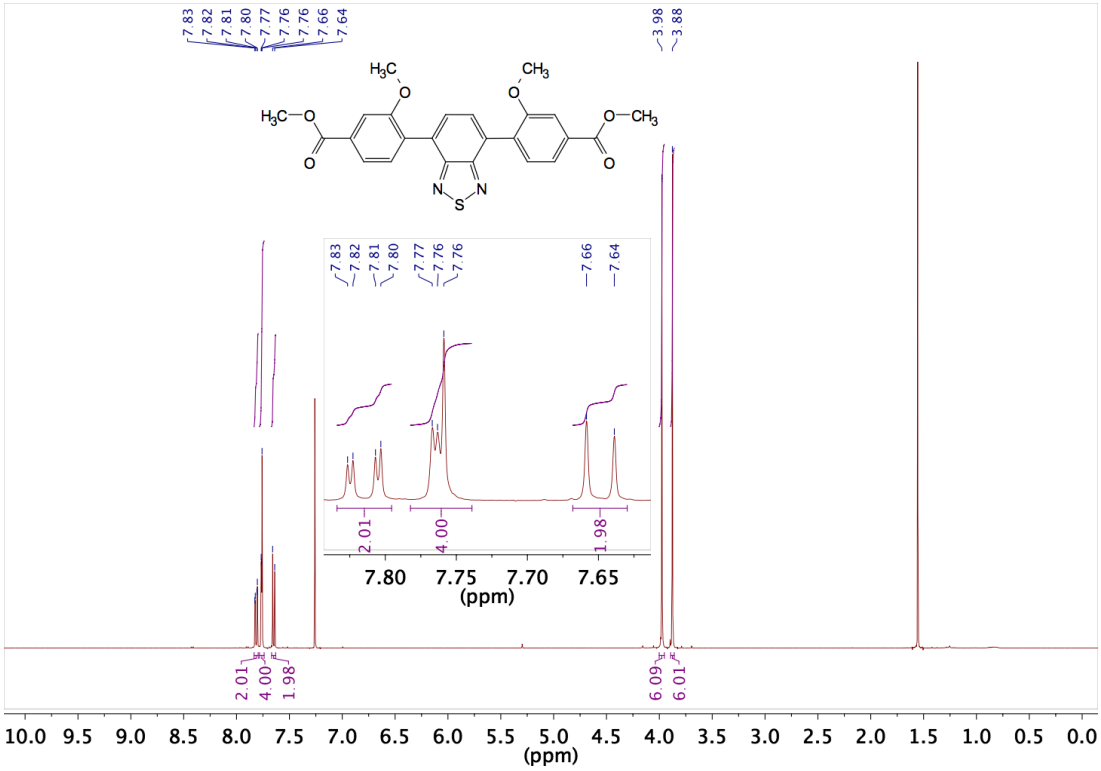
7.83
7.82
7.81
7.80
7.77
7.76
7.76
7.66
7.64
3.98
3.88
H3C
O
CH3
H3C—O
O—CH3
O
O
N
S
N
2.01
4.00
1.98
6.09
6.01
7.80
7.75
7.70
7.65
(ppm)
10.0 9.5 9.0 8.5 8.0 7.5 7.0 6.5 6.0 5.5 5.0 4.5 4.0 3.5 3.0 2.5 2.0 1.5 1.0 0.5 0.0
(ppm)

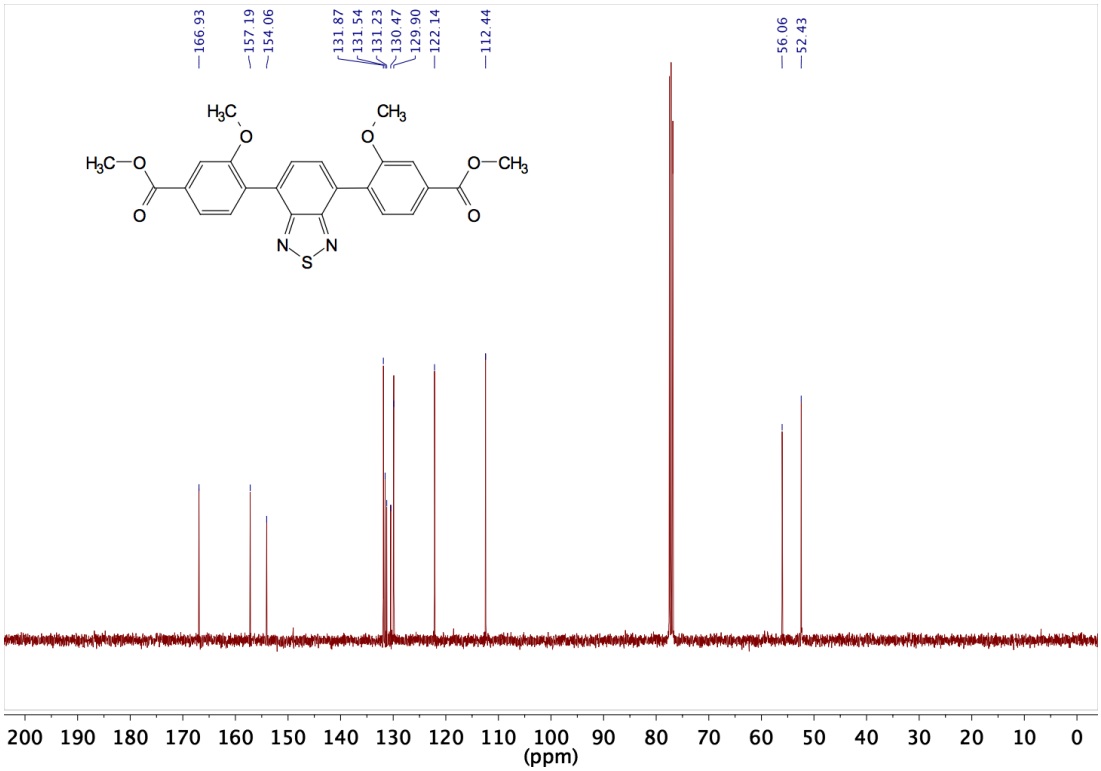
166.93
157.19
154.06
131.87
131.54
131.23
130.47
129.90
122.14
112.44
56.06
52.43
H3C
O
CH3
H3C—O
O—CH3
O
O
N
S
N
200 190 180 170 160 150 140 130 120 110 100 90 80 70 60 50 40 30 20 10 0
(ppm)

3.4

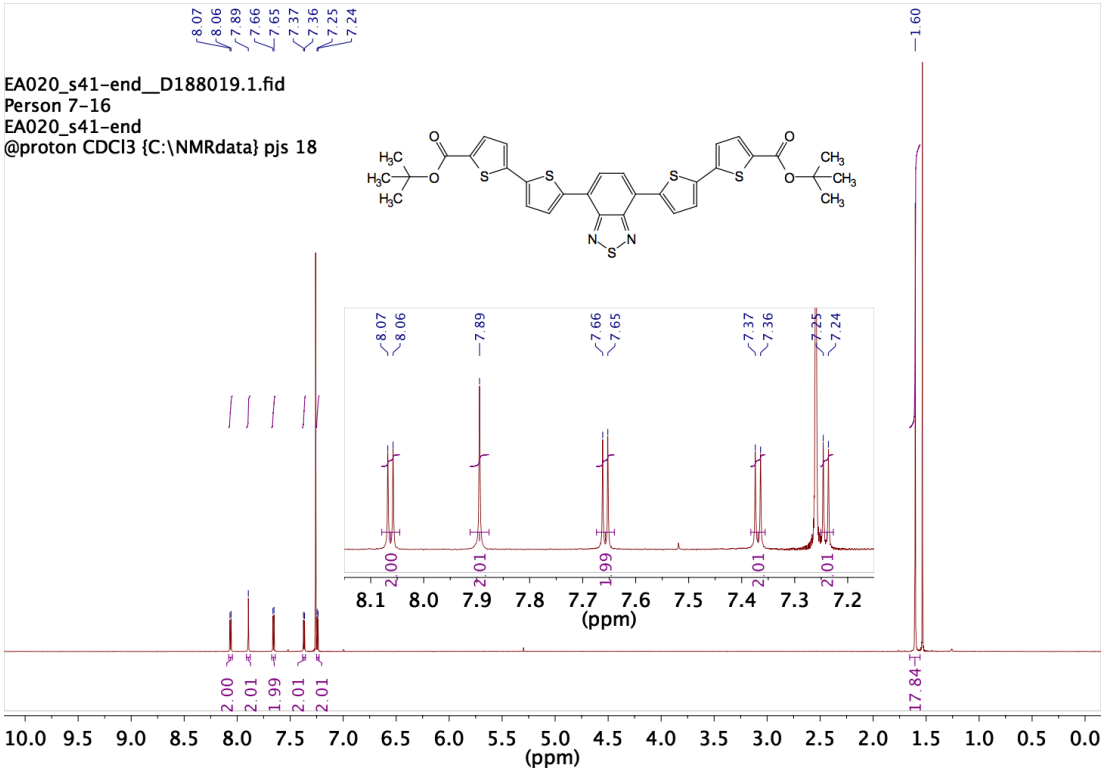
8.07
8.06
7.89
7.66
7.65
7.37
7.36
7.25
7.24
1.60
EA020_s41-end__D188019.1.fid
Person 7-16
EA020_s41-end
@proton CDCl3 {C:\NMRdata} pjs 18
2.00
2.01
1.99
2.01
2.01
17.84
(ppm)

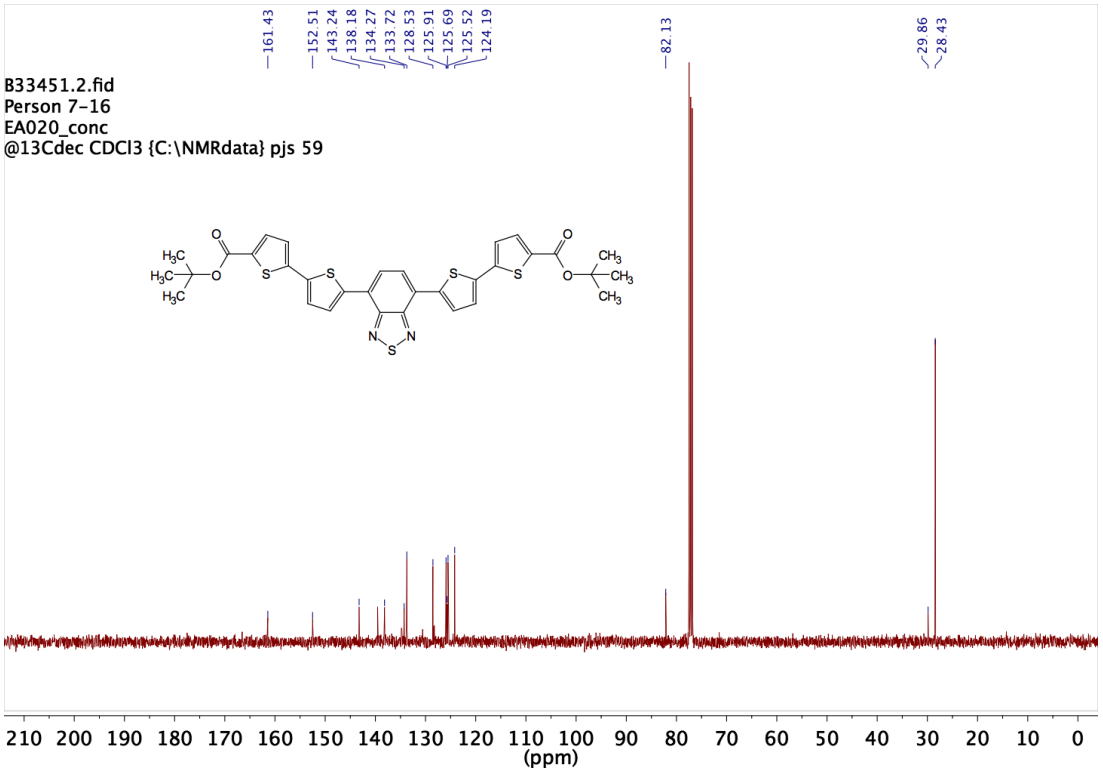
161.43
152.51
143.24
138.18
134.27
133.72
128.53
125.91
125.69
125.52
124.19
82.13
29.86
28.43
B33451.2.fid
Person 7-16
EA020_conc
@13Cdec CDCl3 {C:\NMRdata} pjs 59
(ppm)

3.5

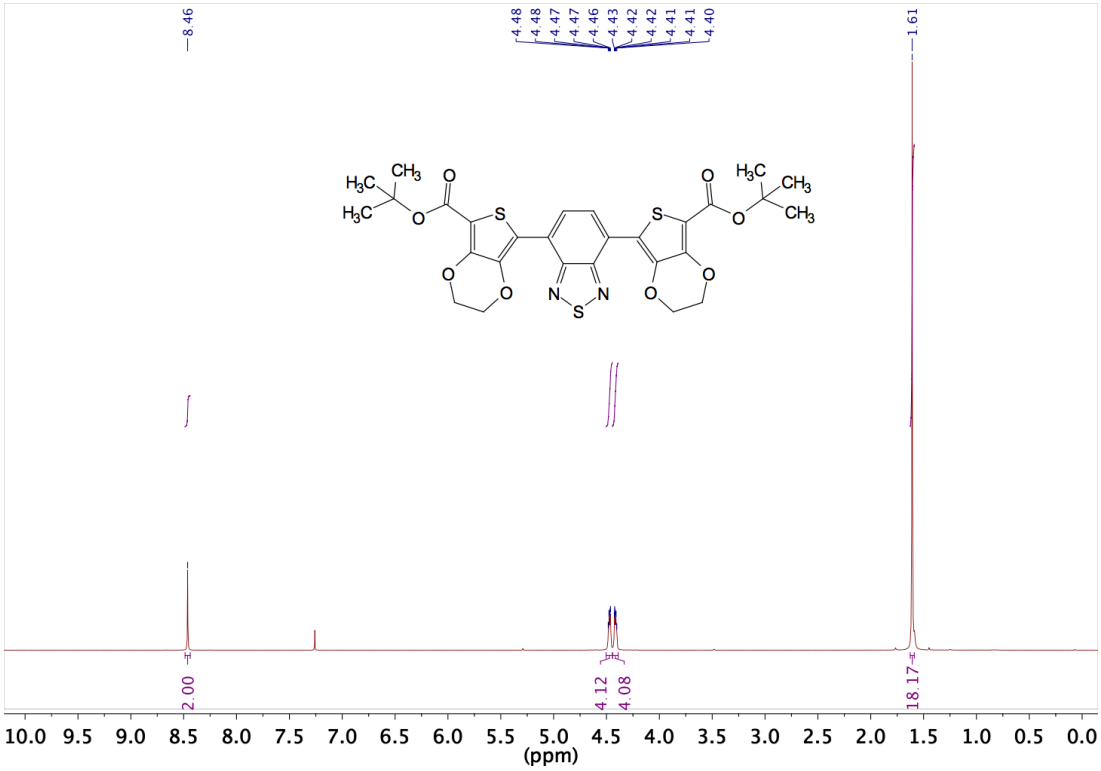
8.46
4.48
4.48
4.47
4.47
4.46
4.43
4.42
4.42
4.41
4.41
4.40
1.61
2.00
4.12
4.08
18.17
10.0 9.5 9.0 8.5 8.0 7.5 7.0 6.5 6.0 5.5 5.0 4.5 4.0 3.5 3.0 2.5 2.0 1.5 1.0 0.5 0.0
(ppm)

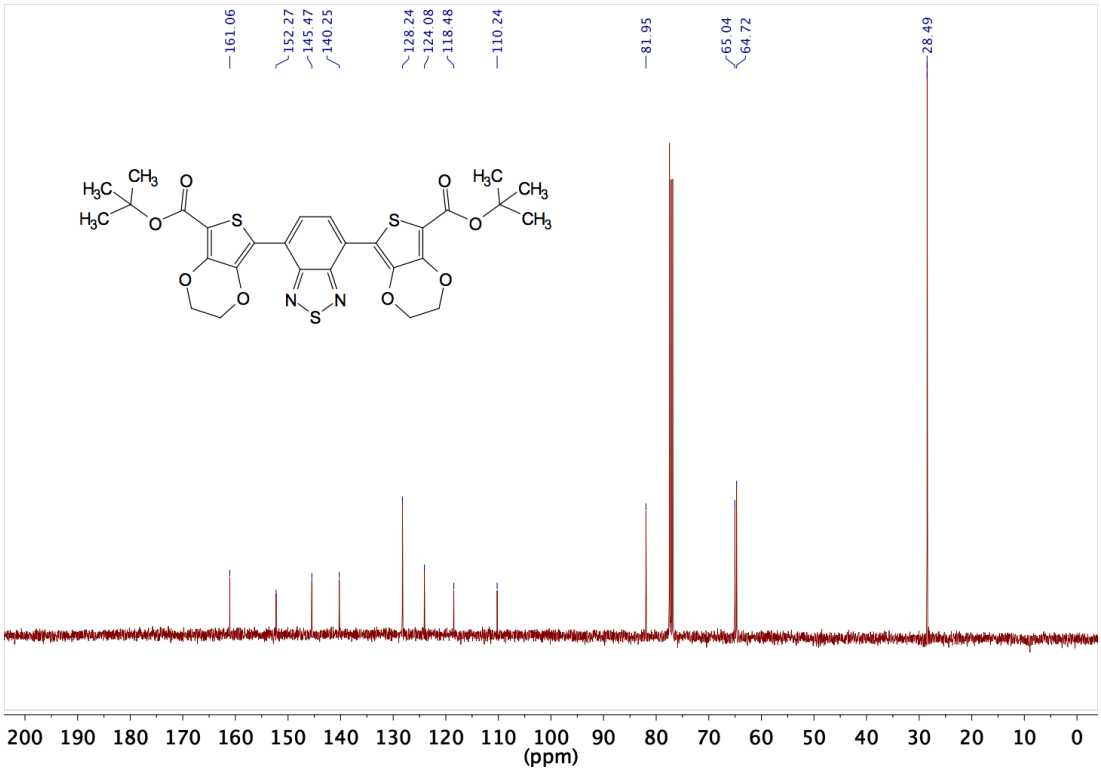
161.06
152.27
145.47
140.25
128.24
124.08
118.48
110.24
81.95
65.04
64.72
28.49
200 190 180 170 160 150 140 130 120 110 100 90 80 70 60 50 40 30 20 10 0
(ppm)

3.7

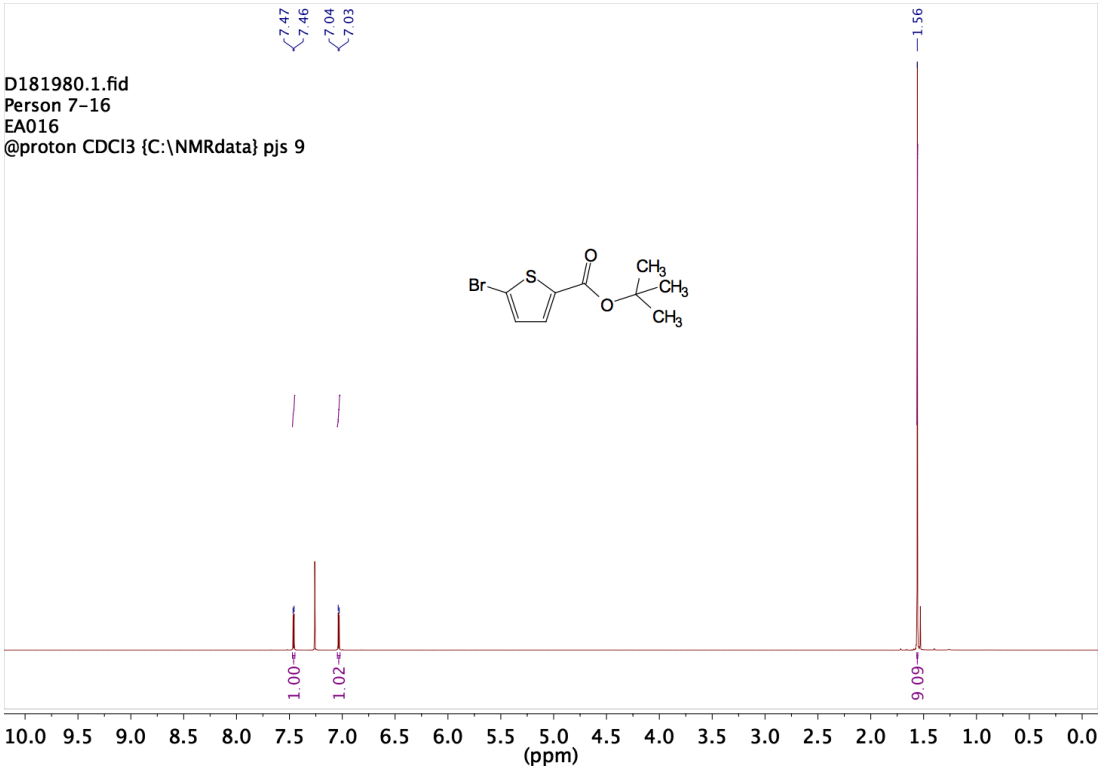
7.47
7.46
7.04
7.03
1.56
D181980.1.fid
Person 7-16
EA016
@proton CDCl3 {C:\NMRdata} pjs 9
Br
S
O
O
CH3
CH3
CH3
1.00
1.02
9.09
10.0 9.5 9.0 8.5 8.0 7.5 7.0 6.5 6.0 5.5 5.0 4.5 4.0 3.5 3.0 2.5 2.0 1.5 1.0 0.5 0.0
(ppm)

3.9

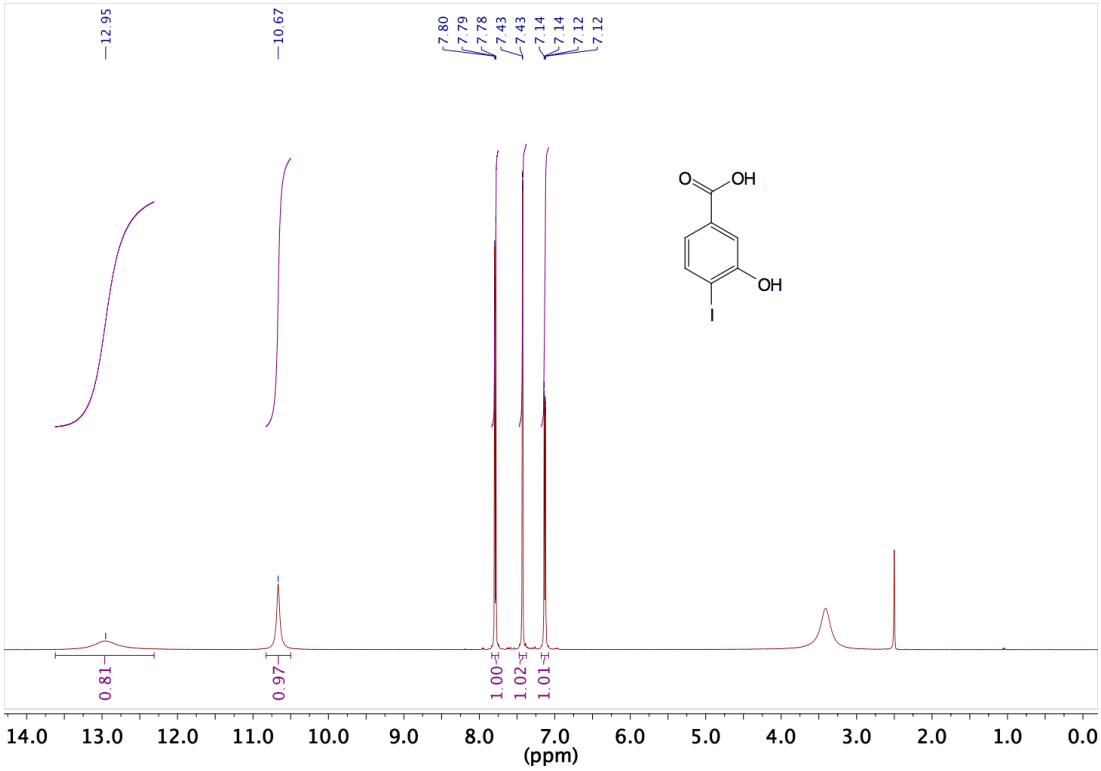
12.95
10.67
7.80
7.79
7.78
7.43
7.14
7.14
7.12
7.12
O
OH
OH
I
0.81
0.97
1.00
1.02
1.01
14.0 13.0 12.0 11.0 10.0 9.0 8.0 7.0 6.0 5.0 4.0 3.0 2.0 1.0 0.0
(ppm)

3.9

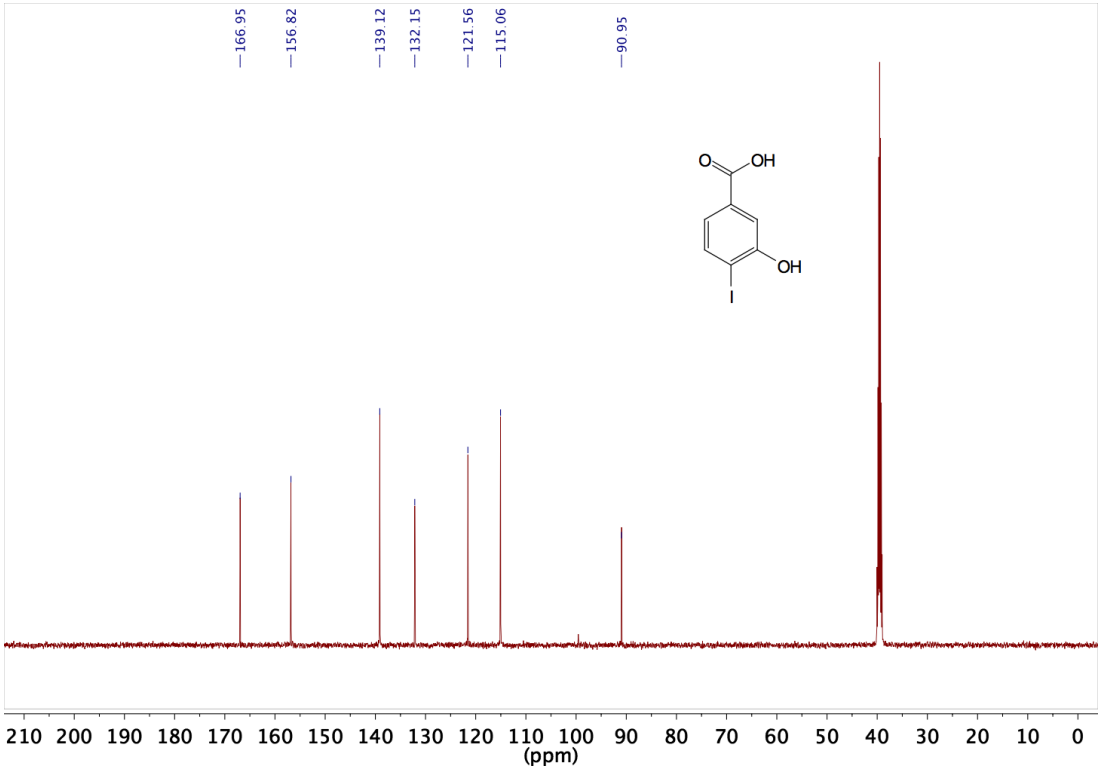
166.95
156.82
139.12
132.15
121.56
115.06
90.95
O
OH
OH
I
210 200 190 180 170 160 150 140 130 120 110 100 90 80 70 60 50 40 30 20 10 0
(ppm)

3.10

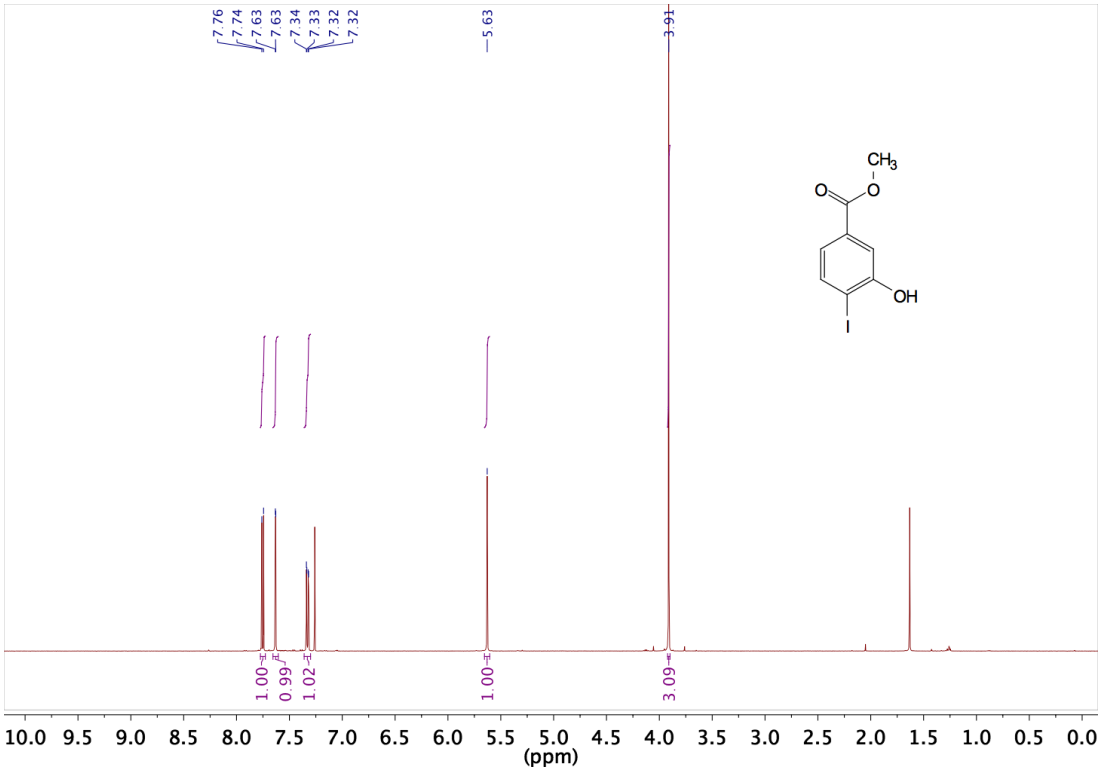
7.76
7.74
7.63
7.63
7.34
7.33
7.32
7.32
5.63
3.91
CH3
O
O
OH
I
1.00
0.99
1.02
1.00
3.09
10.0 9.5 9.0 8.5 8.0 7.5 7.0 6.5 6.0 5.5 5.0 4.5 4.0 3.5 3.0 2.5 2.0 1.5 1.0 0.5 0.0
(ppm)

3.11

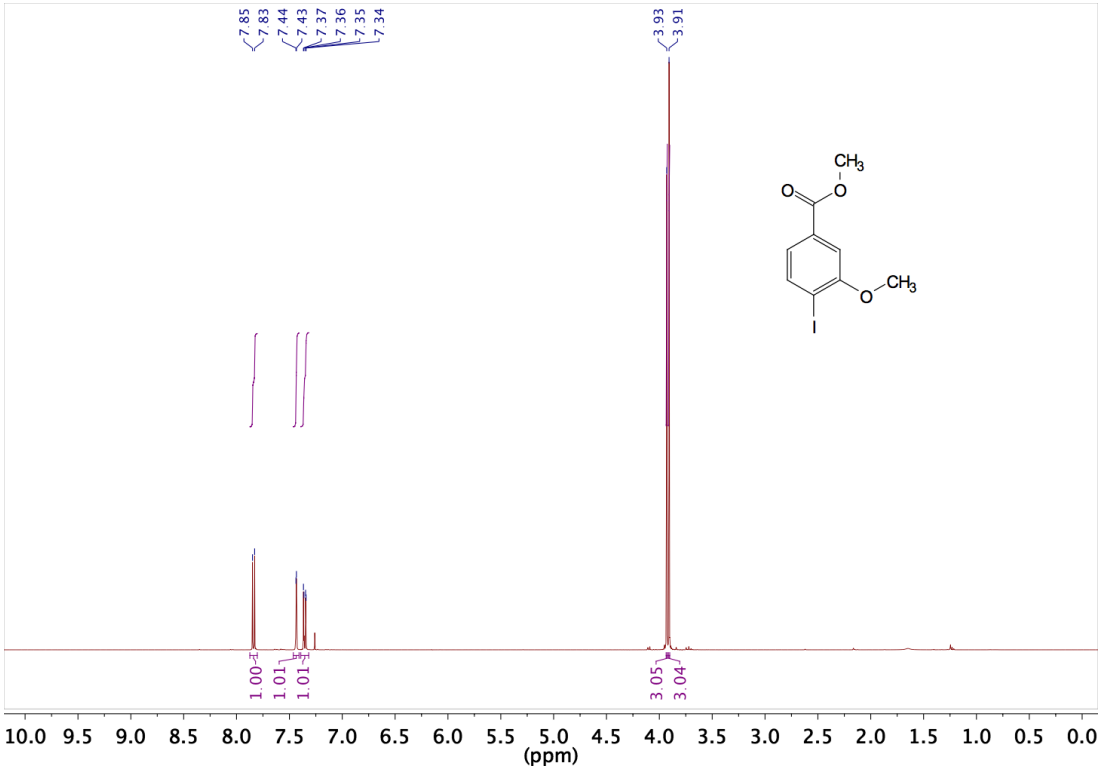
7.85
7.83
7.44
7.43
7.37
7.36
7.35
7.34
3.93
3.91
1.00
1.01
1.01
3.05
3.04
10.0 9.5 9.0 8.5 8.0 7.5 7.0 6.5 6.0 5.5 5.0 4.5 4.0 3.5 3.0 2.5 2.0 1.5 1.0 0.5 0.0
(ppm)

3.13

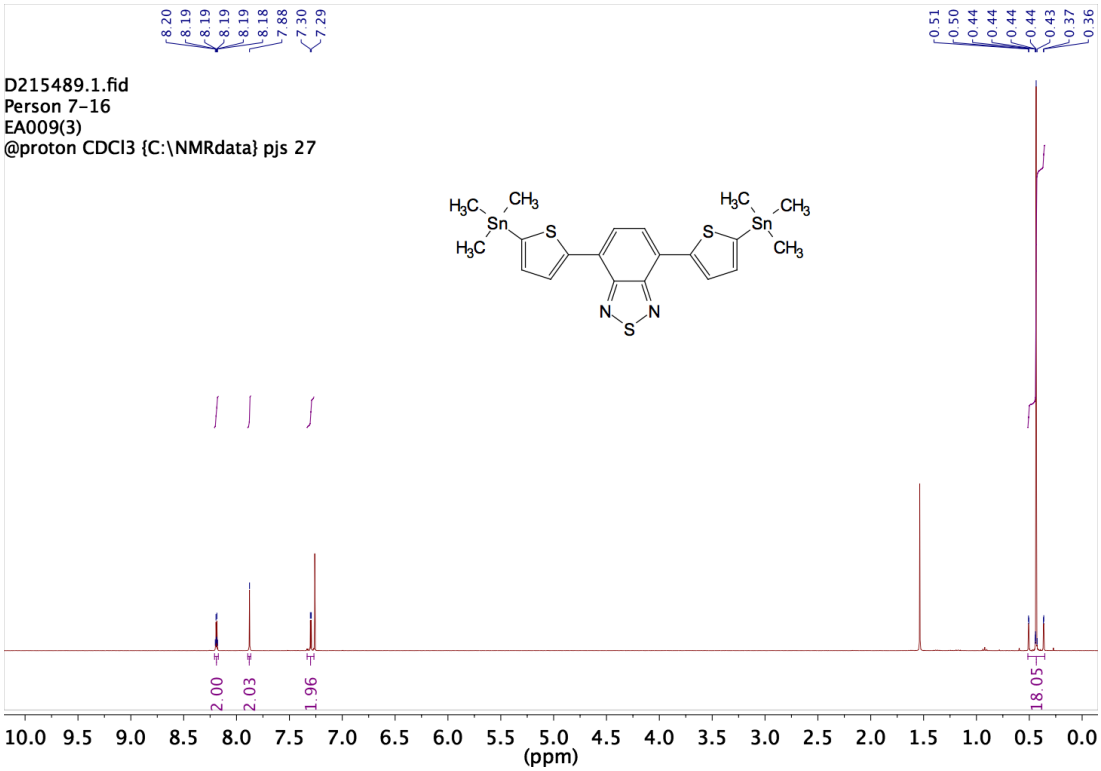
8.20
8.19
8.19
8.19
8.19
8.18
7.88
7.30
7.29
0.51
0.50
0.44
0.44
0.44
0.44
0.43
0.37
0.36
D215489.1.fid
Person 7-16
EA009(3)
@proton CDCl3 {C:\NMRdata} pjs 27
2.00
2.03
1.96
18.05
10.0 9.5 9.0 8.5 8.0 7.5 7.0 6.5 6.0 5.5 5.0 4.5 4.0 3.5 3.0 2.5 2.0 1.5 1.0 0.5 0.0
(ppm)

3.15

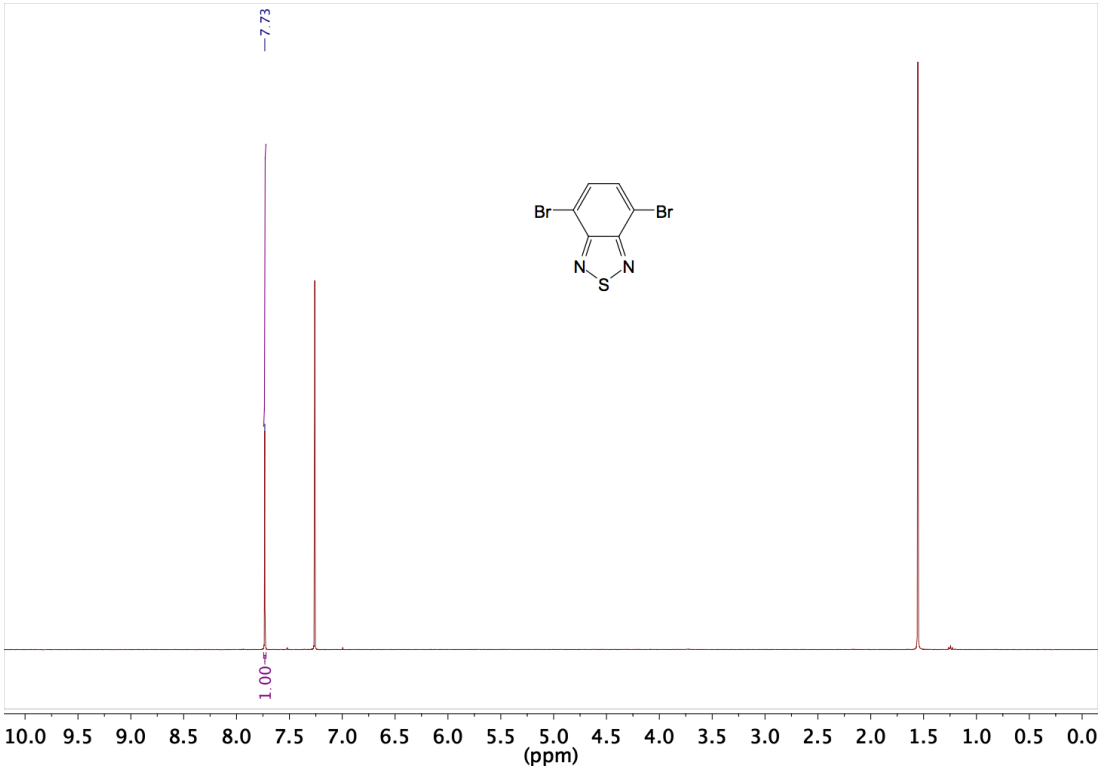
7.73
Br
Br
N
S
N
1.00
10.0 9.5 9.0 8.5 8.0 7.5 7.0 6.5 6.0 5.5 5.0 4.5 4.0 3.5 3.0 2.5 2.0 1.5 1.0 0.5 0.0
(ppm)

3.16

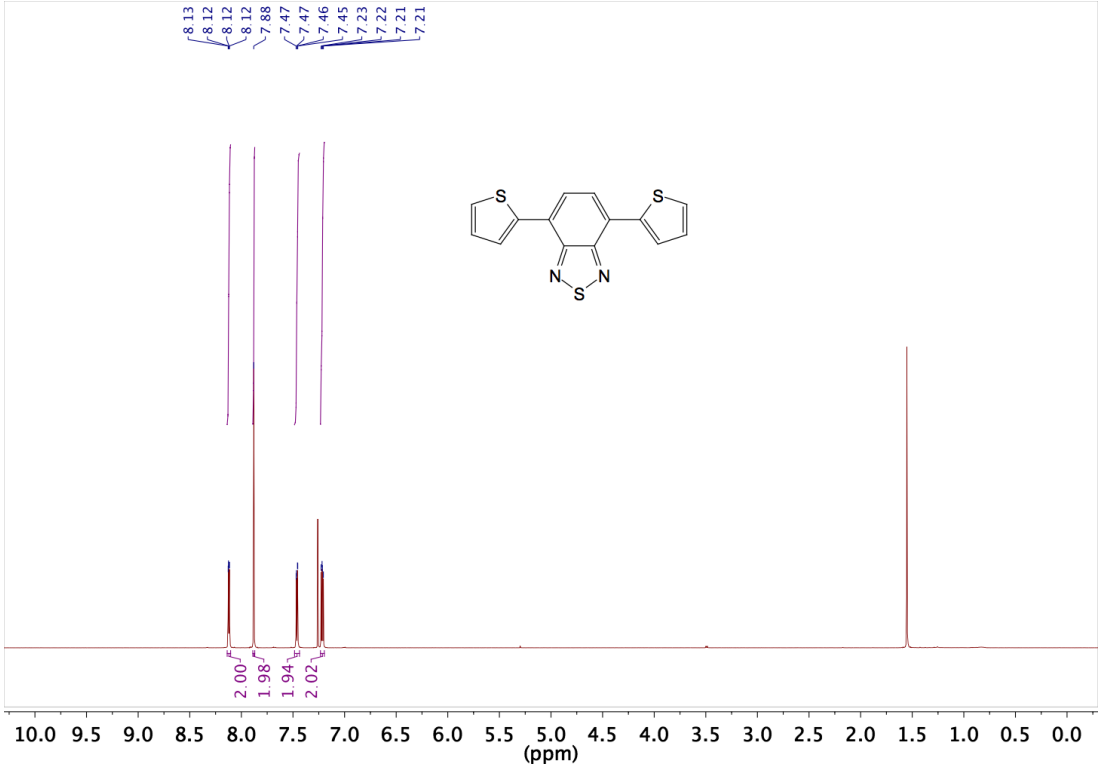
8.13
8.12
8.12
8.12
7.88
7.47
7.47
7.46
7.45
7.23
7.22
7.21
7.21
S
S
N
S
N
2.00
1.98
1.94
2.02
10.0 9.5 9.0 8.5 8.0 7.5 7.0 6.5 6.0 5.5 5.0 4.5 4.0 3.5 3.0 2.5 2.0 1.5 1.0 0.5 0.0
(ppm)

3.16

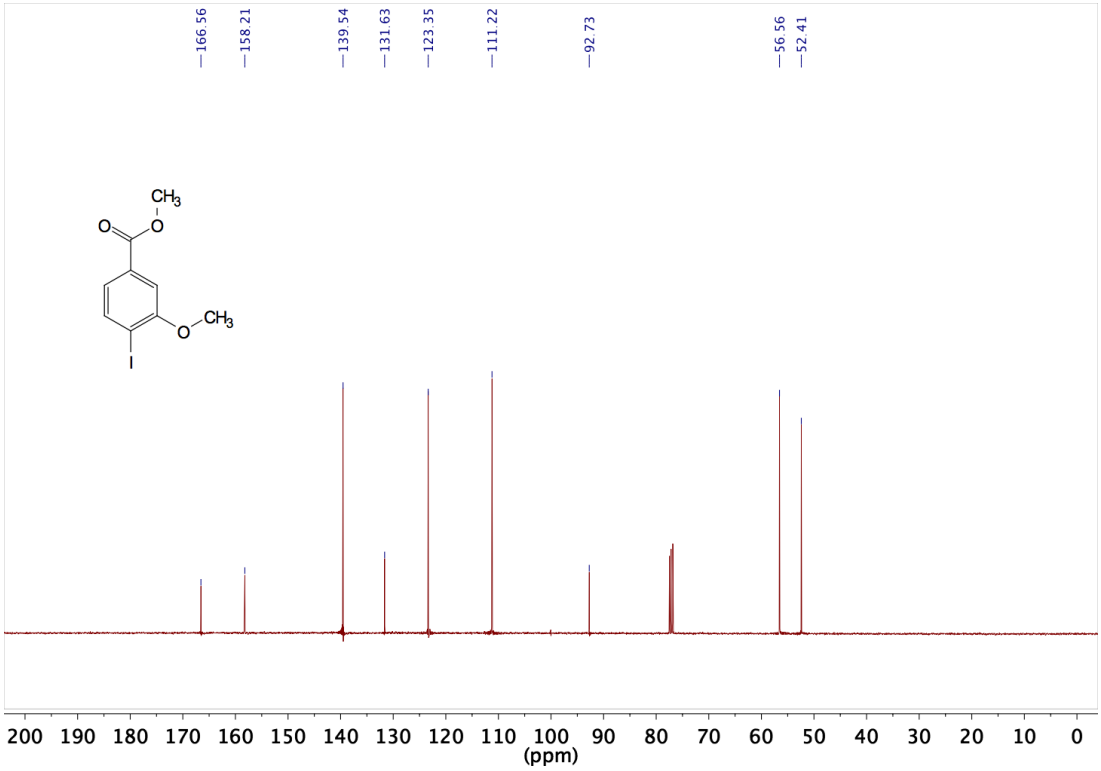
166.56
158.21
139.54
131.63
123.35
111.22
92.73
56.56
52.41
CH3
O
O
O
CH3
I
200 190 180 170 160 150 140 130 120 110 100 90 80 70 60 50 40 30 20 10 0
(ppm)

3.19

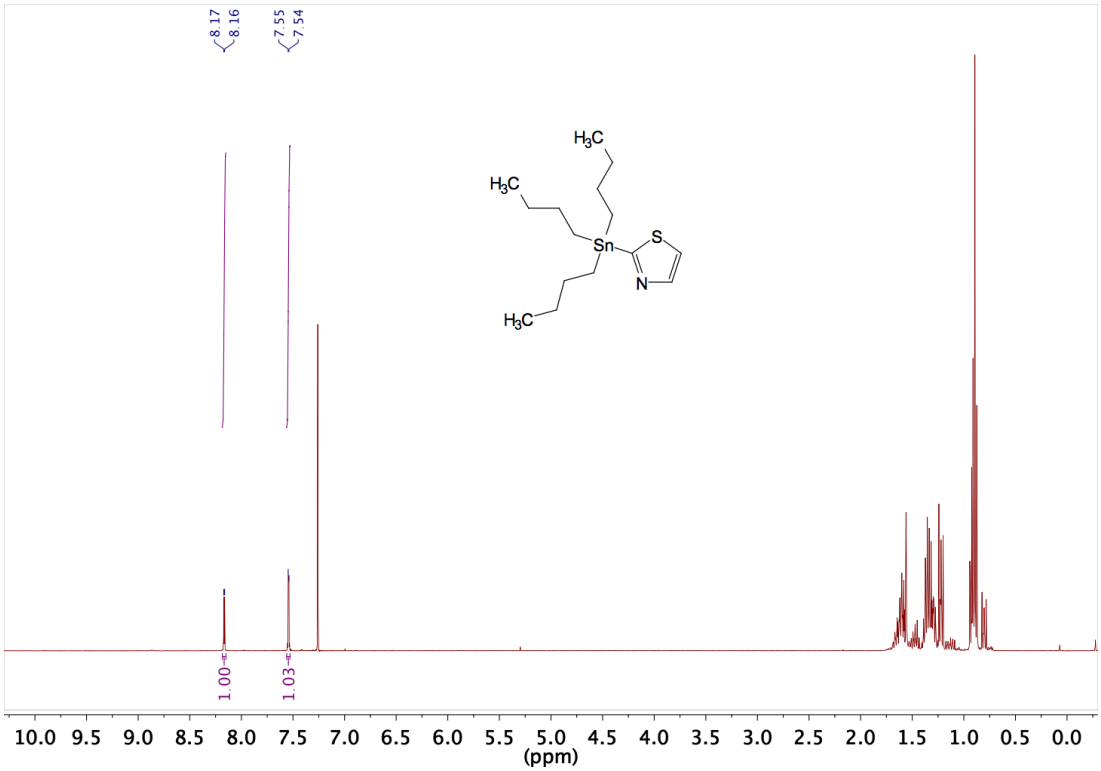
8.17
8.16
7.55
7.54
H3C
H3C
Sn
S
N
H3C
1.00
1.03
10.0 9.5 9.0 8.5 8.0 7.5 7.0 6.5 6.0 5.5 5.0 4.5 4.0 3.5 3.0 2.5 2.0 1.5 1.0 0.5 0.0
(ppm)

3.20

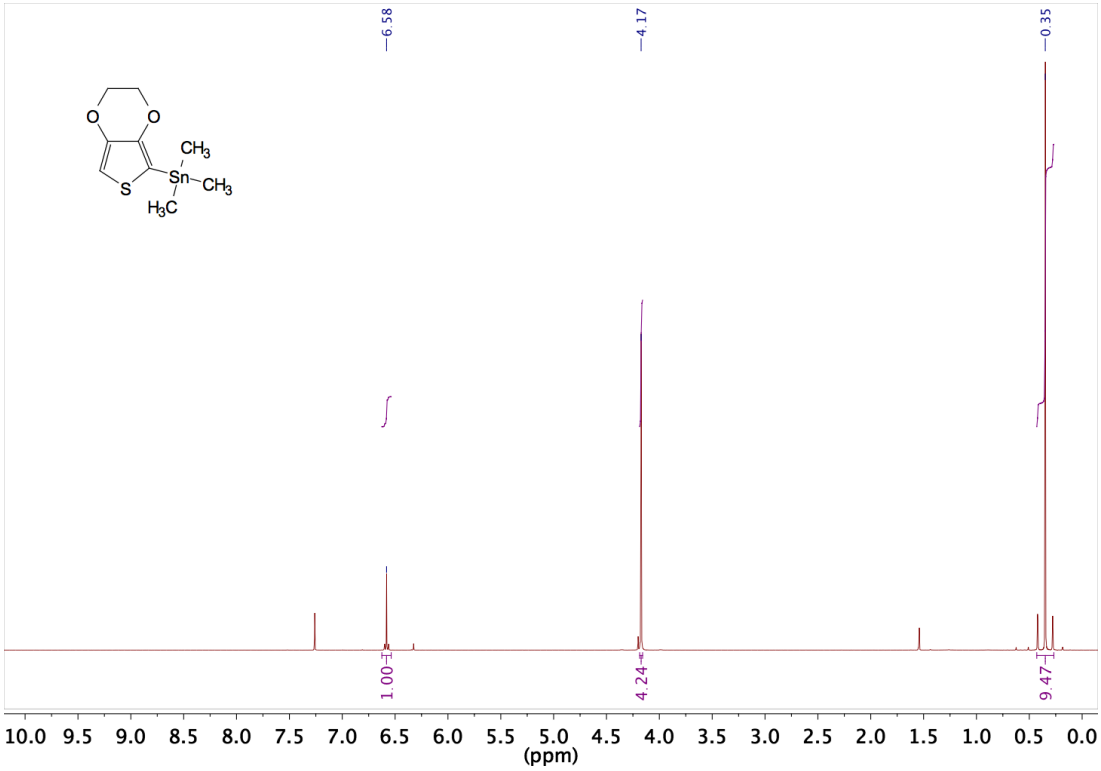

3.21

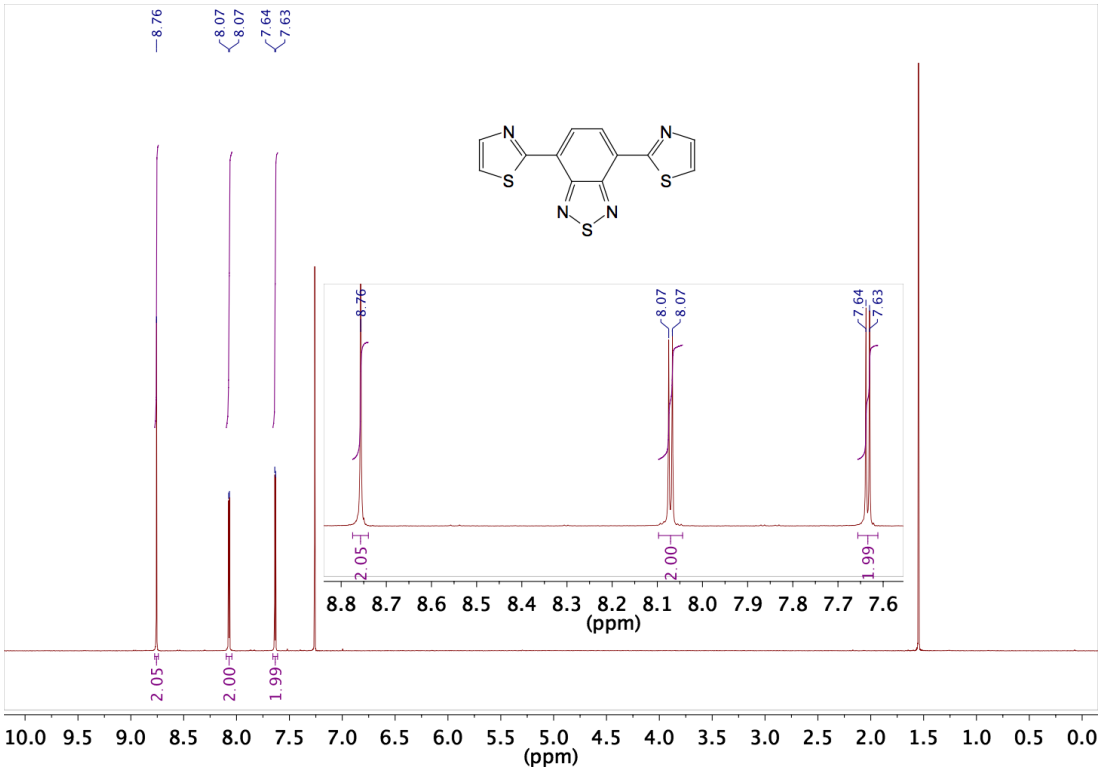

3.21

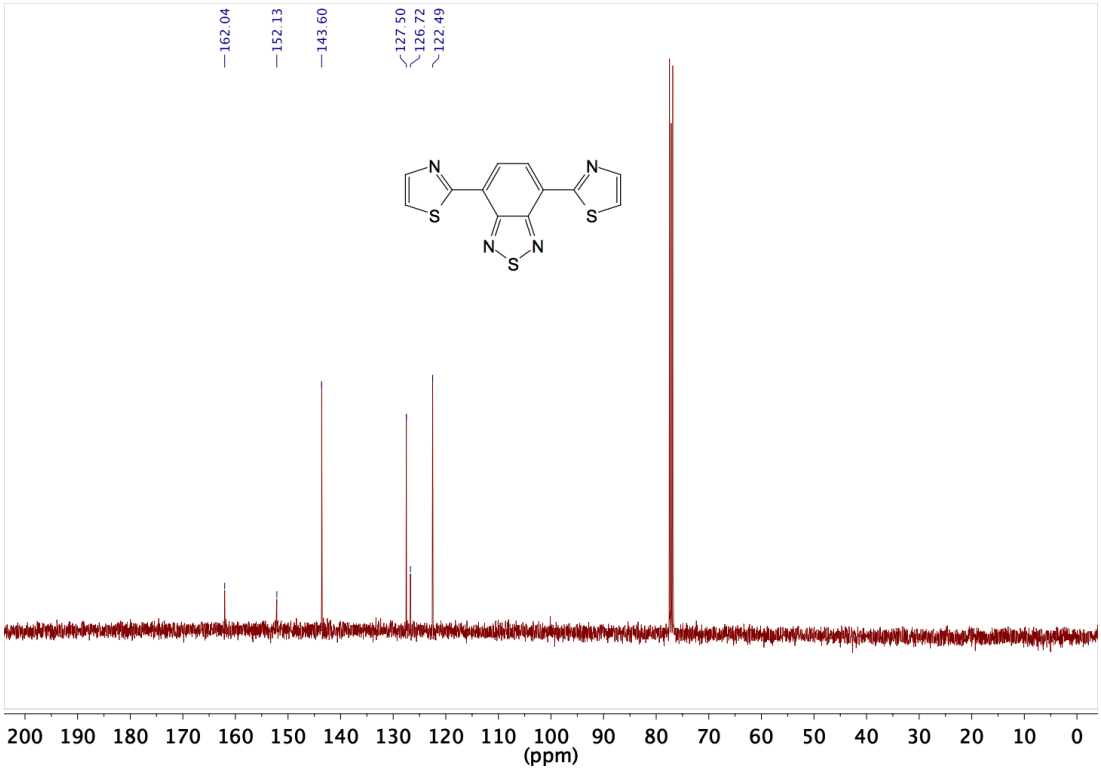
162.04
152.13
143.60
127.50
126.72
122.49
N
S
N
S
N
S
N
200 190 180 170 160 150 140 130 120 110 100 90 80 70 60 50 40 30 20 10 0
(ppm)

3.22

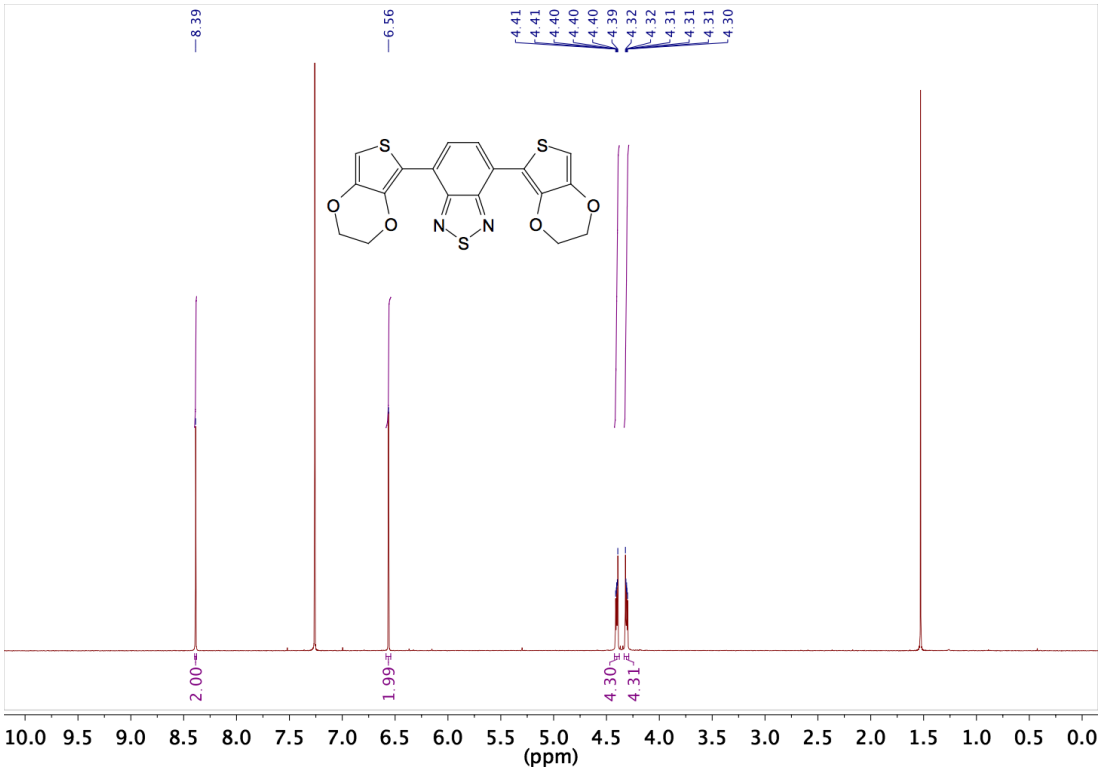
8.39
6.56
4.41
4.41
4.40
4.40
4.40
4.39
4.32
4.32
4.31
4.31
4.31
4.30
S
S
O
O
O
O
N
S
N
2.00
1.99
4.30
4.31
10.0 9.5 9.0 8.5 8.0 7.5 7.0 6.5 6.0 5.5 5.0 4.5 4.0 3.5 3.0 2.5 2.0 1.5 1.0 0.5 0.0
(ppm)

4.1

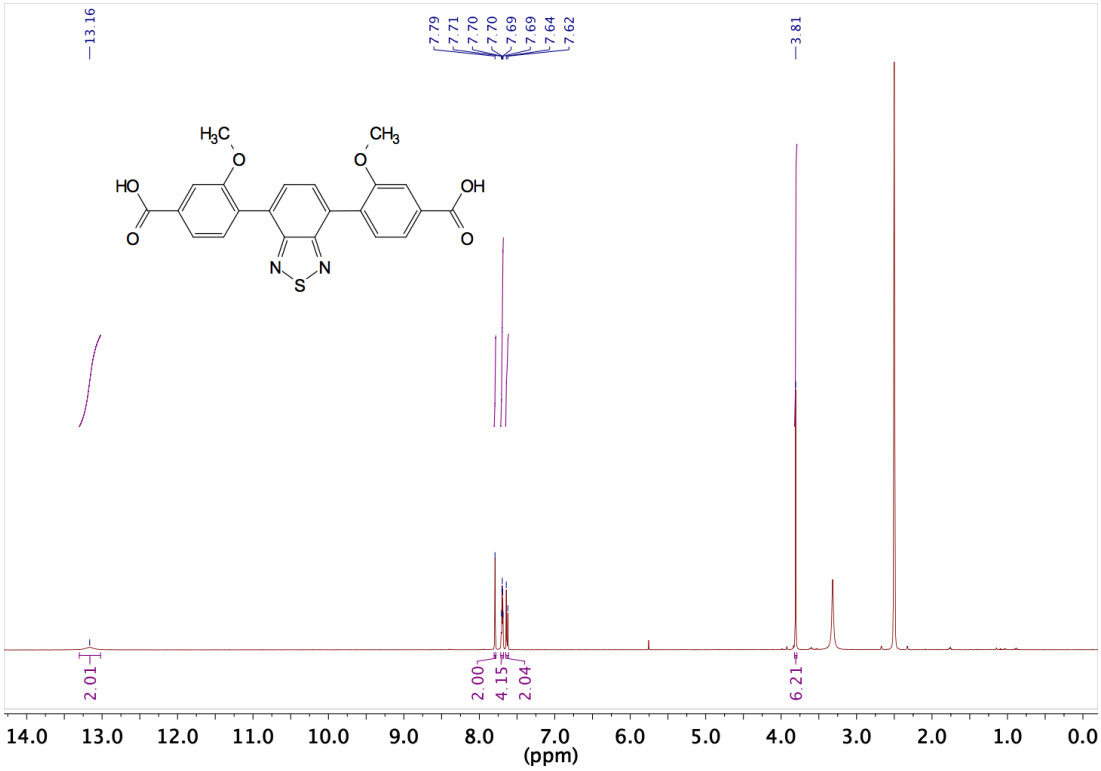
13.16
7.79
7.71
7.70
7.70
7.69
7.69
7.64
7.62
3.81
2.01
2.00
4.15
2.04
6.21
14.0 13.0 12.0 11.0 10.0 9.0 8.0 7.0 6.0 5.0 4.0 3.0 2.0 1.0 0.0
(ppm)

4.1

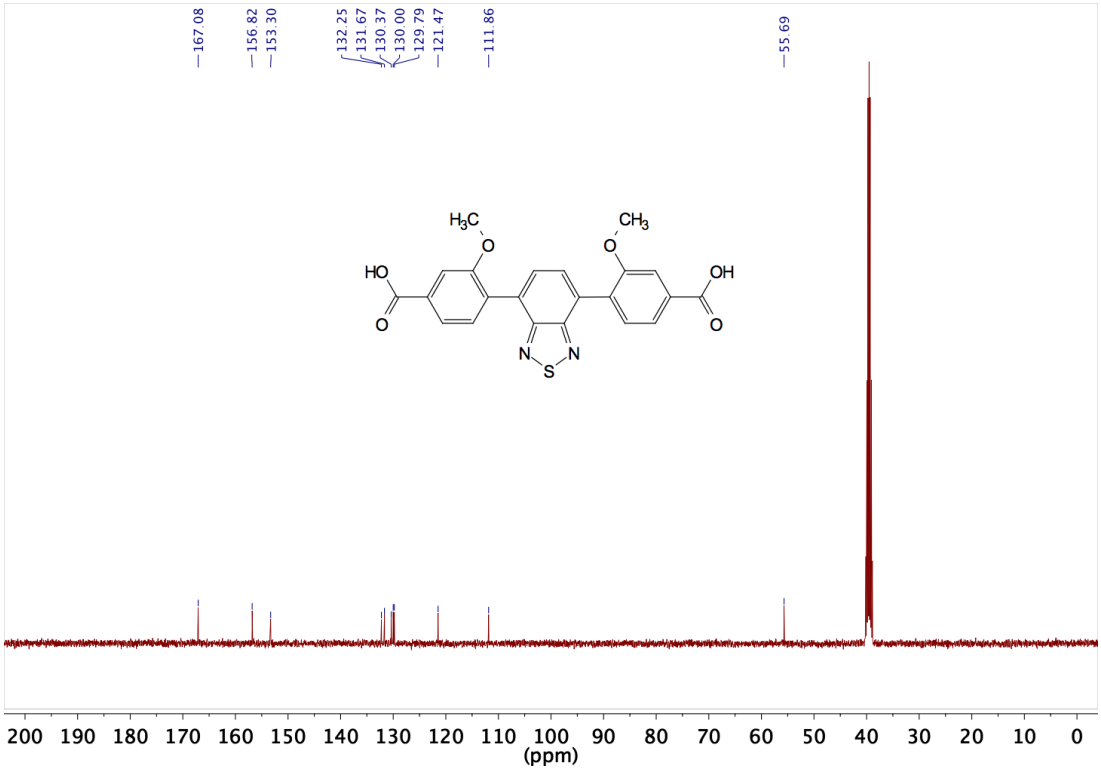
167.08
156.82
153.30
132.25
131.67
130.37
130.00
129.79
121.47
111.86
55.69
200 190 180 170 160 150 140 130 120 110 100 90 80 70 60 50 40 30 20 10 0
(ppm)

4.2

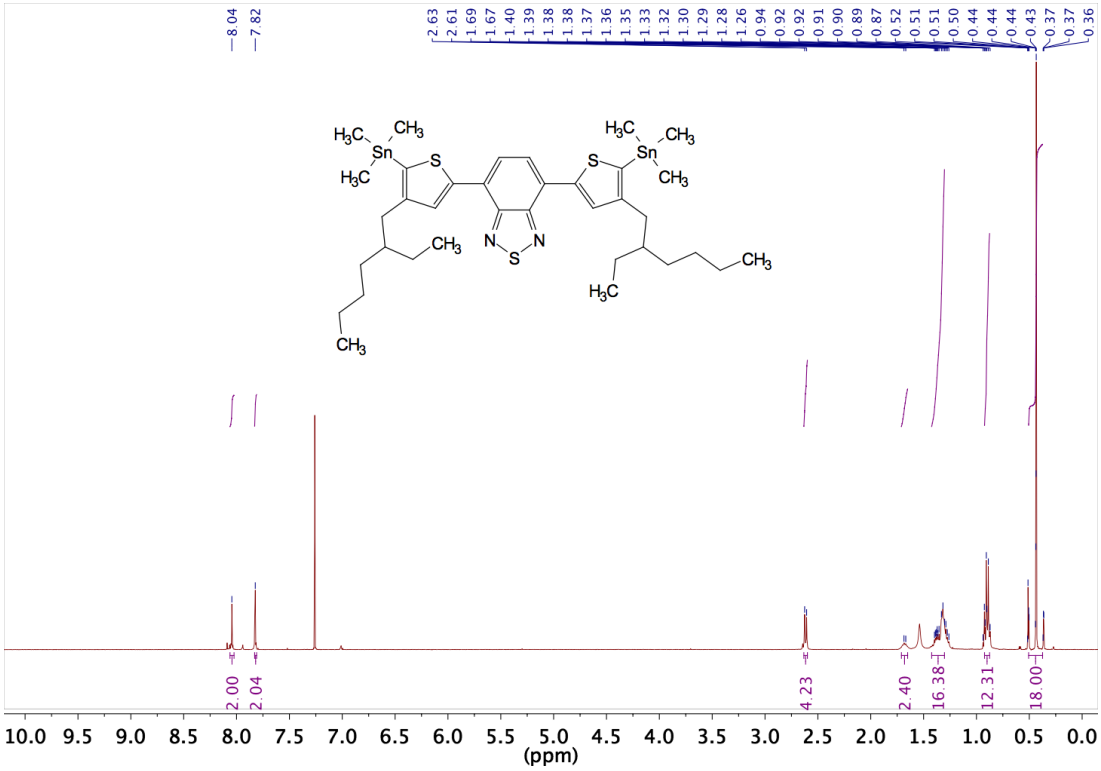
8.04
7.82
2.63
2.61
1.69
1.67
1.40
1.39
1.38
1.38
1.37
1.36
1.35
1.33
1.32
1.30
1.29
1.28
1.26
0.94
0.92
0.92
0.91
0.90
0.89
0.87
0.52
0.51
0.51
0.50
0.44
0.44
0.44
0.43
0.37
0.37
0.36
2.00
2.04
4.23
2.40
16.38
12.31
18.00
10.0 9.5 9.0 8.5 8.0 7.5 7.0 6.5 6.0 5.5 5.0 4.5 4.0 3.5 3.0 2.5 2.0 1.5 1.0 0.5 0.0
(ppm)

4.3

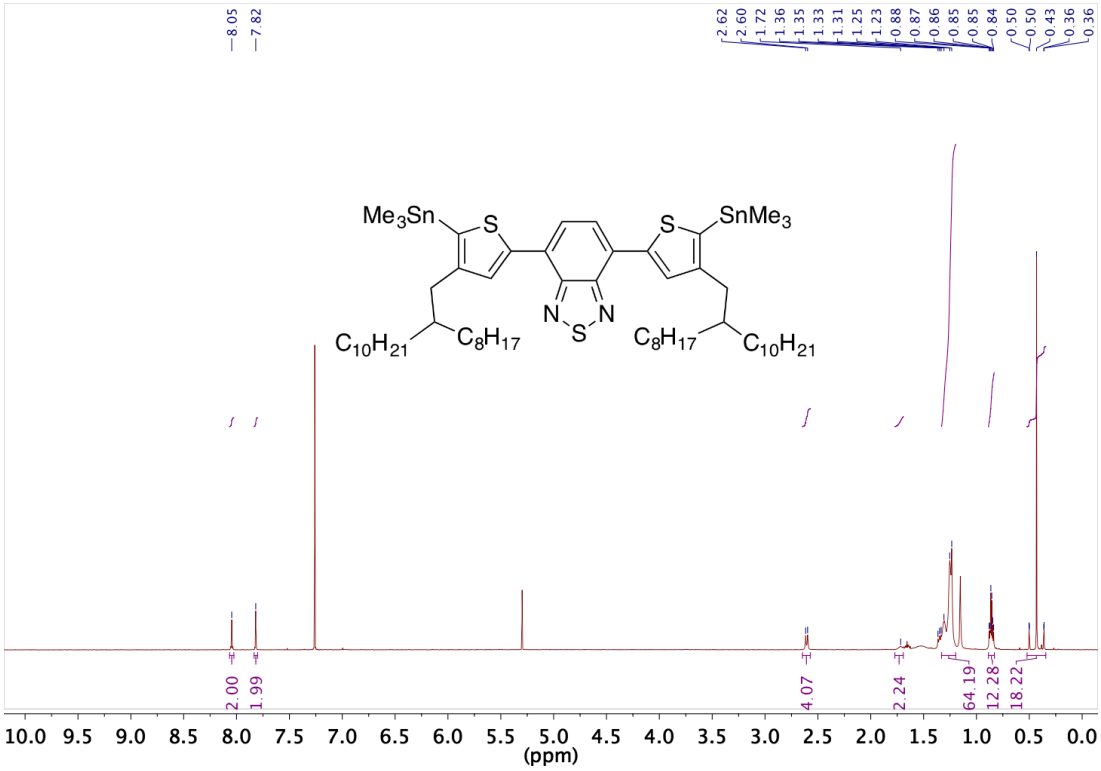
8.05
7.82
2.62
2.60
1.72
1.36
1.35
1.33
1.31
1.25
1.23
0.88
0.87
0.86
0.85
0.85
0.84
0.50
0.50
0.43
0.36
0.36
2.00
1.99
4.07
2.24
64.19
12.28
18.22
10.0 9.5 9.0 8.5 8.0 7.5 7.0 6.5 6.0 5.5 5.0 4.5 4.0 3.5 3.0 2.5 2.0 1.5 1.0 0.5 0.0
(ppm)

4.4

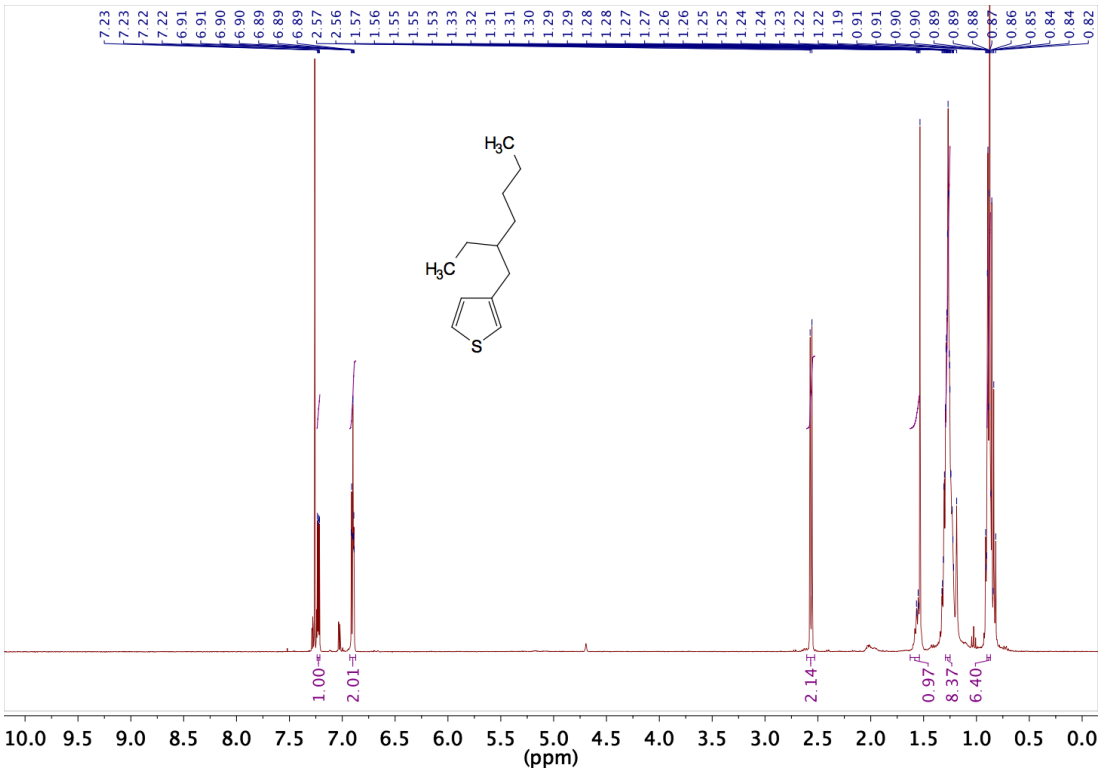
7.23 7.23 7.22 7.22 6.91 6.91 6.90 6.90 6.89 6.89 6.89 2.57 2.56 1.57 1.56 1.55 1.55 1.53 1.33 1.32 1.31 1.31 1.30 1.29 1.29 1.28 1.28 1.27 1.27 1.26 1.26 1.25 1.25 1.24 1.24 1.23 1.22 1.22 1.19 0.91 0.91 0.90 0.90 0.89 0.89 0.88 0.87 0.86 0.85 0.84 0.84 0.82
H3C
H3C
S
1.00
2.01
2.14
0.97
8.37
6.40
10.0 9.5 9.0 8.5 8.0 7.5 7.0 6.5 6.0 5.5 5.0 4.5 4.0 3.5 3.0 2.5 2.0 1.5 1.0 0.5 0.0
(ppm)

4.5

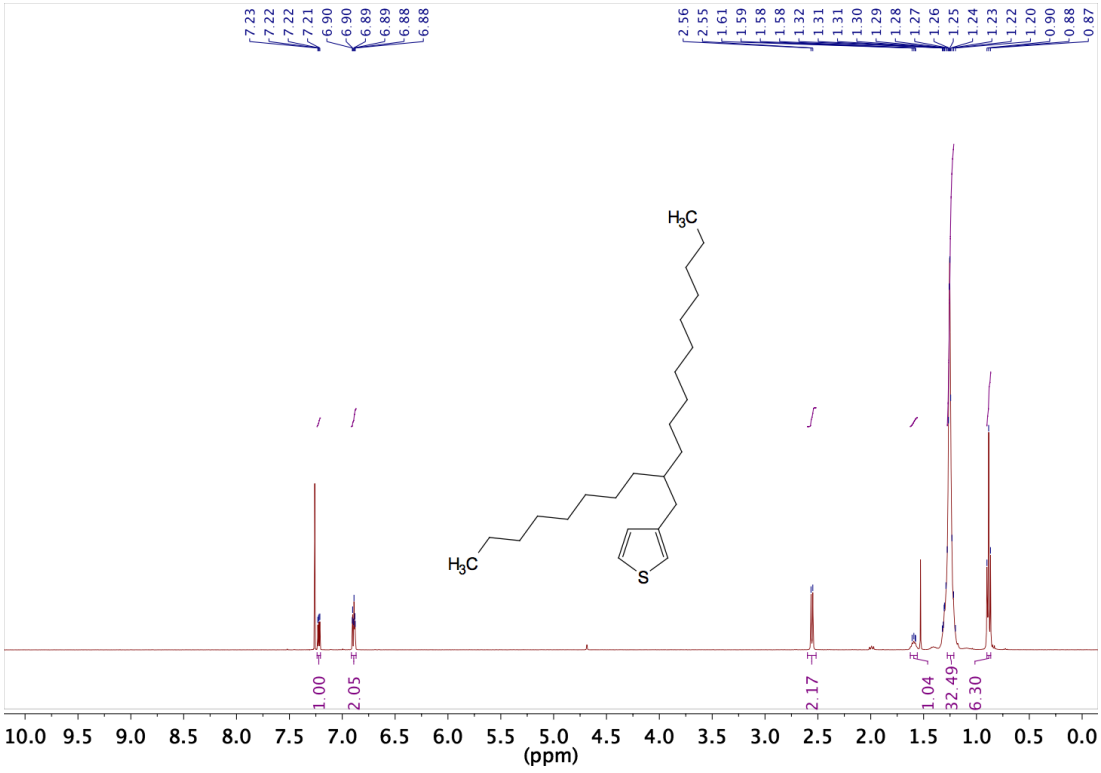
7.23 7.22 7.22 7.21 6.90 6.90 6.89 6.89 6.88 6.88
2.56 2.55 1.61 1.59 1.58 1.58 1.32 1.31 1.31 1.30 1.29 1.28 1.27 1.26 1.25 1.24 1.23 1.22 1.20 0.90 0.88 0.87
H3C
H3C
S
1.00
2.05
2.17
1.04
32.49
6.30
10.0 9.5 9.0 8.5 8.0 7.5 7.0 6.5 6.0 5.5 5.0 4.5 4.0 3.5 3.0 2.5 2.0 1.5 1.0 0.5 0.0
(ppm)

4.6

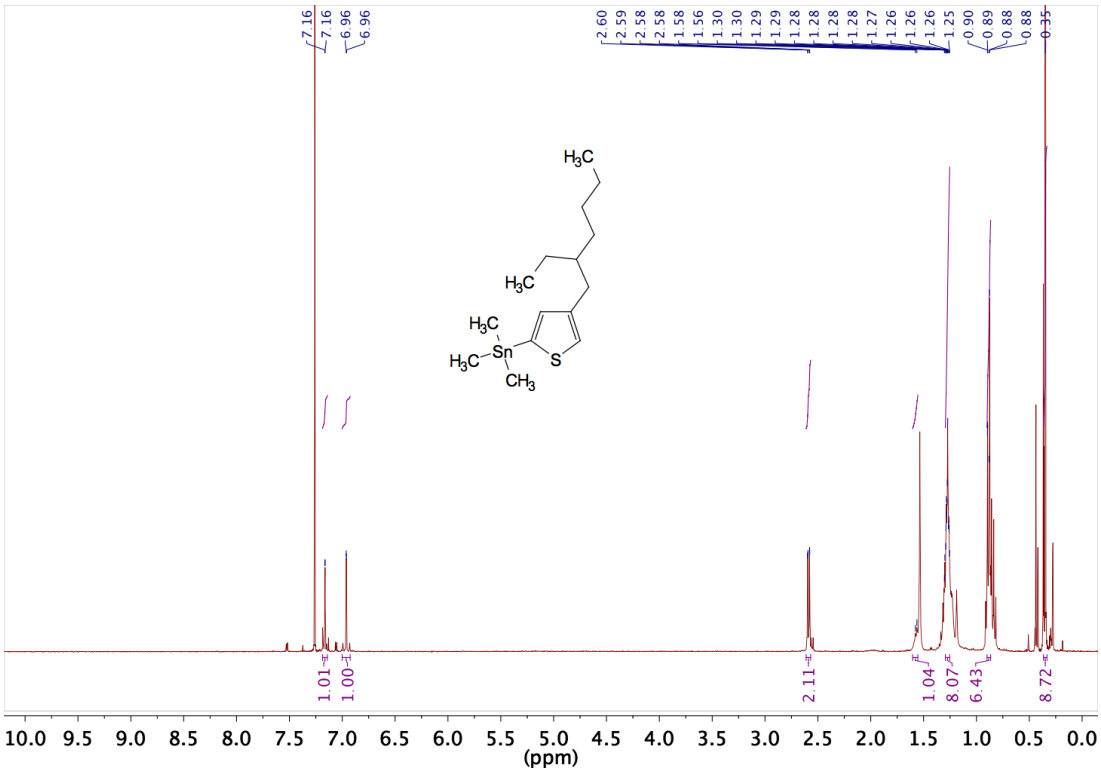
7.16
7.16
6.96
6.96
2.60
2.59
2.58
2.58
1.58
1.56
1.30
1.29
1.29
1.28
1.28
1.28
1.28
1.27
1.26
1.26
1.25
0.90
0.89
0.88
0.88
0.35
H3C
H3C
H3C
Sn
H3C
CH3
S
1.01
1.00
2.11
1.04
8.07
6.43
8.72
10.0 9.5 9.0 8.5 8.0 7.5 7.0 6.5 6.0 5.5 5.0 4.5 4.0 3.5 3.0 2.5 2.0 1.5 1.0 0.5 0.0
(ppm)

4.7

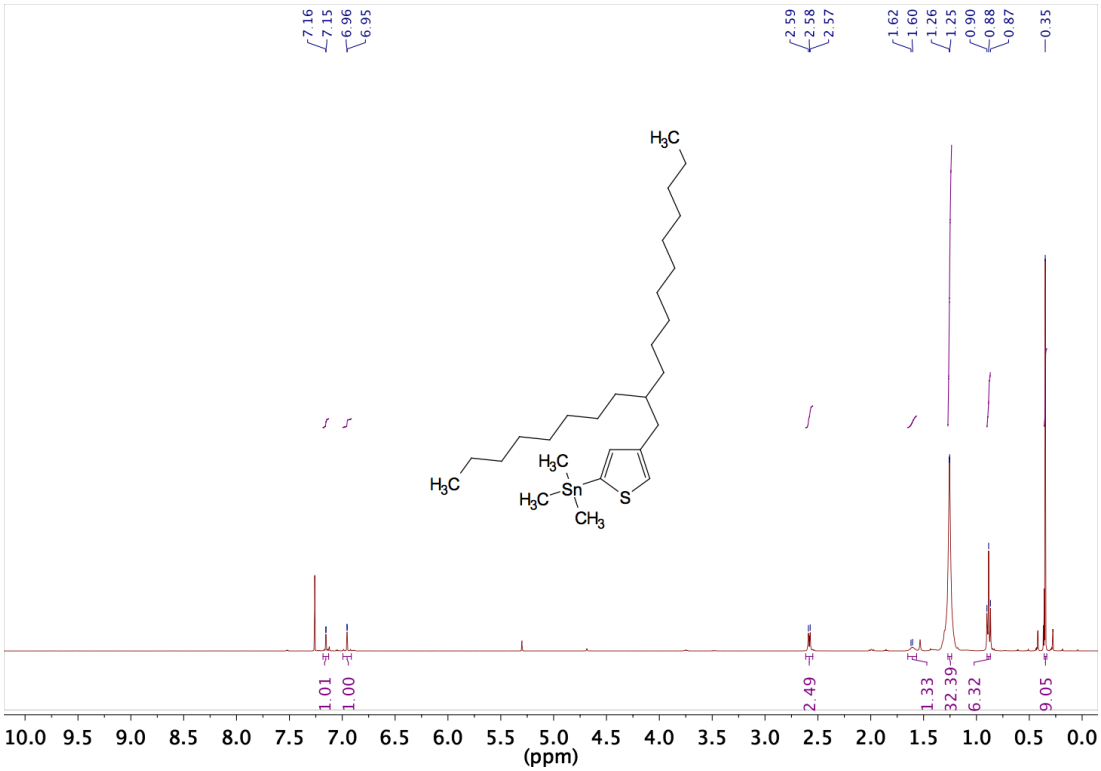
7.16
7.15
6.96
6.95
2.59
2.58
2.57
1.62
1.60
1.26
1.25
0.90
0.88
0.87
0.35
H3C
H3C
H3C
Sn
H3C
CH3
S
1.01
1.00
2.49
1.33
32.39
6.32
9.05
10.0 9.5 9.0 8.5 8.0 7.5 7.0 6.5 6.0 5.5 5.0 4.5 4.0 3.5 3.0 2.5 2.0 1.5 1.0 0.5 0.0
(ppm)

4.8

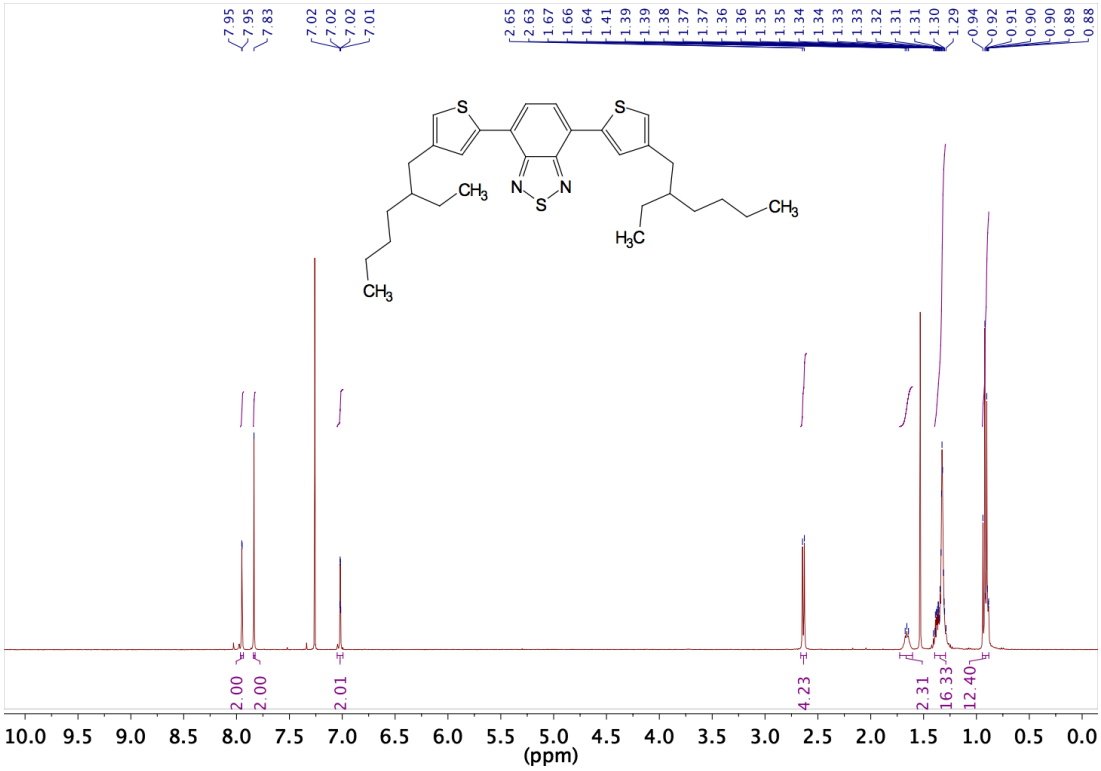
7.95
7.95
7.83
7.02
7.02
7.02
7.01
2.65
2.63
1.67
1.66
1.64
1.41
1.39
1.39
1.38
1.37
1.37
1.36
1.36
1.35
1.35
1.34
1.34
1.33
1.33
1.32
1.31
1.31
1.30
1.29
0.94
0.92
0.91
0.90
0.90
0.89
0.88
S
S
N
S
N
CH3
CH3
H3C
CH3
2.00
2.00
2.01
4.23
2.31
16.33
12.40
10.0 9.5 9.0 8.5 8.0 7.5 7.0 6.5 6.0 5.5 5.0 4.5 4.0 3.5 3.0 2.5 2.0 1.5 1.0 0.5 0.0
(ppm)

4.9

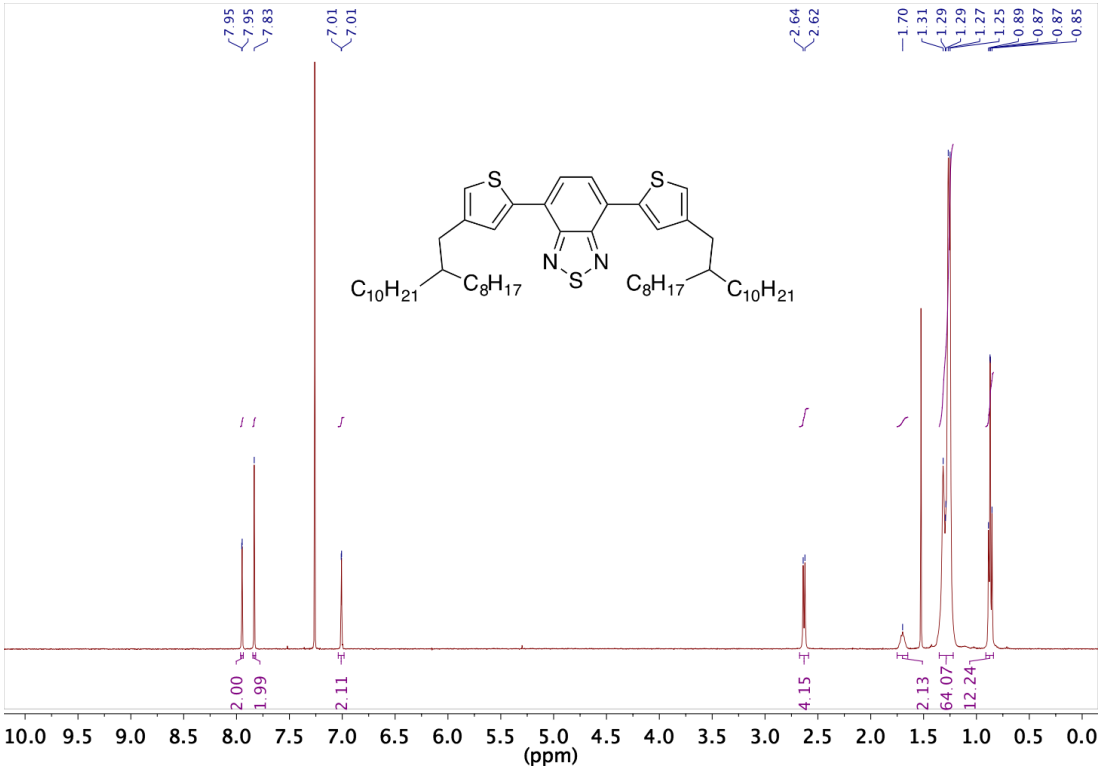
7.95
7.95
7.83
7.01
7.01
2.64
2.62
1.70
1.31
1.29
1.29
1.27
1.25
0.89
0.87
0.87
0.85
S
S
N
S
N
C10H21
C8H17
C8H17
C10H21
2.00
1.99
2.11
4.15
2.13
64.07
12.24
10.0 9.5 9.0 8.5 8.0 7.5 7.0 6.5 6.0 5.5 5.0 4.5 4.0 3.5 3.0 2.5 2.0 1.5 1.0 0.5 0.0
(ppm)

POP-**4.15**

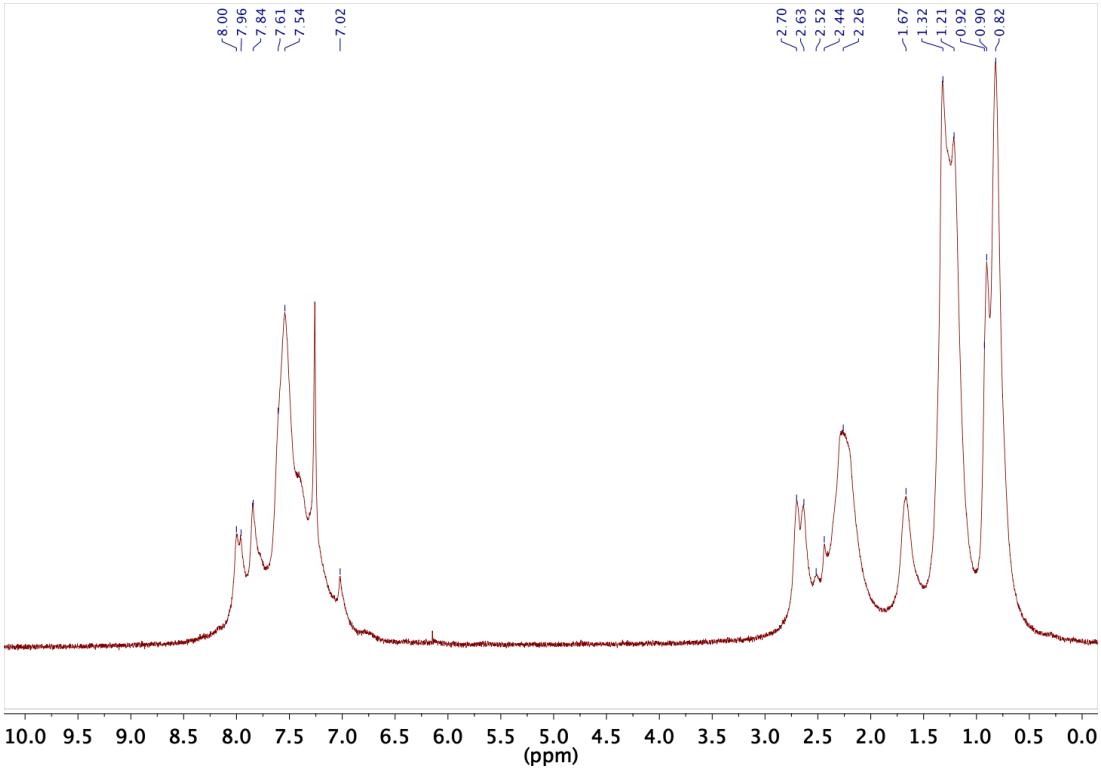

POP-**4.16**

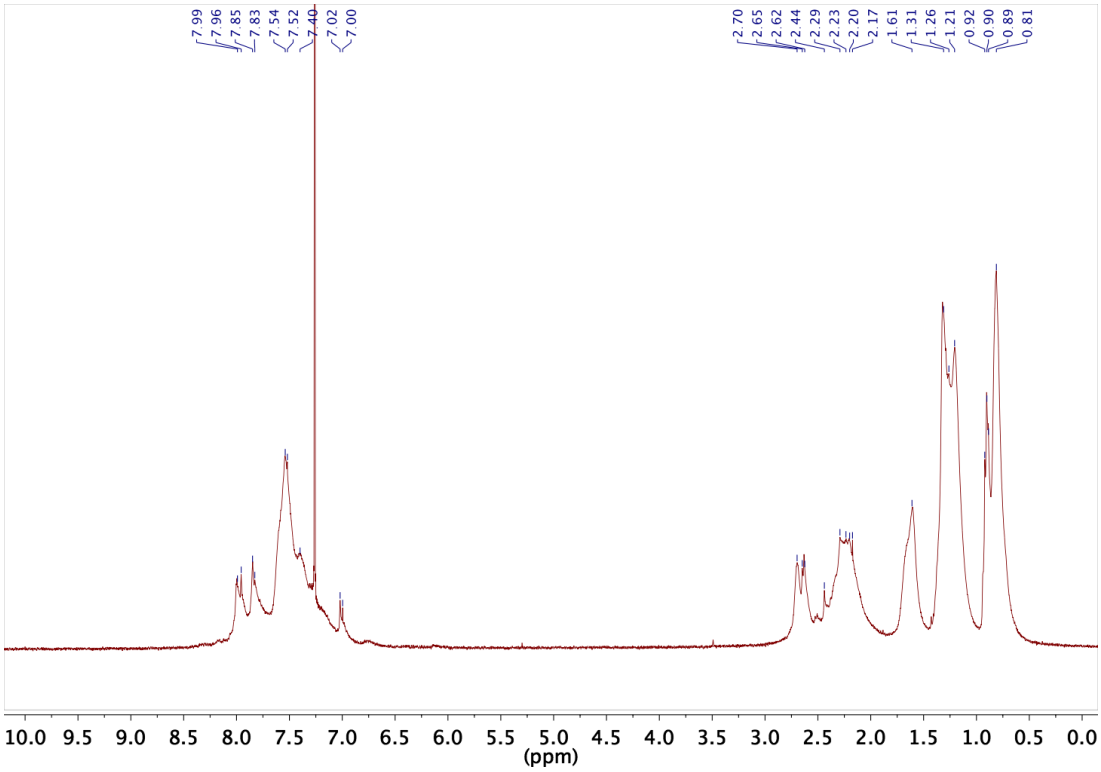

Chapter 8. References

1 P. Atkins, J. De Paula, *Physical Chemistry*, Oxford University Press, **2006**.
2 S. Eliott, *The Physics of Chemistry and Solids*, Wiley, **1998**.
3 A. Rockett, *The Materials Science of Semiconductors*, Springer, **2008**.
4 H. Shirakawa, E. J. Louis, A. G. MacDiarmid, C. K. Chiang, A. J. Heeger, *J. Chem. Soc., Chem. Commun.*, **1977**, *16*, 578.
5 N. J. Findlay, C. Orofino-Pena, J. Bruckbauer, S. E. T. Elmasly, S. Arumugam, A. R. Inigo, A. L. Kanibolotsky, R. W. Martin, P. J. Skabara, *J. Mater. Chem. C*, **2013**, *1*, 2249.
6 A. L. Kanibolotsky, I. F. Perepichka, P. J. Skabara, *Chem. Soc. Rev.*, **2010**, *39*, 2695.
7 J. Roncali, *Macromol. Rapid Commun.*, **2007**, *28*, 1761.
8 J. Zaumseil, H. Sirringhaus, *Chem. Rev.*, **2007**, *107*, 1296.
9 H. Sirringhaus, *Adv. Mater.*, **2014**, *26*, 1319.
10 M. Muccini, *Nat. Mater.*, **2006**, *5*, 605.
11 M. C. Gather, A. Köhnen, K. Meerholz, *Adv. Mater.*, **2011**, *23*, 233.
12 G. M. Farinola, R. Ragni, *Chem. Soc. Rev.*, **2011**, *40*, 3467.
13 S. Günes, H. Neugebauer, N. S. Sariciftci, *Chem. Rev.*, **2007**, *107*, 1324.
14 S.-C. Lo, P. L. Burn, *Chem. Rev.*, **2007**, *107*, 1097.
15 I. D. W. Samuel, G. A. Turnbull, *Chem. Rev.*, **2007**, *107*, 1272.
16 S. W. Thomas, G. D. Joly, T. M. Swager, *Chem. Rev.*, **2007**, *107*, 1339.
17 S. Moller, S. R. Forrest, C. Perlov, W. Jackson, C. Taussig, *J. Appl. Phys.*, **2003**, *94*, 7811.
18 J. Roncali, *Chem. Rev.*, **1997**, *97*, 173.
19 J. Kürti, P. R. Surján, *J. Chem. Phys.*, **1990**, *92*, 3247.
20 D. T. de Lill, N. S. Gunning, C. L. Cahill, *Inorg. Chem.*, **2004**, *44*, 258.
21 J. L. Brédas, *J. Chem. Phys.*, **1985**, *82*, 3808.
22 K.-Y. Jen, M. Maxifield, L. W. Shacklette, R. L. Elsenbaumer, *J. Chem. Soc., Chem. Commun.*, **1987**, 309.
23 P. Frère, J.-M. Raimundo, P. Blanchard, J. Delaunay, P. Richomme, J.-L. Sauvajol, J. Orduna, J. Garin, J. Roncali, *J. Org. Chem.*, **2003**, *68*, 7254.
24 R. J. Waltman, J. Bargon, A. F. Diaz, *J. Phys. Chem.*, **1983**, *87*, 1459.
25 H. A. Ho, H. Brisset, P. Frere, J. Roncali, *J. Chem. Soc., Chem. Commun.*, **1995**, 2309.
26 J. M. Toussaint, J. L. Brédas, *Synth. Met.*, **1993**, *61*, 103.
27 J. Roncali, R. Garreau, A. Yassar, P. Marque, F. Garnier, M. Lemaire, *J. Phys. Chem.*, **1987**, *91*, 6706.
28 J. Roncali, *Chem. Rev.*, **1992**, *92*, 711.
29 J. Roncali, P. Blanchard, P. Frere, *J. Mater. Chem.*, **2005**, *15*, 1589.
30 F. Wudl, M. Kobayashi, A. J. Heeger, *J. Org. Chem.*, **1984**, *49*, 3382.
31 W.-C. Chen, S. A. Jenekhe, *Macromolecules*, **1995**, *28*, 465.
32 E. E. Havinga, W. Hoeve, H. Wynberg, *Polym. Bull.*, **1992**, *29*, 119.
33 C. Kitamura, S. Tanaka, Y. Yamashita, *J. Chem. Soc., Chem. Commun.*, **1994**, 1585.
34 C. Kitamura, S. Tanaka, Y. Yamashita, *Chem. Mater.*, **1996**, *8*, 570.
35 U. Salzner, *J. Phys. Chem. B*, **2002**, *106*, 9214.
36 S. Akoudad, J. Roncali, *Chem. Commun.*, **1998**, 2081.
37 J. Casado, R. P. Ortiz, M. C. Ruiz Delgado, V. Hernández, J. T. López Navarrete, J.-M. Raimundo, P. Blanchard, M. Allain, J. Roncali, *J. Phys. Chem. B*, **2005**, *109*, 16616.
38 I. F. Perepichka, E. Levillain, J. Roncali, *J. Mater. Chem.*, **2004**, *14*, 1679.
39 J. Lakowicz, *Principles of Fluorescence Spectroscopy*, Kluwer Academic/Plenum Publishers, **2006**.
40 D. H. Williams, *Spectroscopic methods in organic chemistry*, Maidenhead, **2008**.
41 J. Kalinowski, M. Cocchi, D. Virgili, V. Fattori, J. A. G. Williams, *Adv. Mater.*, **2007**, *19*, 4000.
42 M. N. Berberan Santos, *PhysChemComm*, **2000**, *3*, 18.
43 M. Pope, H. P. Kallmann, P. Magnante, *J. Chem. Phys.*, **1963**, *38*, 2042.
44 N. C. Greenham, R. H. Friend, *Semiconductor Device Physics of Conjugated Polymers*, Academic Press, **1996**.
45 M. A. Baldo, D. F. O'Brien, Y. You, A. Shoustikov, S. Sibley, M. E. Thompson, S. R. Forrest, *Nature*, **1998**, *395*, 151.
46 L. A. Jones, *J. Opt. Soc. Am.*, **1943**, *33*, 534.
47 W. R. McCluney, *Introduction to Radiometry and Photometry*, Artech House, **2014**.
48 C. J. Humphreys, *MRS Bull.*, **2008**, *33*, 459.
49 Y. Takei, *Sci. Technol. Trends–Quarterly Rev.*, **2009**, *32*, 59.
50 M. Bessho, K. Shimizu, *Electron. Comm. Jpn.*, **2012**, *95*, 1.

51 N. Yukio, I. Masatsugu, S. Daisuke, S. Masahiko, M. Takashi, *J. Phys. D: Appl. Phys.*, **2010**, *43*, 354002.
52 J. Kalinowski, V. Fattori, M. Cocchi, J. A. G. Williams, *Coord. Chem. Rev.*, **2011**, *255*, 2401.
53 S. Mukherjee, P. Thilagar, *Dyes Pigm.*, **2014**, *110*, 2.
54 N. Bardsley, S. Bland, L. Pattison, M. Pattison, K. Stober, F. Welsh, M. Yamada, *Solid-State Lighting Research and Development: Multi-Year Program Plan*, presented at the Lighting Research and Development Building Technologies Program, **2014**.
55 K. Bando, K. Sakano, Y. Noguchi, Y. Shimizu, *J. Light & Vis. Env.*, **1998**, *22*, 2.
56 R.-J. Xie, N. Hirosaki, M. Mitomo, Y. Yamamoto, T. Suehiro, K. Sakuma, *J. Phys. Chem. B*, **2004**, *108*, 12027.
57 R.-J. Xie, N. Hirosaki, K. Sakuma, Y. Yamamoto, M. Mitomo, *Appl. Phys. Lett.*, **2004**, *84*, 5404.
58 J. K. Sheu, S. J. Chang, C. H. Kuo, Y. K. Su, L. W. Wu, Y. C. Lin, W. C. Lai, J. M. Tsai, G. C. Chi, R. K. Wu, *IEEE Photon. Technol. Lett.*, **2003**, *15*, 18.
59 W.-J. Yang, L. Luo, T.-M. Chen, N.-S. Wang, *Chem. Mater.*, **2005**, *17*, 3883.
60 K. T. Kamtekar, A. P. Monkman, M. R. Bryce, *Adv. Mater.*, **2010**, *22*, 572.
61 C. Tang, X.-D. Liu, F. Liu, X.-L. Wang, H. Xu, W. Huang, *Macromol. Chem. Phys.*, **2013**, *214*, 314.
62 N. Thejo Kalyani, S. J. Dhoble, *Renew. Sust. Energ. Rev.*, **2012**, *16*, 2696.
63 I. Moreno, U. Contreras, *Opt. Express*, **2007**, *15*, 3607.
64 N. J. Findlay, J. Bruckbauer, A. R. Inigo, B. Breig, S. Arumugam, D. J. Wallis, R. W. Martin, P. J. Skabara, *Adv. Mater.*, **2014**, *26*, 7290.
65 S. Reineke, M. Thomschke, B. Lüssem, K. Leo, *Rev. Mod. Phys.*, **2013**, *85*, 1245.
66 P. F. Smet, A. B. Parmentier, D. Poelman, *J. Electrochem. Soc.*, **2011**, *158*, R37.
67 Q. Q. Hou, P. X. Zhang, M. F. Zhang, Z. W. Lu, X. Z. Ren, *Adv. Mat. Res.*, **2011**, *158*, 42.
68 Q. Wang, D. Ma, *Chem. Soc. Rev.*, **2010**, *39*, 2387.
69 K. Okamoto, I. Niki, A. Shvartser, Y. Narukawa, T. Mukai, A. Scherer, *Nat. Mater.*, **2004**, *3*, 601.
70 G. Giro, M. Cocchi, J. Kalinowski, P. Di Marco, V. Fattori, *Chem. Phys. Lett.*, **2000**, *318*, 137.
71 P. Nandhikonda, M. D. Heagy, *Chem. Commun.*, **2010**, *46*, 8002.
72 P. Nandhikonda, M. D. Heagy, *Org. Lett.*, **2010**, *12*, 4796.
73 D. Liu, Z. Zhang, H. Zhang, Y. Wang, *Chem. Commun.*, **2013**, *49*, 10001.
74 J. Goodman, L. E. Brus, *J. Am. Chem. Soc.*, **1978**, *100*, 7472.
75 V. S. Padalkar, S. Seki, *Chem. Soc. Rev.*, **2016**, *45*, 169.
76 K.-C. Tang, M.-J. Chang, T.-Y. Lin, H.-A. Pan, T.-C. Fang, K.-Y. Chen, W.-Y. Hung, Y.-H. Hsu, P.-T. Chou, *J. Am. Chem. Soc.*, **2011**, *133*, 17738.
77 Y. Zhao, L. Duan, X. Zhang, D. Zhang, J. Qiao, G. Dong, L. Wang, Y. Qiu, *RSC Adv.*, **2013**, *3*, 21453.
78 J. Karpiuk, E. Karolak, J. Nowacki, *Phys. Chem. Chem. Phys.*, **2010**, *12*, 8804.
79 V. Jankus, P. Data, D. Graves, C. McGuinness, J. Santos, M. R. Bryce, F. B. Dias, A. P. Monkman, *Adv. Funct. Mater.*, **2014**, *24*, 6178.
80 T. Ishisone, S. Seo, Y. Nonaka, T. Kawata, N. Ohsawa, *J. Soc. Inf. Display*, **2014**, *22*, 404.
81 V. Cherpak, P. Stakhira, B. Minaev, G. Baryshnikov, E. Stromylo, I. Helzhynskyy, M. Chapran, D. Volyniuk, Z. Hotra, A. Dabuliene, A. Tomkeviciene, L. Voznyak, J. V. Grazulevicius, *ACS Appl. Mater. Interfaces*, **2015**, *7*, 1219.
82 D. Thirion, M. Romain, J. l. Rault-Berthelot, C. Poriel, *J. Mater. Chem.*, **2012**, *22*, 7149.
83 H. Ma, H. Ren, S. Meng, Z. Yan, H. Zhao, F. Sun, G. Zhu, *Chem. Commun.*, **2013**, *49*, 9773.
84 J.-Y. Hu, Y.-J. Pu, G. Nakata, S. Kawata, H. Sasabe, J. Kido, *Chem. Commun.*, **2012**, *48*, 8434.
85 M. Sharnoff, *J. Lumin.*, **1971**, *4*, 69.
86 S. Yang, M. Jiang, *Chem. Phys. Lett.*, **2009**, *484*, 54.
87 Y. Liu, J. Guo, H. Zhang, Y. Wang, *Angew. Chem. Int. Ed.*, **2002**, *41*, 182.
88 J. Schanda, *CIE Colorimetry*, in *Colorimetry*, John Wiley & Sons, Inc., **2007**, 25.
89 Y.-M. Lam, J. H. Xin, *Color Res. Appl.*, **2002**, *27*, 243.
90 A. Thangthong, N. Prachumrak, S. Saengsuwan, S. Namuangruk, T. Keawin, S. Jungsuttiwong, T. Sudyoadsuk, V. Promarak, *J. Mater. Chem. C*, **2015**.
91 J. Kim, A. R. Han, J. Hong, G. Kim, J. Lee, T. J. Shin, J. H. Oh, C. Yang, *Chem. Mater.*, **2014**, *26*, 4933.

92 T. Khanasa, N. Prachumrak, R. Rattanawan, S. Jungsuttiwong, T. Keawin, T. Sudyoadsuk, T. Tuntulani, V. Promarak, *Chem. Commun.*, **2013**, *49*, 3401.
93 K.-H. Ong, S.-L. Lim, J. Li, H.-K. Wong, H.-S. Tan, T.-T. Lin, L. C. H. Moh, J. C. de Mello, Z.-K. Chen, *Polym. Chem.*, **2013**, *4*, 1863.
94 P. Ledwon, N. Thomson, E. Angioni, N. J. Findlay, P. J. Skabara, W. Domagala, *RSC Adv.*, **2015**, *5*, 77303.
95 B. A. D. Neto, A. A. M. Lapis, E. N. da Silva Júnior, J. Dupont, *Eur. J. Org. Chem.*, **2013**, *2013*, 228.
96 P. Anant, H. Mangold, N. T. Lucas, F. Laquai, J. Jacob, *Polymer*, **2011**, *52*, 4442.
97 J. C. Bijleveld, M. Shahid, J. Gilot, M. M. Wienk, R. A. J. Janssen, *Adv. Funct. Mater.*, **2009**, *19*, 3262.
98 D. Zha, L. Chen, F. Wu, H. Wang, Y. Chen, *J. Polym. Sci. A Polym. Chem.*, **2013**, *51*, 565.
99 P. M. DiCarmine, T. B. Schon, T. M. McCormick, P. P. Klein, D. S. Seferos, *J. Phys. Chem. C*, **2014**, *118*, 8295.
100 S.-i. Kato, T. Matsumoto, T. Ishi-i, T. Thiemann, M. Shigeiwa, H. Gorohmaru, S. Maeda, Y. Yamashita, S. Mataka, *Chem. Commun.*, **2004**, 2342.
101 T. Suzuki, T. Okubo, A. Okada, Y. Yamashita, T. Miyashi, *Heterocycles*, **1993**, *35*, 395.
102 M. Tomura, M. Akhtaruzzaman, K. Suzuki, Y. Yamashita, *Acta Crystallogr. Sect. C-Cryst. Struct. Commun.*, **2002**, *58*, o373.
103 P. Anant, N. T. Lucas, J. Jacob, *Org. Lett.*, **2008**, *10*, 5533.
104 E. Xu, H. Zhong, H. Lai, D. Zeng, J. Zhang, W. Zhu, Q. Fang, *Macromol. Chem. Phys.*, **2010**, *211*, 651.
105 I. V. Kurdyukova, A. A. Ishchenko, *Russ. Chem. Rev.*, **2012**, *81*, 258.
106 C. Orofino-Pena, D. Cortizo-Lacalle, J. Cameron, M. T. Sajjad, P. P. Manousiadis, N. J. Findlay, A. L. Kanibolotsky, D. Amarasinghe, P. J. Skabara, T. Tuttle, G. A. Turnbull, I. D. W. Samuel, *Beilstein J. Org. Chem.*, **2014**, *10*, 2704.
107 C. R. Belton, A. L. Kanibolotsky, J. Kirkpatrick, C. Orofino, S. E. T. Elmasly, P. N. Stavrinou, P. J. Skabara, D. D. C. Bradley, *Adv. Funct. Mater.*, **2013**, *23*, 2792.
108 Q. Hou, Y. Xu, W. Yang, M. Yuan, J. Peng, Y. Cao, *J. Mater. Chem.*, **2002**, *12*, 2887.
109 C. W. Tang, S. A. VanSlyke, *Appl. Phys. Lett.*, **1987**, *51*, 913.
110 C. Adachi, T. Tsutsui, S. Saito, *Appl. Phys. Lett.*, **1989**, *55*, 1489.
111 A. Chihaya, T. Shizuo, T. Tetsuo, S. Shogo, *Jpn. J. Appl. Phys.*, **1988**, *27*, L269.
112 A. Iwan, D. Sek, *Prog. Polym. Sci.*, **2011**, *36*, 1277.
113 S. R. Forrest, D. D. C. Bradley, M. E. Thompson, *Adv. Mater.*, **2003**, *15*, 1043.
114 S. Ye, F. Xiao, Y. X. Pan, Y. Y. Ma, Q. Y. Zhang, *Mater. Sci. Eng. R.*, **2010**, *71*, 1.
115 A. R. Duggal, J. J. Shiang, C. M. Heller, D. F. Foust, *Appl. Phys. Lett.*, **2002**, *80*, 3470.
116 A. R. Duggal, J. J. Shiang, D. F. Foust, L. G. Turner, W. F. Nealon, J. C. Bortscheller, *SID Int. Symp. Dig. Tec.*, **2005**, *36*, 28.
117 B. C. Krummacher, V.-E. Choong, M. K. Mathai, S. A. Choulis, F. So, F. Jermann, T. Fiedler, M. Zachau, *Appl. Phys. Lett.*, **2006**, *88*, 113506.
118 *European Union Pat.*, EP 1 238 041 B1, 2005.
119 V. Gohri, S. Hofmann, S. Reineke, T. Rosenow, M. Thomschke, M. Levichkova, B. Lüssem, K. Leo, *Org. Electron.*, **2011**, *12*, 2126.
120 G. Heliotis, G. Itskos, R. Murray, M. D. Dawson, I. M. Watson, D. D. C. Bradley, *Adv. Mater.*, **2006**, *18*, 334.
121 E. Gu, H. X. Zhang, H. D. Sun, M. D. Dawson, A. R. Mackintosh, A. J. C. Kuehne, R. A. Pethrick, C. Belton, D. D. C. Bradley, *Appl. Phys. Lett.*, **2007**, *90*, 031116.
122 E. Xu, H. Zhong, J. Du, D. Zeng, S. Ren, J. Sun, Q. Fang, *Dyes Pigm.*, **2009**, *80*, 194.
123 T. Fukushima, N. Okazeri, T. Miyashi, K. Suzuki, Y. Yamashita, T. Suzuki, *Tetrahedron Lett.*, **1999**, *40*, 1175.
124 M. Akhtaruzzaman, M. Tomura, J. Nishida, Y. Yamashita, *Synth. Met.*, **2003**, *137*, 873.
125 C. Chi, G. Wegner, *Macromol. Rapid Commun.*, **2005**, *26*, 1532.
126 V. Promarak, M. Ichikawa, T. Sudyoadsuk, S. Saengsuwan, T. Keawin, *Opt. Mater.*, **2007**, *30*, 364.
127 K. Yuan Chiu, T. Xiang Su, J. Hong Li, T.-H. Lin, G.-S. Liou, S.-H. Cheng, *J. Electroanal. Chem.*, **2005**, *575*, 95.
128 L. M. Moshurchak, C. Buhrmester, J. R. Dahn, *J. Electrochem. Soc.*, **2008**, *155*, A129.
129 E. T. Seo, R. F. Nelson, J. M. Fritsch, L. S. Marcoux, D. W. Leedy, R. N. Adams, *J. Am. Chem. Soc.*, **1966**, *88*, 3498.
130 D. Li, G. Qian, Z. Y. Wang, *Synth. Met.*, **2014**, *189*, 26.

131 C. M. Cardona, W. Li, A. E. Kaifer, D. Stockdale, G. C. Bazan, *Adv. Mater.*, **2011**, *23*, 2367.
132 R. Improta, V. Barone, G. Scalmani, M. J. Frisch, *J. Chem. Phys.*, **2006**, *125*, 054103.
133 F. Furche, R. Ahlrichs, *J. Chem. Phys.*, **2002**, *117*, 7433.
134 M. J. Frisch, G. W. Trucks, H. B. Schlegel, G. E. Scuseria, M. A. Robb, J. R. Cheeseman, G. Scalmani, V. Barone, B. Mennucci, G. A. Petersson, H. Nakatsuji, M. Caricato, X. Li, H. P. Hratchian, A. F. Izmaylov, J. Bloino, G. Zheng, J. L. Sonnenberg, M. Hada, M. Ehara, K. Toyota, R. Fukuda, J. Hasegawa, M. Ishida, T. Nakajima, Y. Honda, O. Kitao, H. Nakai, T. Vreven, J. A. Montgomery Jr., J. E. Peralta, F. Ogliaro, M. J. Bearpark, J. Heyd, E. N. Brothers, K. N. Kudin, V. N. Staroverov, R. Kobayashi, J. Normand, K. Raghavachari, A. P. Rendell, J. C. Burant, S. S. Iyengar, J. Tomasi, M. Cossi, N. Rega, N. J. Millam, M. Klene, J. E. Knox, J. B. Cross, V. Bakken, C. Adamo, J. Jaramillo, R. Gomperts, R. E. Stratmann, O. Yazyev, A. J. Austin, R. Cammi, C. Pomelli, J. W. Ochterski, R. L. Martin, K. Morokuma, V. G. Zakrzewski, G. A. Voth, P. Salvador, J. J. Dannenberg, S. Dapprich, A. D. Daniels, Ö. Farkas, J. B. Foresman, J. V. Ortiz, J. Cioslowski, D. J. Fox, *Gaussian 09*, **2009**.
135 Y. Tawada, T. Tsuneda, S. Yanagisawa, T. Yanai, K. Hirao, *J. Chem. Phys.*, **2004**, *120*, 8425.
136 T. Yanai, D. P. Tew, N. C. Handy, *Chem. Phys. Lett.*, **2004**, *393*, 51.
137 N. M. O'Boyle, A. L. Tenderholt, K. M. Langner, *J. Comput. Chem.*, **2008**, *29*, 839.
138 A. J. C. Kuehne, D. Elfström, A. R. Mackintosh, A. L. Kanibolotsky, B. Guilhabert, E. Gu, I. F. Perepichka, P. J. Skabara, M. D. Dawson, R. A. Pethrick, *Adv. Mater.*, **2009**, *21*, 781.
139 R. W. Martin, P. G. Middleton, K. P. O'Donnell, W. Van der Stricht, *Appl. Phys. Lett.*, **1999**, *74*, 263.
140 D. M. Ruthven, *Principles of Adsorption and Adsorption Processes*, Wiley, **1984**.
141 E. Taylor-Shaw, E. Angioni, N. J. Findlay, B. Breig, A. R. Inigo, J. Bruckbauer, D. J. Wallis, P. J. Skabara, R. W. Martin, *J. Mater. Chem. C*, **2016**, *4*, 11499.
142 N. J. Findlay, B. Breig, C. Forbes, A. R. Inigo, A. L. Kanibolotsky, P. J. Skabara, *J. Mater. Chem. C*, **2016**.
143 Q. Verolet, S. Soleimanpour, K. Fujisawa, M. Dal Molin, N. Sakai, S. Matile, *ChemistryOpen*, **2015**, *4*, 264.
144 H. Nakanotani, T. Furukawa, K. Morimoto, C. Adachi, *Science Advances*, **2016**, *2*.
145 J. Kalinowski, *Mater. Sci.-Poland*, **2009**, *27*, 735.
146 J. Kalinowski, G. Giro, M. Cocchi, V. Fattori, P. Di Marco, *Appl. Phys. Lett.*, **2000**, *76*, 2352.
147 C.-C. Yang, C.-J. Hsu, P.-T. Chou, H. C. Cheng, Y. O. Su, M.-k. Leung, *J. Phys. Chem. B*, **2010**, *114*, 756.
148 H. Li, J. Balsells, *Tetrahedron Lett.*, **2008**, *49*, 2034.
149 D. Rankine, A. Avellaneda, M. R. Hill, C. J. Doonan, C. J. Sumby, *Chem. Commun.*, **2012**, *48*, 10328.
150 M. Sauer, J. Hofkens, J. Enderlein, *Basic Principles of Fluorescence Spectroscopy*, in *Handbook of Fluorescence Spectroscopy and Imaging*, Wiley-VCH Verlag GmbH & Co. KGaA, **2011**, 1.
151 X. Zhao, H. Jiang, K. S. Schanze, *Macromolecules*, **2008**, *41*, 3422.
152 Y. G. Vlasov, A. A. Kruchinin, D. S. Ryabukhin, *Russ. J. Appl. Chem.*, **2013**, *86*, 1663.
153 B. R. Henry, J. D. Morrison, *J. Mol. Spectrosc.*, **1975**, *55*, 311.
154 J.-M. Raimundo, P. Blanchard, H. Brisset, S. Akoudad, J. Roncali, *Chem. Commun.*, **2000**, 939.
155 H. Usta, W. C. Sheets, M. Denti, G. Generali, R. Capelli, S. Lu, X. Yu, M. Muccini, A. Facchetti, *Chem. Mater.*, **2014**, *26*, 6542.
156 Y. Cao, T. Lei, J. Yuan, J.-Y. Wang, J. Pei, *Polym. Chem.*, **2013**, *4*, 5228.
157 P. Chávez, C. Ngov, P. d. Frémont, P. Lévêque, N. Leclerc, *J. Org. Chem.*, **2014**, *79*, 10179.
158 K. M. Omer, S.-Y. Ku, K.-T. Wong, A. J. Bard, *J. Am. Chem. Soc.*, **2009**, *131*, 10733.
159 G. M. Saltan, H. Dinçalp, M. Kıran, C. Zafer, S. Ç. Erbaş, *Mater. Chem. Phys.*, **2015**, *163*, 387.
160 J.-L. Bredas, *Mater. Horiz.*, **2014**, *1*, 17.
161 B. Grimm, C. Risko, J. D. Azoulay, J.-L. Bredas, G. C. Bazan, *Chem. Sci.*, **2013**, *4*, 1807.
162 S. Miertuš, E. Scrocco, J. Tomasi, *Chem. Phys.*, **1981**, *55*, 117.
163 A. D. Becke, *J. Chem. Phys.*, **1993**, *98*, 5648.
164 J.-D. Chai, M. Head-Gordon, *Phys. Chem. Chem. Phys.*, **2008**, *10*, 6615.
165 Y. Zhao, D. Truhlar, *Theor. Chem. Acc.*, **2008**, *120*, 215.
166 C. Adamo, V. Barone, *J. Chem. Phys.*, **1999**, *110*, 6158.

167 D. Jacquemin, V. Wathelet, E. A. Perpète, C. Adamo, *J. Chem. Theory Comput.*, **2009**, *5*, 2420.
168 T. C. Parker, D. G. Patel, K. Moudgil, S. Barlow, C. Risko, J.-L. Bredas, J. R. Reynolds, S. R. Marder, *Mater. Horiz.*, **2015**, *2*, 22.
169 J. C. Blakesley, F. A. Castro, W. Kylberg, G. F. A. Dibb, C. Arantes, R. Valaski, M. Cremona, J. S. Kim, J.-S. Kim, *Org. Electron.*, **2014**, *15*, 1263.
170 S. R. Tseng, Y. S. Chen, H. F. Meng, H. C. Lai, C. H. Yeh, S. F. Horng, H. H. Liao, C. S. Hsu, *Synth. Met.*, **2009**, *159*, 137.
171 Y.-H. Lee, T.-C. Wu, C.-W. Liaw, T.-C. Wen, S.-W. Feng, J.-J. Lee, Y.-T. Wu, T.-F. Guo, *Org. Electron.*, **2013**, *14*, 1064.
172 A. Michaleviciute, E. Gurskyte, D. Y. Volyniuk, V. V. Cherpak, G. Sini, P. Y. Stakhira, J. V. Grazulevicius, *J. Phys. Chem. C*, **2012**, *116*, 20769.
173 S. Kwon, K.-R. Wee, C. Pac, S. O. Kang, *Org. Electron.*, **2012**, *13*, 645.
174 L.-Y. Zou, A.-M. Ren, J.-K. Feng, X.-Q. Ran, *J. Phys. Org. Chem.*, **2009**, *22*, 1104.
175 H. Mattoussi, H. Murata, C. D. Merritt, Y. Iizumi, J. Kido, Z. H. Kafafi, *J. Appl. Phys.*, **1999**, *86*, 2642.
176 E. Angioni, M. Chapran, K. Ivaniuk, N. Kostiv, V. Cherpak, P. Stakhira, A. Lazauskas, S. Tamulevicius, D. Volyniuk, N. J. Findlay, T. Tuttle, J. V. Grazulevicius, P. J. Skabara, *J. Mater. Chem. C*, **2016**, *4*, 3851.
177 S. T. Meek, J. A. Greathouse, M. D. Allendorf, *Adv. Mater.*, **2011**, *23*, 249.
178 N. L. Rosi, M. Eddaoudi, J. Kim, M. O'Keeffe, O. M. Yaghi, *CrystEngComm*, **2002**, *4*, 401.
179 H. Li, M. Eddaoudi, M. O'Keeffe, O. M. Yaghi, *Nature*, **1999**, *402*, 276.
180 G. Bellussi, A. Carati, C. Rizzo, R. Millini, *Catal. Sci. Tech.*, **2013**, *3*, 833.
181 G. Ferey, *Chem. Soc. Rev.*, **2008**, *37*, 191.
182 M. Lalonde, W. Bury, O. Karagiaridi, Z. Brown, J. T. Hupp, O. K. Farha, *J. Mater. Chem. A*, **2013**, *1*, 5453.
183 N. L. Rosi, J. Eckert, M. Eddaoudi, D. T. Vodak, J. Kim, M. O'Keeffe, O. M. Yaghi, *Science*, **2003**, *300*, 1127.
184 D. Britt, D. Tranchemontagne, O. M. Yaghi, *Proc. Natl. Acad. Sci. USA*, **2008**, *105*, 11623.
185 D. Zacher, O. Shekhah, C. Woll, R. A. Fischer, *Chem. Soc. Rev.*, **2009**, *38*, 1418.
186 J. Won, J. S. Seo, J. H. Kim, H. S. Kim, Y. S. Kang, S. J. Kim, Y. Kim, J. Jegal, *Adv. Mater.*, **2005**, *17*, 80.
187 J. Lee, O. K. Farha, J. Roberts, K. A. Scheidt, S. T. Nguyen, J. T. Hupp, *Chem. Soc. Rev.*, **2009**, *38*, 1450.
188 L. Ma, C. Abney, W. Lin, *Chem. Soc. Rev.*, **2009**, *38*, 1248.
189 D. Jiang, A. Urakawa, M. Yulikov, T. Mallat, G. Jeschke, A. Baiker, *Chem. Eur. J.*, **2009**, *15*, 12255.
190 K. Brown, S. Zolezzi, P. Aguirre, D. Venegas-Yazigi, V. Paredes-Garcia, R. Baggio, M. A. Novak, E. Spodine, *Dalton Trans.*, **2009**, 1422.
191 M. C. Bernini, F. Gándara, M. Iglesias, N. Snejko, E. Gutiérrez-Puebla, E. V. Brusau, G. E. Narda, M. Á. Monge, *Chem. Eur. J.*, **2009**, *15*, 4896.
192 U. Ravon, M. Savonnet, S. Aguado, M. E. Domine, E. Janneau, D. Farrusseng, *Micropor. Mesopor. Mater.*, **2010**, *129*, 319.
193 T. Osako, Y. Uozumi, *Heterocycles*, **2010**, *80*, 505.
194 S. Proch, J. Herrmannsdörfer, R. Kempe, C. Kern, A. Jess, L. Seyfarth, J. Senker, *Chem. Eur. J.*, **2008**, *14*, 8204.
195 H.-L. Jiang, B. Liu, T. Akita, M. Haruta, H. Sakurai, Q. Xu, *J. Am. Chem. Soc.*, **2009**, *131*, 11302.
196 G. Férey, *J. Solid State Chem.*, **2000**, *152*, 37.
197 S. Surble, F. Millange, C. Serre, G. Ferey, R. I. Walton, *Chem. Commun.*, **2006**, 1518.
198 K. M. L. Taylor-Pashow, J. D. Rocca, Z. Xie, S. Tran, W. Lin, *J. Am. Chem. Soc.*, **2009**, *131*, 14261.
199 H.-L. Jiang, Y. Tatsu, Z.-H. Lu, Q. Xu, *J. Am. Chem. Soc.*, **2010**, *132*, 5586.
200 M. Sadakiyo, T. Yamada, H. Kitagawa, *J. Am. Chem. Soc.*, **2009**, *131*, 9906.
201 S. Takaishi, M. Hosoda, T. Kajiwara, H. Miyasaka, M. Yamashita, Y. Nakanishi, Y. Kitagawa, K. Yamaguchi, A. Kobayashi, H. Kitagawa, *Inorg. Chem.*, **2009**, *48*, 9048.
202 M. D. Allendorf, C. A. Bauer, R. K. Bhakta, R. J. T. Houk, *Chem. Soc. Rev.*, **2009**, *38*, 1330.
203 W. Feng, Y. Xu, G. Zhou, C. Zhang, X. Zheng, *Inorg. Chem. Commun.*, **2007**, *10*, 49.
204 S. Dang, J.-H. Zhang, Z.-M. Sun, *J. Mater. Chem.*, **2012**, *22*, 8868.
205 X.-L. Wang, Y.-F. Bi, H.-Y. Lin, G.-C. Liu, *Cryst. Growth Des.*, **2007**, *7*, 1086.

206 X. Li, X.-W. Wang, Y.-H. Zhang, *Inorg. Chem. Commun.*, **2008**, *11*, 832.
207 D. P. Martin, M. A. Braverman, R. L. LaDuca, *Cryst. Growth Des.*, **2007**, *7*, 2609.
208 Z. Hu, G. Huang, W. P. Lustig, F. Wang, H. Wang, S. J. Teat, D. Banerjee, D. Zhang, J. Li, *Chem. Commun.*, **2015**, *51*, 3045.
209 D. Wu, F. Xu, B. Sun, R. Fu, H. He, K. Matyjaszewski, *Chem. Rev.*, **2012**, *112*, 3959.
210 W. Lu, Z. Wei, D. Yuan, J. Tian, S. Fordham, H.-C. Zhou, *Chem. Mater.*, **2014**, *26*, 4589.
211 B. Beiler, Á. Vincze, F. Svec, Á. Sáfrány, *Polymer*, **2007**, *48*, 3033.
212 C. D. Wood, B. Tan, A. Trewin, F. Su, M. J. Rosseinsky, D. Bradshaw, Y. Sun, L. Zhou, A. I. Cooper, *Adv. Mater.*, **2008**, *20*, 1916.
213 M. Rose, N. Klein, I. Senkovska, C. Schrage, P. Wollmann, W. Bohlmann, B. Bohringer, S. Fichtner, S. Kaskel, *J. Mater. Chem.*, **2011**, *21*, 711.
214 D. A. Olson, L. Chen, M. A. Hillmyer, *Chem. Mater.*, **2008**, *20*, 869.
215 J. K. Kim, S. Y. Yang, Y. Lee, Y. Kim, *Prog. Polym. Sci.*, **2010**, *35*, 1325.
216 P. M. Budd, B. S. Ghanem, S. Makhseed, N. B. McKeown, K. J. Msayib, C. E. Tattershall, *Chem. Commun.*, **2004**, 230.
217 J. Weber, Q. Su, M. Antonietti, A. Thomas, *Macromol. Rapid Commun.*, **2007**, *28*, 1871.
218 B. Li, X. Huang, L. Liang, B. Tan, *J. Mater. Chem.*, **2010**, *20*, 7444.
219 A. P. Côté, A. I. Benin, N. W. Ockwig, M. O'Keeffe, A. J. Matzger, O. M. Yaghi, *Science*, **2005**, *310*, 1166.
220 K. S. W. Sing, *Pure Appl. Chem.*, **1985**, *57*, 603.
221 N. Du, G. P. Robertson, J. Song, I. Pinnau, S. Thomas, M. D. Guiver, *Macromolecules*, **2008**, *41*, 9656.
222 S. S. Han, H. Furukawa, O. M. Yaghi, W. A. Goddard, *J. Am. Chem. Soc.*, **2008**, *130*, 11580.
223 C. J. Doonan, D. J. Tranchemontagne, T. G. Glover, J. R. Hunt, O. M. Yaghi, *Nature Chem.*, **2010**, *2*, 235.
224 R. Dawson, D. J. Adams, A. I. Cooper, *Chem. Sci.*, **2011**, *2*, 1173.
225 Z. Shi, Y. Zhou, D. Yan, *Macromol. Rapid Commun.*, **2006**, *27*, 1265.
226 M. R. Abidian, D. H. Kim, D. C. Martin, *Adv. Mater.*, **2006**, *18*, 405.
227 I. Pulko, J. Wall, P. Krajnc, N. R. Cameron, *Chem. Eur. J.*, **2010**, *16*, 2350.
228 S. J. Pierre, J. C. Thies, A. Dureault, N. R. Cameron, J. C. M. van Hest, N. Carette, T. Michon, R. Weberskirch, *Adv. Mater.*, **2006**, *18*, 1822.
229 C. E. Chan-Thaw, A. Villa, P. Katekomol, D. Su, A. Thomas, L. Prati, *Nano Lett.*, **2010**, *10*, 537.
230 J. Huang, C.-a. Tao, Q. An, W. Zhang, Y. Wu, X. Li, D. Shen, G. Li, *Chem. Commun.*, **2010**, *46*, 967.
231 X. Hu, G. Li, M. Li, J. Huang, Y. Li, Y. Gao, Y. Zhang, *Adv. Funct. Mater.*, **2008**, *18*, 575.
232 S. Altarawneh, L. Nahar, I. U. Arachchige, A. a. O. El-Ballouli, K. M. Hallal, B. R. Kaafarani, M. G. Rabbani, R. K. Arvapally, H. M. El-Kaderi, *J. Mater. Chem. A*, **2015**, *3*, 3006.
233 A. Thomas, F. Goettmann, M. Antonietti, *Chem. Mater.*, **2008**, *20*, 738.
234 A. H. Lu, F. Schüth, *Adv. Mater.*, **2006**, *18*, 1793.
235 T. Kida, M. Mouri, M. Akashi, *Angew. Chem. Int. Ed.*, **2006**, *45*, 7534.
236 M. R. Buchmeiser, *Angew. Chem. Int. Ed.*, **2001**, *40*, 3795.
237 J. Bolton, T. S. Bailey, J. Rzayev, *Nano Lett.*, **2011**, *11*, 998.
238 J.-X. Jiang, A. I. Cooper, *Microporous Organic Polymers: Design, Synthesis, and Function*, in *Functional Metal-Organic Frameworks: Gas Storage, Separation and Catalysis*, Springer Berlin Heidelberg, **2010**, 1.
239 M. Mastalerz, *Angew. Chem. Int. Ed.*, **2008**, *47*, 445.
240 T. Ben, H. Ren, S. Ma, D. Cao, J. Lan, X. Jing, W. Wang, J. Xu, F. Deng, J. M. Simmons, S. Qiu, G. Zhu, *Angew. Chem. Int. Ed.*, **2009**, *48*, 9457.
241 D. Yuan, W. Lu, D. Zhao, H.-C. Zhou, *Adv. Mater.*, **2011**, *23*, 3723.
242 S. D. Kimmins, N. R. Cameron, *Adv. Funct. Mater.*, **2011**, *21*, 211.
243 H. Zhang, A. I. Cooper, *Soft Matter*, **2005**, *1*, 107.
244 X. Feng, X. Ding, D. Jiang, *Chem. Soc. Rev.*, **2012**, *41*, 6010.
245 S. Pramanik, C. Zheng, X. Zhang, T. J. Emge, J. Li, *J. Am. Chem. Soc.*, **2011**, *133*, 4153.
246 Y. Yuan, H. Ren, F. Sun, X. Jing, K. Cai, X. Zhao, Y. Wang, Y. Wei, G. Zhu, *J. Mater. Chem.*, **2012**, *22*, 24558.
247 X. Wu, H. Li, B. Xu, H. Tong, L. Wang, *Polym. Chem.*, **2014**, *5*, 4521.
248 J.-X. Jiang, A. Trewin, D. J. Adams, A. I. Cooper, *Chem. Sci.*, **2011**, *2*, 1777.
249 L. Guo, D. Cao, *J. Mater. Chem. C*, **2015**, *3*, 8490.

250 D. Wang, L. Li, W. Yang, Y. Zuo, S. Feng, H. Liu, *RSC Adv.*, **2014**, *4*, 59877.
251 S. Brunauer, P. H. Emmett, E. Teller, *J. Am. Chem. Soc.*, **1938**, *60*, 309.
252 C. Weidenthaler, *Nanoscale*, **2011**, *3*, 792.
253 A. Schaate, P. Roy, A. Godt, J. Lippke, F. Waltz, M. Wiebcke, P. Behrens, *Chem. Eur. J.*, **2011**, *17*, 6643.
254 Thanks to Dr Neil J. Findlay for have kindly provided these compounds.
255 P. I. Ravikovitch, A. V. Neimark, *Langmuir*, **2006**, *22*, 11171.
256 E. Stockel, X. Wu, A. Trewin, C. D. Wood, R. Clowes, N. L. Campbell, J. T. A. Jones, Y. Z. Khimyak, D. J. Adams, A. I. Cooper, *Chem. Commun.*, **2009**, 212.
257 K. S. Walton, R. Q. Snurr, *J. Am. Chem. Soc.*, **2007**, *129*, 8552.
258 S. R. Forrest, M. E. Thompson, *Chem. Rev.*, **2007**, *107*, 923.
259 C. Duan, F. Huang, Y. Cao, *J. Mater. Chem.*, **2012**, *22*, 10416.
260 Y. Lin, Y. Li, X. Zhan, *Chem. Soc. Rev.*, **2012**, *41*, 4245.
261 A. S. Özen, C. Atilgan, G. Sonmez, *J. Phys. Chem. C*, **2007**, *111*, 16362.
262 N. Hergué, C. Mallet, G. Savitha, M. Allain, P. Frère, J. Roncali, *Org. Lett.*, **2011**, *13*, 1762.
263 X. Guo, N. Zhou, S. J. Lou, J. W. Hennek, R. Ponce Ortiz, M. R. Butler, P.-L. T. Boudreault, J. Strzalka, P.-O. Morin, M. Leclerc, J. T. López Navarrete, M. A. Ratner, L. X. Chen, R. P. H. Chang, A. Facchetti, T. J. Marks, *J. Am. Chem. Soc.*, **2012**, *134*, 18427.
264 X. Guo, J. Quinn, Z. Chen, H. Usta, Y. Zheng, Y. Xia, J. W. Hennek, R. P. Ortiz, T. J. Marks, A. Facchetti, *J. Am. Chem. Soc.*, **2013**, *135*, 1986.
265 G. C. Welch, R. C. Bakus, S. J. Teat, G. C. Bazan, *J. Am. Chem. Soc.*, **2013**, *135*, 2298.
266 G. C. Welch, L. A. Perez, C. V. Hoven, Y. Zhang, X.-D. Dang, A. Sharenko, M. F. Toney, E. J. Kramer, T.-Q. Nguyen, G. C. Bazan, *J. Mater. Chem.*, **2011**, *21*, 12700.
267 G. C. Welch, G. C. Bazan, *J. Am. Chem. Soc.*, **2011**, *133*, 4632.
268 M. Pomerantz, Y. Cheng, *Tetrahedron Lett.*, **1999**, *40*, 3317.
269 M. Pomerantz, A. S. Amarasekara, H. V. R. Dias, *J. Org. Chem.*, **2002**, *67*, 6931.
270 J. A. Irvin, I. Schwendeman, Y. Lee, K. A. Abboud, J. R. Reynolds, *J. Polym. Sci. A Polym. Chem.*, **2001**, *39*, 2164.
271 H. Huang, Z. Chen, R. P. Ortiz, C. Newman, H. Usta, S. Lou, J. Youn, Y.-Y. Noh, K.-J. Baeg, L. X. Chen, A. Facchetti, T. Marks, *J. Am. Chem. Soc.*, **2012**, *134*, 10966.
272 T. Chivers, I. Krouse, M. Parvez, I. Vargas-Baca, T. Ziegler, P. Zoricak, *Inorg. Chem.*, **1996**, *35*, 5836.
273 Y.-H. Tian, M. Kertesz, *Macromolecules*, **2009**, *42*, 2309.
274 A. J. Cohen, P. Mori-Sánchez, W. Yang, *Science*, **2008**, *321*, 792.
275 A. J. Cohen, P. Mori-Sánchez, W. Yang, *Chem. Rev.*, **2012**, *112*, 289.
276 S. P. Kwasniewski, L. Claes, J.-P. François, M. S. Deleuze, *J. Chem. Phys.*, **2003**, *118*, 7823.
277 C. H. Choi, M. Kertesz, A. Karpfen, *Chem. Phys. Lett.*, **1997**, *276*, 266.
278 Y. Zhao, D. G. Truhlar, *J. Phys. Chem. A*, **2006**, *110*, 10478.
279 K. H. DuBay, M. L. Hall, T. F. Hughes, C. Wu, D. R. Reichman, R. A. Friesner, *J. Chem. Theory Comput.*, **2012**, *8*, 4556.
280 G. Raos, A. Famulari, V. Marcon, *Chem. Phys. Lett.*, **2003**, *379*, 364.
281 S. Kozuch, J. M. L. Martin, *J. Chem. Theory Comput.*, **2013**, *9*, 1918.
282 K. E. Riley, J. A. Platts, J. Řezáč, P. Hobza, J. G. Hill, *J. Phys. Chem. A*, **2012**, *116*, 4159.
283 A. I. Krylov, P. M. W. Gill, *Wiley Interdiscip. Rev. Comput. Mol. Sci.*, **2013**, *3*, 317.
284 M. Feyereisen, G. Fitzgerald, A. Komornicki, *Chem. Phys. Lett.*, **1993**, *208*, 359.
285 J. S. Sears, R. R. Chance, J.-L. Brédas, *J. Am. Chem. Soc.*, **2010**, *132*, 13313.
286 M. Katouda, S. Nagase, *J. Chem. Phys.*, **2010**, *133*.
287 N. E. Jackson, B. M. Savoie, K. L. Kohlstedt, M. Olvera de la Cruz, G. C. Schatz, L. X. Chen, M. A. Ratner, *J. Am. Chem. Soc.*, **2013**, *135*, 10475.
288 T. S. Moore, T. F. Winmill, *J. Chem. Soc., Trans.*, **1912**, *101*, 1635.
289 W. M. Latimer, W. H. Rodebush, *J. Am. Chem. Soc.*, **1920**, *42*, 1419.
290 G. Conboy, *Synthesis and characterisation of conjugated 4,8-benzobisthiazole derivatives for organic electronics*, PhD Thesis, University of Strathclyde, **2015**.
291 S.-W. P. Hwang, Eun-Rang; Chung, Yeon-Joon; Bae, Young-Ju; Kim, In-Tae, *Bull. Korean Chem. Soc.*, **2011**, *32*, 2446.
292 J.-G. Kang, H.-G. Cho, S. K. Kang, C. Park, S. W. Lee, G. B. Park, J. S. Lee, I. T. Kim, *J. Photochem. Photobiol. A*, **2006**, *183*, 212.
293 J.-G. Kang, H.-J. Kim, Y.-K. Jeong, M.-K. Nah, C. Park, Y. J. Bae, S. W. Lee, I. T. Kim, *J. Phys. Chem. B*, **2010**, *114*, 3791.

294 I. T. Kim, S. W. Lee, S. Y. Kim, J. S. Lee, G. B. Park, S. H. Lee, S. K. Kang, J.-G. Kang, C. Park, S.-H. Jin, *Synth. Met.*, **2006**, *156*, 38.
295 M. Domagała, S. J. Grabowski, *J. Phys. Chem. A*, **2005**, *109*, 5683.
296 J. Wirz, *Pure Appl. Chem.*, **1984**, *56*, 1289.
297 S. F. Boys, F. Bernardi, *Mol. Phys.*, **1970**, *19*, 553.
298 S. Grimme, *J. Chem. Phys.*, **2003**, *118*, 9095.
299 R. A. Distasio Jr, M. Head-Gordon, *Mol. Phys.*, **2007**, *105*, 1073.
300 S. Kozuch, J. M. L. Martin, *J. Comput. Chem.*, **2013**, *34*, 2327.
301 A. S. Özen, F. De Proft, V. Aviyente, P. Geerlings, *J. Phys. Chem. A*, **2006**, *110*, 5860.
302 J. G. Angyan, R. A. Poirier, A. Kucsman, I. G. Csizmadia, *J. Am. Chem. Soc.*, **1987**, *109*, 2237.
303 G. Raos, A. Famulari, S. V. Meille, M. C. Gallazzi, G. Allegra, *J. Phys. Chem. A*, **2004**, *108*, 691.
304 J. Emsley, *Chem. Soc. Rev.*, **1980**, *9*, 91.
305 J. Grunenberg, *J. Am. Chem. Soc.*, **2004**, *126*, 16310.
306 G. Conboy, H. J. Spencer, E. Angioni, A. L. Kanibolotsky, N. J. Findlay, S. J. Coles, C. Wilson, M. B. Pitak, C. Risko, V. Coropceanu, J.-L. Bredas, P. J. Skabara, *Mater. Horiz.*, **2016**, *3*, 333.
307 G. R. Fulmer, A. J. M. Miller, N. H. Sherden, H. E. Gottlieb, A. Nudelman, B. M. Stoltz, J. E. Bercaw, K. I. Goldberg, *Organometallics*, **2010**, *29*, 2176.
308 J. C. de Mello, H. F. Wittmann, R. H. Friend, *Adv. Mater.*, **1997**, *9*, 230.
309 E. Miyamoto, Y. Yamaguchi, M. Yokoyama, *J. Imaging Sci. Technol.*, **1989**, *28*, 364.
310 V. Cherpak, A. Gassmann, P. Stakhira, D. Volyniuk, J. V. Grazulevicius, A. Michaleviciute, A. Tomkeviciene, G. Barylo, H. von Seggern, *Org. Electron.*, **2014**, *15*, 1396.
311 N. C. Greenham, R. H. Friend, D. D. C. Bradley, *Adv. Mater.*, **1994**, *6*, 491.
312 M. A. F. Baldo, S. R.; Thompson, M. E. , *Organic Electroluminescence*, CRC Press, **2005**.
313 N. F. Mott, R. W. Gurney, *Electronic Processes in Ionic Crystals*, Oxford University Press, **1940**.
314 L. Malatesia, M. Angoletta, *J. Chem. Soc.*, **1957**, 1186.
315 J. Cremer, E. Mena-Osteritz, N. G. Pschierer, K. Mullen, P. Bauerle, *Org. Biomol. Chem.*, **2005**, *3*, 985.
316 C. van der Pol, M. R. Bryce, M. Wielopolski, C. Atienza-Castellanos, D. M. Guldi, S. Filippone, N. Martín, *J. Org. Chem.*, **2007**, *72*, 6662.
317 G. Hughes, C. Wang, A. S. Batsanov, M. Fern, S. Frank, M. R. Bryce, I. F. Perepichka, A. P. Monkman, B. P. Lyons, *Org. Biomol. Chem.*, **2003**, *1*, 3069.
318 M. E. Walther, J. Grilj, D. Hanss, E. Vauthey, O. S. Wenger, *Eur. J. Inorg. Chem.*, **2010**, *2010*, 4843.
319 M. Frizler, J. Schmitz, A.-C. Schulz-Fincke, M. Gütschow, *J. Med. Chem.*, **2012**, *55*, 5982.
320 B. Fu, J. Baltazar, Z. Hu, A.-T. Chien, S. Kumar, C. L. Henderson, D. M. Collard, E. Reichmanis, *Chem. Mater.*, **2012**, *24*, 4123.
321 B. P. Karsten, J. C. Bijleveld, L. Viani, J. Cornil, J. Gierschner, R. A. J. Janssen, *J. Mater. Chem.*, **2009**, *19*, 5343.
322 C. Edder, J. M. J. Fréchet, *Org. Lett.*, **2003**, *5*, 1879.
323 W.-Y. Wong, X. Wang, H.-L. Zhang, K.-Y. Cheung, M.-K. Fung, A. B. Djurišić, W.-K. Chan, *J. Organomet. Chem.*, **2008**, *693*, 3603.
324 D. Huesmann, P. M. DiCarmine, D. S. Seferos, *J. Mater. Chem.*, **2011**, *21*, 408.
325 D.-J. Cai, P.-H. Lin, C.-Y. Liu, *Eur. J. Org. Chem.*, **2015**, *2015*, 5448.
326 K. M. N. de Silva, E. Hwang, W. K. Serem, F. R. Fronczek, J. C. Garno, E. E. Nesterov, *ACS Appl. Mater. Interfaces*, **2012**, *4*, 5430.
327 J. Zhou, S. Xie, E. F. Amond, M. L. Becker, *Macromolecules*, **2013**, *46*, 3391.